Doctoral Dissertation

Towards Ion Transport Manipulation and Single Particle Sensing with Solid-State Nanopores

Iat Wai LEONG

submitted in partial satisfaction of the requirements for the degree of

DOCTOR OF PHILOSOPHY

in Chemistry,

Graduate School of Science, Osaka University

Examination Committee:

Professor Masateru Taniguchi, Chair

Professor Yasuhiro Nakazawa

Professor Takuya Matsumoto

OSAKA UNIVERSITY

January 2023

Abstract

Nanopore technology was first envisaged as a DNA sequencer, which already became a practical technology in a form of a bio-engineered transmembrane protein in a lipid bilayer. The sensor mechanism is based on resistive pulse sensing that can acquire physical information of an analyte by measuring the ionic blockade current characteristics as it passes through a pore in a thin membrane. In recent years, it has been rigorously discussed to expand the sensor's ability beyond the sequencing by leveraging the advanced nanofabrication techniques to form a hole of arbitral size from the scale of micrometer to nanometer. One of the goals has been to realize the characterizations of three-dimensional shapes and surface charge distributions of nanomaterials by nanopore sensing. To this end, however, the dynamics of mass and ion transportation in nanopores still remain poorly understood, and it is of crucial importance to deepening the fundamental understanding of the physics and chemistry behind the sensing mechanism. This research is devoted to studying the ion and mass transport in a solid-state nanopore of a low depth-to-diameter structure under a salinity gradient. The size of the pore is chosen to be at the sub-micrometer scale, where the ionic current and particle translocation tend to be affected by multiple physical features including electrophoresis/electromigration, electroosmosis, and diffusioosmosis. The membrane surface was fabricated by dielectric coatings to explore the roles of zeta potentials at the channel wall on the ion transport behavior as well as the nanoparticle translocation dynamics. Multi-physics simulations are used in combination with the ionic current measurements to elucidate the interplay of these factors and find a route toward optimal materials and designs of solid-state nanopores for characterizing nanomaterials.

Chapter 1 is a general introduction to the solid-state nanopores providing a brief explanation of the ionic current measurements. The effect of applying a salt gradient in the nanopore sensor is explained. Then, Chapter 2 describes the experimental methods including nanopore fabrications, ionic current measurements, SEM observations, COMSOL simulations, and data analyses.

In Chapter 3, asymmetric ion transport in a non-permselective nanopore was reported. Under uniform salt concentration conditions, the cross-pore ionic current showed ohmic characteristics with no bias polarity dependence. In stark contrast, despite the weak ion selectivity expected for the relatively large nanopores employed, nanopores exhibited diode-like behavior when a salt gradient was imposed across the thin membrane. An intriguing interplay between electro-osmotic flow and local ion density distributions in a solid-state pore is found to induce highly asymmetric ion transport. Chapter 4 shows negative differential resistance to resistive switching characteristics appeared under a 100-fold difference in the cross-membrane salt concentrations. In Chapter 5, a partial coating method to alter the nonlinear ionic current through a salt-gradient-biased pore was reported.

Chapter 6 - 8 focus on the topic of single nanoparticle sensing. In Chapter 6, the interference of ion diffusion kinetics at liquid-electrode interfaces in nanopore sensing was reported. A slow and large decrease was observed in the ionic current through a nanopore suggestive of the considerable influence of the growing impedance at the liquid-metal interfaces via Cottrell diffusion. In Chapter 7, the impact of using polymers as insulating layers in solid-state nanopores for single-particle detection is discussed. In Chapter 8 reports on single-nanoparticle translocation dynamics in a nanopore under salt gradients, wherein the effect

of EOF on the capture-to-translocation dynamics of analytes is studied. Chapter 9 explains the conclusions of this thesis and the future direction in nanotechnology with solid-state nanopores.

Keywords: ionic current, ion transport, nanofluidic, nanopores, electroosmotic flow

Towards Ion Transport Manipulation and Single Particle Sensing with Solid-State Nanopores

Table of contents

List of figures

List of tables

Chapter 1 Introduction

1.1. General introduction

In the present day, independent science is unable to cope with immediate technical bottlenecks. Therefore, interdisciplinary fields have emerged and developed, like the study of nanotechnologies that enables the creation of artificial nanomaterials with rich chemical and physical properties. To expand the development of nanomaterials, meanwhile, it is critical to be able to properly analyse and evaluate techniques at the nano-microscale.

Common analytical methods, such as spectroscopy (X-ray, UV-visible, IR or Raman), mass spectrometry, nuclear magnetic resonance spectroscopy, electrochemical analysis, or thermal analysis have all reached maturity. Those methods can characterize and evaluate the different characteristics of nanomaterials both qualitatively and quantitatively. Nevertheless, the information collected by those methods is an average of a group's behavior. Therefore, they cannot be used for the correct evaluation of the sample at a level of individual nanomaterials.

On the other hand, the most relevant nanotechnology in terms of sensor technology is perhaps electron microscopy (TEM or SEM) and scanning probe microscopy (SPM). The microscopy technique is good for analysing individual characteristics. Although it can obtain the information of a single sample very accurately, the requirements for sample preparation are generally strict, and it is difficult to measure a large number of samples at the same time.

Solid-state nanopore used for DNA sequencing is an emerging technology with high

throughput and the ability to analyse at the single molecule level. If the tiny pore expands to any size in proportion to the size of the sample passing through, the nanopores can be applied to the nano-micro scale by measuring the current signal in an aqueous solution without further pre-treatment (Figure 1.1).

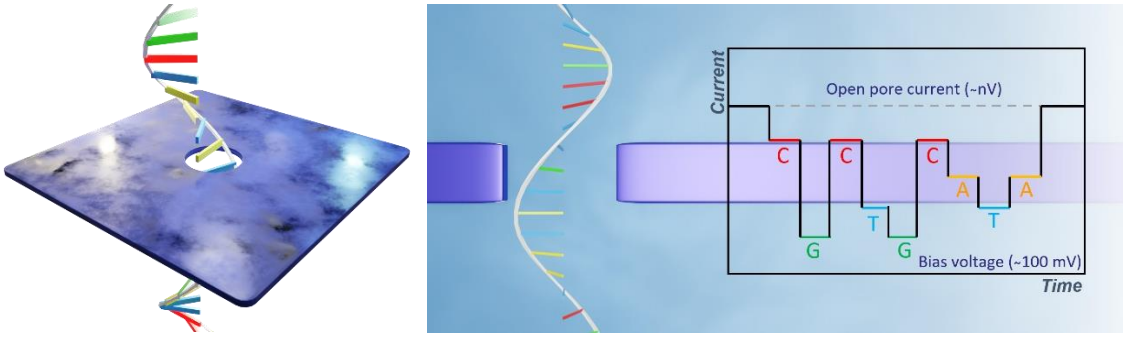

Figure 1.1 Single molecule and single particle sensing using solid-state nanopores

1.2. Solid-state nanopores

Nanopores are tiny pores at the nanoscale. The first results of DNA transport through a bio-nanopore were reported using a-hemolysin in 1996.[1] Soon after, the passage of DNA through solid-state nanopores was also first reported in 2001.[2] The solid-state nanopores, as the name suggests, are fabricated on solid membranes such as SiO_2, SiN_x. Using ionic current signals through a small aperture as a biosensing mechanism was first proposed in Coulter's invention in 1953.[3] The principle of resistive pulse sensing is shown in Figure 1.2. In brief, a bias voltage is applied at both ends of the nanopore to form an electric field, and ions move along the electric field according to their own charges resulting in an ionic current. At this point, if a substance passes through a nanopore, blocking the ionic current can reveal information about the substance. The surface of the nanopore has surface charges (in the case of SiN_x, it is generally negatively charged), and an electrical double layer (EDL) is formed by the solid surface (Figure 1.3a). The parameter to evaluate the size of EDL is called Debye length:

$$\lambda_D \equiv \sqrt{\frac{\epsilon_r \epsilon_0 k_B T}{e^2 \sum_j z_j^2 c_j}} \tag{1-1}$$

where ϵ_r and ϵ_0 are, respectively, the relative dielectric permittivity of the solvent and the vacuum permittivity, k_B is the Boltzmann constant, T is the thermodynamic temperature, e is the elementary charge, z_j is the valence of the jth ionic species, and c_j is the concentration of the jth ionic species.

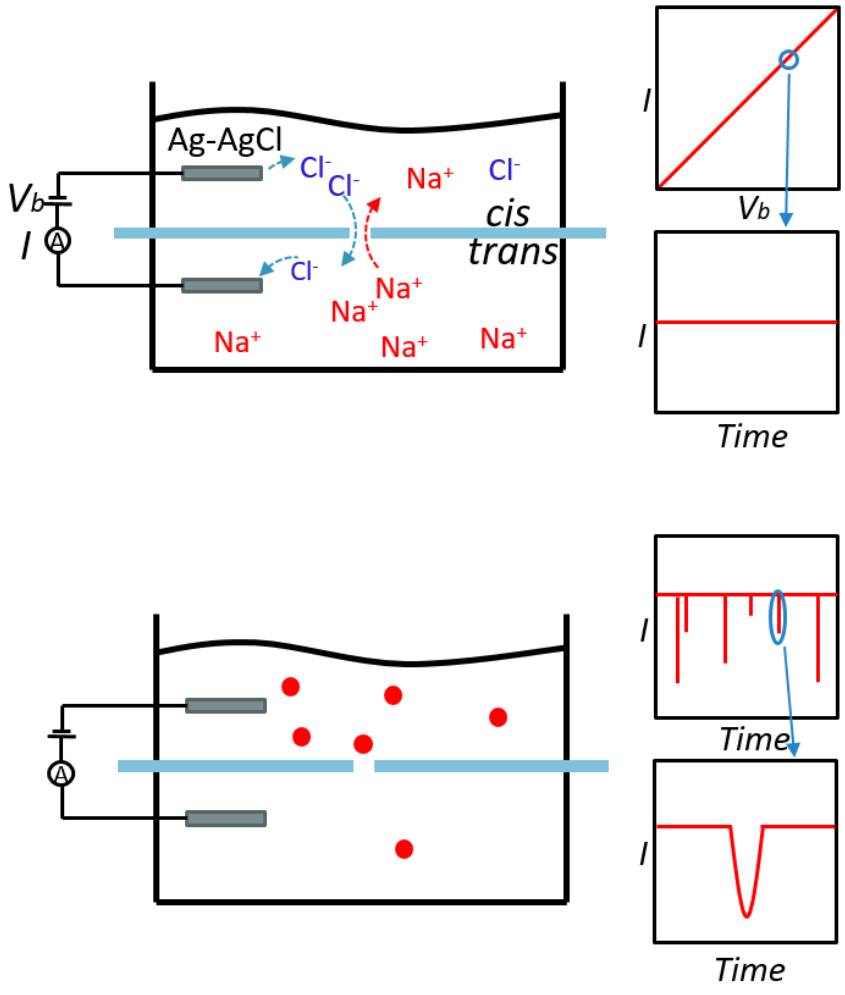

Figure 1.2 Principle of resistive pulse sensing

If the nanopore is smaller than the Debye length, it will form a situation that restricts the passage of counter ions, which is so-called ion selectivity. In addition, a fluid flow is generated on the charged surface, known as electroosmotic flow (Figure 1.3c). In general, the estimation of electroosmotic flow is as follows:

$$u_{\mathrm{EOF}} = -\frac{-\varepsilon \zeta_0 E}{\mu} \tag{1-2}$$

where ε is the relative permittivity of the fluid, ζ_0 is the surface charge (zeta potential) at the nanopore surfaces, E is the electric field, and μ is the dynamic viscosity of the fluid.

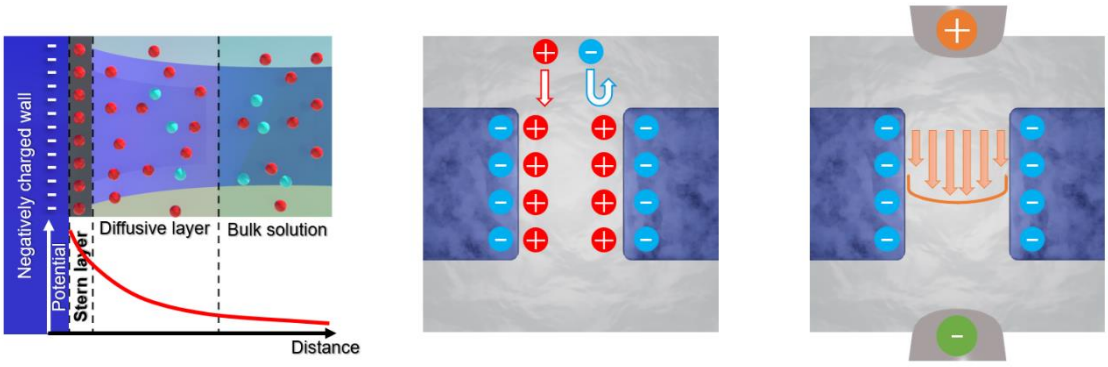

Figure 1.3 The physical phenomena of electrical double layer (EDL), ion selectivity and electroosmotic flow (EOF) in solid-state nanopores

By measuring the ionic current in the nanopore, the conductivity of the nanopore can be estimated. The concept of Maxwell access resistance [4] is the classic result for ions to the pore mouth (Figure 1.4). The resistance of the whole system in the experiment is given as follows:

$$R_{opening} = R_{pore(cylindrical)} + R_{access} = \frac{4\rho l}{\pi d^2} + \frac{\rho}{d} \quad (1\text{-}3)$$

Where ρ is the conductivity of electrolyte, d is the diameter of nanopore, l is the thickness of the free-standing membrane. The effective sensing space inside nanopore is fixed, so addressing the effective radius for access resistance will reflect the ionic current blockage event for the detected sample.

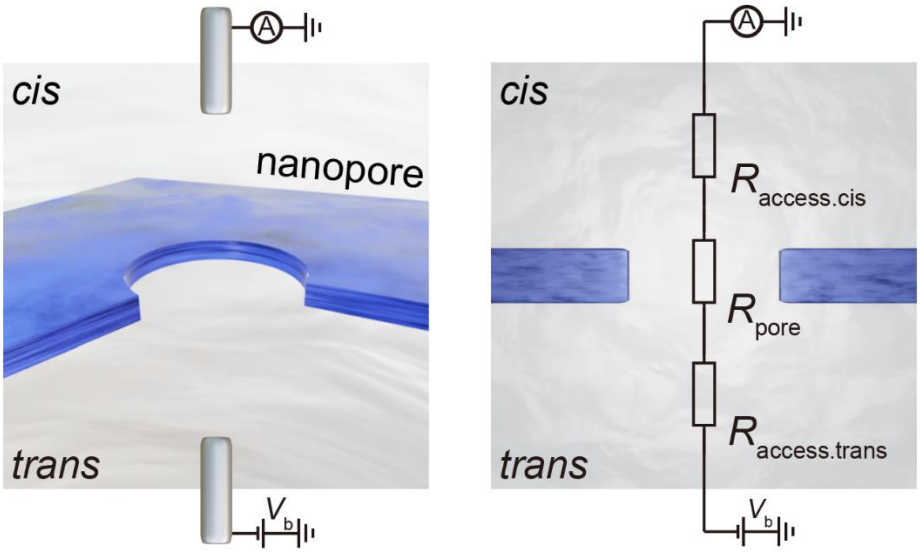

Figure 1.4 Maxwell access resistance in nanopore measurement

Even though solid-state nanopores have made remarkable progress in the past 20 years, compared with commercialized biological nanopores (Oxford Nanopore Technologies), solid-state nanopores still have many shortcomings. For improving the availability of solid-state nanopores, scientists combine advanced technologies (*i.e.*, FETs, gate voltages, optical enchantments). Among these approaches, the simple concept of applying a concentration gradient in nanopore experiments was first proposed by M. Wanunu *et al.* in 2010.[5] As the result of nanopore measurement under asymmetric ion concentration conditions, the capture rates were enhanced and translocation times of DNA were prolonged. The most interesting thing is that, in addition to being used as a sensor, this situation can also be used as a nanofluid transistor and osmotic power generator. However, this scenario happens only with ion-selective nanopores. This raises the question of what happens to the ion transport and single-sample detection if there are no EDL-overlapping.

1.3. Salt gradient in nanopore sensing

When the nanopore is much larger than the thickness of EDLs, both anions and cations can pass through the nanopore, resulting in the ion selectivity to almost disappearing. At this point, the effects of EOF will be stronger than that in the ion-selective nanopore (Figure 1.5a). If a particle translocation is carried out in this case, the influence of EOF on the particle will be much greater and more complex (Figure 1.5b). This thesis studies this unexplored topic of salt gradient-mediated ion and mass transport in sub-micrometer-scale conduits, where the ionic current and particle translocation motions are affected by several physical phenomena, including electrophoresis/electromigration, electroosmosis, and diffusioosmosis.

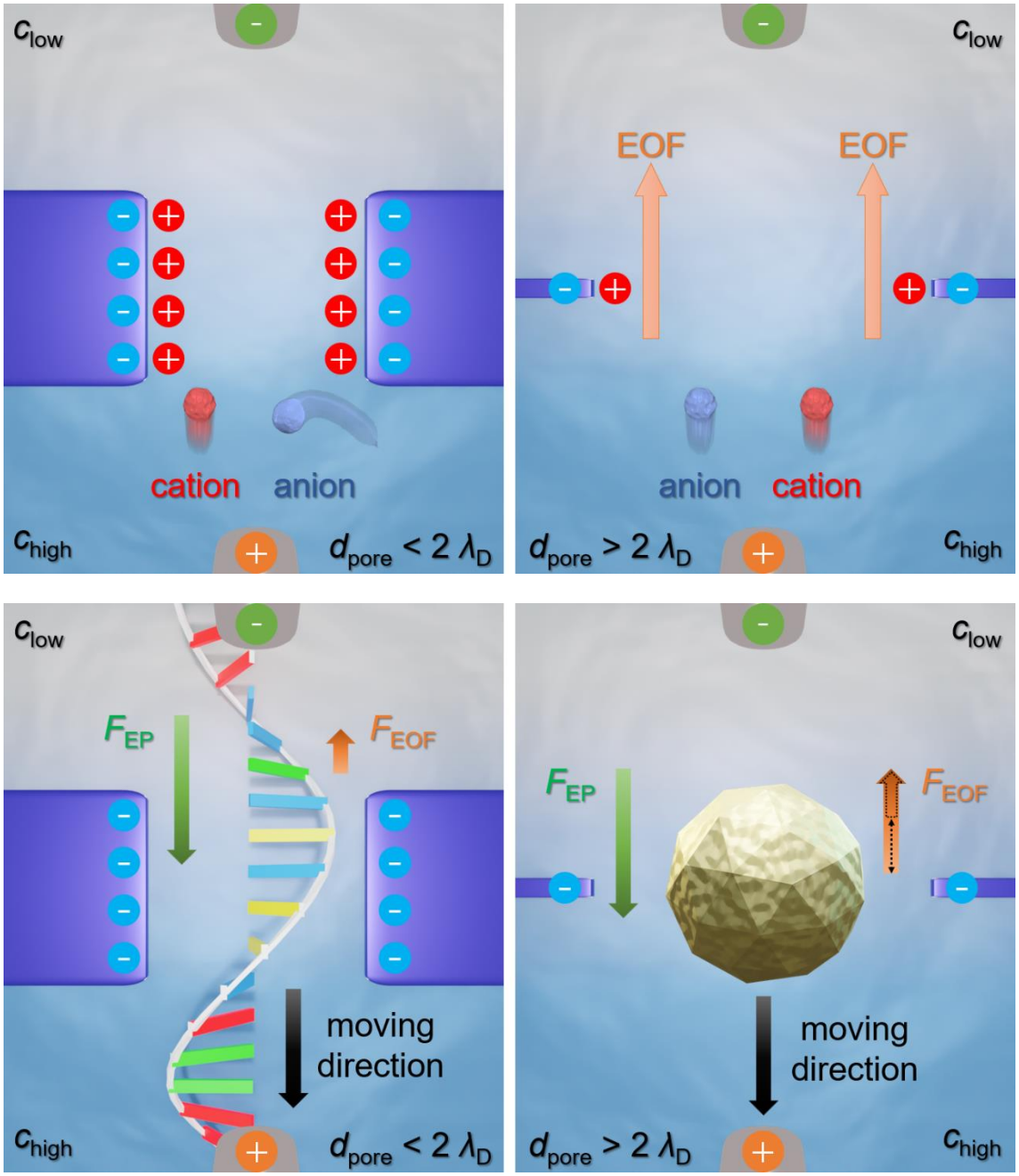

Figure 1.5 Comparison of ion transport (upper figure) and material passage (lower figure) in the case of nanopore size (relative to Debye length)

1.4. Outline

In this introduction, Chapter 1, the background of analytical methods for characterization in nanoscale, solid-state nanopores, and ionic current measurement was reviewed. In Chapter 2, the fabrication process, experimental methods, general measurement setup, and data progressing method have been summarized.

First, an asymmetric ion transport in a low thickness-to-diameter aspect ratio nanopore with a salt gradient was reported in Chapter 3. Under uniform salt concentration conditions, the cross-pore ionic current showed ohmic characteristics with no bias polarity dependence. In stark contrast, despite the weak ion selectivity expected for the relatively large nanopores employed, diode-like behavior was observed when a salt gradient was imposed across the thin membrane. Furthermore, in Chapter 4, quasi-stable ionic current characteristics and negative differential resistance behavior were presented when the cross-membrane salt concentrations increased to a 100-fold difference. In Chapter 5, a simple method to alter the nonlinear ionic current through a pore by partial dielectric coatings was studied. A variety of dielectric materials are examined on both the inner and outer surfaces of the channel with four different patterns of coated or uncoated surfaces. By controlling the specific part of the surface charge, the pore can behave like a resistor, diode, and bipolar junction transistor. Numerical simulations provide the reason for the asymmetric ion transport in the pore and illustrates the relationship between specifically charged surfaces and electroosmotic flow.

In Chapter 6, the interference of ion diffusion kinetics at liquid-electrode interfaces in nanopore sensing was elucidated. Using platinum as electrodes, a slow and large decrease was observed in the ionic current through a 300-nm sized nanopore in a salt solution

suggestive of the considerable influence of the growing impedance at the liquid-metal interfaces via Cottrell diffusion. When detecting nanoparticles, the resistive pulses became weaker following the steady increase in the resistance at the partially polarizable electrodes. The interfacial impedance was also demonstrated to couple with the nanopore chip capacitance thereby degrading the temporal resolution of the ionic current measurements in a time-varying manner. In Chapter 7, the influence of polymer coating on the temporal resolution of solid-state nanopores was systematically investigated. A SiN_x nanopore integrated with a polyimide sheet partially covering the substrate surface was used to compare the signals of ionic current blockage from single particle detection. Upon detecting the nanoparticles dispersed in an electrolyte buffer by ionic current measurements, a larger resistive pulse height was observed along with a faster current decay at the tails under larger coverage of the polymeric layer, thereby suggesting a prominent role of the water-touching SiN_x thin film as a significant capacitor serving to retard the ionic current response to the ion blockade by fast translocation of particles through the nanopores. In Chapter 8, the fine control of capture-to-translocation dynamics of analytes in solid-state nanopores using an applied salt gradient was discussed. The result showed a decrease up to a factor of 3 in the electrophoretic speed of nanoparticles at the pore exit along with an over 3-fold increase in particle detection efficiency by subjecting a 5-fold ion concentration difference across the dielectric membrane. The improvement in the sensor performance was elucidated to be a result of the salt-gradient-mediated electric field and electroosmotic flow asymmetry at nanochannel orifices.

Finally, Chapter 9 reviews all studies made in this thesis. And the outline research direction in future have been discussed.

Chapter 2 Fabrications and methods

2.1. Nanopores fabrication

The first solid-state nanopore was created by Golovchenko's group at Harvard University in a silicon nitride (SiN_x) membrane via a method called "ion beam sculpting".[6] Afterward, various methods have been invented for the pore drilling including focused electron beam (TEM drilling),[7] chemical etching,[8] and dielectric breakdown.[9] In this study, nanopores were formed in another way by drawing a fine patten on a layer of resist with electron-beam lithography (Elionix inc.) followed by reactive-ion etching for drilling the SiN_x layer.[10] Unless otherwise noted, these nanopores were formed in a 50 nm-thick SiN_x membrane. It allowed to fabricate a circular hole of various diameters as shown in Figure 2.1 for a case of a 300-nm sized nanopore.

The fabrication process starts with a 4-inch silicon wafer, which has a 50 nm thick silicon nitride thin film coated on its both sides by low-pressure chemical vapor deposition. Alignment marks are defined on the top side of the silicon wafer using photo-lithography and a chrome lift-off process (Figure 2.2). On the backside of the wafer, a metal mask was placed and treated it with reactive ion etching using CF_4 as the etchant gas to partially remove SiN_x of 1 mm × 1 mm square area. The wafer is then diced and divided into 25 x 25 mm components. The Si in the 1 mm × 1 mm square area was then dissolved in a 20% w/w KOH solution heated at 80 °C. By completely removing Si, a 50 nm-thick free-standing SiN_x film is obtained (Figure 2.3). After that, on the free-standing membrane side, an electron beam resists (ZEP520A) was spin-coated. Subsequently, a circle of a specific diameter was delineated by standard electron beam lithography. After development, the remaining resist layer was used

as a mask to open a nanopore by reactive ion etching (CF_4). The residual resist layer was removed by keeping the nanopore chip in *N, N*-dimethylformamide overnight followed by rinsing in isopropanol, ethanol, and acetone. The nanopore device is accomplished. (Figure 2.3)

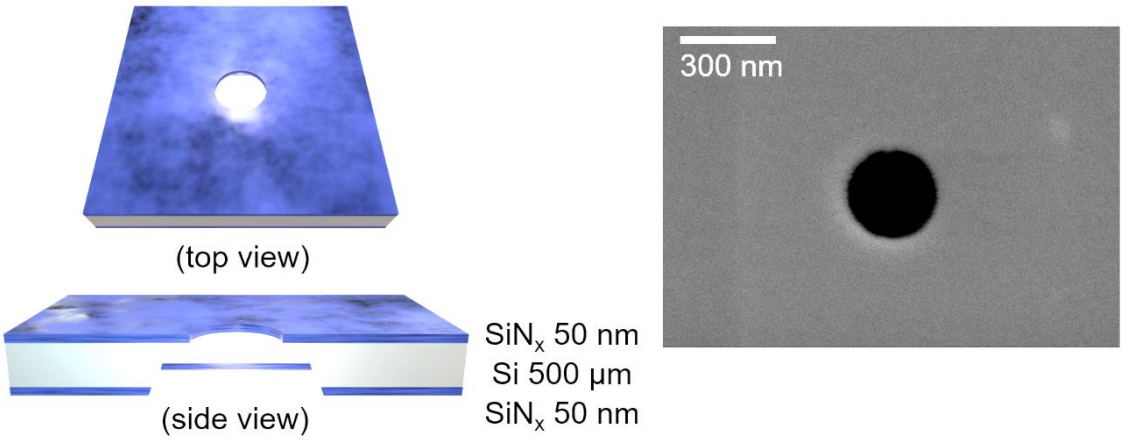

Figure 2.1 Sketch of a SiN_x nanopore device structure (left) and a scanning electron micrograph of a 300-nm sized nanopore formed in a 50 nm-thick SiN_x membrane on a Si chip.

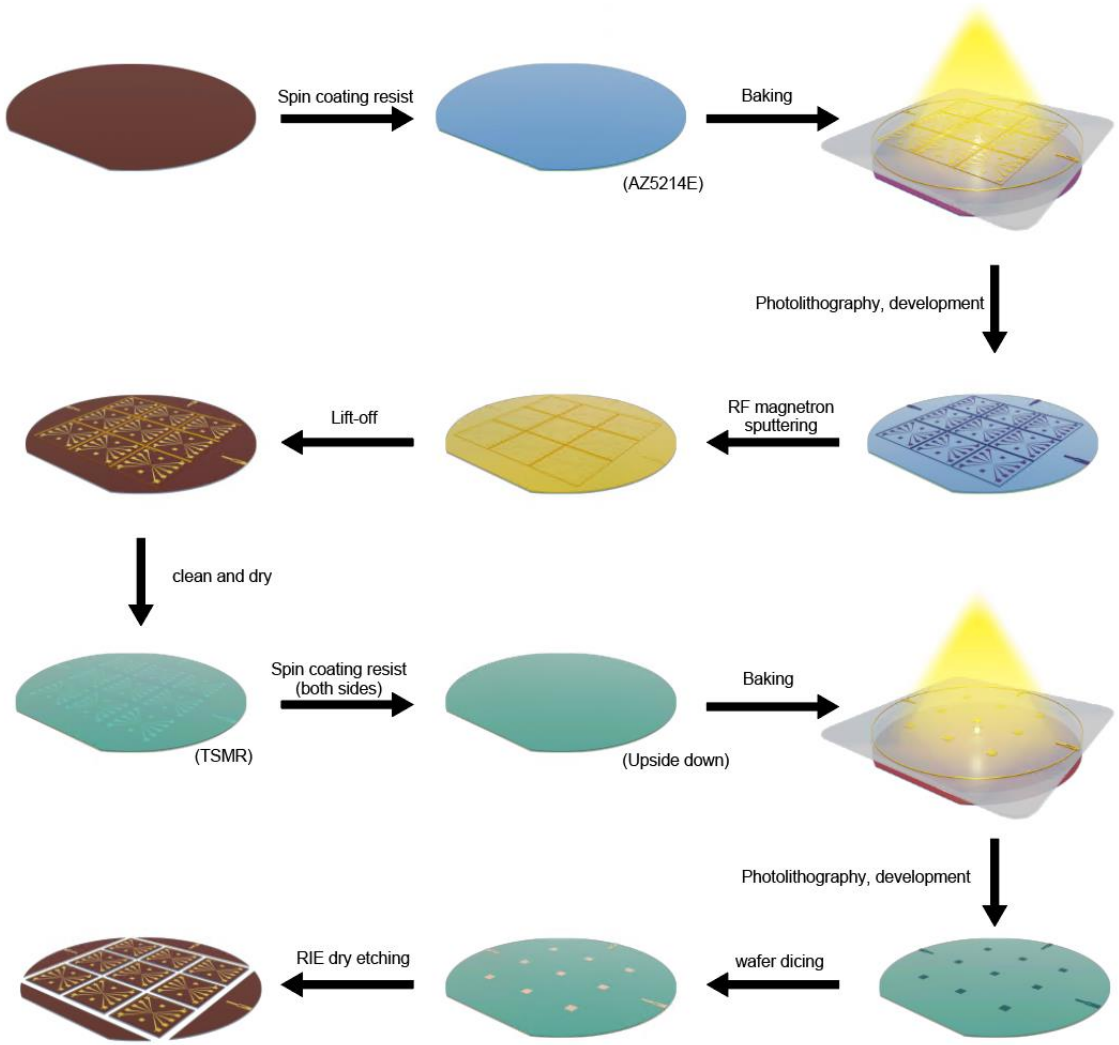

Figure 2.2 Pre-preparation processes for fabricating nanopore chips

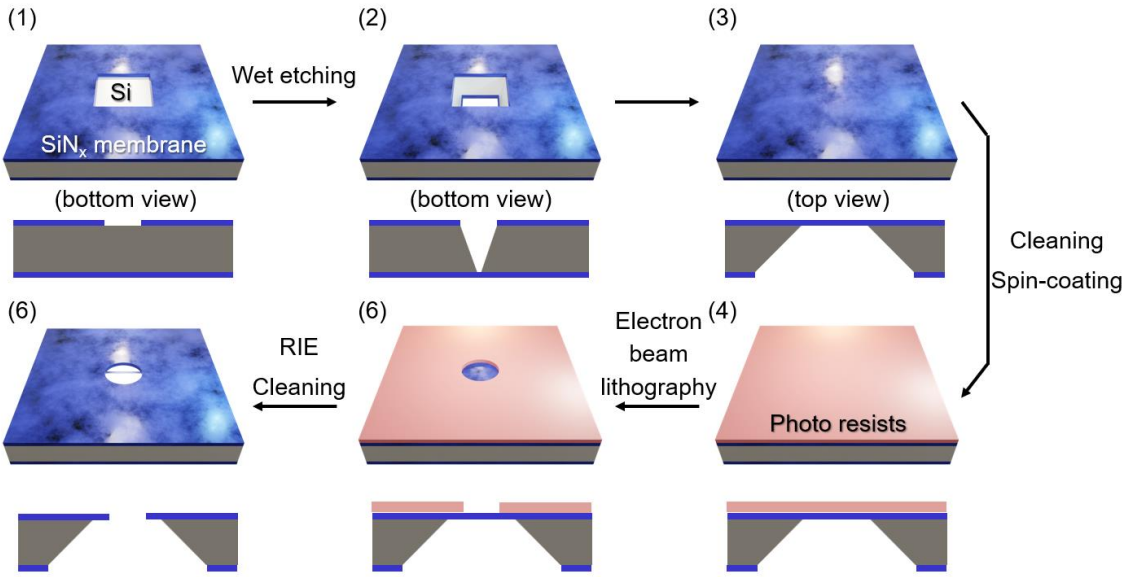

Figure 2.3 Fabrication procedure for forming SiN_x free standing membrane and drilling a nanopore

2.2. Measurements and data analysis

To measure the ionic current and detect particle translocation through a nanopore, a polydimethylsiloxane (PDMS; SYLGARD 184, Dow Corning) flow cell was used for sample injection and electrode connection. The PDMS blocks were created by imprinting on a SU-8/Si mold. For this, the surfaces of the PDMS blocks were pre-treated with oxygen plasma in prior to bond them together. Three holes in each block were used as an inlet and outlet to introduce PBS as well as a place to fix an Ag/AgCl electrode for ionic current measurements. PBS was capillary-injected into the channel-integrated pore. Two Ag/AgCl rods were then placed at both sides of the membrane via the holes punched in the PDMS block (Figure 2.4).

Ionic current versus voltage characteristics was measured and the resistance of the nanopore was compared to a theoretical estimation to ensure that the experimental configuration was setup in an appropriate manner. To obtain the ionic current- voltage characteristic data, PBS or KCl aqueous solution was used. All chemicals were purchased from a local distributor (Wako co., ltd.) and without further purification. The salt solution was diluted to specific ion concentrations with deionized water (Milli-Q IQ 7000 ultrapure water system). Filling the solution into the *cis* and *trans* using a syringe, the cross-membrane ionic current was measured using a pair of Ag/AgCl electrodes. The bias voltage was swept and the ionic current was recorded by Keithley 6487 (Keithley). For the *I-V* characteristic curve used in the experiment in each chapter, a 50 mV step was used for the sweep. All the measurements were conducted at room temperature in a Faraday cage under a program coded in LabVIEW.

For the nanoparticle translocation experiment, the ionic current flowing through the nanopore was recorded by applying a DC voltage to one of the Ag/AgCl electrodes and

measuring the output current at the other electrode via preamplification using a custom-designed current amplifier and digitizing using a fast digitizer (PXI-5922, National Instruments). All the measurements were conducted at room temperature in a Faraday cage under a program coded in LabVIEW.

Resistive pulse extractions and waveform analyses including the estimations of the pulse heights and widths as well as the pulse-to-pulse time were performed by custom scripts in Python3. Meanwhile, OriginPro software is used for further mathematical processing (such as exponential fit).

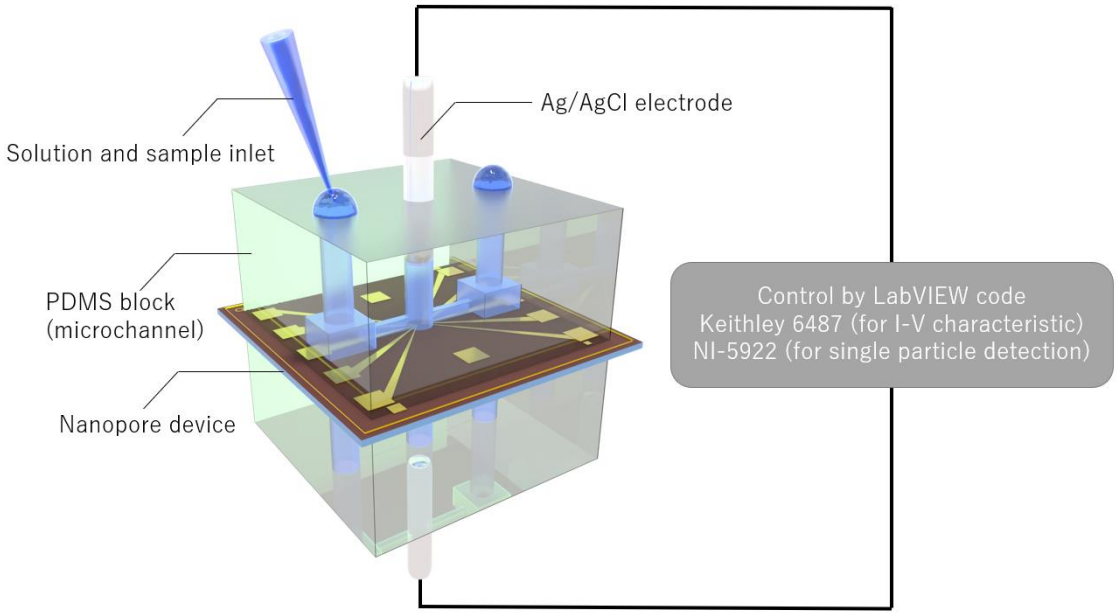

Figure 2.4 Sample injection and measurement setup

2.3. Multiphysics simulation

Finite element calculations were used to simulate ion transport, fluidic flow and the forces exerted on nanoparticle at a nanopore. A cylindrical pore was defined in a 2D axisymmetric model. The detail of the geometry, meshing setting and boundary conditions used in the finite element simulations are shown in Figure 2.5 and also in Table 2-1. The cross-pore ion and fluid transport was then simulated by solving coupled Poisson–Nernst–Planck and Navier–Stokes equations using COMSOL Multiphysics 5.6 software with AC/DC and chemical species transport and fluid flow modules. All equations were solved under steady-state by a MUMPS direct solver.

Specifically, Poisson-Nernst-Planck equation (ionic flux consists of diffusion, convection, and electromigration) is given as,

$$-\varepsilon_f \nabla^2 \phi = \rho_e,$$
$$\nabla \cdot \mathbf{J}_i = \nabla \cdot \left[C_i \mathbf{u} - D_i \left(\nabla C_i + \frac{F}{RT} z_i C_i \nabla \phi \right) \right] = 0, \quad (2\text{-}1)$$

On the other hand, Navier-Stokes equation is described as,

$$\nabla \cdot \mathbf{u} = 0,$$
$$\eta \nabla^2 \mathbf{u} - \nabla p - \rho_e \nabla \phi = \mathbf{0}. \quad (2\text{-}2)$$

The surface charge density at the SiN_x nanopore was changed from 0 to −100 mC/m² (Figure 3.3d). Generally, the value of surface charge density at the SiN_x membrane was assumed to be -10 – -15 mC/m² (also see Chapter 3 and Chapter 8). The ionic current can be calculated as follows.

$$I_{open} = \int_S F \left(\sum_{i=1}^{2} z_i J_i \right) \cdot n dS \quad (2\text{-}3)$$

In Chapter8, the electrophoretic and drag force acting on nanoparticle were estimated by the procedure reported in the previous literature.[11]

For example, the electrophoretic force (on a particle) is obtained through,

$$\overrightarrow{F_{\mathrm{EP}}} = -e \oiint \vec{E} \sigma ds \tag{2-4}$$

For the viscous drag force (on a particle), it is expressed as,

$$\overrightarrow{F_{\mathrm{EOF}}} = \oiint \overrightarrow{f_{\mathrm{EOF}}} ds = -\eta \oiint \frac{\partial \overrightarrow{u}}{\partial r} ds \tag{2-5}$$

All symbols are explained in Table 2-1.

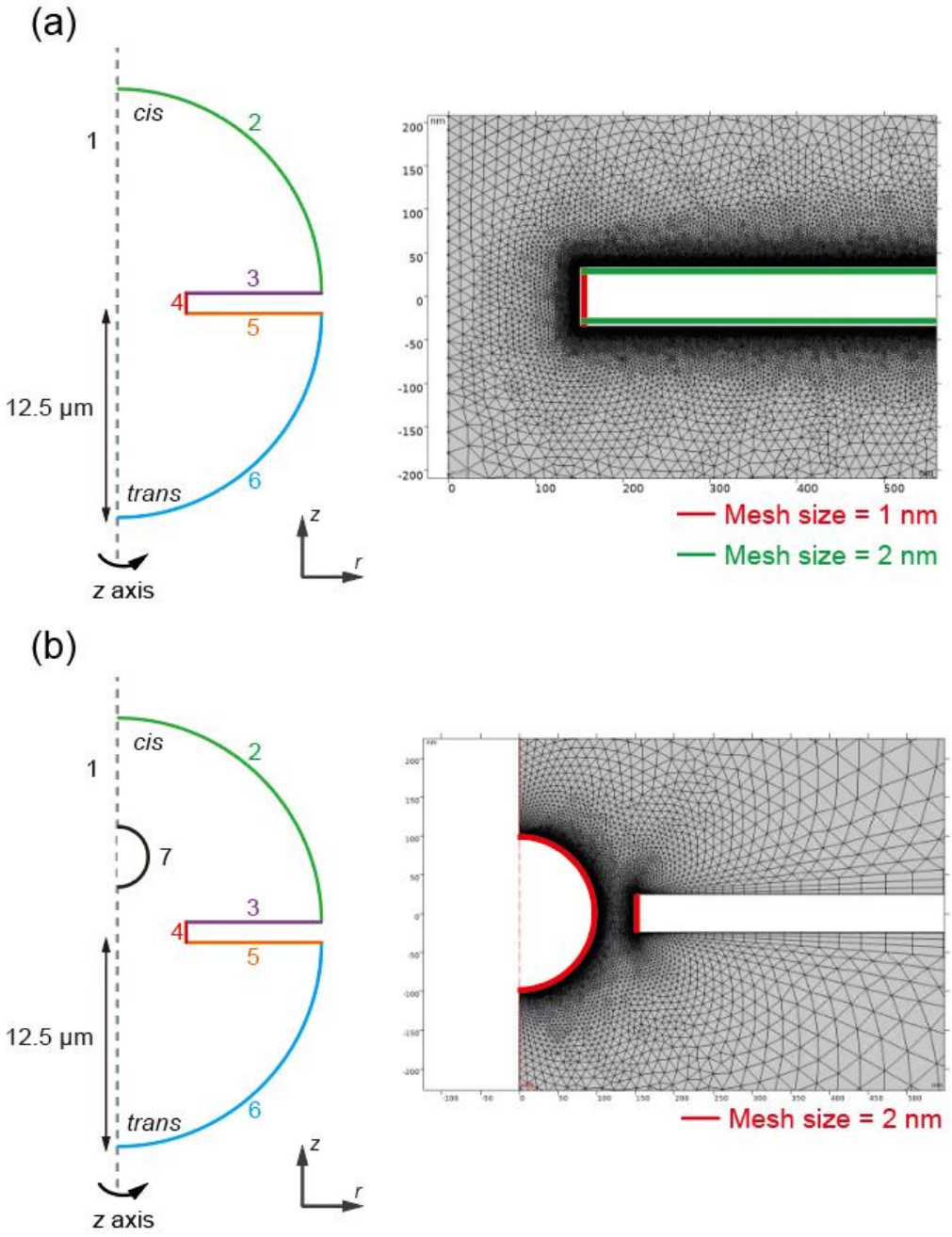

Figure 2.5 Mesh conditions used in the finite element simulations

The model of boundary and mesh conditions is used in Chapter 3-5 (a) and Chapter 6, 8 (b). The chambers at both the *cis* and *trans* sides were modeled as a circle with a radius of 12.5 μm.

Table 2-1 Boundary conditions used in simulation

The following symbols Φ, σ, c, n, Ni, p, and v are the surface potential, the surface charge density of the corresponding surface, the concentration of KCl or NaCl (PBS) solution, normal vector, the flux of ions (K^+, Na^+ and Cl^-), pressure and fluid velocity, respectively. [11]

Physics field	**AC/DC**	**Laminar flow**	**Chemical species transport**
Boundary			
1	axis-symmetry		
2	grounded ($\Phi = 0$)	bulk concentration ($c = c_{cis}$)	No slip ($v = 0$)
6	applied terminal bias ($\Phi = V_b$)	bulk concentration ($c = c_{trans}$)	
3	constant surface charge density ($\sigma_{surface.cis}$)	Zero pressure ($p = 0$)	Ion-impenetrable ($n \cdot N_i = 0$)
4	constant surface charge density ($\sigma_{wall.inner}$)		
5	constant surface charge density ($\sigma_{surface.trans}$)		
7 (if applicable)	constant surface charge density (σ_{bead})		

Chapter 3 Electric field–driven ion transport through solid-state nanopores under a salt gradient

3.1. Introduction

Electric field–driven ion transport in fluidic channels has been extensively studied for ionic electronics[12–15] and energy harvest.[16–19] Functional nanochannels with various ion transport properties have been reported, such as artificial ion channels,[20] rectification,[21,22], and even memristive switching.[23] Generally, surface charge effects play a central role in rendering the unique characteristics through the electrostatic interactions with mobile electrolyte ions in the sub-Debye length scale conduits with overlapped electric double layers.[24,25] This in turn predicts function-less fluidic devices with characteristic sizes much larger than a screening length, as the ion conductivity will largely be determined by the bulk properties. In contrast, the study shows that ionic current rectifications in a symmetric nanopore of diameter are much larger than the Debye length under a salt gradient bias, wherein any surface effects are anticipated to become weak to render notable influence on the cross-membrane ion transport.

The anomalous feature was attributed to the surface charge-induced fluid flow, known as electroosmosis,[26–29] that effectively modulated the bulk ion distributions around the pores, thereby causing ion flow asymmetry to diode-like ionic current response against the cross-membrane voltage. In this chapter, the ionic current rectification based on asymmetric electroosmotic flow will be elaborated. The extended application of this effect in resistive switches and the surface effect of the nanopore are discussed in Chapter 4 and 5, respectively.

3.2. Ion transport asymmetry under a salt gradient

The ionic current (I_{ion}) through a nanopore of 300 nm diameter formed in a 50 nm-thick SiN_x membrane was measured under the bias voltage (V_b) swept from −1.5 to 1.5 V with a pair of Ag/AgCl electrodes (Figure 3.1). The fabrication method has been described in Chapter 2. In the experiment, the *cis* and *trans* chambers were filled with phosphate-buffered saline (PBS) of various ionic concentrations by diluting with ultrapure water. Specifically, the concentration of Na^+ and Cl^- at 1370 mM (10x PBS), 137 mM (1x PBX), and 13.7 mM (0.1x PBS) were used (thereafter, c_o = 137 mM is used to denote the ion concentration conditions). Then, a salinity gradient was added to the nanopore by pouring the buffer of different dilutions into the *cis* and *trans* chambers, which was described by the concentration ratio $r_{conc} = c_{high}/c_{low}$ between the *cis* (c_{high}) and *trans* (c_{low}).

Figure 3.2a displays I_{ion}-V_b curves recorded with no salt gradient across the membrane, i.e., r_{conc} = 1. The results showed linear characteristics with little difference at the negative and positive V_b regimes. The slope denotes the open pore conductance ($G_{pore} = R_{pore}^{-1}$) in the disk-shaped channel of diameter (d_{pore}) and length (L_{pore}) filled with the electrolyte buffer of resistivity (ρ), which can be expressed as a series resistance model composed of the components inside (pore resistance, R_{pore}) and outside the pore (access resistance, R_{access}) as equation 1-3. For the symmetric shape of the channel as well as the same ρ at both sides of the chambers, $R_{cis} = R_{trans} = \rho/2d_{pore}$. In this case, the analytical model yields R_{pore} = 0.36 MΩ with R_{pore} = 0.062 MΩ and R_{access} = 0.29 MΩ for the case of 10 × PBS with ρ = 0.088 Ωm, which is in fair agreement with Figure 3.2a. It is also noticeable that $R_{access} \gg R_{pore}$, signifying the predominant influence of the ion transport characteristics at exterior areas of the nanopore due to the low thickness-to-diameter aspect ratio motifs.

If the equivalent circuit is valid for describing the nanopore conductance under differing ionic concentrations at *cis* and *trans* sides, it was observed the symmetric and linear I_{ion}-V_b characteristics with the slope 1 / (R_{cis} + R_{trans}) even though the two compartments were filled with different concentrations of buffers. Contrary to the anticipation, however, the I_{ion}-V_b characteristics under r_{conc} > 1 were found to be asymmetric with the conductance being always lower under negative V_b (it should be reminded that the ionic concentration was set to be higher at the *cis* side). In addition, the diode-like behavior became more pronounced as the result of larger salinity gradients with the rectification ratio (r_{rec}) reaching 20 under r_{conc} = 100 at ±1 V (Figure 3.2b).

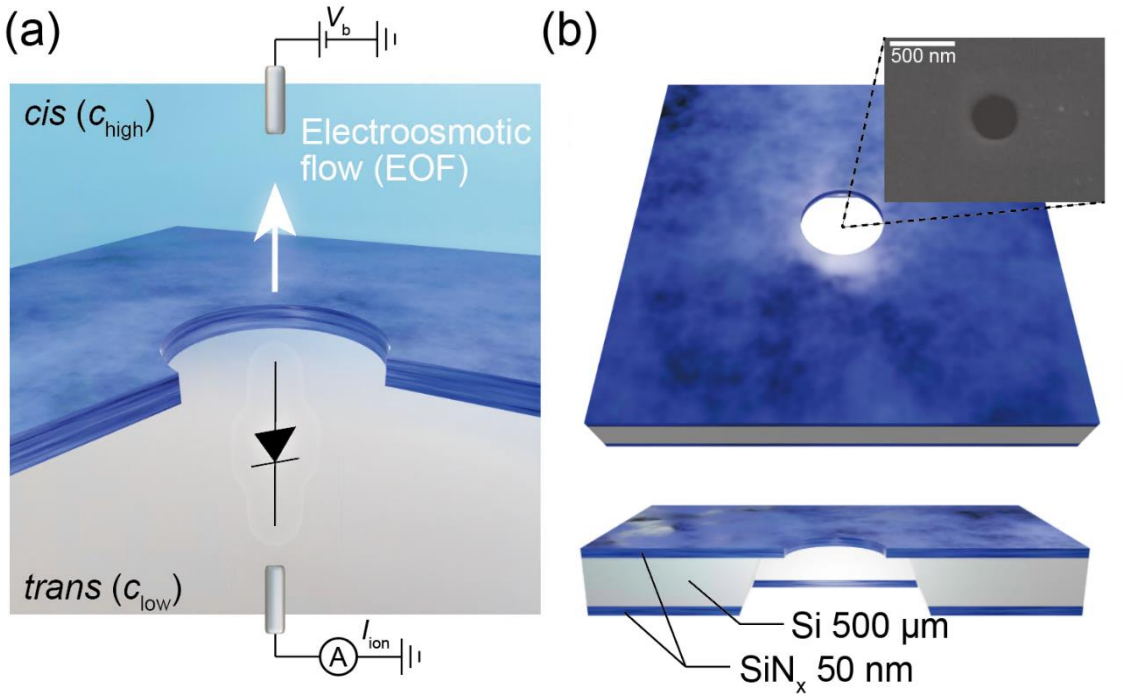

Figure 3.1 Schematic illustration of the nanopore device with a salt gradient

(a) A schematic model of the experiment of a 300 nm-sized nanopore under a salt gradient. Two Ag/AgCl electrodes were used to apply V_b and record I_{ion} through the single pore. The *cis* and *trans* sides are filled with buffer solutions of various ion concentrations c_{high} and c_{low}. (b) Structure of a SiN_x nanopore device and a scanning electron micrograph (SEM) of the 300 nm-sized nanopore. Reproduced and adapted with permission from ref.[30]. Copyright 2020 American Chemical Society.

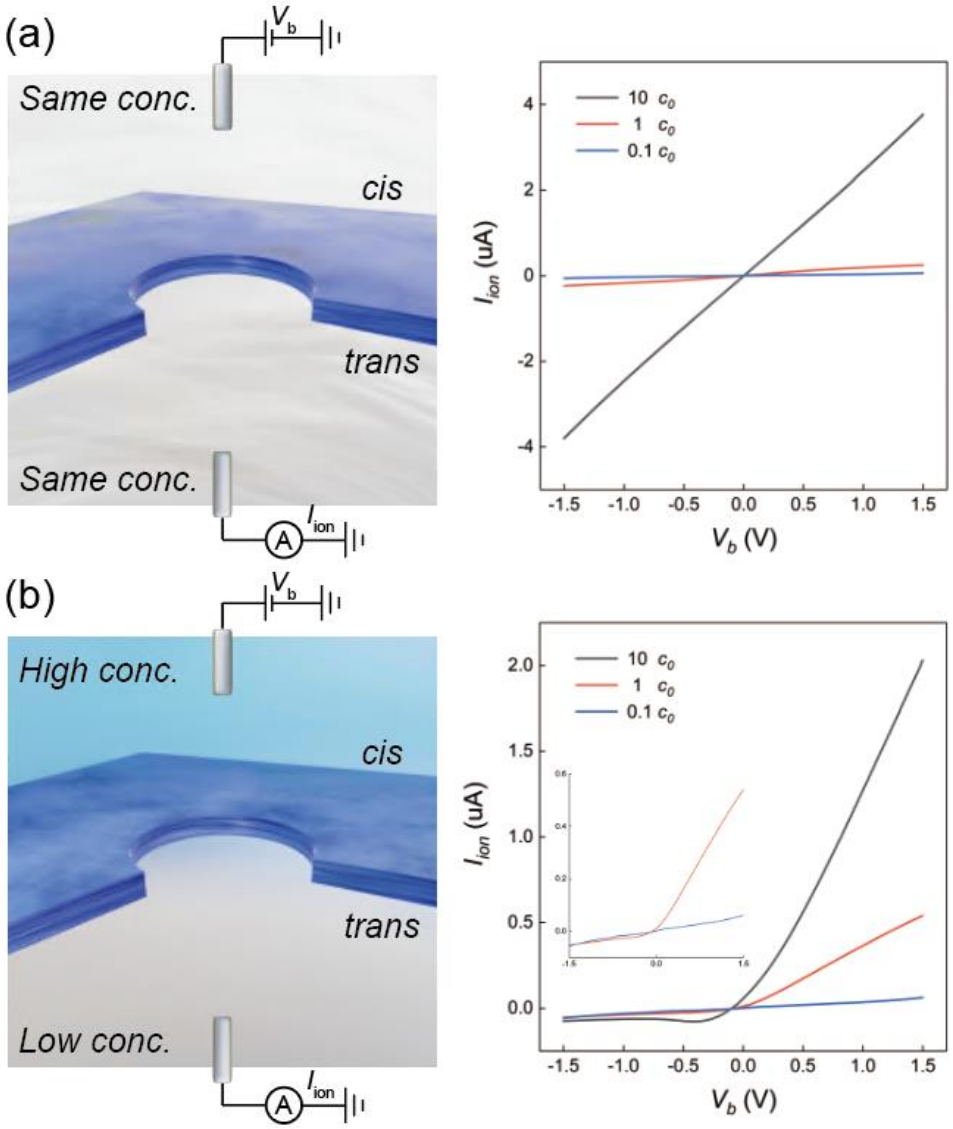

Figure 3.2 Measurement results of recorded I_{ion}-V_b characteristics

(a) Linear I_{ion}-V_b curves were observed when *cis* and *trans* were filled with the buffer of the same ion concentration in a 300 nm-sized low thickness-to-diameter aspect ratio nanopore. c_0 denotes the electrolyte concentration of 1x PBS as 137 mM. (b) Ionic current rectification (ICR) occurred in the salt-gradient applied conditions. Reproduced and adapted with permission from ref.[30]. Copyright 2020 American Chemical Society.

While the above findings demonstrate a predominant role of the salt gradient on the ion flow asymmetry, it also precludes the applicability of the analytical model for describing the observed phenomenon. To shed light on a physical mechanism underlying the asymmetric ion transport characteristics, it was conducted that a finite element analysis using an axisymmetric two-dimensional model was applied to understand the ion transport of salt gradient-biased nanopore.[26] The numerical simulations solved Navier–Stokes, and Nernst–Planck equations under steady-state conditions in COMSOL Multiphysics. The detailed simulation experiment setup has been explained in Chapter 2. The calculated ionic current reproduced the symmetric and asymmetric I_{ion}-V_b characteristics upon setting r_{conc} of 1 and over 1, respectively (slight quantitative deviations from the experimental results are presumably due to the difference in the surface charge destiny at the nanopore wall surface in the simulations, which was estimated as −10 mC/m², also see Figure 3.3). This corroborates that the ionic current rectification is indeed an intrinsic property unique to the salinity gradient applied to low aspect ratio nanopores. Nevertheless, its interpretation is not straight forward since the conventional idea[24,25] of the surface charge-derived ion selectivity in the sub-Debye-length-sized nanochannels cannot be applied in the present model as the nanopores had d_{pore} of 300 nm (which is more than 2 orders of magnitude larger than the screening length in the buffer used). What is more, the surface-to-volume ratio is small in the disk-like nanopores which further indicates the minor contributions of the ion selectivity. In fact, the short circuit voltage (V_{short}), which represents the self-built potential in ion-selective nanopores under a salt gradient,[31] demonstrated no notable correlation with the rectification properties for the 300 nm-sized nanopores. The ion transport asymmetry should thus be ascribed to factors other than surface charge-derived electrostatic interactions.

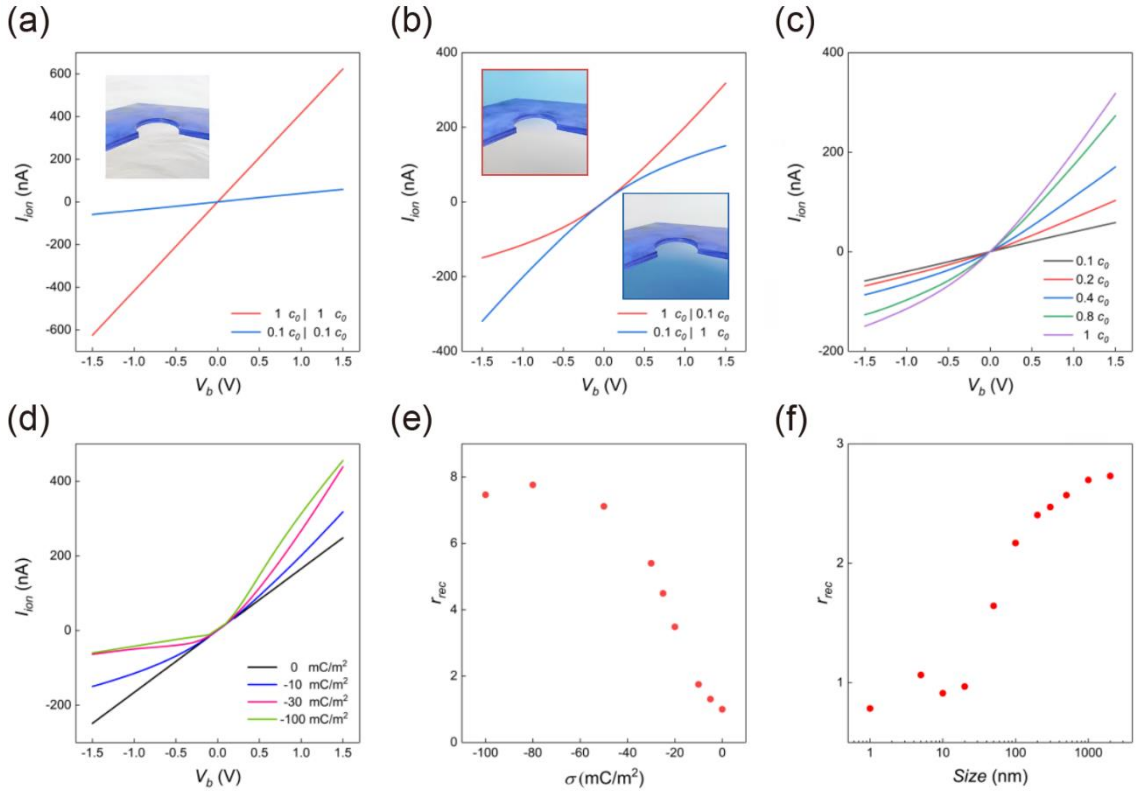

Figure 3.3 Surface effects in ion transport with a salt gradient

(a, b) Simulated I_{ion} versus V_b characteristics under r_{conc} = 1 with $c_{high,\ low}$ = 0.1 (blue), and 1 c_0 (red). Ionic current rectification under concentration ratio r_{conc} = 10 when c_{high} > c_{low} (red) and c_{low} > c_{high} (blue). (c) Simulation results of the I_{ion}- V_b characteristics in a 300-nm diameter and 50-nm thick SiN_x nanopore. Electrolytes of the *trans* chamber are fixed to 0.1 c_0 while that of *cis* is varied from 0.1 to 1 c_0, where c_0 = 137 mM denotes the electrolyte concentration of PBS. (d) Simulated I_{ion}- V_b in the nanopore with the applied salt gradient at r_{conc} = 10 under different surface charge density conditions σ at the SiN_x membrane surface. (e) r_{conc} at V_b = ±1 V plotted as a function of surface charge density σ. (f) The rectification ratio r_{rec} at V_b = ±1 V in the nanopore of various diameter dpore with the thickness-to-diameter aspect ratio of 1 with the applied salt gradient r_{conc} = 10. Reproduced and adapted with permission from ref.[30]. Copyright 2020 American Chemical Society.

3.3. Electroosmosis-driven ionic current rectification

The asymmetric I_{ion}-V_b characteristics infer the presence of a voltage-dependent force field acting to change the ion distributions around the nanopores. Electroosmosis is such a phenomenon that brings a fluid flow along the cross-membrane electric field.[32] To examine its effect, the fluid flow speed (v_{fluid}) was mapped under V_b. It illustrated high v_{fluid} regions near the channel wall signifying the nanoscopic Debye length in the buffer used that provides mobile counterions only at proximity to the SiN_x surface. The water flow as a whole directs toward the negative potential due to the migration of the counter-cations on the negatively charged wall surface. These V_b-dependent hydrodynamics was found to modify the ion density profiles at the nanopore orifices in a way that dense ions tend to move along the hydrodynamic flow making the ion concentration around the nanopore to be higher (lower) under the negative (positive) applied voltage; or more directly, it can be envisioned as a polarity-dependent change in the local solution conductivity (Figure 3.4 and Figure 3.5). The electroosmotic contribution can thus be a plausible explanation for the asymmetric I_{ion}-V_b curves considering that the open pore conductance of the shallow nanopores is largely determined by the access resistance rather than the resistance. These results prove the use of electroosmosis to create and modulate the ion depletion region for building nanopore diodes of size much larger than the Debye length.

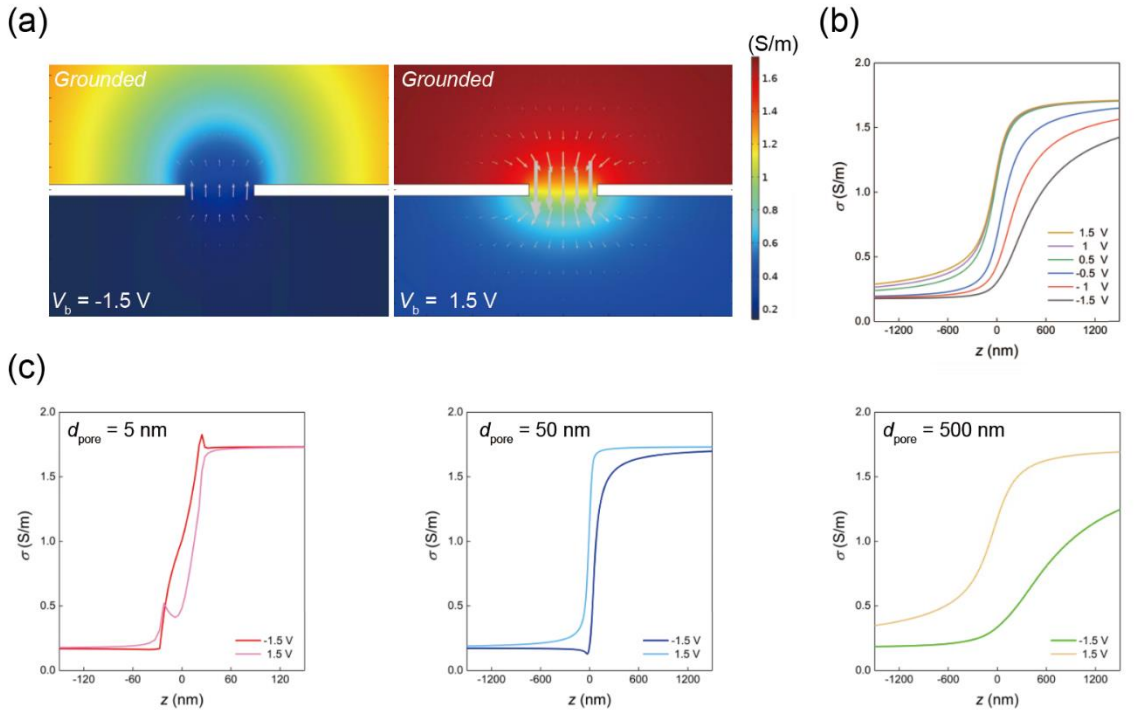

Figure 3.4 Shifted ionic conductivity distributions by EOF

(a) Ionic conductivity profiles at V_b = −1.5 V (left) and +1.5 V (right). (b) Axial variation of the ionic conductivity under different V_b. The ionic conductivity is 1.73 S/m when 1 c_0. All the results are obtained for the 300 nm diameter and 50 nm thick nanopore. (c) Axial variation in the cross-sectional ionic conductivity in nanopores having the aspect ratio of 10 (left), 1 (middle), and 0.1 (right). Reproduced and adapted with permission from ref.[30]. Copyright 2020 American Chemical Society.

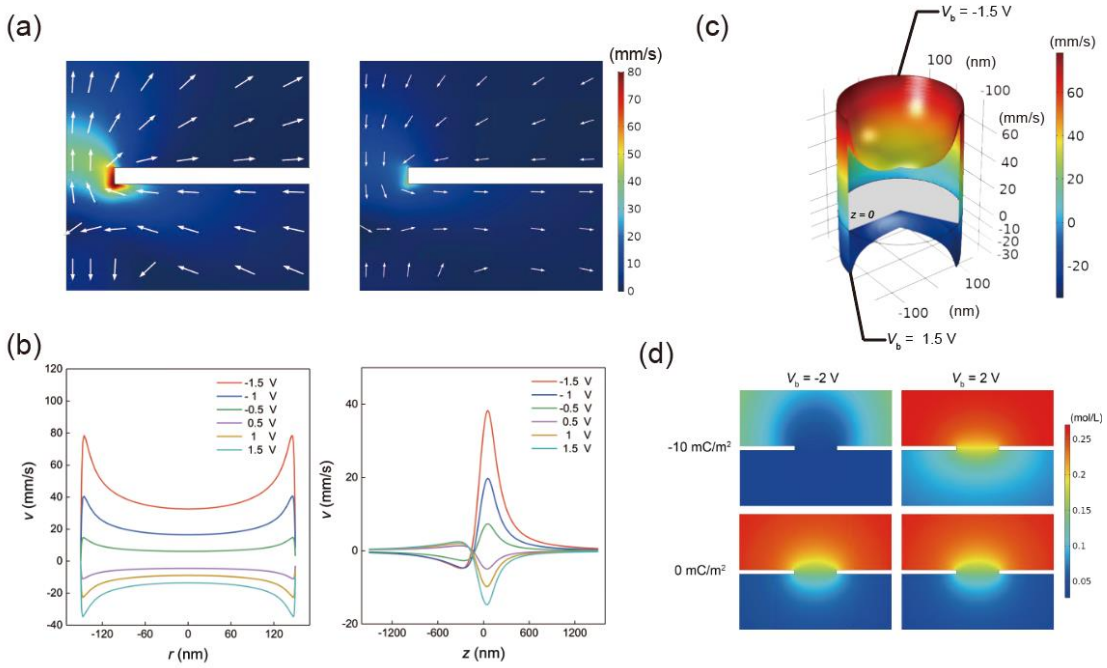

Figure 3.5 Calculated results of electroosmotic flow in a nanopore

Fluid velocity in the 300 nm-sized pores. (a) Fluid velocity profiles simulated at V_b = −1.5 V (left) and 1.5 V (right). The white arrow indicates the direction of water flow. (b) The fluid velocity along the radial (r) and axial (z) directions under different V_b. (c) Two-dimensional map of the fluid velocity at z = 0 under V_b = −1.5 V (top) and +1.5 V (bottom). (d) Roles of electroosmosis on the ion concentration distribution at nanopore orifices. The nanopore has a 500 nm in d_{pore} in a 50 nm in L_{pore}. The pore wall surface was considered to have a negative surface charge density of -10 mC/m^2 (top) and electrically neutral (bottom) in the simulations. A 2D colored profile of the ion concentration revealed an asymmetric salt gradient under V_b = -2 V (left) and 2 V (right) for the negatively-charged nanopore while almost symmetric when there is no charge on the wall surface thereby suggesting the vital role of the electroosmosis to modulate the ion concentration distributions by the applied voltage. Reproduced and adapted with permission from ref.[30]. Copyright 2020 American Chemical Society.

3.4. Roles of Nanopore Geometries

It is interesting to investigate whether the diode-like behavior can only be seen in nanopores having low aspect ratio structures. Hence, the COMSOL simulations were extended to inspect for the pores of different d_{pore} and L_{pore}. The calculated r_{rec} at V_b = ± 2 V revealed two regimes regarding the channel structure dependence as displayed in Figure 3.6a. Under extremely low aspect ratio conditions, r_{rec} is around 2 irrespective of dpore in the range from 10 to 500 nm (Region I). This manifests a rather universal role of the electroosmotic flow that induces asymmetric ion transport to ionic current rectification via the hydrodynamically modulated access resistance. Similarly, r_{rec} tends to level off at about 4 with increasing L_{pore} (Region III).

The result can be interpreted as a consequence of the electroosmosis to change the ion concentration inside the long pore in a V_b-dependent manner that causes an appreciable change in R_{pore} (note that R_{pore} » R_{acc} for the high-aspect-ratio channels). In contrast, the rectification ratio demonstrated nontrivial dependence on the pore configurations in the intermediate range of the aspect ratio (Region II). An obvious difference can be found for d_{pore} larger than 100 nm and smaller than 20 nm. The former pores presented a nonlinear increase in r_{rec} to 4 with increasing lpore that can be explained as a gradual shift from the R_{access}- to R_{pore}-dominant nanofluidic diode characteristics. The small d_{pore}, however, showed almost no rectification behavior suggesting little contributions of electroosmosis on the ionic current due to the overlapped electric double layer (Figure 3.7). In fact, the finite element analysis of the in-pore fluid dynamics predicted rapid reduction in the water flow speed vfluid with increasing L_{pore} (Figure 3.8). The exception is the case of a 50 nm-sized nanopore representing a r_{rec} enhancement above 4 in Region II. In this particular channel structure, surface charge effects are weakly confined at the wall due to the nanoscale dimension

comparable to the Debye length that makes v_{fluid} high even at the middle of the pore, thereby giving rise to more pronounced diode behavior via the electroosmosis contributions.

The present study in Chapter 3 demonstrated for the first time that the resistance outside a nanopore plays a significant role in signal retardation in resistive pulse analyses rather than the resistance at the pore. Charging at the cross-membrane net capacitance was also found to contribute equally to retard the signal along with the RC-relevant resistance. More importantly, the present findings preclude the anticipated cause of the inevitably large in-pore resistance of single-nanometer scale nanopores, thereby paving a way for ultrafast genome sequencing and single-protein analyses.

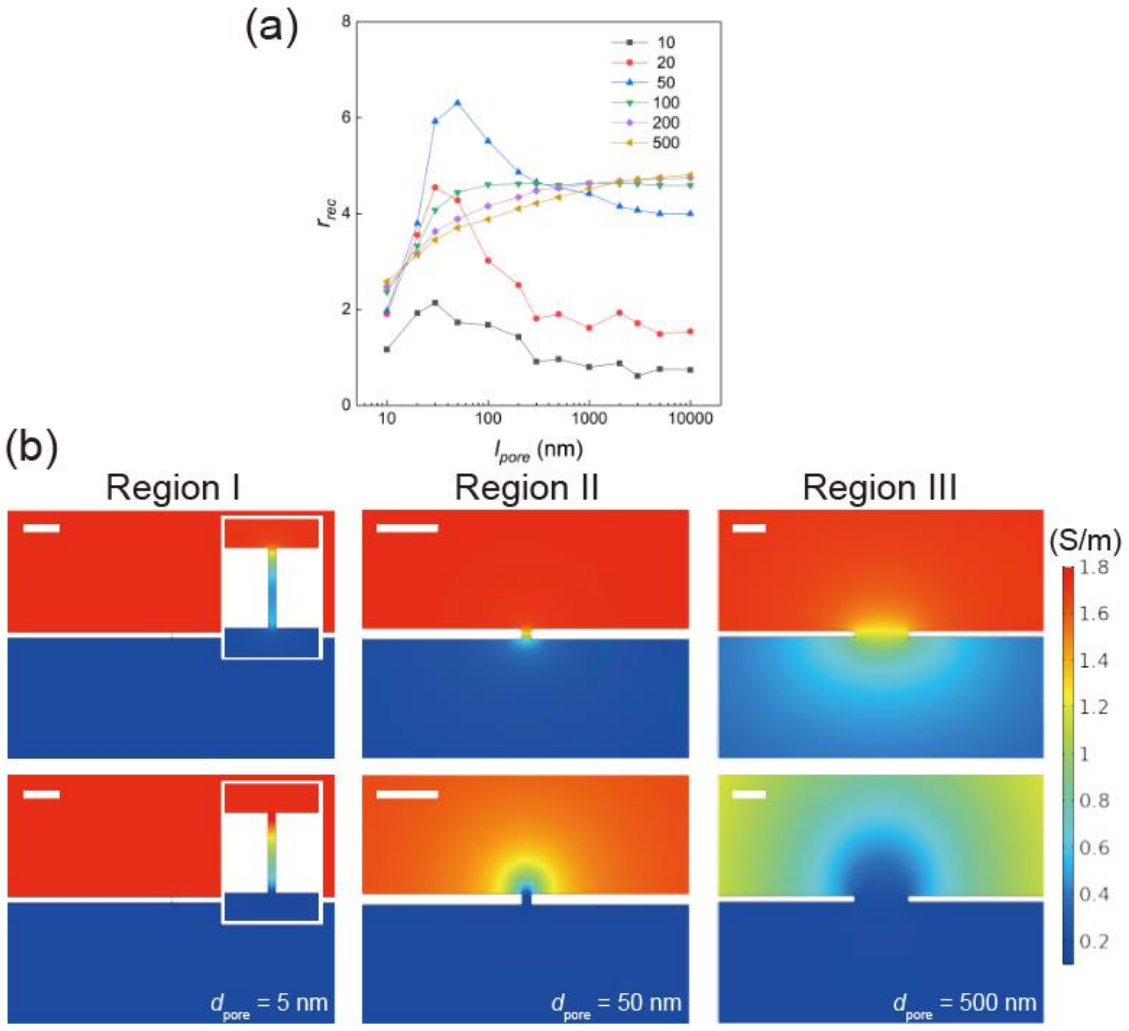

Figure 3.6 Nanopore structure dependence of the rectifying properties

(a) Influence of d_{pore} and L_{pore} on the rectification ratio r_{rec}. (b) Ionic conductivity profiles under V_b = 2 V(top) and −2 V for 50 nm-thick nanopores of d_{pore} = 5 nm (left), 50 nm (middle), and 500 nm (right). Scale bars denote 300 nm. Reproduced and adapted with permission from ref.[30]. Copyright 2020 American Chemical Society.

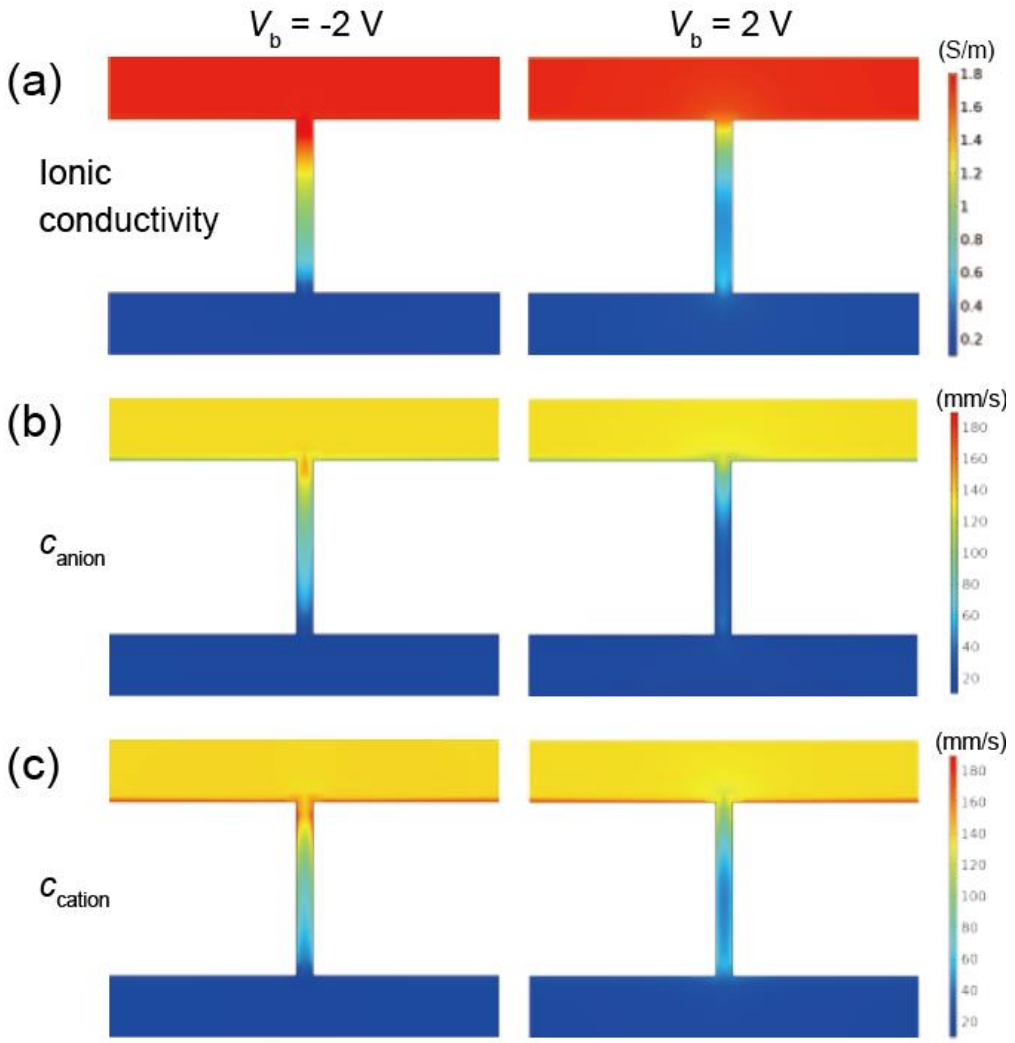

Figure 3.7 Extended result of nanopore structure dependence of the rectifying properties

Ionic conductivity(a), the concentration of anion(b) and cation(c) profiles under V_b = -2 V (left) and 2 V (right) for 50 nm-thick nanopores of d_{pore} = 5 nm. Reproduced and adapted with permission from ref.[30]. Copyright 2020 American Chemical Society.

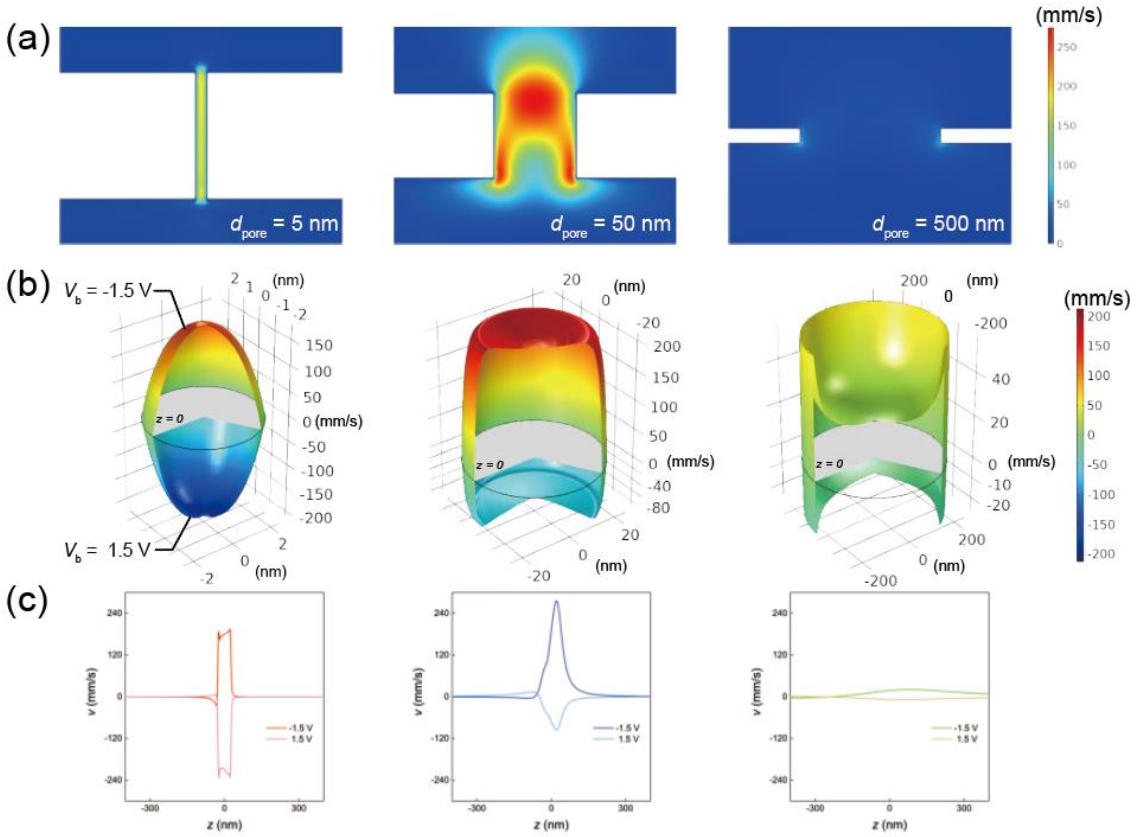

Figure 3.8 Electroosmotic flow velocity v_{fluid} in nanopores of different diameters

(a) Ionic conductivity profiles under V_b = −1.5 V. (b) Two-dimensional maps of the fluid velocity plotted with height expression at V_b = −1.5 V and +1.5 V. (c) v_{fluid} as a function of the axial position z. Reproduced and adapted with permission from ref.[30]. Copyright 2020 American Chemical Society.

Chapter 4 Negative differential resistance and resistive switching in solid-state nanopores

4.1. Introduction

Ion transport in a fluidic channel has been intensively studied for promising applications including energy harvesters,[19,33–36] iontronics,[13,37–40] artificial neurons,[23] and single-molecule sensing.[41,42] It implements electric field-driven ion and mass transport in a confined space, wherein electrostatics and fluid dynamics reflect rich properties of the wall surface to induce pronounced ion selectivity and the associated unique ionic current characteristics that cannot be expected in bulk systems as described in Chapter 3. According to this principle, nanofluidic devices demonstrated a variety of ion transport properties such as ionic current rectification (ICR) and negative differential resistance (NDR)[21,22] via geometric structure engineering,[43] membrane material designs,[44,45] and molecular functionalizations[14,40,46,47] to provide high-density surface charge to the walls[21] and increase the surface-to-volume ratio of fluidic channels. The surface effects were, however, known to be effective only in a small channel of sub-Debye length size because of screening of the electrostatic field at the wall by the electrolyte ions. The details of this effect are detailed in Chapter 5.

A salinity gradient across a conduit was recently found to enable asymmetric ion transport concerning bias voltage polarity[22,43,48] even in channels of micrometer-scale diameter.[12] The peculiar ionic current characteristics were explained by voltage-driven modulation of the cross-membrane salt gradient under the influence of diffusio-osmotic and electro-osmotic fluid flow.[29,49–53] For instance, Rabinowitz et al.[48] observed ICR in 25 nm diameter glass

pipettes with an ion concentration ratio between 10 and 21, which was ascribed to electro-osmosis-induced Eddy current driving more or less concentrated solution into the channel in a voltage-dependent manner.[48] Moreover, NDR was reported by Lin et al.[22] for 100 and 400-nm-sized nanopores in a 12 μm thick PET membrane under a concentration ratio between 10 and 1000, where the authors found the influence of the interplay between electro-osmotic and diffusio-osmotic contributions on the asymmetric ion transport characteristics.[22] Whereas this chapter found the rectifying behavior in fluidic channels having a relatively high length-to-diameter aspect ratio structure. Herein, such electrokinetic effects are observable even in low thickness-to-diameter aspect-ratio micropores where any surface charge effects were anticipated to become negligibly small under the orders of magnitude larger space given for the ion transport with respect to the Debye length. Surprisingly, more pronounced electro-diffusio-osmotic contributions in the shallow channels were found that led to anomalous ionic current characteristics from NDR to resistive switching.

4.2. Negative differential resistance with solid-state nanopores

In the experiments in this chapter, a 1-μm diameter pore was fabricated in a 50 nm thick SiN_x membrane by electron beam lithography and reactive ion etching as detailed in Chapter 2. A pair of Ag/AgCl electrodes were used for measurements of the ionic current (I_{ion}) versus cross-membrane bias voltage (V_b) characteristics in phosphate-buffered saline (PBS). The ionic strength was varied by diluting the buffer with ultrapure water from 10 c_o to 0.01 c_o, where c_o = 137 mM is the concentration of Na^+ and Cl^- in 1x PBS. A salt gradient was formed across the pore by filling the *cis* and *trans* chambers with PBS of high (c_{high}) and low (c_{low}) ion concentrations (Figure 4.1a). Hereafter, $r_{conc} = c_{high}/c_{low}$ is used to describe the salinity

difference ratio.

Under a uniform ion concentration condition (r_{conc} = 1), the ionic resistance R_{total} complied with an analytical expression of $R_{total} = R_{access} + R_{pore}$ (Figure 4.1b). Note that for the present channel having a low thickness-to-diameter aspect ratio structure, R_{access} is an order of magnitude larger than R_{pore}.[54–56] Whereas I_{ion}-V_b characteristics were observed to be linear at r_{conc} = 1, diode-like behavior occurred when applying a 10-fold difference between c_{high} and c_{low} (r_{conc} = 10) with a rectification ratio r_{rec} of 4.6 at ±1 V. This ion transport asymmetry was ascribed to voltage-dependent salt gradient modulations by the electro-osmotic flow (EOF) that lowers (enhances) the effective ion concentration around the micropore under the positive (negative) V_b.[43,44] The plots were also confirmed to be reproducible under repeated bias ramps, suggesting reversible ion distributions under the V_b-driven hydrodynamic control. Enlarging the salt gradient to r_{conc} = 100 (red curve in Figure 4.1c), I_{ion}-V_b characteristics became more asymmetric with the rectification ratio as high as 24.8. Unexpectedly, it also revealed NDR behavior at around V_b = −0.56 V. Considering the predominant role of EOF in the ion flow asymmetry,[57] this feature can be naturally interpreted as a consequence of the augmented electro-diffusio-osmotic flow at critical V_b that diluted the local ion concentration at the pore orifice and thereby led to a rapid increase in R_{access}.

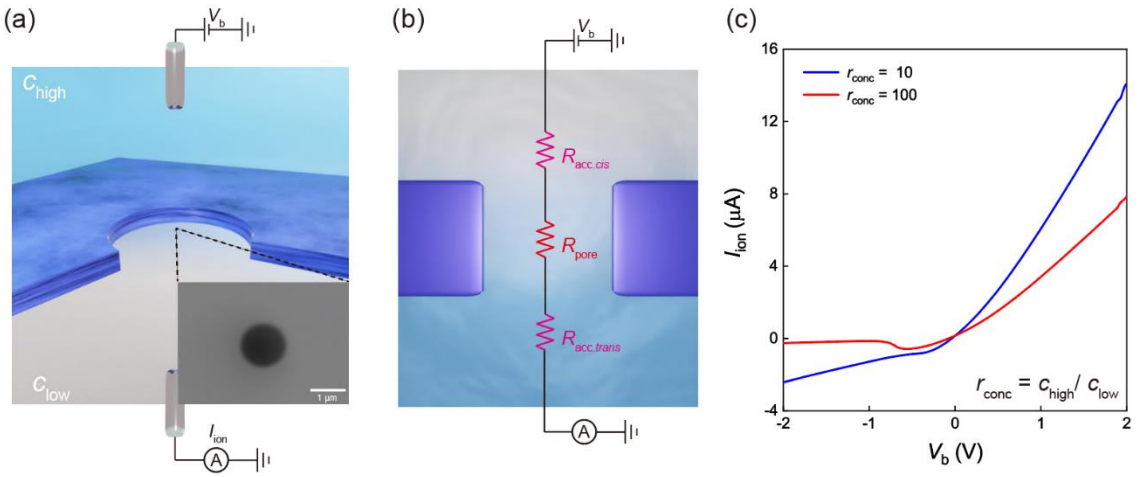

Figure 4.1 Measurements of the ionic current through a solid-state pore in a thin dielectric membrane

(a) Schematic model of a SiN_x pore, both sides filled with either electrolyte buffers of high (green) or low (blue) ionic concentration buffers. The bias voltage V_b is applied to the pore at the *cis* chamber, and the resulting ionic current I_{ion} is measured at the other side with a pair of Ag/AgCl electrodes. The inset shows a scanning electron micrograph (SEM) image of the 1 µm-sized micropore. (b) Equivalent circuit model for the pore system. $R_{acc.cis}$ and $R_{acc.trans}$ are the access resistance in the *cis* and *trans* compartments, respectively. R_{pore} is the pore resistance inside the pore. (c) Typical current−voltage characteristics of a low thickness-to-diameter aspect-ratio pore (1 µm diameter and 50 nm thick) under the moderate (blue curve) and large (red curve) salt gradients. r_{conc} is the ratio of the bulk salt concentrations at the *cis* and *trans*. Reproduced and adapted with permission from ref.[58]. Copyright 2020 American Chemical Society.

To theoretically verify the mechanism underlying the NDR behavior, finite element analyses of the cross-membrane ion transport by solving time-independent Poisson–Nernst–Planck and Navier–Stokes equations in a framework of a finite element method using COMSOL software were performed. The model is constructed with a disk-shaped pore having a diameter (d_{pore}) of 1 μm in a SiN_x membrane of 50 nm thickness (L_{pore}).[29,52] The entire surface of the membrane was considered as negatively charged at −15 mC/m². The rest of the boundary conditions are described in Chapter 2. The simulation reproduced NDR and ICR when setting r_{conc} = 100 (c_{cis} = 1 c_0; c_{trans} = 0.01 c_0) and r_{conc} = 10 (c_{cis} = 1 c_0; c_{trans} = 0.1 c_0), respectively, which are in good agreement with the experimental results. Further calculations revealed an ICR-to-NDR transition point at around r_{conc} = 14 (Figure 4.2). and the important role of the pore wall surface charge is also checked. It is found that decreasing the number of negative charges on the membrane led to a weaker NDR. It elucidated the profound influence of the entire membrane surface. No NDR behavior happened in cases when only a part of the surface was set to be charged (Figure 4.3a). This was confirmed in experiments as well where the disappearance of the NDR feature when the number of negative charges on the surfaces was reduced by coating a 20-nm thick Al_2O_3 layer on the nanopore (Figure 4.3b). These results manifest a crucial role of the surface charge in the salt gradient-derived asymmetric ion transport characteristics. However, the effect of surface effects of solid-state nanopores on ion transport is discussed in more detail in Chapter 5.

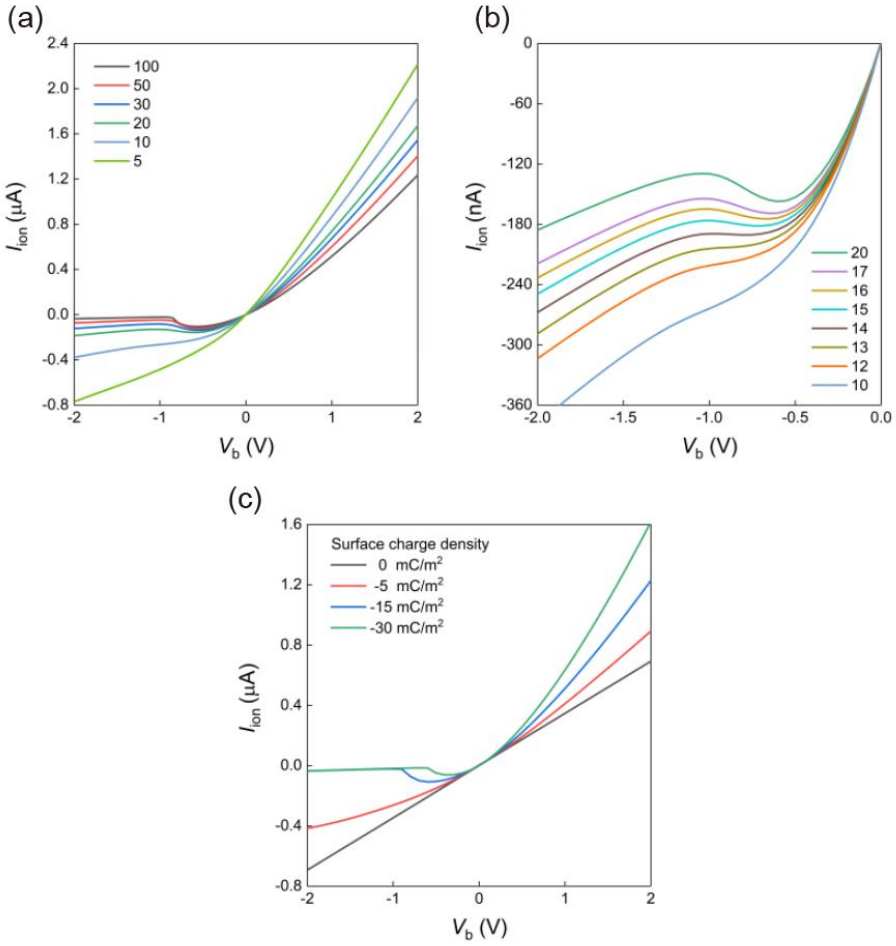

Figure 4.2 Simulated results of ionic current-voltage characteristics

(a) Simulated ionic current-voltage (I_{ion}-V_b) characteristics results in a 300 nm-diameter and 50 nm-thick SiN_x pore under various *cis*-to-*trans* ion concentration ratio (r_{conc}) conditions (denoted by different colors). The concentration of NaCl solution filled in the top reservoir is fixed at 1 c_0. (b) The result shows that clear negative differential resistance behavior starts to appear at r_{conc} > 14. (c) Simulated I_{ion}-V_b curves for a SiN_x pore in 1 μm-diameter and 50 nm-thick under the *cis*-to-*trans* ion concentration ratio of 100. The values of charge density were set to 0 (black), -5 (red), -15 (sky blue), and -30 mC/m^2 (green). Reproduced and adapted with permission from ref.[58]. Copyright 2020 American Chemical Society.

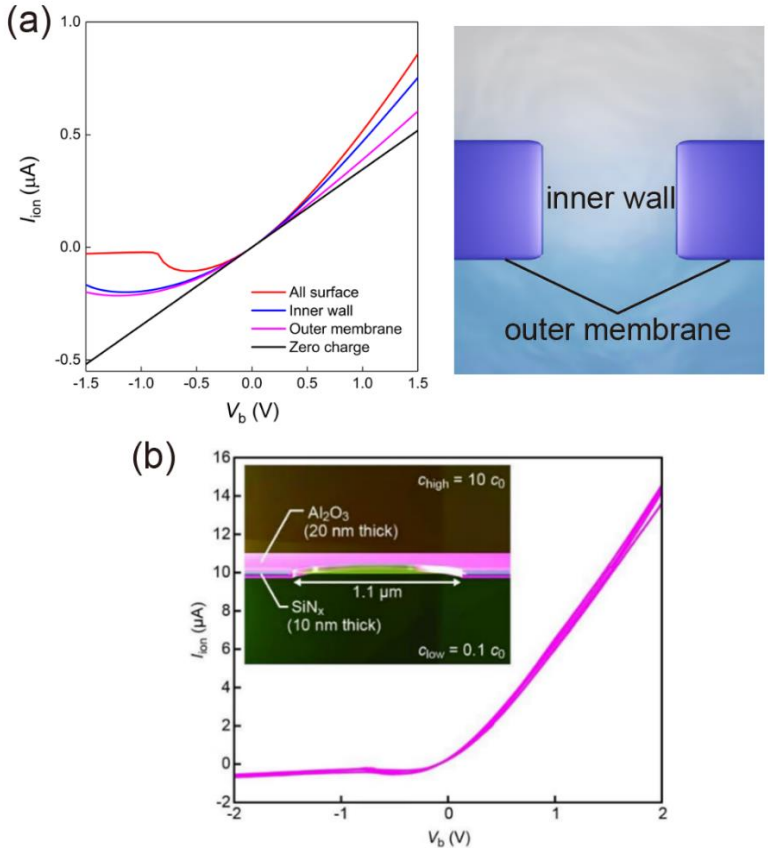

Figure 4.3 Schematic models depicting three different surface charge conditions

(a) Negative charges on the entire membrane surface, only on the pore wall, and only on the top and bottom surfaces. Ionic current characteristics are simulated under different surface charge conditions. Color maps denote the fluid velocity profiles at V_b = -0.5 V. When the entire surface of the SiNx membrane was considered to be charged, the curve demonstrated clear NDR behavior (red). On the other hand, when the membrane was only partially charged, the NDR feature became less obvious. (b) Measured current-voltage curves under the cis-to-trans ion concentration ratio of 100 for a 1.1 μm-diameter Al_2O_3 pore, which was created by coating 20 nm-thick Al_2O_3 via radio frequency magnetron sputtering from both sides of the 10 nm-thick SiNx membrane. The voltage was swept from -2 V to 2 V and also from 2 V to -2 V for 5 cycles. As shown by the curves, the NDR feature is very weak, which is ascribed to the less amount of negative surface charge on the Al_2O_3 compared to that on SiN_x as

revealed by surface zeta-potential measurements using a zeta-sizer: the zeta-potentials were -43.2 and -32.7 mV for the bare SiN_x and 20 nm-thick Al_2O_3-coated SiN_x surfaces, respectively. Reproduced and adapted with permission from ref.[58]. Copyright 2020 American Chemical Society.

By mapping the local ion concentration near the pore (Figure 4.4), both cation and anion concentrations have a rapid decrease when lowering V_b below −0.55 V. This tendency is in qualitative accordance with the expected influence of the EOF streaming from *trans* side to *cis* side to alter from R_{access}, or equivalently the total resistance (R_{total}) for the present low-aspect-ratio micropore, larger by diluting the ions in the pore region at $V_b < -0.55$ V. NDR can thus be explained as a consequence of the faster voltage-driven fluid speed (v_{fluid}) in more dilute electrolyte solution due to the extensive surface charge effects under the longer screening length,[43] which eventually causes the ionic current to decrease with increasing $|V_b|$.

How about the EOF velocity then? Figure 4.5 shows the fluid velocity contours at V_b = −0.5 V, −0.8 V, and − 1.5 V under r_{conc} = 100. At −0.5 V, the flow speed is fast only near the wall surface because of the short Debye length under the high in-pore ion concentration condition, as depicted by the ion density isosurfaces (Figure 4.5a). Enlarging the voltage to −0.8 V (Figure 4.5b), on the other hand, the flow speed suddenly becomes more significant in the entire channel. This characteristic feature is revealed as stemming from the concomitant weakening of the diffusio-osmotic effect for the stronger EOF, which makes the ion density in the channel more homogeneous (Figure 4.5d-f).[22] It is perhaps this self-catalytic effect that depletes ions at the channel openings more significantly than the current gain by larger $|V_b|$, thus bringing about NDR at the specific range of negative voltage. Meanwhile, further voltage sweep (Figure 4.5c) led to a linear decrease in I_{ion} with a slope close to 1/R under $c_{high} = c_{low} = 0.01\ c_0$, as the ion concentration at the *cis* and *trans* orifices is already close to clow. These findings elucidate the important roles of electro-diffusio-osmosis on the highly asymmetric ion transport in low-aspect-ratio pores (Figure 4.6).

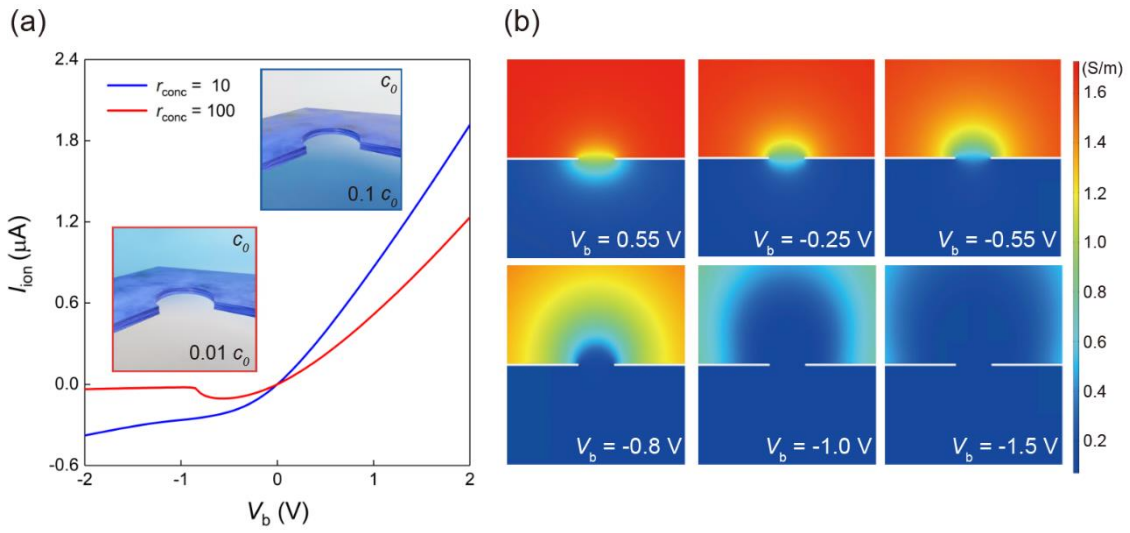

Figure 4.4 Finite element analyses of ion transport in the salt gradient-applied low-aspect-ratio pore

(a) Calculated I_{ion}-V_b characteristics of a 1 μm diameter and 50 nm thick SiN_x pore. c_0 = 137 mM denotes the concentration of Na^+ and Cl^- in the electrolyte buffer used. Blue and red curves are the results when r_{conc} is 10 and 100, respectively. (b) Cross-sectional views of the two-dimensional conductivity around the pore under different V_b. Reproduced and adapted with permission from ref.[58]. Copyright 2020 American Chemical Society.

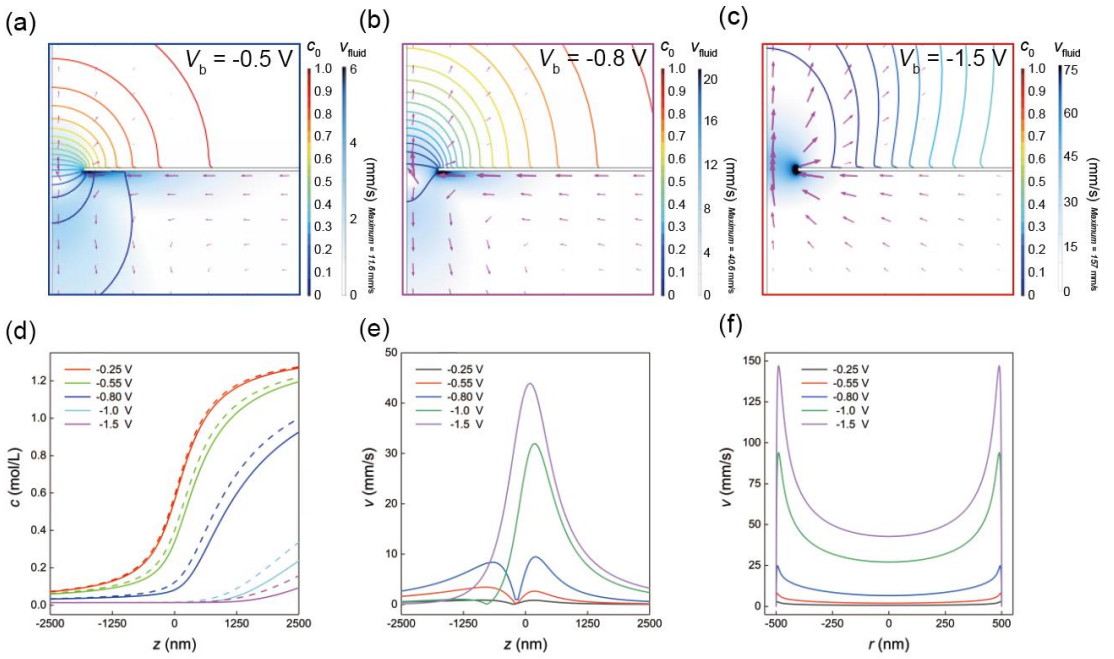

Figure 4.5 Voltage-dependent ion concentration distributions

(a-c) Simulation results of ion concentration isosurfaces around a 1 μm diameter and 50 nm thick SiN_x pore under (a) V_b = −0.5 V, (b) −0.8 V, and (c) − 1.5 V. Blue contrasts and purple arrows depict the electro-diffusioosmosis-driven fluid flow speed and directions, respectively. (d-f) d, The ion concentration *c* along the pore axis. Solid line = cation; dotted line = anion. Fluid velocity profiles along the *z* axial (e) and *r* radial directions (f). Reproduced and adapted with permission from ref.[58]. Copyright 2020 American Chemical Society.

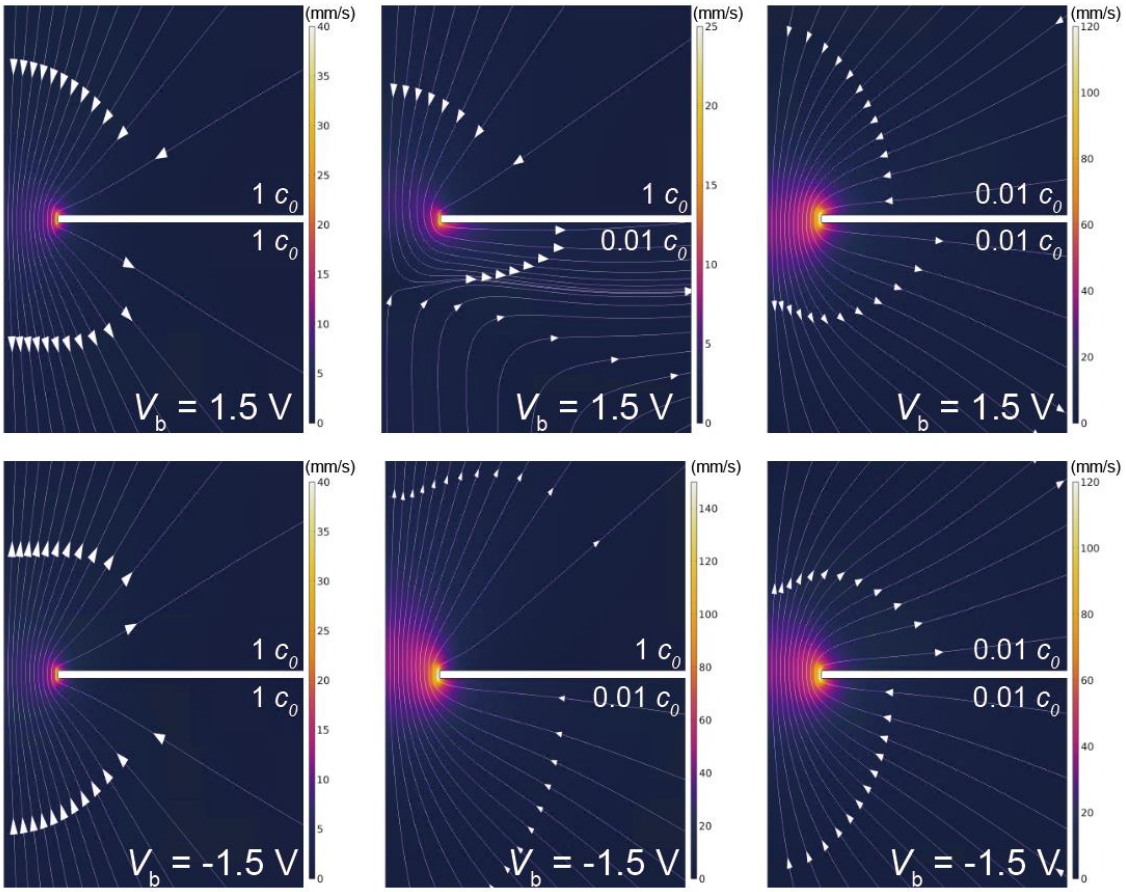

Figure 4.6 Simulated EOF velocity heatmaps and streamlines

Simulated EOF velocity heatmaps and streamlines for the 1 μm-diameter and 50 nm-thick SiN_x pore under the applied cross-membrane voltage V_b of 1.5V and -1.5 V. Asymmetric water flow can be seen when the cis-to-trans ion concentration ratio is 100 (middle), while the flow is symmetric against the voltage polarity under the uniform ion concentration conditions (left and right). Reproduced and adapted with permission from ref.[58]. Copyright 2020 American Chemical Society.

Both the experimental and simulation results consistently suggest the predominant role of EOF in the NDR characteristics. Interestingly, while the channel length (L_{pore}) was increased from 50 to 1000 nm in the numerical simulations (Figure 4.7), the NDR features were found to occur at a smaller V_b. This is an intriguing result that reflects the relative influence of R_{access} and R_{pore} on the pore conductance as well as the different voltage dependences of the EOF. For example, R_{acc} tends to determine the open pore resistance of channels having lower-aspect-ratio structures, which also suggests a more moderate potential gradient at the orifices[59,60] and hence a weaker electric field across the membrane. The resulting EOF during the voltage sweep is therefore expected to be also weak compared to that in the channels of higher-aspect-ratio motifs. Moreover, R_{acc} will be affected only when the ion concentration at the pore orifices is changed appreciably by the fluid flow, which was found to take place only under relatively large voltages in the simulations (Figure 4.7b). On the other hand, the cross-membrane electric potential tends to drop more sharply inside the channels in the case of higher-aspect-ratio pores. The resulting stronger EOF induces a more facile change in the in-pore ion concentrations by the cross-membrane voltage (Figure 4.7c). Meanwhile, unlike the shallow channels, such a change in the ion density causes a large impact on the resistance of the high-aspect-ratio conduits because $R_{pore} > R_{access}$ and hence gives rise to NDR features at lower V_b compared to the lower-aspect-ratio pore counterparts.

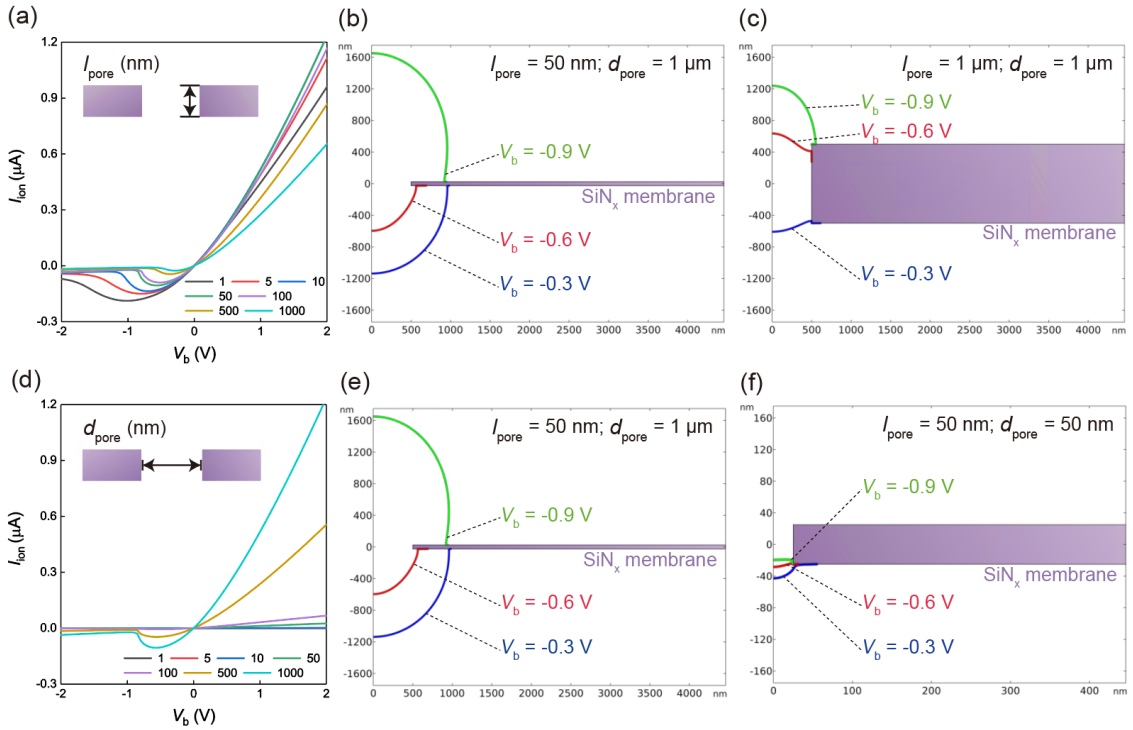

Figure 4.7 Pore structure-dependent ionic current characteristics

(a-c). (a) COMSOL-simulated I_{ion}-V_b characteristics of a 1 μm diameter pore in a SiN_x membrane of various thicknesses from 1000 to 1 nm ($c_{bulk.cis}$ = 1 c_0, $c_{bulk.trans}$ = 0.01 c_0). (b, c) Moving ion concentration isosurface at 0.1 c_0 under voltage sweep for (b) 50 nm and (c) 1 μm thick pores. (d-f). (d) COMSOL-simulated I_{ion}-V_b curves deduced for pores of various diameters from 1000 to 1 nm in a 50 nm-thick SiN_x membrane. NDR features disappear in pores smaller than 50 nm due to inefficient effects of electroosmotic flow on the cross-membrane ion transport. (e-f) V_b-dependent ion density profiles around the 1000 nm- (e) and 50 nm-sized (f) pores. Isosurface indicates 0.1 c_0 ($c_{bulk.cis}$ = 1 c_0, $c_{bulk.trans}$ = 0.01 c_0) under the applied bias voltage of -0.3 V (blue), -0.6 V (red), and -0.9 V (green). Reproduced and adapted with permission from ref.[58]. Copyright 2020 American Chemical Society.

4.3. Resistive switching in solid-state nanopores

How robust are the NDR characteristics? Because the salt gradient was created by merely injecting electrolyte buffers of different dilutions into the trans and cis chambers without careful manipulations, it was not guaranteed that there will always be a symmetrical ion concentration difference with respect to the membrane as modeled in the simulations. In fact, whereas stable NDR features were often observed persisting under several V_b sweeps, as shown in Figure 4.9 and Figure 4.10, completely different characteristics demonstrating V_b-controlled bimodal conductance switching were also found (Figure 4.8c). When this was the case, the I_{ion}-V_b curves showed no clear rectification behavior, keeping the high conductance state even at the negative voltage regime (Figure 4.10). Meanwhile, the current tended to drop sharply under a large negative voltage. After the switching from high- to low-conductance states at the voltage of an off-like state (V_{off}), there was another current jump taking place at the voltage of an on-like state (V_{on}) upon reversing V_b to zero. The unipolar conductance switching behavior contained hysteresis characterized by the difference between V_{on} and V_{off}.

During several cycles of voltage sweeps, this hysteresis became smaller and eventually disappeared, as displayed in Figure 4.8d. Thereafter, it showed stable NDR features (Figure 4.8e) similar to those shown in Figure 4.8a. The results can be understood as a consequence of a nonsymmetrical salt gradient along the pore axis formed before the measurements. More specifically, the fact that the conductance at negative V_b was similar to that in the positive regime suggests a certain extent of intrusion of high-concentration buffer into cis during the liquid injection (Figure 4.8f). However, the salt gradient was presumably quasi-stable under the repeated EOF processes, so it gradually deformed into the symmetric one after several

cycles of I_{ion}-V_b recordings (Figure 4.8g). This not only proves the robustness of the ionic NDR but also indicates a possible application as memristors[23,61–63] by adding control over the quasi-stable salt gradient across the membrane.

The presence and absence of resistive switching behavior are thus attributed to the varying initial salt gradient conditions that were not controllable under the experimental procedure used where the high-concentration electrolyte buffer was injected to one side of the membrane and then the low-concentration one to the other side using a syringe. As a consequence, the ion distribution around the micropores was presumably asymmetric in some cases at the first point, resulting in the resistive switching behavior, as shown in Figure 4.8c. Otherwise, when the ion distribution was symmetric, the I_{ion}-V_b curves showed stable NDR characteristics under the repetitive voltage sweeps (Figure 4.8a).

In summary, asymmetric ion transport characteristics in a low-aspect-ratio solid-state pore under the applied 100-fold salt concentration difference across the membrane were demonstrated. The mutual roles of diffusio-osmosis and electro-osmosis in rapidly decreasing the local ion density at the channel orifices under negative voltage sweeps and thereby causing NDR behavior were found. This characteristic was also suggested to take place only under a symmetric salt gradient across the channel. Otherwise, the electro-diffusio-osmotic effects induce conductance switching until the asymmetric local ion density distribution becomes symmetric via EOF under the repeated voltage ramps. The present results in Chapter 4 may provide a guide to designing micro- and nanofluidic memristors.

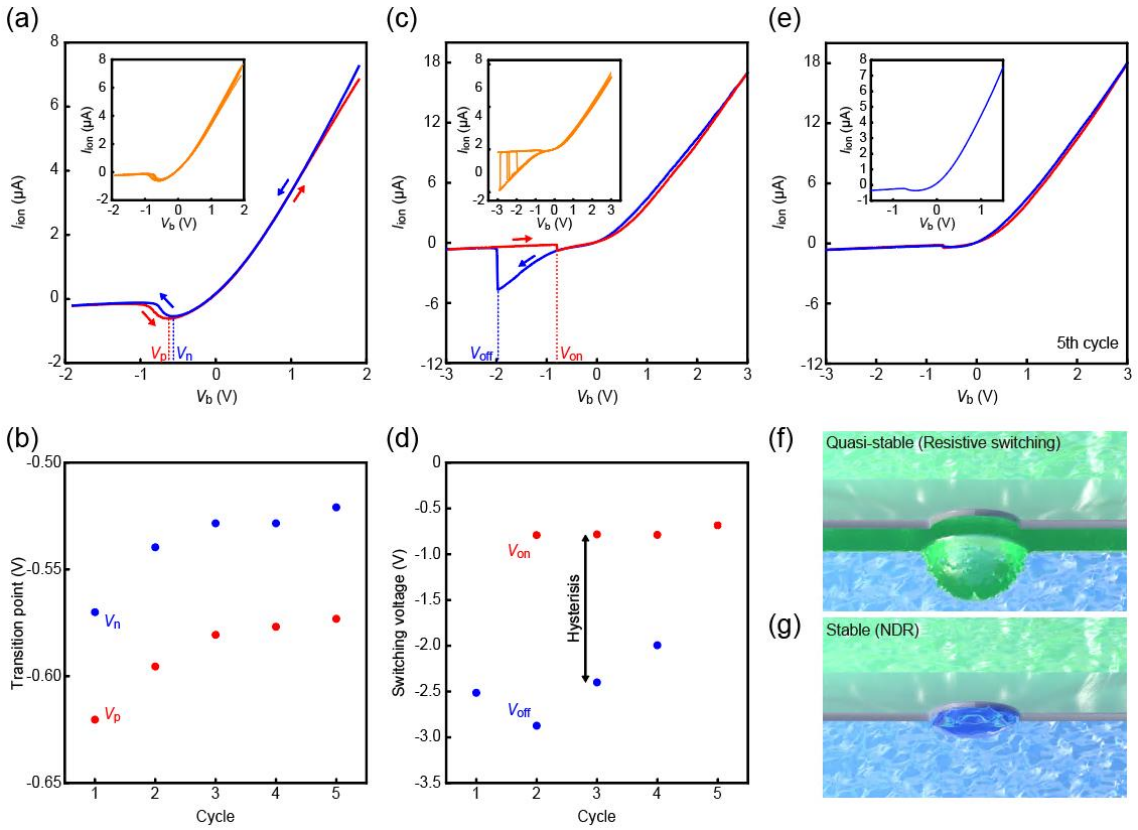

Figure 4.8 Observed phenomenon of resistive switching in micropore

Example of an experimental data set of resistive switching recorded by a 1 μm diameter and 50 nm thick pore when r_{conc} = 100 (c_{cis} = 10 c_0 and c_{trans} = 0.1 c_0). (a) Repeated I_{ion}-V_b measurements with little hysteresis under positive and negative sweeps. The ionic current changed smoothly under the V_b sweeps. The inset shows the results of five cycles of the I_{ion}-V_b measurements. (b) The voltage at I_{ion} minima in (a) during the positive (V_p) and negative (V_n) voltage sweeps. (c) I_{ion}-V_b curves with large hysteresis. The inset shows the results of five cycles of the measurements. The conductance tends to jump from high to low states during the voltage sweeps in a negative direction at V_{off} (blue). Subsequently, the conductivity was reset to the original state at Von when scanning back the voltage (red). (d) Change in V_{on} and V_{off} during several cycles of V_b sweeps, demonstrating smaller hysteresis by repeating the voltage scans. (e) The result of the fifth measurement with no resistive

switching but a clear NDR feature (the inset is a magnified view), is almost identical to that in (a). (f, g) Schematic models describing (f) symmetric and (g) asymmetric ion density distributions responsible for the stable NDR and quasi-stable resistive switching behaviors. Reproduced and adapted with permission from ref.[58]. Copyright 2020 American Chemical Society.

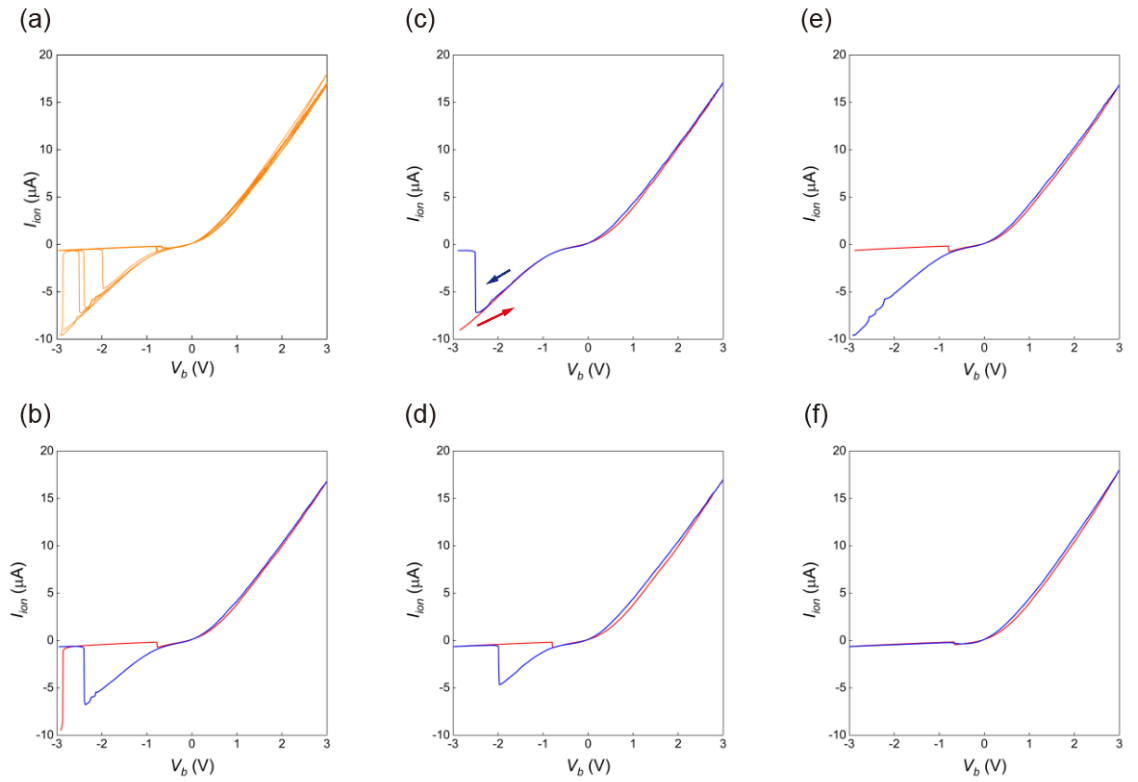

Figure 4.9 Example of experimental results when resistive switching happening

Experimental results of resistive switching were observed in a 1 μm-diameter and 50 nm thick SiNx pore. (a-f) The I_{ion}-V_b curves acquired under 5 cycles of voltage sweeps from 3 V to – 3 V (a). The Iion – Vb characteristics in each cycle from the first (b) to the fifth (f) sweeping (b-f). Blue and red curves are the data obtained during negative and positive voltage sweeps as indicated by the arrows. (g-m) Another experimental result of the resistive switching behavior. Reproduced and adapted with permission from ref.[58]. Copyright 2020 American Chemical Society.

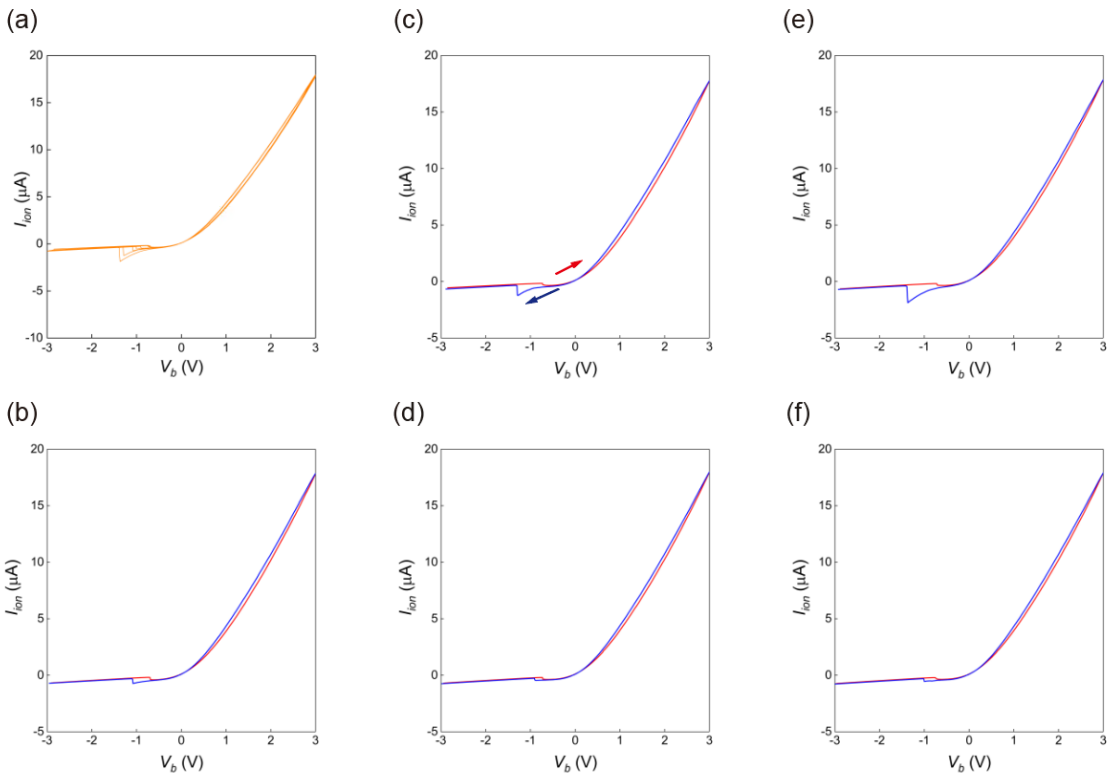

Figure 4.10 Example of experimental results when resistive switching happening

The pore was the same as the one used in (a-f). The I_{ion}-V_b curves acquired under 5 cycles of voltage sweeps from 3 V to -3 V (g). The I_{ion}-V_b characteristics in each cycle from the first (h) to the fifth (m) sweeping. Blue and red curves are the data obtained during negative and positive voltage sweeps (h-m). Reproduced and adapted with permission from ref.[58]. Copyright 2020 American Chemical Society.

Chapter 5 Surface effect of electroosmosis-driven nanofluidic diodes

5.1. Introduction

Understanding and controlling mass and ion transport in the nanoscale is of importance for fluidic circuits,[64] biosensing,[65], and energy harvesting.[35,66] The innovative solution can directly address the water-energy nexus[67,68] through the application of forward osmosis and reverse osmosis. The use of ion-selective materials such as graphene,[69,70] MXenes,[71,72], and metal-organic framework[73,74] is usually employed in related studies. Recently, solid-state nanopores have demonstrated remarkable controllability of ion transport that opens the way to develop a feasible ionic circuit.[75]

The ion transport phenomena in nanochannels are related to the electrostatic effect of surface charges on the wall.[76] Generally, negatively charged surfaces (usually found in silicon-based channels) attract countercations. In a fluidic channel of size much larger than the Debye length, the electrostatic potential at the wall causes negligible influence on the ion transport due to the screening by ions. On the other hand, if the size of the channel is comparable to the thickness of the electrical double layer, the negative surface potential tends to effectively impede the migration of anions via the electrostatic repulsion.[57] In this situation, the nanopore rectifies the ion cross-membrane ion flow in a voltage-dependent manner under the imposed asymmetry in the solution properties as well as channel geometries, thereby enabling diode-like characteristics called ionic current rectification (ICR).[77,78]

The strength of ion selectivity depends on the channel size and Debye length, which are closely related to the ion concentration and mobility, and the physical conditions of the channel.[57,79] In addition, multi-component and multivalent electrolyte solutions also have varying degrees of influence on ion transport[80,81] because of the ion-dependent surface charge regulation.[82] Therefore, many approaches are used to modify the properties of ion transport, including but not limited to, molecule modification,[83–85] high-dimensional materials,[86–89], and gate potential.[13,90] Furthermore, bipolar channel[12,91–94] or Janus membrane[95] are reported to achieve the function of an ionic diode, even a solid-state bipolar junction transistor (BJT).[96]

As the diameter of the nanopore increases, the electric double layer doesn't overlap, which means that ion selectivity fails, and so does the ICR of the nanofluidic. In a non-uniform solution system, ion transport in low-aspect-ratio nanopores includes electromigration, electroosmosis, and diffusion-osmosis. The direction of ion diffusion is fixed from high to low concentration, but the direction of electroosmotic flow (EOF) is determined by the potential bias, and this difference causes ICR. In the case where EOF can resist ion diffusion, nanopores can achieve the effect of ICR even without ion selectivity or ion polarization.[30,48] The entrance effect of nanochannels was thoroughly studied with channel size[97] and geometry[98] in numerical simulation. The ICR effect of nanopores functionalized with molecule brushes has been reproduced and studied using theoretical simulations, followed by a comparison of the inner- and outer-surfaces of nanochannels[99–102]. In addition, research groups modified anodic aluminum oxide membrane[103,104] and nanopipette[14] with polymers to control ion transport.

Besides the application as iontronics building blocks, the present approach may be useful in resistive pulse sensing of nanoparticles and molecules considering the pivotal roles of the electroosmotic flow in the capture-to-translocation dynamics of the analytes as described in Chapter 3 and Chapter 4. For example, the present results in this chapter suggest that the direction and speed of EOF can be largely controlled by the coating material on the inner wall of a pore. Meanwhile, one can choose the dielectrics on the top surface to vary the contribution of the electrostatic interactions between the analytes and the membrane charges.[105] It would also be important to choose the suitable side of the membrane to add the analytes as the fluidic diode may provide a critically low open pore current for implementing resistive pulse sensing. Another example is the osmotic power generators, where it is known that the surface charge densities at both the inner and the outer surface of a nanopore membrane are important for attaining high energy conversion efficiency.[106] To this end, the partial coating method would allow fine control of the entrance effects to the ion selectivity by the choice of the dielectric layer on the top surface.[104,107]

In the present work, a method of manufacturing nanopores with oxide coating to gain control of ion transport is discussed. Compared with chemical ways of surface modification with soft organic monolayers, physical approaches such as sputtering is a convenient method to coat nanopores with hard dielectric thin films. In the previous literature, various coating materials (SiO_2,[108,109] HfO_2,[110,111] ZnO,[112,113] TiO_2,[114,115] and Al_2O_3[116,117]) were employed to study the effect of controlling mass and ion transport. Herein, the coating materials and patterns of a dielectric layer on solid-state nanopores were qualitatively examined. By testing coating materials of various isoelectric points and a wide range of pH conditions, the effect of surface charge on the EOF-derived ICR was fully investigated. Meanwhile, a numerical simulation is

used to illustrate the fluidic phenomenon near the nanopore. Even without ion selectivity, the ionic current characteristics can be changed from resistor to diode via surface charge control through dielectric coatings. As a result of the present finding in this chapter, it became evident that modifiable surfaces can be used as building blocks to create novel nanostructures with thin film deposition.

5.2. Surface charge effects with oxide thin film deposition

First, an experiment was performed to confirm that ICR occurred under asymmetric solution conditions and a single pore with a diameter of d_{pore} = 300 nm in a L_{pore} = 50 nm thick SiN_x membrane was used. In the experiments in this chapter, all measurements were performed in a potassium chloride (KCl) solution. The KCl solution of 1 mM and 100 mM was filled into the *cis* (top) and *trans* (bottom) chambers (Figure 5.1a). While the chambers are filled with uniform electrolyte (c_{cis} = c_{trans}), linear ionic current (I_{ion}) - bias voltage (V_b) curves were obtained. In contrast, the I_{ion} - V_b curves demonstrated ICR under an applied salinity gradient (Figure 5.1b, and 5.2). It is noted here that the Debye lengths are 0.97 nm and 9.7 nm under the KCl concentrations of 100 mM and 1 mM, respectively.

It is thus difficult to expect ion selectivity in the nanopore since the diameter is larger than 30 times larger than the Debye length. Instead, it is more natural to anticipate the EOF-driven mechanism for the ICR observed,[30] which can be qualitatively explained by a serial resistance model.[54,118] In this, the total resistance of the nanopore is considered as three resistors connected in series: pore resistance and access resistance in *cis*/*trans* sides (R_{total} = R_{pore} + $R_{access.cis}$ + $R_{access.trans}$). The pore resistance results from the physical space in the nanopore (R_{pore} = $4\rho L/\pi d^2$) and the access resistance is due to the ions accessing the

nanopore in bulk solution from both cis and trans sides ($R_{access} = d/2\rho$). [4] In the case of the 300 nm-diameter cylindrical pores in SiN_x membrane with L_{pore} = 50 nm, $R_{access} \gg R_{pore}$. When there is no salt concentration difference between *cis* and *trans*, R_{access} remains almost unchanged during the voltage sweeps that give rise to the linear I_{ion} - V_b characteristics. With a concentration gradient, on the other hand, $R_{access.cis} > R_{access.trans}$ when $c_{cis} < c_{trans}$. Changing the transmembrane potential, meanwhile, the EOF pushes the water of a high (low) ion concentration into the pore so as to increase (decrease) R_{total} in a voltage-dependent manner, thus causing ICR (Figure 5.1c).

Table 5-1 The estimated values of zeta potential

The estimated values of zeta potential (ζ) corresponding to materials and pH value were collected from ref.[119].

Materials	Zeta potential (mV, pH 3)	Zeta potential (mV, pH 7)	Zeta potential (mV, pH 11)
SiO_2	30	-50	-80
SiN_x	40	-50	-75
TiO_2	45	10	-30
HfO_2	25	10	-25
Al_2O_3	80	10	-55
ZnO	50	-10	-40

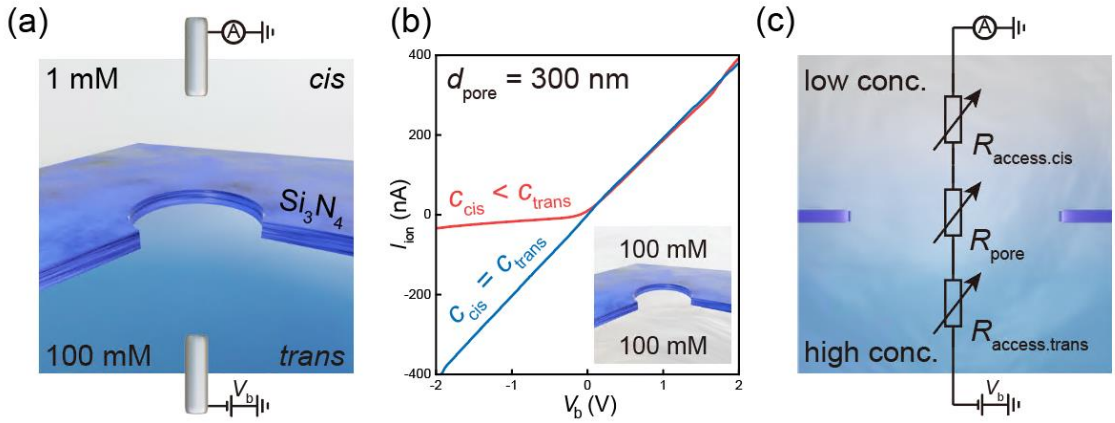

Figure 5.1 Resistance model for the nanopores

(a) Schematic setup of a 300-nm sized nanopore experiment. The objects are not to scale. The solutions with a lower (1 mM) and higher (100 mM) KCl concentration were in the cis and trans chambers. The ionic current (I_{ion}) is recorded by applying a potential bias (V_b) with a pair of Ag/AgCl electrodes. (b) I_{ion} – V_b characteristic of a nanopore under symmetric (blue curve) and asymmetric solution conditions (red curve) at pH 11. (c) . Equivalent circuit model of the nanopore under asymmetric solution conditions. $R_{access.cis}$ and $R_{access.trans}$ are the access resistances cis- and trans-side of the chamber. Rpore is the resistance inside the nanopore. All resistance is marked as variable resistance. Reproduced and adapted with permission from ref.[120]. Copyright 2023 American Chemical Society.

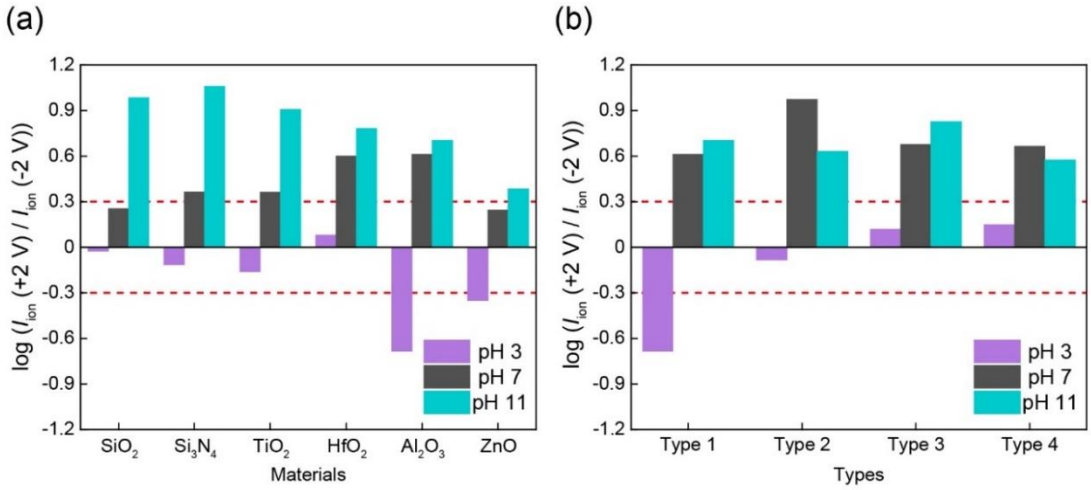

Figure 5.2 The result of the ICR ratio for coating materials and patterns

The result of the ICR ratio for coating materials (a) and coating patterns (b) at V_b = ±2 V is in Figure 5.3 and Figure 5.5. It can be seen that the logarithmic rectification ratio tends to be largely negative (positive) for nanopores coated with dielectric materials of higher (lower) isoelectric points as the pore wall surface tends to be charged more positively (negatively) at larger (smaller) pH. Pores with an ICR ratio greater than log 2 or smaller than log 0.5 are regarded as diode-like behavior, which is marked with red dotted lines in the figure. Reproduced and adapted with permission from ref.[120]. Copyright 2023 American Chemical Society.

In the next experiment, the surface effects of nanopores were investigated with the properties of oxide materials on nanopores (Figure 5.3). Figure 5.3b shows I_{ion} - V_b curves for a SiN_x pore along with the ones with a 10 nm-thick layer of SiO_2, HfO_2, ZnO, TiO_2, and Al_2O_3 deposited on the entire surface including the pore wall. The devices were verified by SEM and the diameter of the nanopores was 280 nm ± 18 nm due to fabrication errors (Figure 5.3d). Coating materials have independent isoelectric points (Figure 5.3e and Table 5-1), and by controlling the pH value under acidic (purple curve), neutral (black curve), and alkaline (cyan curve) conditions, each shows their corresponding $I_{ion} - V_b$ characteristic result (Figure 5.3b, see also Figure 5.4 for the result without salt gradient).

The ICR ratio of all the experiments at V_b = ±2 V was sorted out and compared with the collected zeta potential (ζ) of the material at the corresponding pH value (the values used are described in Table 5-1).[119] To see the dependence of the rectification behaviors on the surface potential, the logarithmic ICR ratio was plotted as a function of ζ for the cases of pH 3, 7, and 11 (Figure 5.2a), so that the difference in the rectification directions can be easily judged by their positive and negative values (note that the positive and negative values of the logarithmic ICR ratio signify different rectification directions). The result clearly showed the different rectification directions for the cases of positive and negative zeta potentials. Interestingly, a linear relationship was also observed between the logarithmic ICR ratio and the ζ irrespective of the coating materials (Figure 5.3c), which can be interpreted as a consequence of the stronger electroosmotic flow to modulate the ion concentration distributions at the nanopore orifices during the voltage sweeps. The results clearly demonstrate the effectiveness of the dielectric coating approach for controlling the EOF-driven ICR behaviors through membrane surface charge engineering.

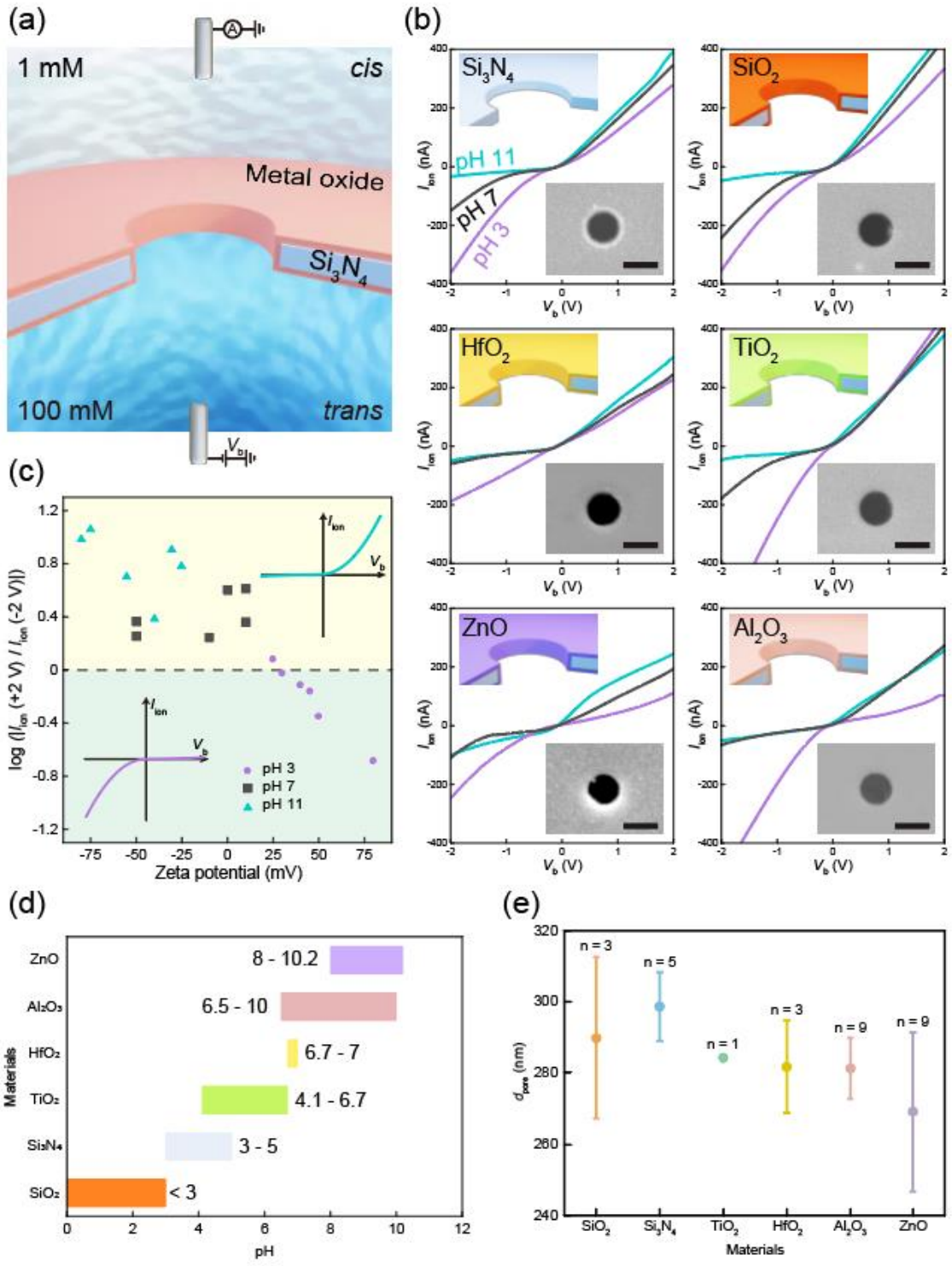

Figure 5.3 Schematic setup of the experiment with coating materials on nanopores

(a) Schematic setup of the experiment with coating materials on nanopores. The objects are not to scale. The solutions with a lower (1 mM) and higher (100 mM) KCl concentration were

in the cis and trans chambers. (b) I_{ion} - V_b curves for the SiNx pore and the coating materials of SiO_2, HfO_2, ZnO, TiO_2, and Al_2O_3 at pH 11, pH 7, and pH 3. Inserts are the images of the nanopore obtained by scanning electron micrographs. The black scale bar is 300 nm in length. (c) ICR ratio in a logarithmic scale with zeta potential. The ICR ratios rare collected from all data in (b) while V_b = ±2 V. The insert shows the direction of rectification. (d) Comparing the reduction of nanopore diameter (d_{pore}) after the oxide coating process in scanning electron micrographs (SEM). SEM images were used to estimate the size of the nanopores with an oxide coating, where n is the number of samples. (e) The pH range of the isoelectric point of oxide materials used in nanopores. Reproduced and adapted with permission from ref.[120]. Copyright 2023 American Chemical Society.

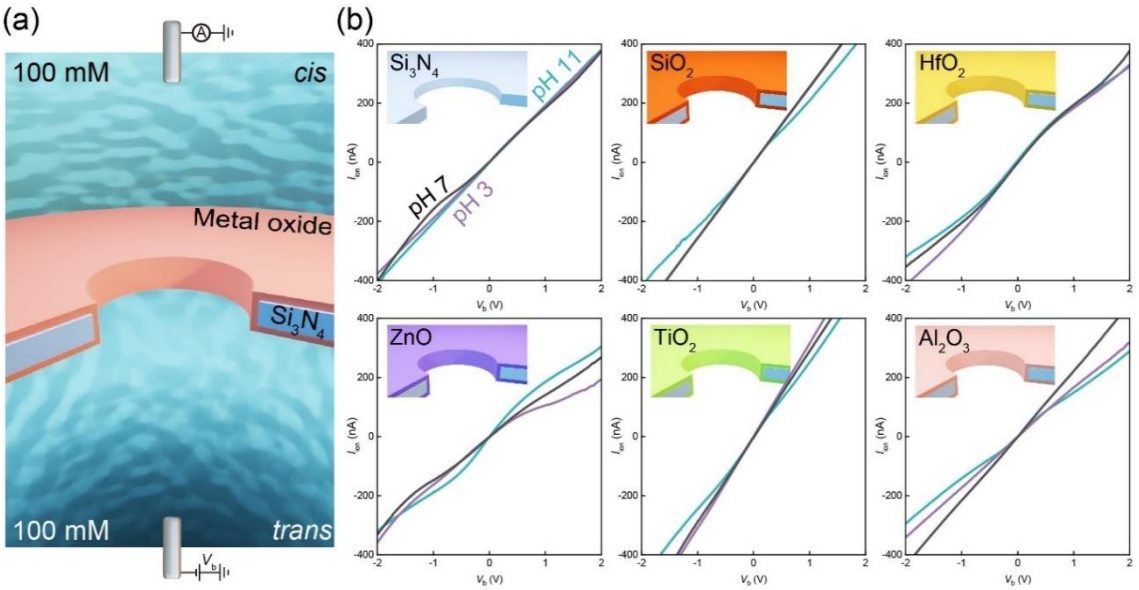

Figure 5.4 I_{ion} - V_b characteristics of a symmetric condition

(a) Schematic setup of the experiment under a uniform solution. The objects are not to scale. The solutions with 100 mM KCl are filled in both the cis and trans chambers. (b) I_{ion} - V_b curves for SiNx pores and the coating materials of SiO_2, HfO_2, ZnO, TiO_2, and Al_2O_3 at pH 11, pH 7, and pH 3. All pores are 300 nm in diameter. Reproduced and adapted with permission from ref.[120]. Copyright 2023 American Chemical Society.

5.3. Partial coating with different patterns

From the results in the previous section, it was shown that the ζ successfully changed by using oxide coatings and pH adjustment, allowing us to control ICR in a nanopore. The next question is, what is the role of pore surfaces in ICR? To understand the role of the three surfaces of the nanopore: $wall_{\text{inner}}$, $surface_{\text{cis}}$ (the lower concentration side), and $surface_{\text{trans}}$ (the higher concentration side) (Figure 5.5a), a fabrication method was designed, through fabricating a nanopore with or without an oxide materials layer on the three surfaces. By arranging the sequence of the manufacturing process, four types of structures with an Al_2O_3-coated surface can be produced (Figure 5.5). Scanning electron microscope observations revealed a similar appearance of these nanopores, while the $I_{\text{ion}} - V_{\text{b}}$ characteristics showed a wide variation ascribable to the difference in the zeta potentials. Type 1 exhibits diode-like behaviors of different polarities at pH 3 and pH 11, for example, while Type 2 and Type 3 display diode and resistor behaviors, respectively. Based on the results above, only Type 1 pore had reverse ICR at pH 3, indicating that only a completely positive charge could cause EOF to reverse. As a supplement, if the salt gradient is removed, all types of pores will obtain a linear $I_{\text{ion}} - V_{\text{b}}$ curve (Figure 5.6).

Since the construction of Type 2 and Type 3 pores are asymmetric, the $I_{\text{ion}} - V_{\text{b}}$ curve will be changed if the direction of the salt gradient was reversed (Figure 5.6). The outer surface behaves differently in higher and lower concentrations because the phenomenon has been reported within Debye-overlap ICR.[101] It was generally believed that the outer surface effect on ion transport was negligible, but the experimental results show that the outer surface will influence the fluidic flow on a sub-100 nm scale, thereby affecting the $I_{\text{ion}} - V_{\text{b}}$ characteristics. In addition, Type 4 pore exhibited a BJT-like behavior at pH 3 (Figure 5.5). Both $surface_{\text{cis}}$

and $surface_{trans}$ are positively charged and $wall_{inner}$ is negatively charged. From the results of $I_{ion} - V_b$, the entire pore exhibits lower conductivity at higher V_b. The solution with lower conductivity occupies the entire nanopore regardless of positive or negative bias. This phenomenon shows that the fluid always flows from the thinner side to the higher concentration side. From this experiment, It was demonstrated that it is possible to change the ICR properties of the $I_{ion} - V_b$ characteristic by modifying the specifically charged surfaces.

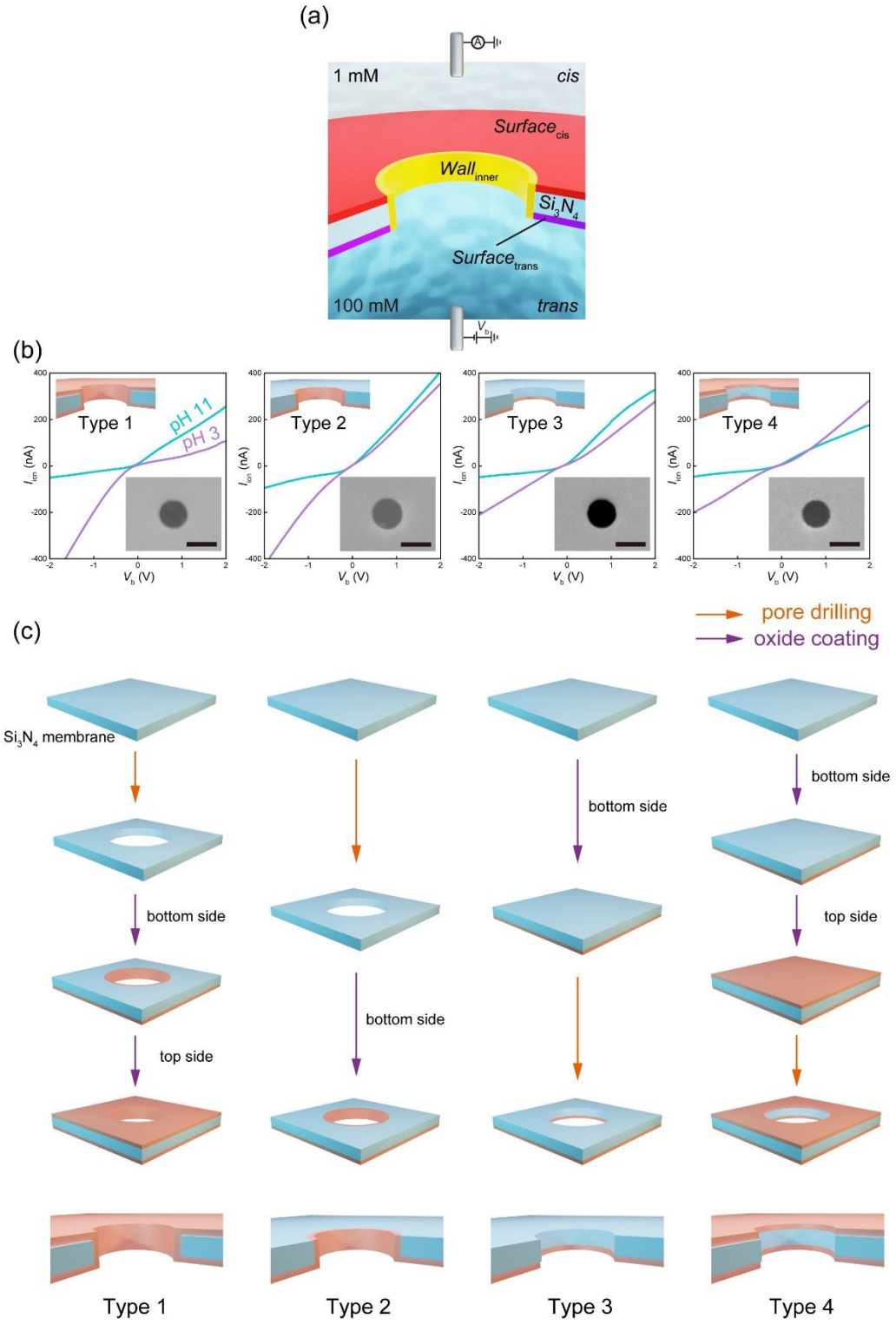

Figure 5.5 Schematic illustration of the surface composition of four types of nanopores

(a) Three modifiable surfaces: *surface*$_{cis}$, *wall*$_{inner}$ and *surface*$_{trans}$ (marked as red, yellow, and

purple). (b) I_{ion} - V_b curves for the 4 types of Al_2O_3-coated nanopore with d_{pore} = 300 nm under a 100-fold concentration gradient at pH 11 and pH 3. Inserts are the images of the scanning electron micrograph. The black scale bar is 300 nm in length. (c) Fabrication processes for the four types of nanopore clips. The coating method was reported in previous literature.[121] Briefly, the freestanding membrane was subjected to radio-frequency magnetron sputtering (SVC-700LRF, Sanyu Electron) for HfO_2, ZnO, TiO_2, and Al_2O_3 and CVD (PD-200STP, Samco) for SiO_2 (all deposition materials were purchased from Samco). Thus, the entire coated surface with a 10 nm-thick dielectric layer was made by monitoring the growth rate. If needed, another side of the chip was also covered with oxide coatings of the same thickness. On the membrane surface, an electron beam resists ZEP520A-7 (Zeon) on the top side of the membrane was spin-coated and delineated a 300 nm-diameter circle by electron beam lithography (50 kV, Elionix). After the development with ZEP-N50 (Zeon), the nanopore was drilled by reactive ion etching with CH_4 etchant gas. Following this, the nanopore chip was immersed in N, N-dimethylformamide (DMF) overnight to dissolve the resist before being rinsed several times with isopropanol and acetone. Reproduced and adapted with permission from ref.[120]. Copyright 2023 American Chemical Society.

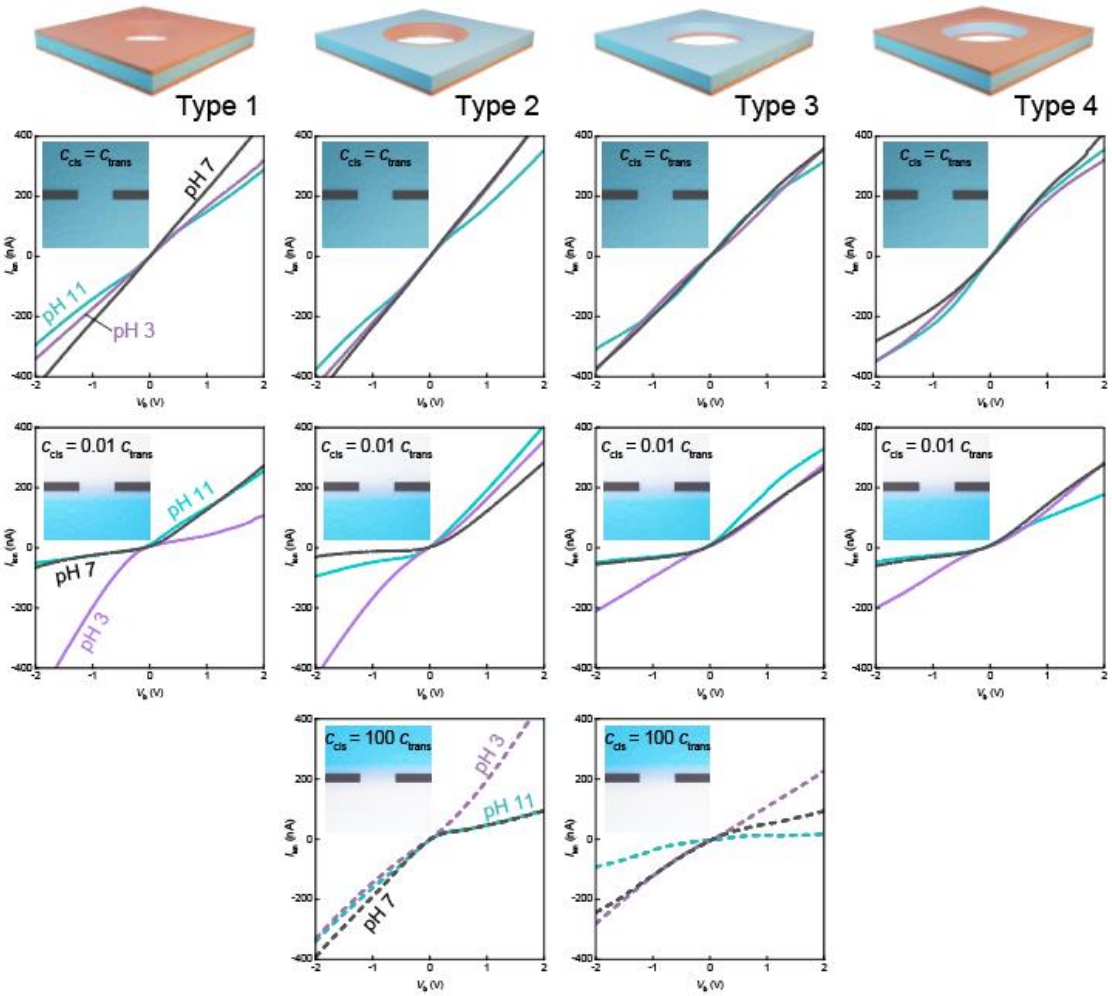

Figure 5.6 I_{ion} - V_b result of Type 1 – Type 4 pores with uniform concentration condition

Recorded I_{ion} - V_b curves for the 4 types of 300-nm sized and Al_2O_3-coated pores under a uniform concentration (first row), forward salt gradient (second row), and reverse salt gradient (third row). The same devices were used in Figure 5.5. Reproduced and adapted with permission from ref.[120]. Copyright 2023 American Chemical Society.

5.4. Extended result with numerical simulation

It can be seen from the measurement results that the order of the influence of the surface on the EOF-driven ICR is $wall_{inner}$, $surface_{cis}$, and $surface_{trans}$. However, limited by the experimental conditions, it is difficult for us to independently test the effect of a single surface on ion transport.

Numerical simulations were performed to predict the ionic current and the EOF to better understand the ion transport properties in nanopores. An existing model was used for estimating I_{ion} and EOF in the nanopores under salinity gradients.[48,102,122,123] More specifically, a 2D axis-symmetric model was used to simulate the electric field, ion transport, and fluidic flow by numerically solving the Poisson–Nernst–Planck and Navier–Stokes equations in COMSOL software. The diameter and thickness of the nanopore model are d_{pore} = 300 nm and L_{pore} = 70 nm. The ζ of various materials[119] were compared at different pH and converted into surface charge densities for easy input into the software. Comparing the converted values and referring to past literature,[119] and a surface charge density of σ = -10 mC/m² was used as a standard value for the SiN_x membrane. The surface charge density was set for a certain surface and set the non-participating surface to zero charges in the simulation. Meanwhile, special care was put on the validity of the estimations of EOF, where finer meshes were used near the membrane and pore wall surfaces compared to those in the bulk compartments. Technically, the verification was exhibited by testing different mesh sizes and finding a convergence of the EOF speed. The other detailed setting of the nanopore model used in each calculation and the boundary conditions are described in Chapter 2 (also see Figure 5.7 for the surface charged density set on the pore wall).

In the first place, it can be observed that if a negatively charged boundary is placed with a concentration gradient of 10 mM KCl in the cis chamber and 100 mM KCl in the trans chamber, the simulation results of $I_{ion} - V_b$ will be linear if a concentration gradient is not present or if surface charge density is very small (-1 μC/m²). ICR will only be triggered if there is a concentration gradient and a charged surface on nanopores (Figure 5.8a). Further, the research target was set to the surface charges on different surfaces. The simulated $I_{ion} - V_b$ for charged $wall_{inner}$ (red curve in Figure 5.8b) is very similar to the model of all charged surfaces (black curve in Figure 5.8b), and charged $surface_{cis + trans}$ has a weaker ICR result (blue curve in Figure 5.8b). Likewise, the result of comparing charged $surface_{cis}$ and $surface_{trans}$ (Figure 5.8c) also revealed that the surface with a lower concentration ($surface_{cis}$ in this case) has a larger influence. Based on the simulation results, the order of influence is $wall_{inner}$, $surface_{cis}$, and $surface_{trans}$. In addition, considering the different surface charges due to the solution concentration, it was shown that $surface_{cis}$ and $surface_{trans}$ have varying negative charges (Figure 5.9), which can evaluate the effect of surface charge differences caused by concentration regulation on ICR.

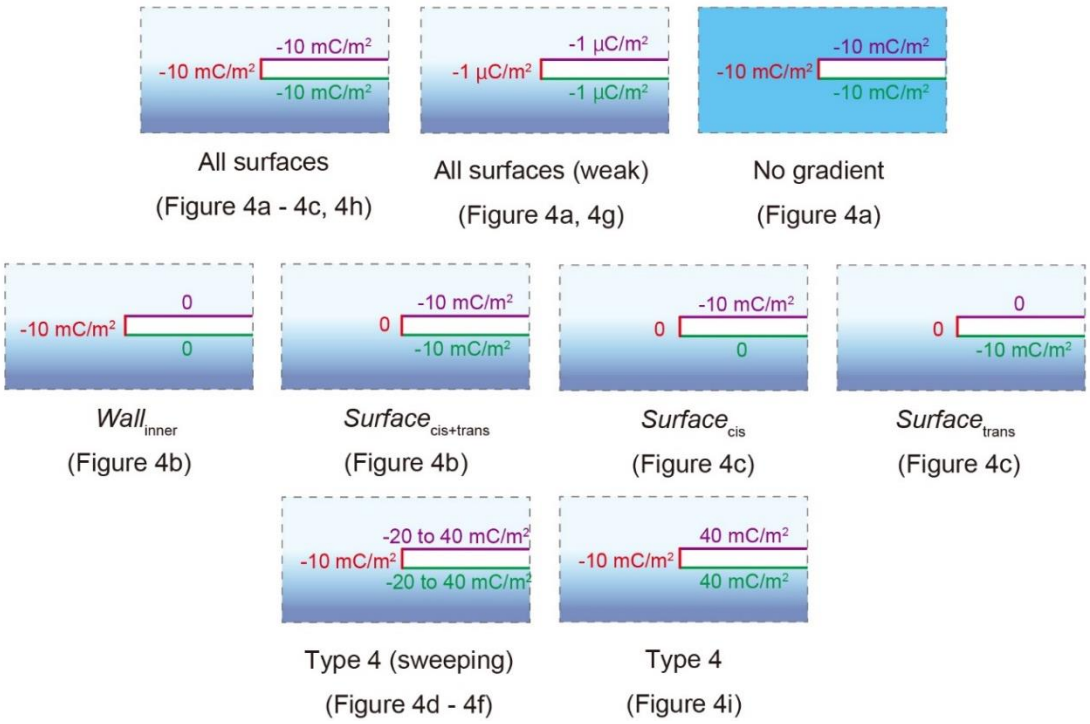

Figure 5.7 Surface charge conditions used in this chapter

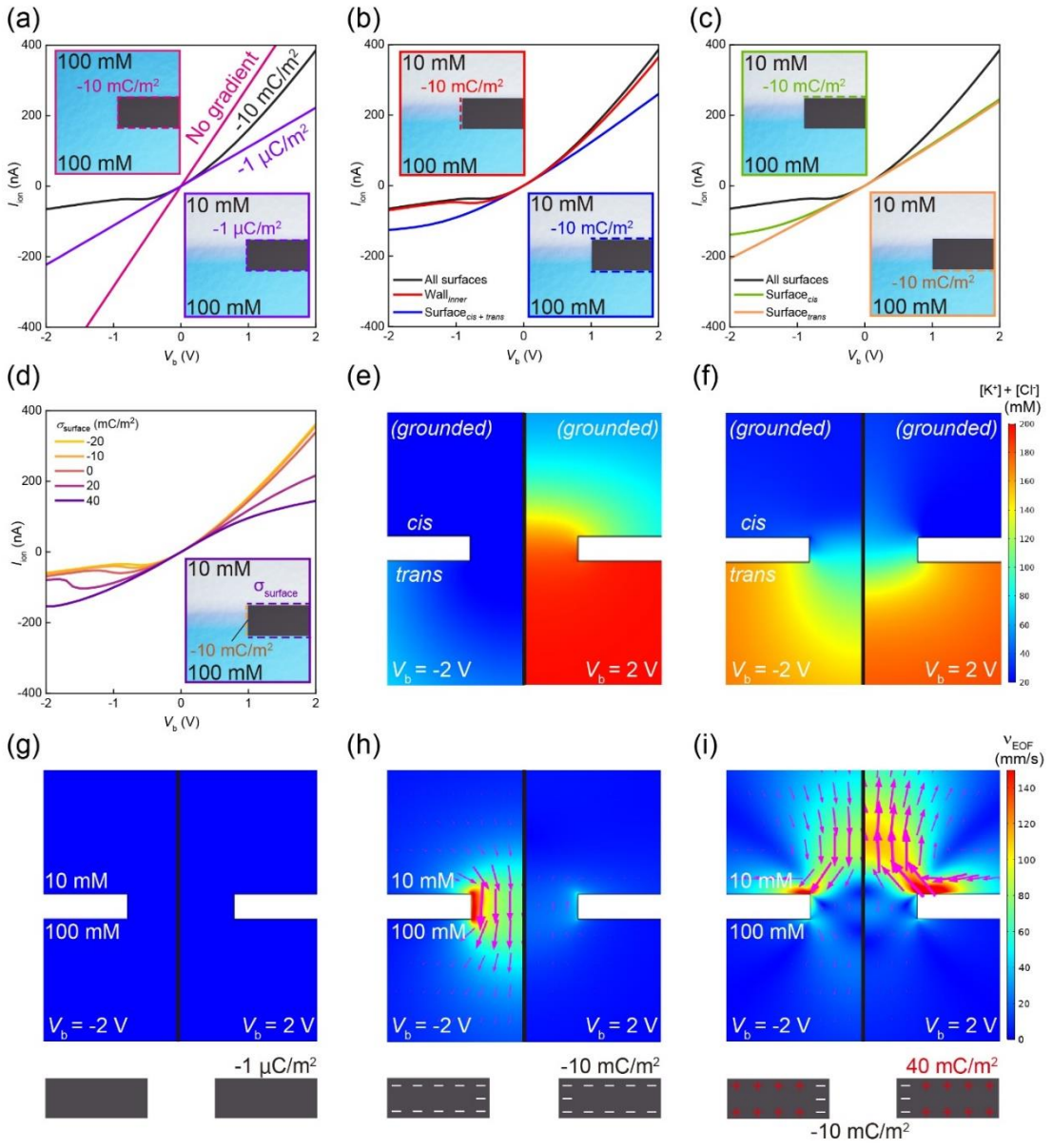

Figure 5.8 Ion transport properties of a nanopore in numerical simulations

The diameter and membrane thickness of the nanopore model is 300 nm and 70 nm. The surface charge density is set to -10 mC/m^2. I_{ion} - V_b characteristics are calculated when c_{cis}/c_{trans} = 10 (with a salt gradient). (a) Simulated result of I_{ion} - V_b curves under symmetric (pink curve) and asymmetric (black curve) solution conditions. For the non-charged surfaces, the surface charge density is set to 1 µC/m^2 (purple curve). (b) Simulated result of I_{ion} - V_b curves of comparison for the charged inner wall ($wall_{inner}$, red curve) and outer surfaces

(*surface*$_{cis+trans}$, blue curve) (c) Simulated I_{ion} - V_b curves of comparison for the charged surface on *surface*$_{cis}$ and *surface*$_{trans}$. (d) Simulated I_{ion} - V_b curves for the solid-state BJT-like behavior with Type 4 pore. The surface charge density on *wall*$_{inner}$ is fixed to -10 mC/m^2, with variable values on the outer surfaces (*surface*$_{cis}$ and *surface*$_{trans}$) from -20 to +40 mC/m^2. (e, f) The concentration distribution profiles of ions at V_b = ±2 V. (g - i) The color mapping of the EOF magnitudes (v_{EOF}, with arrows depicting the directions) for the representative comparison between the cases of resistor- (g), diode- (h), and BTJ- (i) like behavior when V_b = -2 V (left) and +2 V (right). Reproduced and adapted with permission from ref.[120]. Copyright 2023 American Chemical Society.

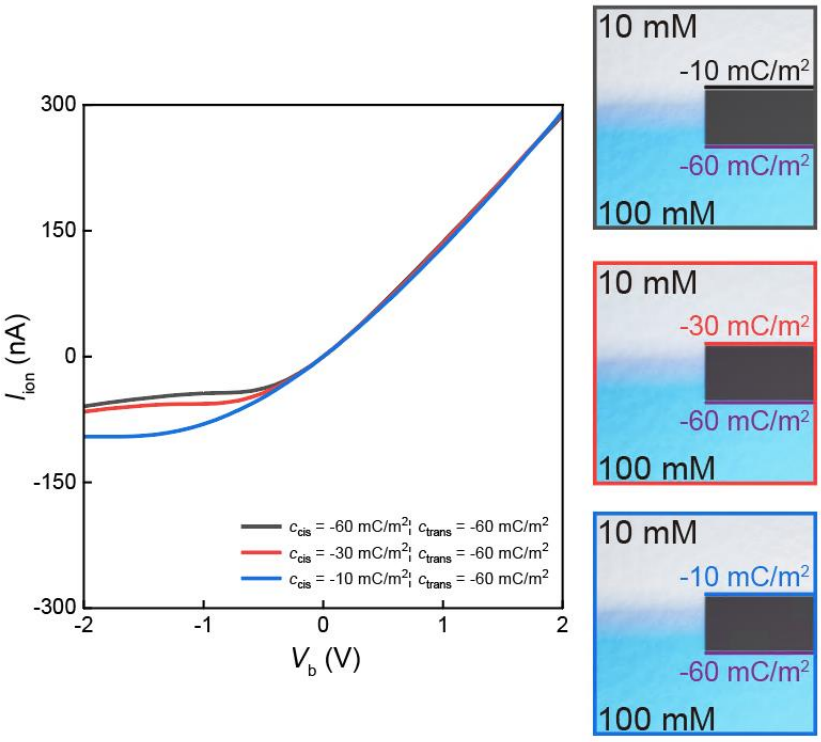

Figure 5.9 Simulated result for the outer surface

Simulated results of I_{ion} - V_b characteristics for surface charge regulation by a concentration gradient. To evaluate the effect of surface charge differences caused by concentration regulation on ICR. The surface charge density is set to -60 mC/m^2 on trans membrane, while the surface charge density on cis membrane is set to -10, -30 and -60 mC/m^2, respectively. Reproduced and adapted with permission from ref.[120]. Copyright 2023 American Chemical Society.

For the special case of the BJT-like ICR situation, the surface charge density on $wall_{inner}$ is kept at -10 mC/m², and the surface charge density of both $surface_{cis}$ and $surface_{trans}$ is varied from -20 to 40 mC/m². The result of I_{ion} - V_b is limited at both positive and negative bias when the surface charge density reaches 40 mC/m² (Figure 5.8d). Compared with the negatively charged Type 1 pore, the EOF direction of type 4 under uniform concentration conditions is reversed after the salt gradient was added, there will be an EOF in the opposite direction above the pore. The local ion concentration distribution can explain the BJT-like behavior (Figure 5.8e and Figure 5.8f): no matter whether the positive or negative bias is increased, ion migration reached the same saturation state and was maintained by the EOF, which leads to the appearance of BJT-like ion transport.

The numerical simulation explains how the situation of ion transport acts like a resistor, diode, and BJT in the pores (Figure 5.8g-4i). For the Type 1 pore with a weak surface charge, EOF of equal magnitude and opposite direction will be generated at both positive and negative bias that creates a resistor-like property (Figure 5.8g). If the surface charge density increased to -10 mC/m², on the other hand, the nanopore acts as a diode because of the asymmetric EOF (Figure 5.8h). For the Type 4 pore working under an asymmetric salt condition, this concentration gradient induces fluid vortices and nonlinear EOF, driving the pore to exhibit BJT-like characteristics (Figure 5.8i). Especially, the calculated ion distribution results also satisfy the resistance model consisting of R_{pore} and R_{access} (Figure 5.1c). Notably, even $surface_{cis}$ influence is much more significant than $surface_{trans}$. The heatmap of EOF magnitudes (v_{EOF}) show that $wall_{inner}$ contributes more power to EOF than $surface_{cis + trans}$ (Figure 5.10). Under the condition of an applied bias V_b = -2 V, it can be

observed that the EOF result for Type 1 can be split into the sum of the $wall_{\text{inner}}$ and $surface_{\text{cis + trans}}$.

Additional experiments were performed for extending the pore radius and membrane thickness. If the radius of the Type 4 pore increases, the BJT-like $I_{\text{ion}} - V_{\text{b}}$ characteristic does not diminish even at 500 nm (Figure 5.11c). Conversely, the BJT-like $I_{\text{ion}} - V_{\text{b}}$ characteristic disappears quickly with increasing membrane thickness to 1000 nm (Figure 5.11d). This evidence suggests that the lower-aspect-ratio structure is helpful for the formation of a functional nanofluidic transistor, depending on whether the EOF has sufficient influence.

Unlike ion-selective pores, oxide-modified pores exhibit the properties of solid-state BJT-like ICR by electromigration and electroosmosis. If a bipolar pattern is applied to this model, the result of BJT-like ICR will not appear in the numerical simulation (Figure 5.12). Finally, It was found that materials with different isoelectric points between the surfaces on the pore also affect the $I_{\text{ion}} - V_{\text{b}}$ results. It shows that even without the positively charged layer such as an Al_2O_3 layer at pH 3, other materials will influence ion transport by asymmetric EOF (Figure 5.13 shows the results with TiO_2-coated pore). The nanoscale fluid properties can be used to create nanodevices with the resistor, diode, and BJT-like properties through partial surface oxide coating.

In this chapter, it was shown that the ICR properties have been successfully changed in low-aspect-ratio pores by using a 10 nm-thick dielectric layer. Not only the coating materials but also the coating patterns affect the *I-V* characteristic. It demonstrated that the models experimentally and theoretically evaluated the impact of the 4 types of pores on ion transport. The numerical simulation shows that ICR occurs in extended-size bipolar nanopores without

ion-selectivity. Therefore, nanoscale pore structure can be demonstrated like a resistor, diode, or BJT under certain conditions. The direction of the electric potential bias, salinity gradient, and fluidic flow affects the ionic circuit properties based on nanopores. The result provides a novel approach that electrophoresis- and electroosmosis- driven transport in nanochannels can be modified by manipulating surfaces.

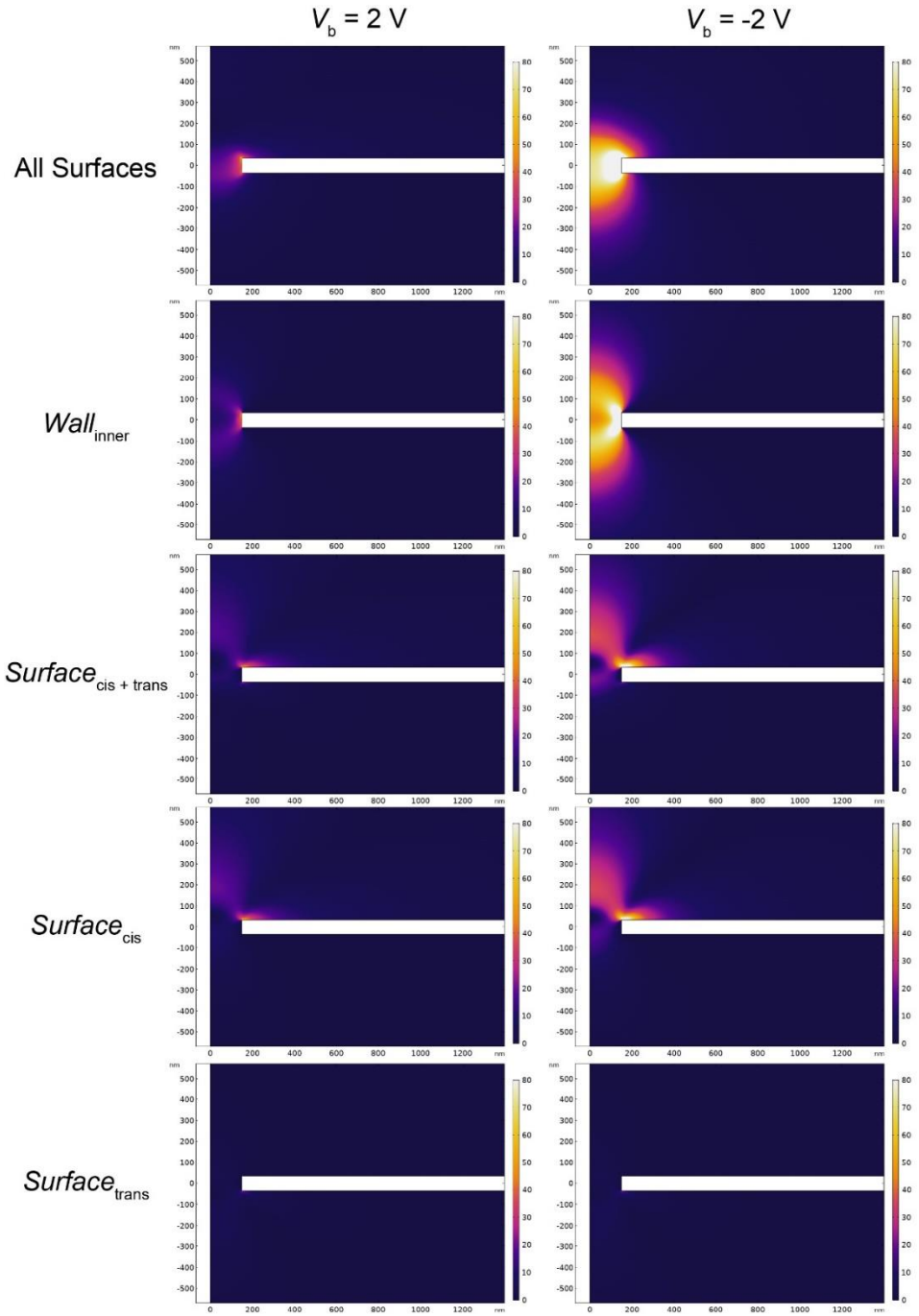

Figure 5.10 Simulated EOF results in 2D colour mapping

The heatmap for magnitudes of EOF when V_b = ±2 V by setting the value of surface charge density as -10 mC/m^2 on corresponding surfaces, and the other surfaces to zero charge. Reproduced and adapted with permission from ref.[120]. Copyright 2023 American Chemical Society.

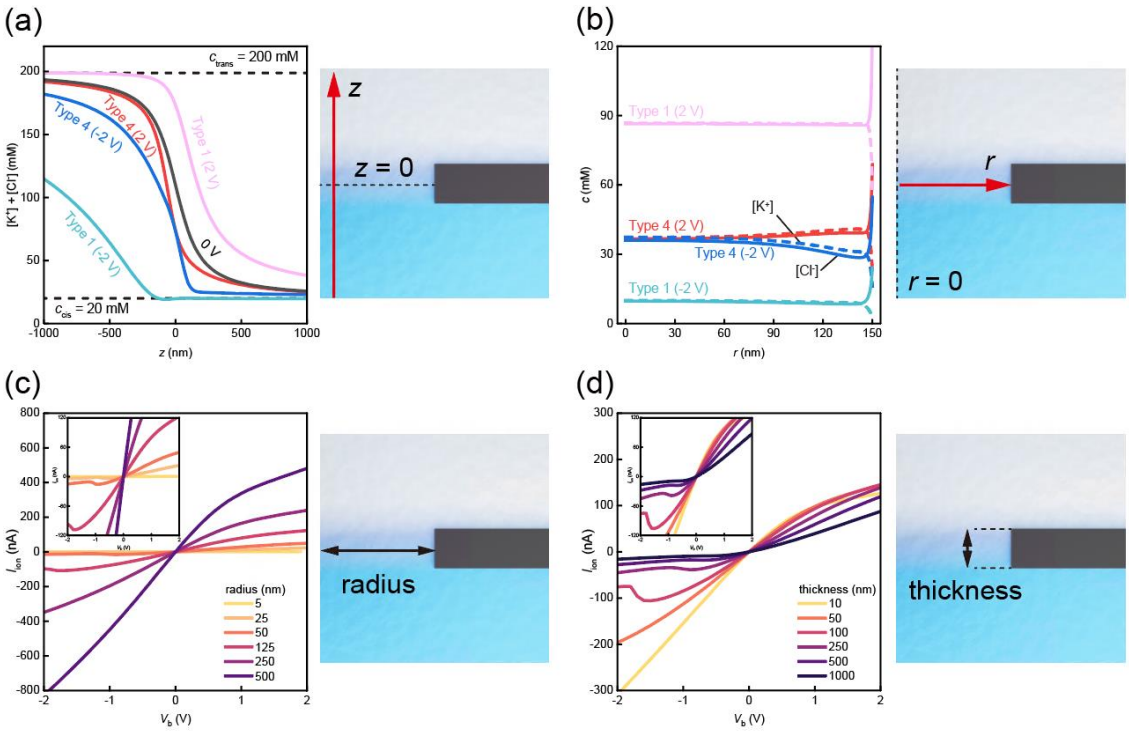

Figure 5.11 Geometry effect in the ICR

(a, b) Comparison of the axial concentration change between the Type 1 and the Type 4 nanopore at V_b = ±2. (a) Axial variation of total ion concentration along the z-axis. (b) The concentration of K^+ and Cl^- along the radial direction. (c, d) Pore size- and thickness-dependent ICR characteristics. Simulated I_{ion} - V_b curves deduced for pores of various radii from 5 nm to 500 nm in a 70 nm-thick SiNx membrane (c) and various thicknesses from 10 nm to 1000 nm in a 300 nm-sized pore (d). Reproduced and adapted with permission from ref.[120]. Copyright 2023 American Chemical Society.

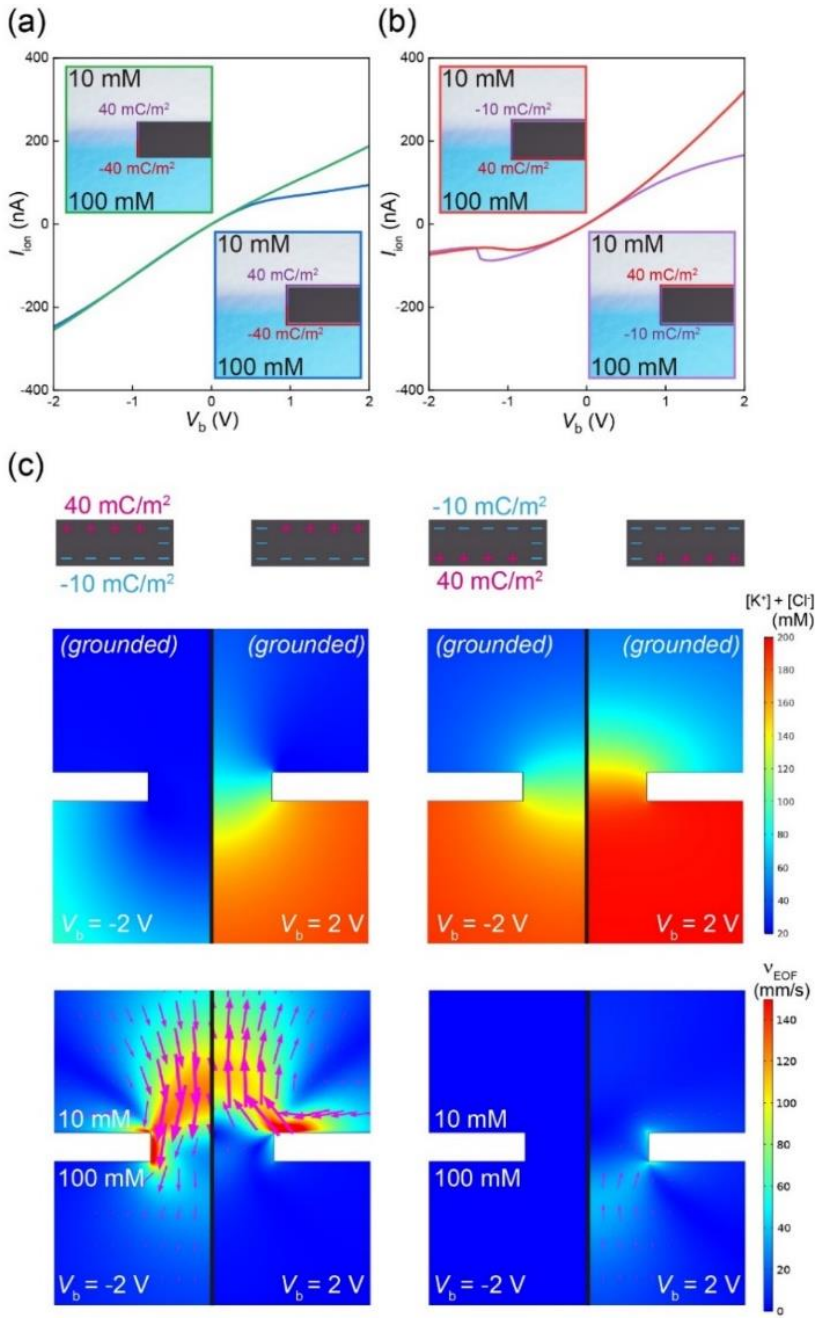

Figure 5.12 Simulated result for the Type 4 pore

(a, b) Simulated result of I_{ion} - V_b curves for bipolar membrane by setting the corresponding surface charge density to *surface*$_{cis}$, *wall*$_{inner,}$ and *surface*$_{trans}$. (c) The result for ion concentration profiles and EOF magnitudes when V_b = ±2 V. Reproduced and adapted with permission from ref.[120]. Copyright 2023 American Chemical Society.

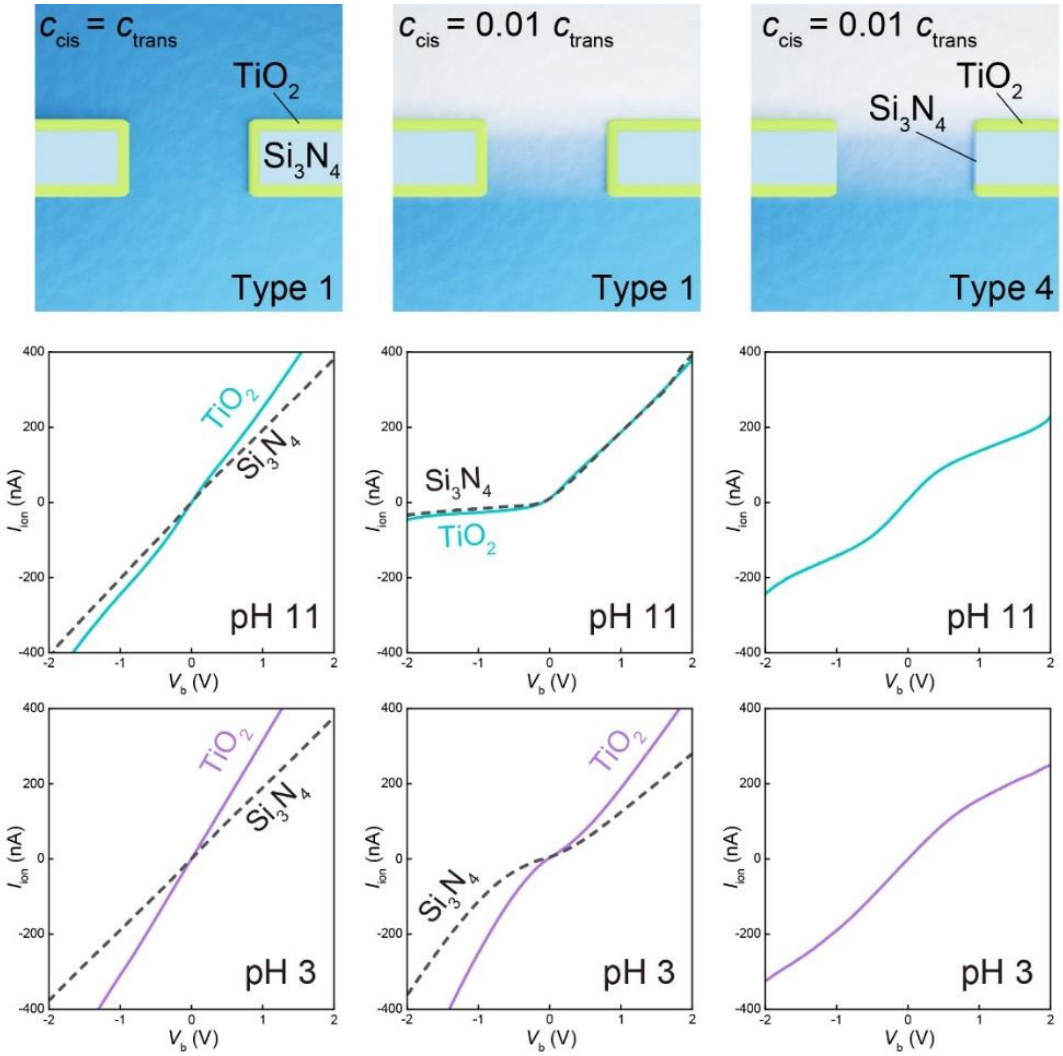

Figure 5.13 The result of TiO_2-coated devices

A comparison of I_{ion} - V_b characteristics between Type 1 and Type 4 pores with a 10 nm TiO_2 layer on a 300 nm-sized pore at pH 3 and pH 11. The black dashed curve represents the result obtained from SiN_x pore without oxide coating. Reproduced and adapted with permission from ref.[120]. Copyright 2023 American Chemical Society.

Chapter 6 Electrode effect in single particle sensing

6.1. Introduction

Nanopore technology is a powerful tool for analyzing biological samples at a single-molecule level.[64,65,124,125] It is a conductometer that detects a temporal change of the ion flow in a nanoscale conduit upon translocation of an object via ionic current measurements,[126] the simple mechanism of which has been demonstrated to enable a versatile sensor for identifying miscellaneous analytes from cells to genomes.[64,65,124–127] Being electrochemical in nature, meanwhile, the electrical current generally reflects the dynamic phenomena at the electrode-liquid interfaces.[128,129] Specifically, the application of voltage perturbs the local ion distribution by overconsuming reactants for the electrochemical reactions, which induces subsequent ion motions in the bulk to relax the acute ion concentration gradient near the electrode surface. This Cottrell diffusion causes a gradual decrease in the ionic current over time, whose characteristics provide rich information concerning the properties of ions in chronoamperometry.[130,131] However, little effort has been devoted to investigating its relevance to nanopore sensing,[129] where the time-course change in the impedance outside the pore may cause critical effects on the temporal resolution of the ionic current measurements for detecting small molecules and particles.[11,132,133] In this chapter, therefore, the issue of comparing resistive pulse measurements of nanoparticles was explored by using multiple kinds of electrodes (Figure 6.1).

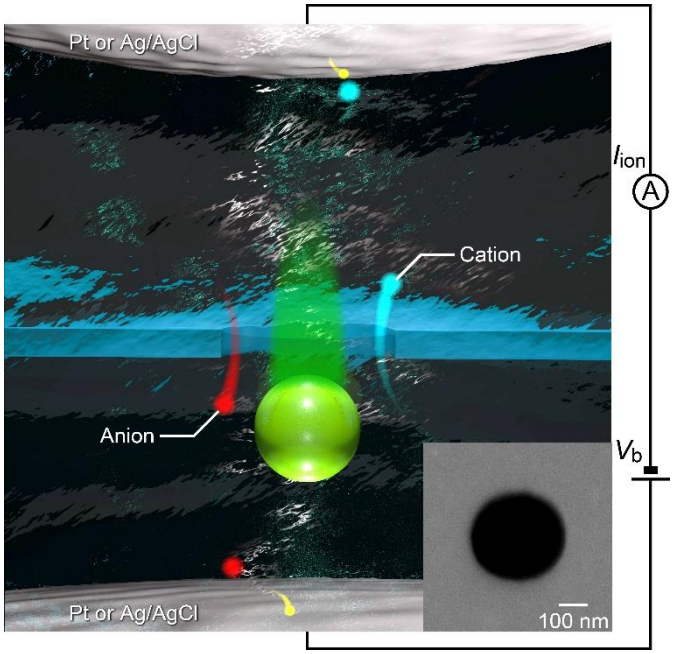

Figure 6.1 Schematic model for the concept of electrode effect in nanopore sensing

The ionic current I_{ion} flowing through a nanopore in a SiN_x membrane is measured in a phosphate-buffered saline (PBS containing various concentrations of NaCl under the applied voltage V_b. Transient drops in Iion upon electrophoretic translocation of the negatively charged polymeric nanobeads were recorded using two different electrodes, Ag/AgCl and Pt. Inset is a scanning electron micrograph (SEM) image of a 300 nm diameter pore in a 40 nm thick SiN_x membrane used for the resistive pulse measurements. Reproduced and adapted with permission under a CC BY-NC-ND 4.0 License from ref.[134]. Copyright 2022 Elsevier.

6.2. Resistive pulse measurements using Ag/AgCl electrodes

In the experiments in this chapter, a nanopore of diameter 300 nm in a 40-nm thick SiN_x membrane was used to detect 178-nm-sized polymeric beads in phosphate-buffered saline (PBS) at a concentration of 10^9 particles/mL (zeta potential of −37 to −30 mV in the electrolyte buffer of pH 7.6 containing 55 to 137 mM NaCl as measured by a zetasizer (Malvern)) by recording the ionic current (I_{ion}) under the applied bias voltage (V_b; 0.4 V was used, unless otherwise noted). First, the case of Ag/AgCl, which is a typical compound used in nanopore measurements,[135,136] was used to verify the single particle sensing. It provided a persistent current flow with slow ups and downs (Figure 6.2a) associated with concentration fluctuations of reactants and products via their adsorption and precipitation at the surface under the electrochemical reactions in chloride solutions. In the meantime, resistive pulses were observed as the polymer nanoparticles passed through the pore by electrophoresis. These signals showed little variations in their heights (Figure 6.2b) representative of the narrow size distributions of the synthetic nanobeads (varying by less than 11% from the average particle diameter of 178 nm as confirmed by a dynamic light scattering method (Malvern)). There are also no notable changes in the pulse-like waveforms with time for the entire range of the salt concentration conditions tested, which suggested a minor influence of the ion diffusion at the solution-electrode interfaces on the resistive pulse sensing.

To verify the accuracy of the single-particle measurements, the ionic blockade current was theoretically estimated by the polymeric sphere.[137,138] Finite element calculations based on coupled Poisson-Nernst Planck and Navier Stokes equations (also see Chapter 2) predicted a drop in I_{ion} (ΔI_{ion}) by approximately 15 nA when a 170-nm-sized particle was moved along the pore axis under the salt concentration of 123 mM NaCl (Figure 6.2c). The experimental ΔI_{ion}

- t traces revealed similar features except the asymmetric signal line-shapes demonstrating the relatively slow motions at the nanopore orifice due to the hydrodynamic dragging under the electroosmotic flow (water flows in a direction opposite to the electrophoresis of the negatively charged particles in the SiN_x nanopore for its negative native charge on the wall surface).[27,139]

Moreover, the simulations indicated a linear rise in the resistive pulse height I_p with the open pore current I_{open} (Figure 6.2d), which is in fair agreement with the experimental observations (Figure 6.2e). It can be interpreted by the fact that the electrolyte concentrations affect the homogeneous resistivity of the solution ($1/\rho$) including the open volume in the partially occluded nanopore by the particle. This in turn provides a transmission line circuit model of the fluidic system as a simple resistor of the resistance $R_{pore} = \rho\,(4L / \pi\, d_{pore}^2 + 1 / d_{pore})$ at the nanopore with negligible contributions of the electrodes (apart from the slight change in I_p in response to the time-course decrease in I_{open} by less than 10% ascribable to the small yet finite effects of the resistance at the electrolyte solution-Ag/AgCl interfaces (Figure 6.3).

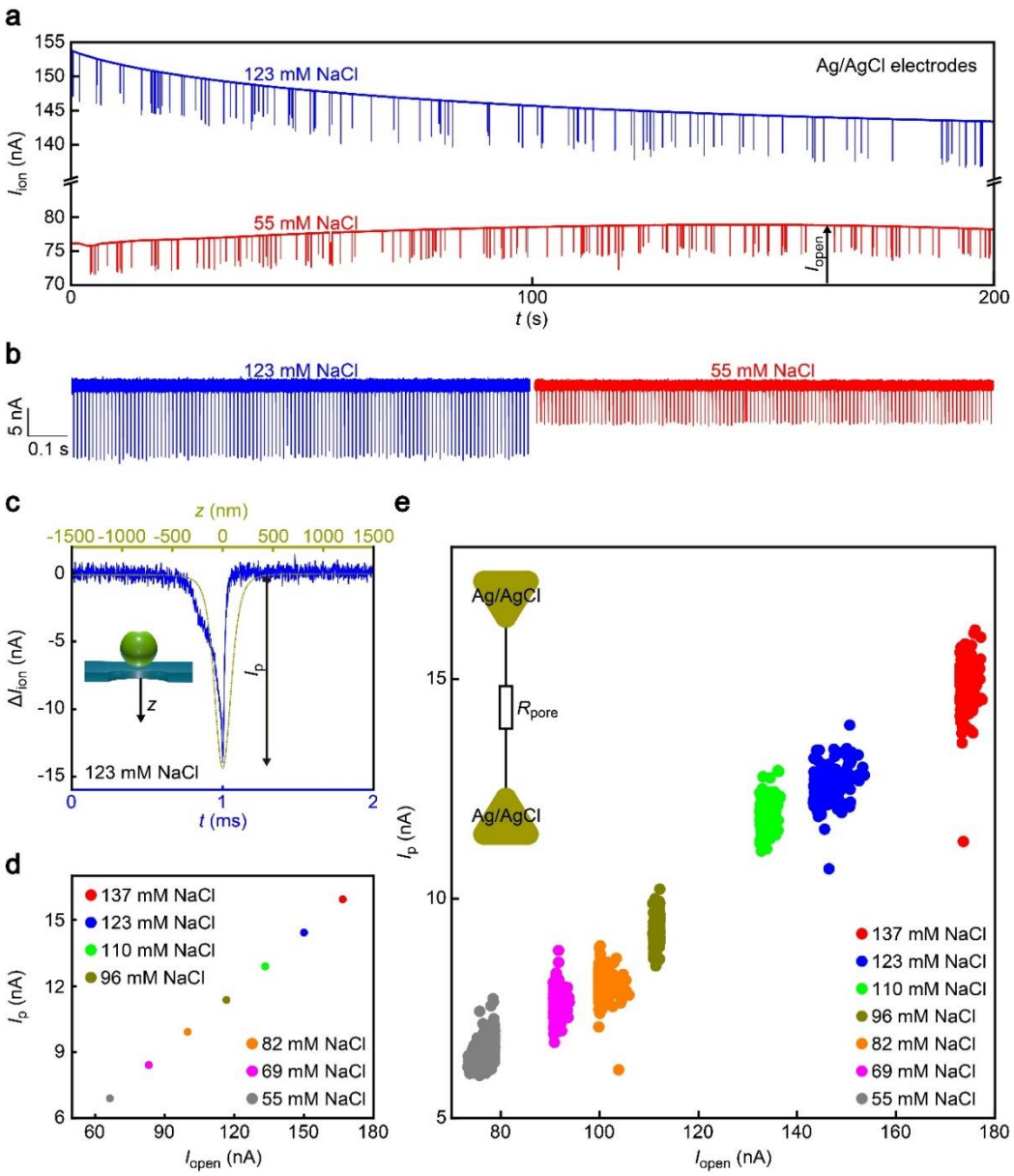

Figure 6.2 Open pore and blockade current characteristics observed with Ag/AgCl electrodes

(a) Partial ionic current traces recorded in a dilute suspension of 186 nm-sized polymeric nanobeads in phosphate-buffered saline containing 123 mM (blue) and 55 mM (red) NaCl using a 300 nm-sized SiN_x nanopore with Ag/AgCl electrodes under the transmembrane voltage V_b of 0.4 V. (b) Resistive pulses of equal heights detected in the 123 mM (blue) and 55 mM (red) NaCl solutions. The open pore current is offset to zero. (c) A magnified view of

a resistive pulse in 123 mM NaCl (blue) compared with a simulated ionic signal for a 170 nm particle passing through a 300 nm diameter channel (dark yellow). The open pore current is offset to zero. *z* denotes the position of the particle center. (d) The resistive pulse height Ip versus the open pore current I_{open} obtained by the finite element simulations of the particle translocation in aqueous solutions of various NaCl concentrations. (e) Experimental Ip under various salt concentration conditions plotted as a function of the open pore current I_{open} at the moment when the resistive pulses were detected. Inset is an equivalent circuit model of the nanopore. There is no additional impedance at the solution/electrode interfaces due to the electrochemical nature of Ag/AgCl in the chloride solution. Reproduced and adapted with permission under a CC BY-NC-ND 4.0 License from ref.[134]. Copyright 2022 Elsevier.

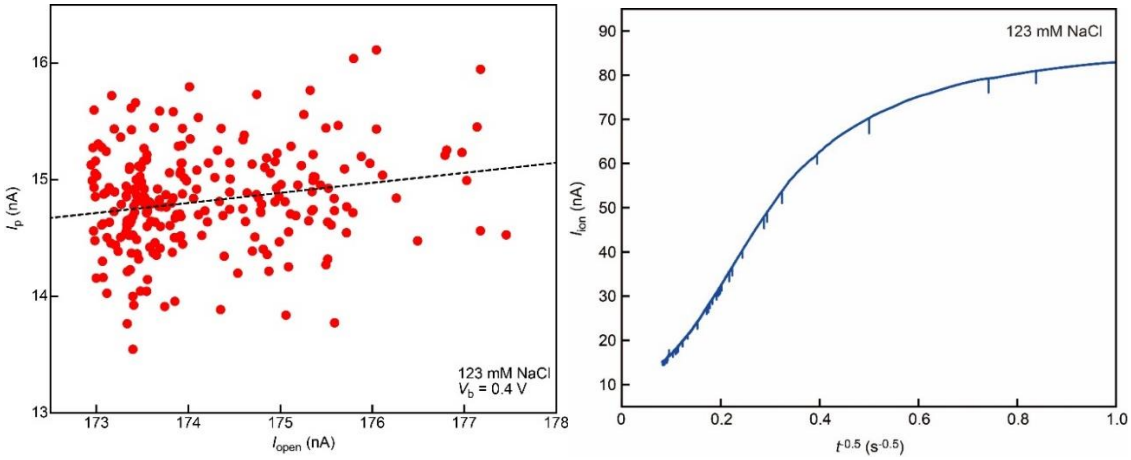

Figure 6.3 The relationship between I_p and I_{open} and the expanded view of the ionic current trace

The resistive pulse height I_p plotted as a function of the open pore current I_{open} for the measurement of the 178 nm-sized polymeric beads in 123 mM NaCl solution under the applied transmembrane voltage V_b of 0.4 V using Ag/AgCl electrodes. The dashed line is a linear fit to the plots that show a weak dependence of I_p on I_{open} due to the small yet finite impedance at the interface between the Ag/AgCl and the electrolyte buffer. In the right figure, note that the ionic current initially decreases more slowly than that predicted by the Cottrell equation. This is attributed to the fact that the interfacial resistance is negligibly small compared to the nanopore resistance at the moment when the voltage was applied to the electrodes. As it grows over time, meanwhile, the ionic current decreases more rapidly. Eventually, the $t^{-0.5}$ dependence was observed when the interfacial resistance became much larger than the nanopore resistance at $t^{0.5} < 0.2$. Reproduced and adapted with permission under a CC BY-NC-ND 4.0 License from ref.[134]. Copyright 2022 Elsevier.

6.3. Cottrell diffusion observed in Pt electrodes

Next, it was found that quite different ionic current characteristics showed a large decrease in I_{open} over time by measuring the polymeric beads using the same nanopore but with platinum electrodes instead of Ag/AgCl. (Figure 6.4a). While the nanoparticles still could be detected, the resistive pulses became steadily weaker along the diminishing open pore current (Figure 6.4b-e). Here, what is different in platinum from Ag/AgCl is the electrochemical reactions in the chloride solution involving no precipitation/adsorption of the reactants. In such a case, the Faraday current is expected to diminish monotonically rather than stay stable at a certain level, as the non-equilibrium ion concentration gradients at the voltage-biased electrode surface tend to be flattened by time via the diffusive motions of ions in the bulk solution.[132] In the case of parallel plate electrodes without a nanopore membrane, Fick's law describes the time-dependent Faraday current to behave as: $I_{ion} = nFAD^{0.5}c/(\pi t)^{0.5}$, where F is the Faraday constant, A is the water-touching electrode area, D and c is the diffusion constant and the concentration of ions, and n is the number of electrons worked in the electrochemical reaction.[132] Indeed, the deep I_{open} drop was found to occur as $t^{-0.5}$ (Figure 6.4c) thereby manifesting that the transmembrane ionic current is limited by the ion diffusion at the electrodes. More quantitatively, tentatively assuming water dissociation reactions on Pt surfaces in the pH7.6 buffer,[140,141] D of 7.0×10^{-8} m²/s was obtained from the $t^{-0.5}$ fitting (solid line in Figure 6.4c) with the electrode area of 2.7×10^{-5} m². While this value is close to the diffusion constants of H^+ and OH^- at ambient conditions,[142,143] it should also be pointed out that V_b is lower than the voltage required for initiating Faraday electrolysis of water. Further efforts should thus be devoted to shedding light on the electrochemical reactions responsible for I_{ion} in the Pt/nanopore/Pt system.

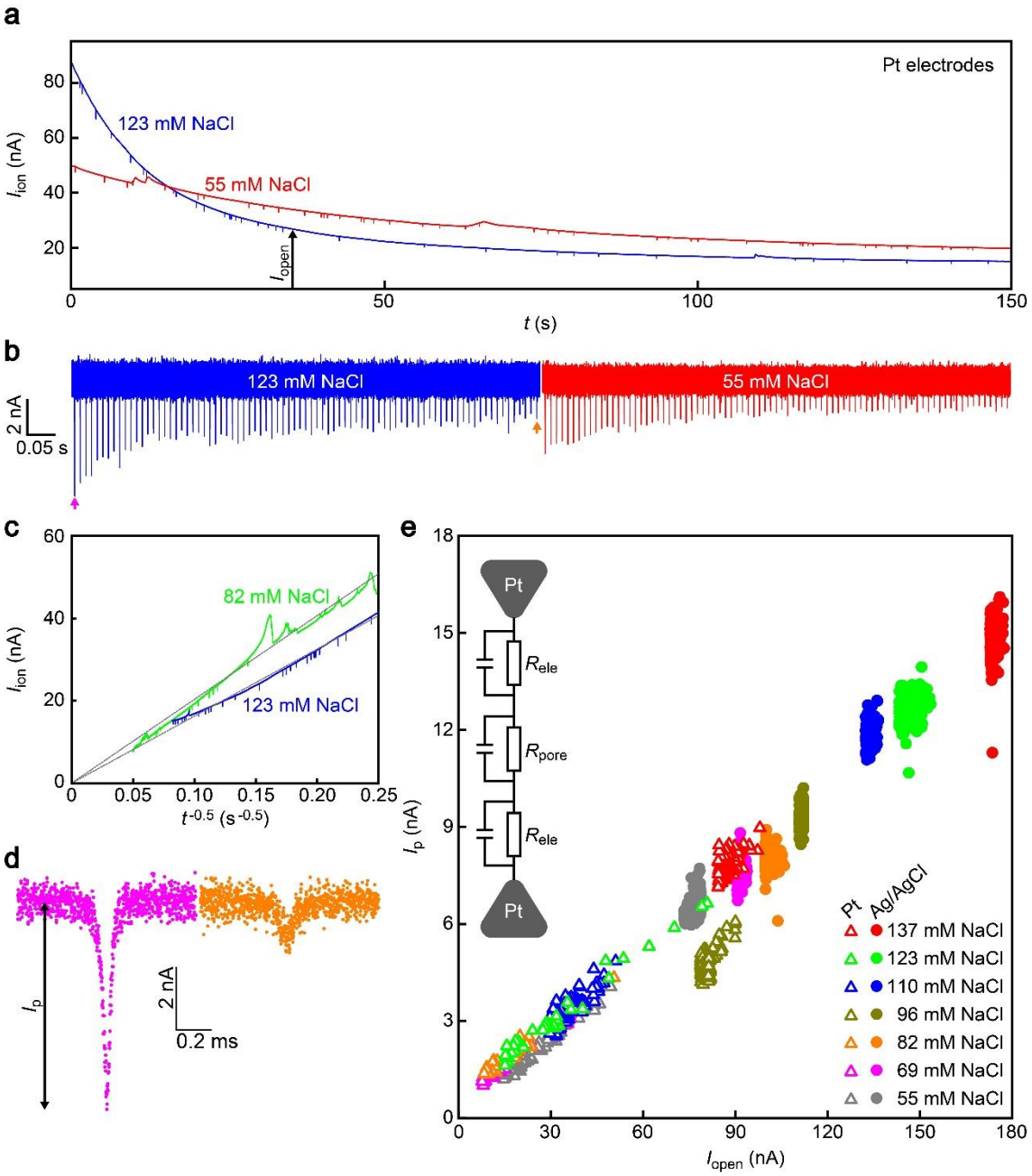

Figure 6.4 Time-varying Faraday current and resistive pulses in a Pt-nanopore-Pt setup

(a) Partial Iion traces in 123 (blue) and 55 mM (red) NaCl solutions were recorded using a 300 nm-sized nanopore with Pt electrodes under V_b of 0.4 V. Large spike-like features are presumably due to charging/discharging. (b) Resistive pulses of varying heights were

observed in 123 (blue) and 55 mM (red) NaCl. (c) The ionic current curves are displayed as a function of $t^{0.5}$. Gray lines are linear fitting to the data. (d) Resistive pulses were observed at the beginning (pink arrow in (b)) and the end (orange arrow in (b)) of one measurement. (e) The measured Ip with Pt (open triangles) and Ag/AgCl (filled circles) plotted with respect to I_{open} at the moment when the resistive pulses appeared. Inset is a circuit model of the Pt-nanopore-Pt system with impedance at the solution/ electrode interfaces serially connected to the resistance at the pore. Reproduced and adapted with permission under a CC BY-NC-ND 4.0 License from ref.[134]. Copyright 2022 Elsevier.

6.4. Electrode material and electrolyte dependence of Cottrell behaviors

Extending the experiments to different electrode materials (Figure 6.5a), stable ionic current, as well as uniform height resistive pulses of the polystyrene nanoparticles with Ti, was obtained (Figure 6.5b). This demonstrates that Ti is equally useful to Ag/AgCl for nanopore sensing owing presumably to its dissolution reactions under the electric potential difference.[144] In the case of Ag, the open pore current as well as the resistive pulse heights tended to become lower over time. It is naturally ascribed to the absence of AgCl for the precipitation/adsorption-mediated electrochemical reactions that led the Cottrell diffusion to become observable in the ionic current traces. Au also displayed similar behavior due to its electrochemically inert properties.

Moreover, salts other than NaCl were tested. In the case of a mixture of an aqueous solution of $K_3Fe(CN)_6$ and $K_4Fe(CN)_6$ (Figure 6.5c), the redox reactions involving precipitations,[145] similar to those occurring at the Ag/AgCl electrodes in chloride solutions, provided stable ionic current even with Pt electrodes though not applicable for the resistive pulse detections (Figure 6.5d) perhaps due to the aggregation of the polystyrene nanobeads via the electrostatic interactions with the multivalent ions in the solution. On the other hand, a Cottrell behavior was observed when replacing the solution with the one containing only $K_3Fe(CN)_6$ since the redox reactions cannot take place without $K_4Fe(CN)_6$. These results were consistent to validate the pronounced roles of the electrochemical ion diffusion on nanopore sensing.

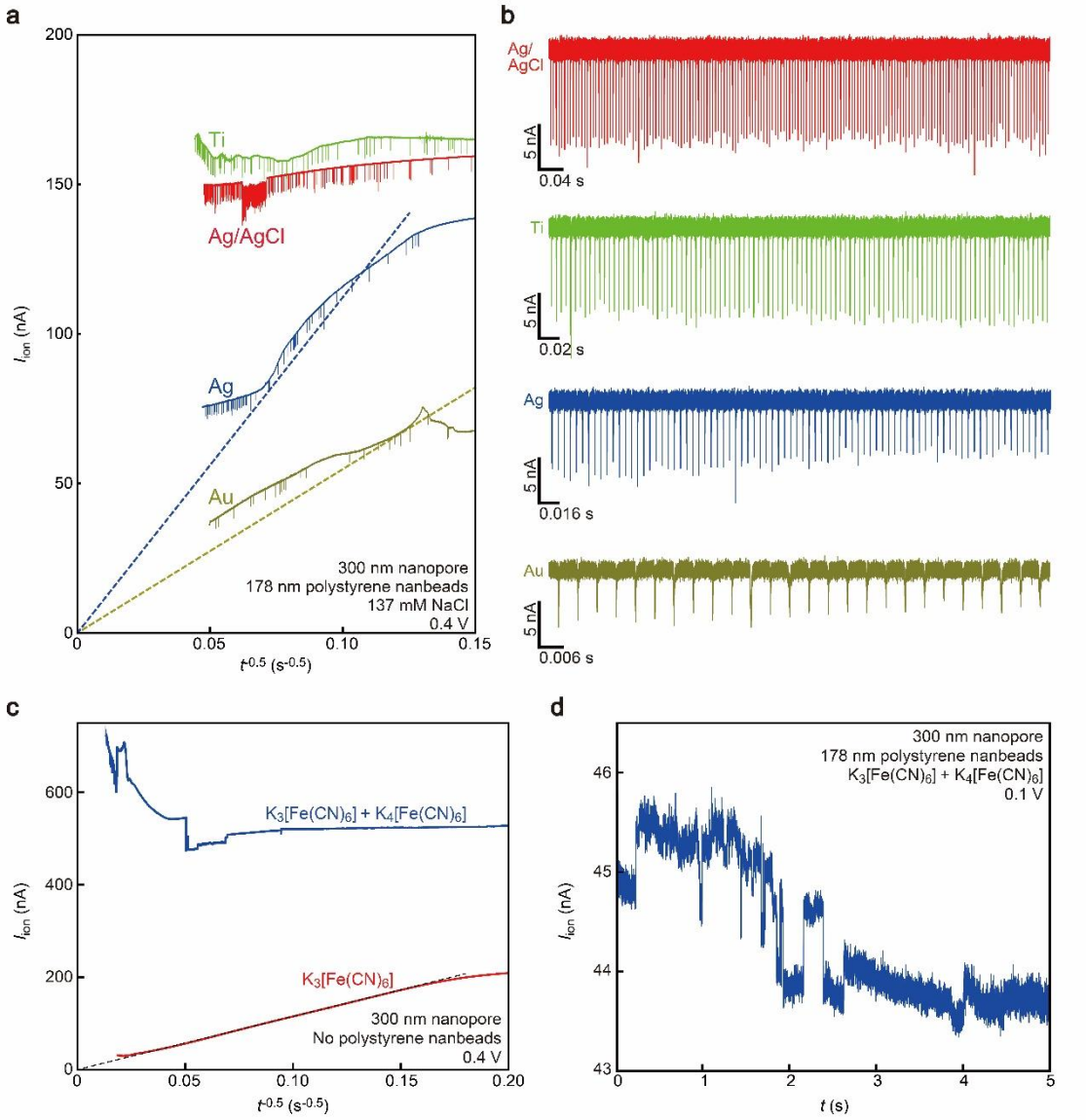

Figure 6.5 Electrode material and electrolyte dependence of the ionic current characteristics

(a) I_{ion} traces were recorded using a 300 nm nanopore under 0.4 V with different metal electrodes: Ag/AgCl (red), Ti (greed), Ag (blue), and Au (dark yellow. Dashed lines are fitting with I_{ion}-$t^{0.5}$. (b) Resistive pulses were obtained for the 178 nm nanobeads within 15 min with various electrodes. (c) Ionic current traces were recorded in aqueous solutions of ferrocyanide using a 300 nm-sized nanopore with platinum electrodes under the

transmembrane voltage of 0.4 V. Blue curve is the result in the water solution containing potassium hexacyanoferrate(III) ($K_3[Fe(CN)_6]$) and potassium hexacyanoferrate(II) trihydrate ($K_4[Fe(CN)_6]$) at 0.1 V while red curve is the result in the solution containing only $K_3[Fe(CN)_6]$ at 0.1 M. The ionic current is plotted against t 0.5. A stable ionic current was observed with $Fe(CN)_6^{4-}/Fe(CN)_6^{3-}$ due to the redox reaction at the platinum electrodes. In contrast, the absence of reactants with only $K_3[Fe(CN)_6]$ led to diffusion-limited ionic current manifested by the decay in I_{ion} by $t^{0.5}$ (dashed line is a fit with I_{ion}-$t^{0.5}$). (d) Resistive pulse measurements of the 178 nm-sized polystyrene beads in the solution of 0.1 M $Fe(CN)_6^{4-}/Fe(CN)_6^{3-}$. No notable features suggestive of particle translocation were observed due presumably to aggregation of the polymeric beads. Reproduced and adapted with permission under a CC BY-NC-ND 4.0 License from ref.[134]. Copyright 2022 Elsevier.

How about its impact on nanopore sensing? The resistive pulses were already explained to become smaller over time (Figure 6.4d). To be more quantitative, the signal heights were plotted with respect to the I_{open}. They revealed a proportionality between I_p and I_{open} even for the data in a single measurement under a specific salt concentration condition (Figure 6.4e), which implies a direct relevance of the impedance at the solution/platinum interfaces on the ionic blockade current. Interestingly, the Ag/AgCl results were also in line with the linear dependence. Nevertheless, it should be noted that the underlying mechanisms are completely different. In the Ag/AgCl measurements, the resistivity of the whole nanopore system was changed by the salt concentration conditions that affected I_p and I_{open} on the same footing.[126] On the other hand, the ion diffusion at the voltage-biased platinum yielded local impedance at the liquid-electrode interfaces. In this sense, I_p is expected to scale with I_{open}^2 when assuming a serially connected resistor of resistance R_{ele} at the two electrodes. It thus requires further analyses to explain the linear dependence observed in Figure 6.4e.

In fact, significant blunting of the resistive pulse waveforms was found via interplay between the resistance and capacitance.[146] Its effect was examined by fitting the tails with the following: $\Delta I_{ion} \sim \exp(-t/\tau_1)$, where τ_1 = RC is the time constant of a parallel RC circuit model assumed (Figure 6.6a and 6.6b). This expression is valid unless the translocation motions of the nanoparticles exiting the nanopore are much faster than the RC-mediated temporal resolution of the ionic current measurements. The signal pattern analysis revealed a linear relationship between τ1 and the resistance of the nanopore system, $R_{total} = V_b/I_{open}$ (Figure 6.6c; see also Figure 6.8), in the whole resistive pulse data including those recorded with not only Ag/AgCl but also Pt electrodes. The relationship as a whole implied the direct relevance of the time-varying R_{ele} to the temporal resolution of nanopore sensors (note that τ_1 scales

linearly with R even within the data acquired under a certain salt concentration condition). In this context, it is noticeable that similar trends were reported when varying solution resistance at external regions of nanopores by integrating microchannels on membranes.[147] The τ_1 - R dependence thus indicates the major contribution of R_{ele} to alter the out-of-pore resistance contributing to the signal retardation. It is speculated that this gave rise to the linear I_p - I_{open} dependence in Figure 6.7b.

In contrast, the curvatures at the left-half of the resistive pulses, which reflects the motions of the nanoparticles at the nanopore entrance, demonstrated a non-trivial manner. While the RC retardation is expected to be equally effective to blunt the signals at the onsets and the tails, the time constant τ_2 (assessed by the exponential fits as shown in Figure 6.7a and 6.7b) revealed only faint dependence on R (Figure 6.7c). This is in part due to the considerable scattering in the pulse onset line shapes reflecting the stochastic nature of the nanoparticles drawn into the nanopore at random angles (which is not the case after escaping the pore where the inertial effects tend to regulate their translocation motions).[138] Another thing is the slow electrophoretic motions of the polymeric beads at the orifice (note that τ_2 is relatively longer than τ_1) allowing the ionic current to catch up with the change in their positions, hence obscuring the trait of the RC retardation.

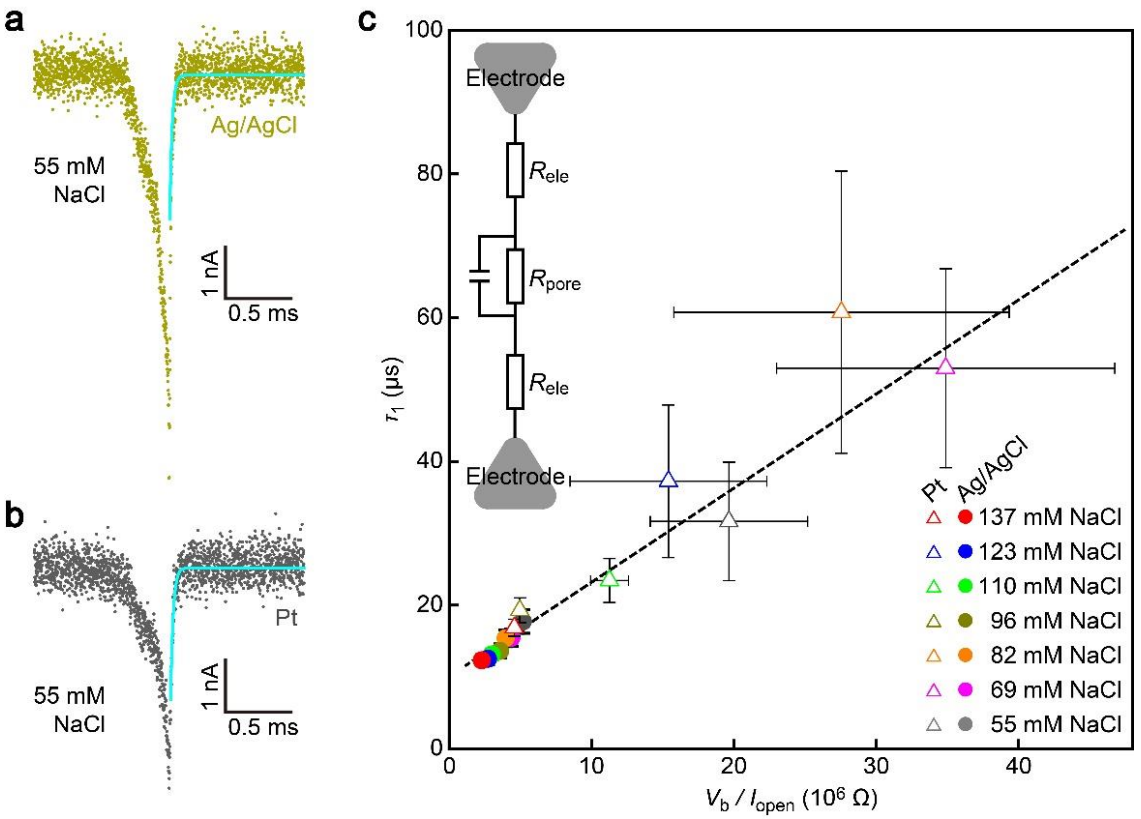

Figure 6.6 Impedance-limited temporal resolution of the nanopore sensing (leaving)

(a,b) Typical resistive pulses recorded for the 186 nm-sized nanobeads in 55 mM NaCl solutions with Ag/AgCl (a) and Pt (b) electrodes under V_b of 0.4 V. Sky blue curves are the exponential fits by $I_{ion} \sim \exp(-t/\tau_1)$ at the signal tails. (c) τ_1 versus V_b / I_{open} scatter plots. Open triangles and filled circles are the data obtained with Pt and Ag/AgCl electrodes, respectively. Error bars denote the standard deviations. The dashed line is a linear fit to the whole plot. Inset is a refined equivalent circuit explaining the overall dependence of t_1 on the nanopore resistance.

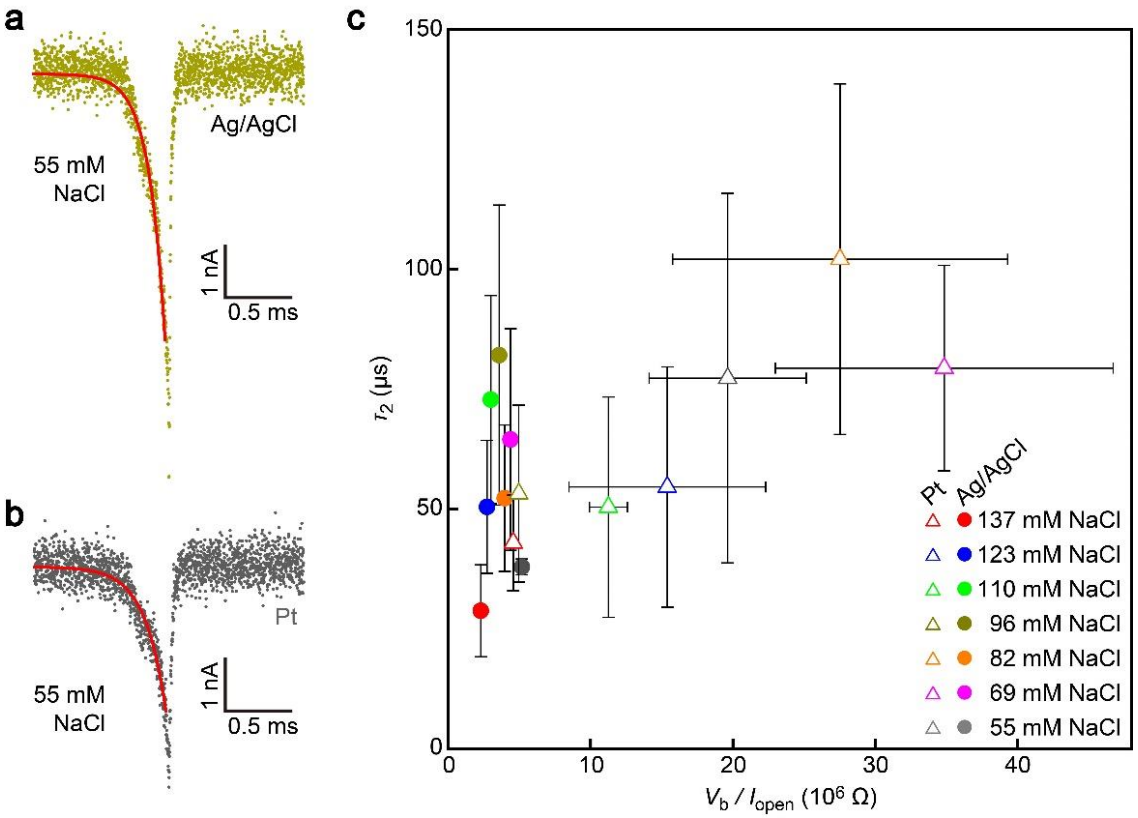

Figure 6.7 Impedance-limited temporal resolution of the nanopore sensing (entering)

Resistive pulse onset line-shapes (a, b) Resistive pulses recorded using Ag/AgCl (a) and Pt (b) with fit curves in red by $I_{ion} \sim \exp(-t/\tau_2)$. (c) τ_2 versus V_b / I_{open} scatter plots shown by open triangles and filled circles for the data obtained with Pt and Ag/AgCl electrodes, respectively. Error bars denote the standard deviations. Reproduced and adapted with permission under a CC BY-NC-ND 4.0 License from ref.[134]. Copyright 2022 Elsevier.

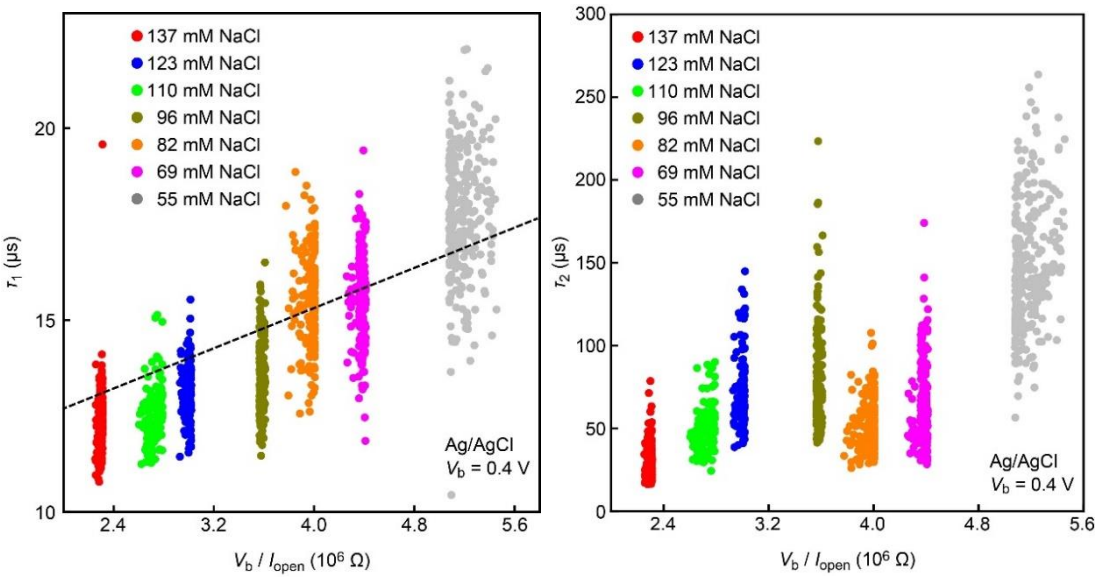

Figure 6.8 The time constant τ1 and τ2 for the measurements

The time constant τ_1 (left) and τ_2 (right) for the measurements of the 178 nm-sized polymeric particles using a 300 nm diameter SiN_x nanopore with Ag/AgCl electrodes, which was calculated by fitting the resistive pulse tails with $\Delta I_{ion} \sim \exp(-t/\tau)$. The dashed line in the left figure is a linear fit to the results including those obtained with Pt electrodes. The plots reveal longer τ_2 under lower ion concentration conditions, which suggests a more significant influence of the electroosmotic flow to slow down the nanoparticle motions in the buffers of lower ionic strengths. Reproduced and adapted with permission under a CC BY-NC-ND 4.0 License from ref.[134]. Copyright 2022 Elsevier.

6.5. Influence of electrode ion diffusion on particle translocation dynamics

It is also noticeable that τ_2 is electrode-material dependent. In the case of Ag/AgCl, it could find a tendency that τ_2 to become longer with R_{total} when decreasing the salt concentrations (Figure 6.8). Considering that the resistive pulse onsets mostly represent the translocation dynamics at the orifice rather than the RC effects, it can be explained by the slower motions of the polymeric particles under the more effective electroosmotic flow in the diluter electrolyte solution imposing stronger hydrodynamic drag forces to push them back (Figure 6.9).[11,27,148] This is different for the results obtained with Pt electrodes, where τ2, or equivalently the time t_{cap} for the nanobeads to be drawn into the nanopore (Figure 6.10A), scatters more and tends to become gradually shorter by time within the data collected under a constant salt concentration condition.

Since it is hard to imagine a gradual decrease in the mobility of the polymer spheres or ionic strength of the electrolyte buffer during the resistive pulse measurements, physical mechanisms other than the RC coupling should be responsible for the τ_2 (t_{cap}) characteristics. What largely determines the particle motions at the orifice is the balance between the counteracting electrophoretic and hydrodynamic drag forces.[11,27,148,149] As these forces both become stronger with the transmembrane voltage, it gives non-straightforward V_b dependence of the translocation dynamics.[150] For the present system, increasing voltage led to a monotonic elongation of t_{cap} manifesting a more rapid increase in the hydrodynamic drag force compared to the electrophoretic counterpart (Figure 6.10b; see also Figure 6.11 that explains why t_{cap} increases rapidly at above 0.4 V),[11] i.e. faster translocation under lower V_b (here, Ag/AgCl was used to avoid the influence of the ion diffusion at the solution/electrode

interfaces). Analogous discussion can be made to explain the plots in Figure 6.7c and 6.10a. At the beginning of the measurement with Pt electrodes, the impedance at the solution/electrode interfaces was low so a large portion of V_b was focused at the nanopore. Later, however, the Cottrell diffusion steadily enlarged the interfacial resistance R_{ele} at the electrodes. When it became comparable to R_{pore}, the voltage started to drop largely at the electrodes. As a consequence, the electric potential difference V_{eff} across the nanopore became weaker over time (Figure 6.10c). Concurrently, it led to shorter t_{cap} by the altered balance between the electrophoretic and hydrodynamic drag forces. In contrast to Pt, the low electrode impedance at the solution-Ag/AgCl interfaces led to $V_{eff} - V_b$, and hence relatively long τ_2 due to the electroosmotic flow-derived slow motions of the nanoparticles at the nanopore entrance (with the aforementioned influence of the ionic strength as shown in Figure 6.8). Although it is not possible to quantify the effect of the interfacial impedance on the translocation dynamics of the nanoparticles due to the uncertainty in the time-evolved resistance distributions between the electrodes and the membrane, the above results elucidate another outcome of the electrode ion diffusion to vary the translocation motions of analytes.

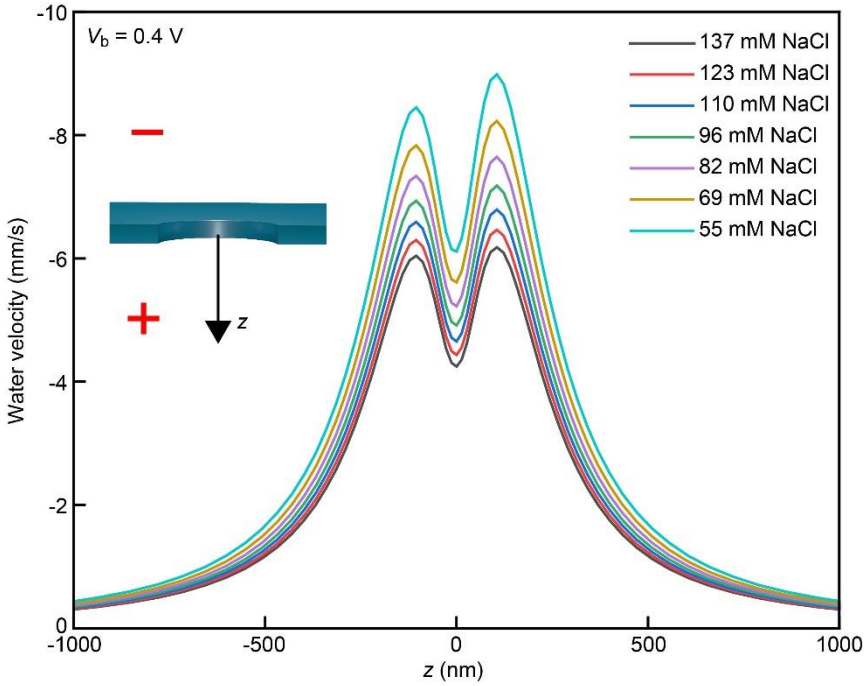

Figure 6.9 Electroosmotic flow velocity estimated by finite element calculations

The electric potential was +0.4 V at the bottom side of the nanopore membrane. The negative velocity denotes water flow in a direction from positive-to-negative electric potentials, which is opposite to that of the electrophoresis of negatively charged objects. The inset image shows the direction of *z*. Reproduced and adapted with permission under a CC BY-NC-ND 4.0 License from ref.[134]. Copyright 2022 Elsevier.

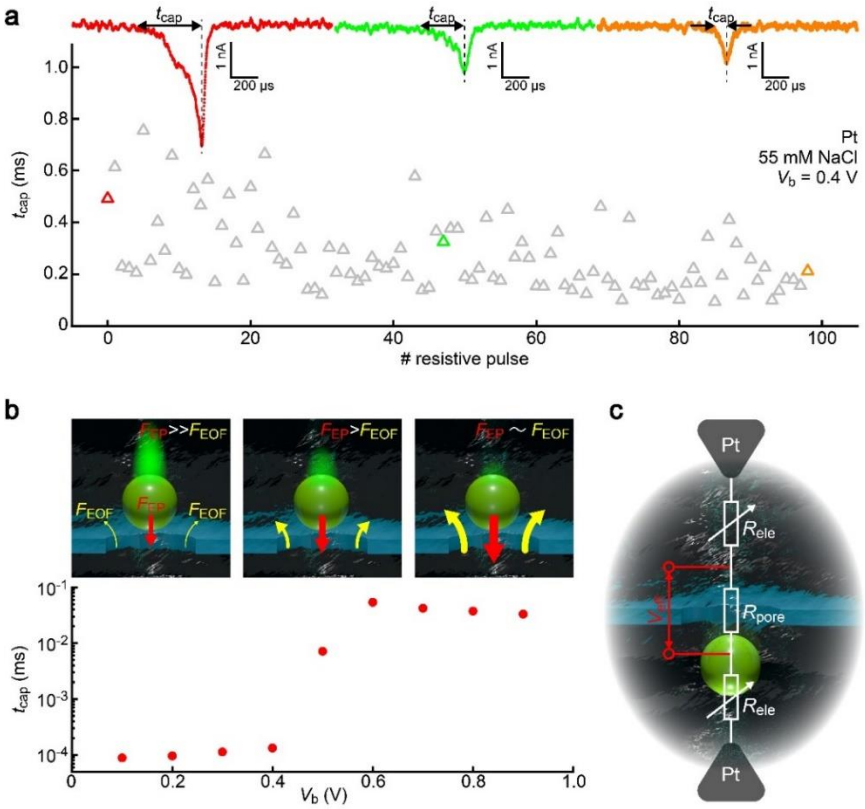

Figure 6.10 Transmembrane voltage-dependent particle capture dynamics

(a) The width t_{cap} at the first half of the resistive pulses obtained with the Pt-nanopore-Pt setup represents the time required for the particles to be electrophoretically drawn into the nanopore. The resistive pulses correspond to the data displayed as red, green, and orange triangles. (b) Change in t_{cap} with V_b observed in the resistive pulse measurements using Ag/AgCl electrodes in 55 mM NaCl solution. t_{cap} increases steadily when increasing V_b from 0.1 to 0.6 V signifying a more rapid increase in the electroosmotic forces F_{EOF} than the electrophoretic counterpart (F_{EP}). The sketches depict the relative strength of the electrophoretic and hydrodynamic drag forces on the particles at the nanopore orifice under different transmembrane voltages. (c) A circuit model explaining the time-varying electric potential difference at the nanopore V_{eff} due to the growing impedance at the solution/Pt interfaces. Reproduced and adapted with permission under a CC BY-NC-ND 4.0 License from ref.[134]. Copyright 2022 Elsevier.

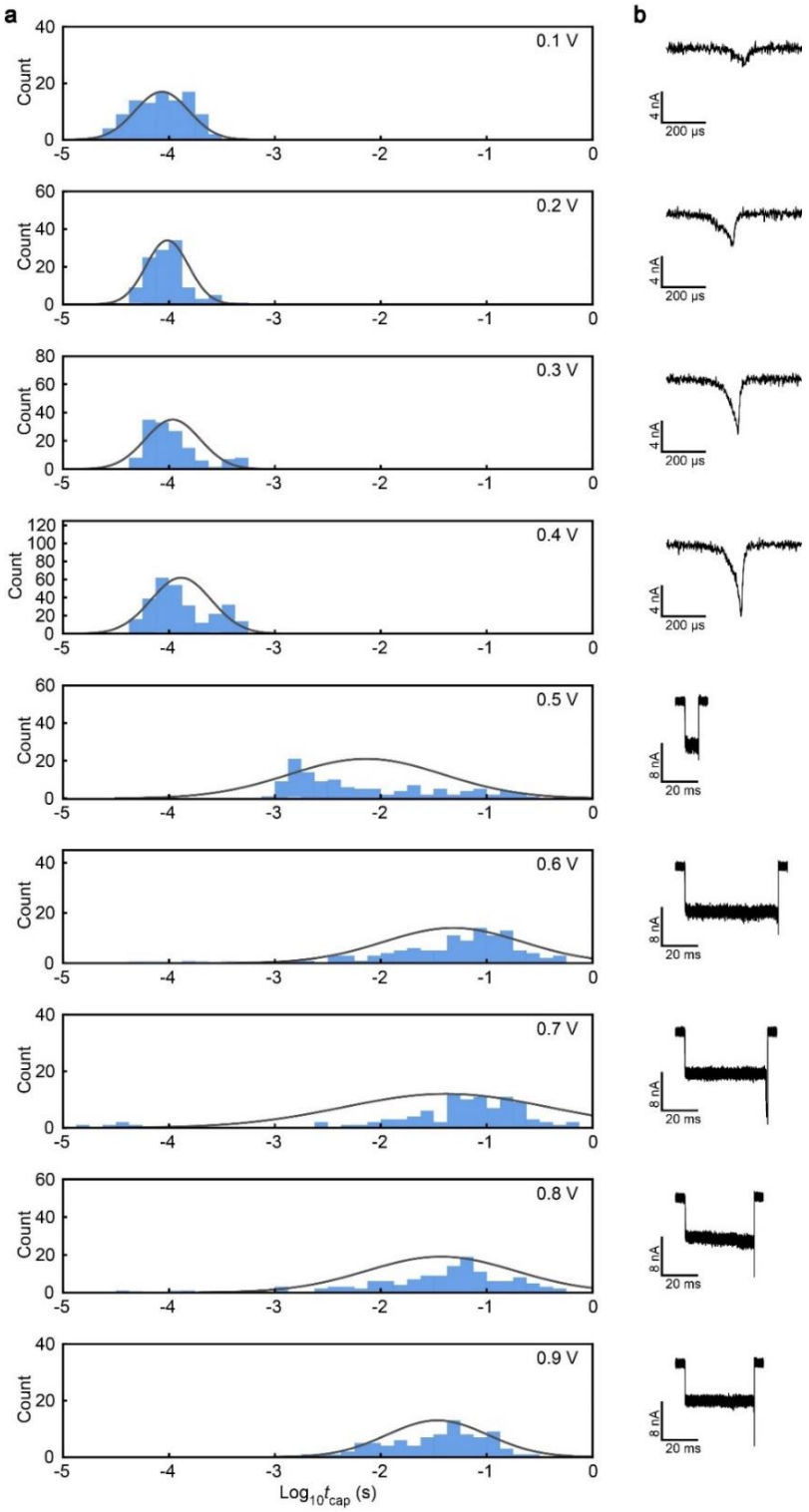

Figure 6.11 Variations of the capture time t_{cap}

Variations of the capture time t_{cap} obtained from the resistive pulses for the 178 nm-sized nanoparticles passed through a 300 nm-diameter nanopore under the various

transmembrane voltage from 0.1 (top) to 0.9 V (bottom). Grey curves are Gaussian fits the distributions. Typical resistive pulse signals are shown on the right side. Note the different scales for the data at voltages higher than 0.4 V. The high-voltage signals above 0.6 V demonstrate the anomalously long translocation time of the nanobeads attributed to the trapping by the balanced electrophoretic and hydrodynamic drag forces in the nanopore. The trap durations were long enough for another particle to be drawn into the pore that pushed the trapped one. As such, t_{cap} at the high voltage showed only weak dependence on V_b. Reproduced and adapted with permission under a CC BY-NC-ND 4.0 License from ref.[134]. Copyright 2022 Elsevier.

It should be noted that the present work studied the roles of electrode materials for only 300 nm diameter nanopores. Considering that smaller nanopores possess larger R_{pore}, the roles of the Cottrell diffusion may change as the voltage division at R_{ele} would become smaller. On contrary, the choice of electrode materials is predicted to become more important when using micropores where smaller pore resistance gives rise to a more pronounced influence of R_{ele} on the ionic current characteristics. Further efforts should be devoted to clarifying this point.

However, the present findings in this chapter prove the important roles of electrode materials in nanopore sensing. Ag/AgCl is confirmed to be particularly useful to obtain persistent ionic current in a chloride solution for reliable resistive pulse detections of particles and molecules. Unlike the non-polarizable electrodes, electrochemical reactions at the platinum surfaces involve no precipitation/adsorption of reactants, and so induce growing interfacial impedance. This Cottrell diffusion-derived resistance was demonstrated to substantially degrade the temporal resolution of the ionic current measurements as well as to change the translocation dynamics of analytes in a time-varying manner, which would be fatal to discriminate analytes such as viruses[151] and proteins[152,153] by the difference in the ionic signal waveforms. Yet, electrochemistry predicts a way to make such electrodes still useful by employing a large electrode surface area with high ionic strength for mitigating the impedance increase to allow resistive pulse sensing for a certain period of time before it becomes comparable to the resistance at a nanopore. Conversely, it also cautions that care should be taken when utilizing microfabricated electrodes that may augment the electrode ion diffusion interference even with Ag/AgCl.[154]

Chapter 7 Polymer coating for solid-state nanopore sensors

7.1. Introduction

Solid-state nanopores have been used as a useful sensor platform for detecting individual nanoscopic objects[42,155–158] and studying their fast translocation in a confined nanofluidic system.[159–163] This monitors ion transport through a nanoscale conduit sculpted in a thin membrane using a pair of electrodes in an electrolyte buffer. When a particle passes through the nanochannel, the ion flow is obstructed which is seen as a temporal drop of the ionic current. The thus obtained resistive current pulses were found to contain rich information concerning the size,[164,165] shape,[166,167] surface charges,[168,169] and even surface chemical and biological components of analytes when the pore is surface-functionalized to add bio- and chemo-selectivity,[170–175] that enables the identification of miscellaneous bio-samples from cells to nucleotides by resistive pulse waveforms.

In this nanosensor, temporal resolution is a fundamental yet crucial factor for implementing the single-particle analysis wherein the ionic current needs to respond rapidly enough to the actual ion blockade events so as to reflect the physical properties of analytes in the associated resistive pulses.[133] Otherwise, fine features would be smeared leading to critical difficulty in identifying objects or on the worse side, weakening the signals down to undetectable levels. This would be in fact a vital issue, particularly in small nanopores for detecting nanometer-sized molecules such as proteins and nucleotides because, despite the expected short translocation time, it calls for infinitesimal channels in an ultrathin membrane to render

enough spatial resolution that inevitably brings huge capacitance and resistance, and hence a long charging time.[176]

The polymer coating has been recently reported as a promising strategy for improving temporal resolution.[146,177,178] By covering the nanopore substrate with a thick organic dielectric layer, the ionic current tended to respond faster presumably because of the decrease in the net cross-membrane capacitance. However, it still requires further studies to elucidate how a polymer layer contributes to the current response speed. In the present work in this chapter, therefore, systematic experiments were performed to explore the roles of the polymeric cover to clarify where and what materials should be added to engineer the impedance sensor performance.

7.2. Fabrication of polyimide layer on solid-state nanopores

The membrane-side of the SiNx surface was then covered with a 5 μm-thick photo-reactive polyimide by spin-coating. Using a photo-mask, we patterned and created a 50 μm diameter hole in the polyimide. Here, the position of the micropore was centered on the location of the SiNx nanopore. Also, the photolithography created the polymeric sheet to have a width and length of 5 mm and L_{layer} ranging from 1 to 16 mm, respectively. Finally, the polyimide was baked at 350 °C for hardening (Figure 7.1).

For the back-covered nanopore chip fabrications, we first prepared a nanopore chip by the aforementioned procedure based on electron-beam lithography and reactive ion etching. After that, we spin-coated PMMA (Aldrich) on the back side of the Si substrate, that is, the opposite side of the membrane surface. There, the deep Si trench was protected from being coated with PMMA by adhering to a small piece of plastic tape. The PMMA cover was then baked at 180 °C. Finally, the PMMA surface was coated with 20 nm-thick SiO2 by chemical vapor deposition for adhering the PDMS block upon the ionic current measurements. PBS was capillary-injected into the channel-integrated pore. Two Ag/AgCl rods were then placed at the bottom side of a micropore and the outer ends of the SU-8 microchannels via holes punched in a PDMS block (Figure 7.2). The cross-pore ionic current Iion was measured by applying the bias voltage V_b between the rods and recording the output current through pre-amplification using a home-built current amplifier backed by a fast digitizer (NI-5922, National Instruments). All the measurements were carried out at room temperature.

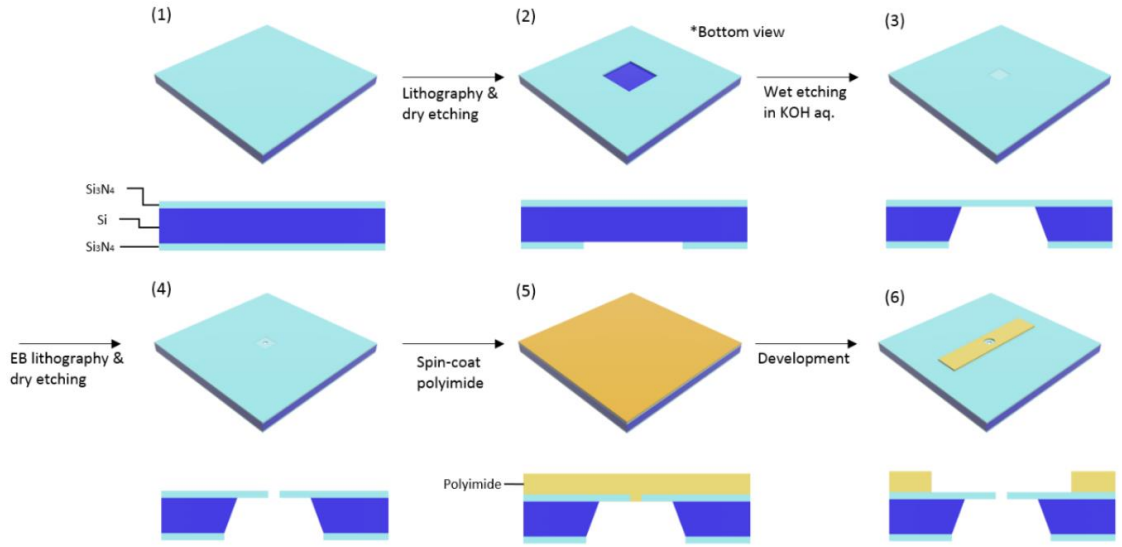

Figure 7.1 Fabrication procedure of polyimide-coated nanopores

A 25 mm^2 square piece of a Si wafer on both sides covered with 50 nm-thick SiNx (1) was exposed to reactive ion etching to partially remove the SiNx at the back side surface (2). The substrate was then immersed in KOH solution to wet-etch the Si layer to create a membrane of size 100 μm x 100 μm on the front-side (3). On the membrane, a nanopore of diameter 300 nm was formed by an electron beam lithography followed by reactive ion etching (4). Subsequently, 5 μm-thick photo-sensitive polyimides were spin-coated on the front surface (5). By irradiating UV light via a photo mask, a polyimide micropore around the SiN_x nanopore was formed (6). Reproduced and adapted with permission under a CC BY-NC-ND 4.0 License from ref.[179]. Copyright 2019 American Chemical Society.

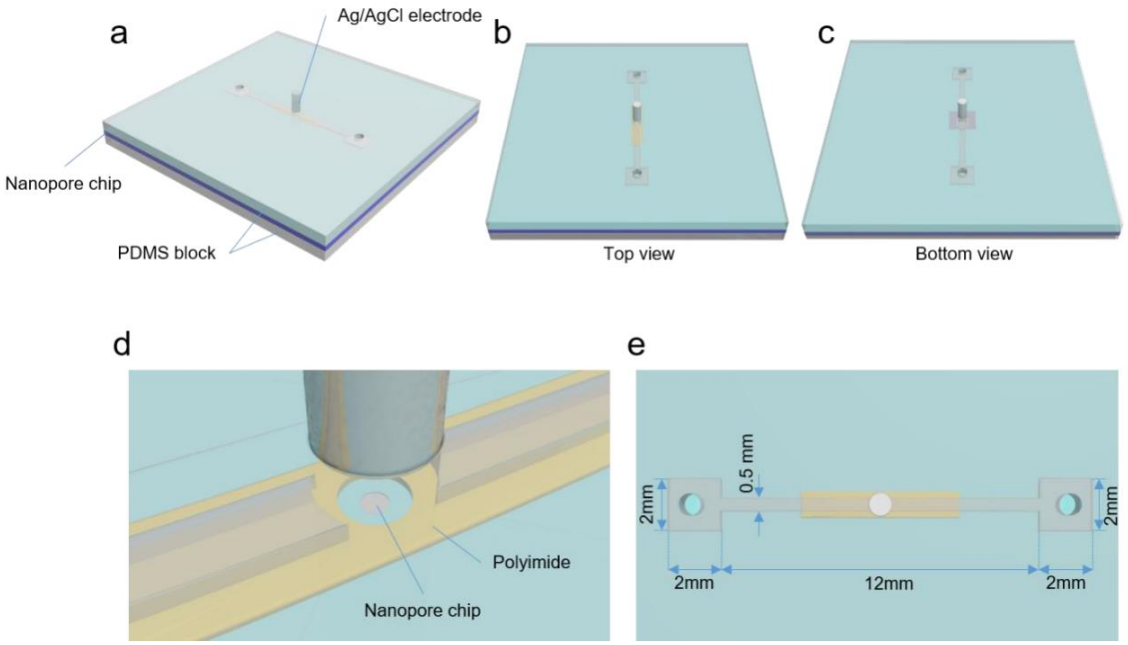

Figure 7.2 Schematic models of a PDMS block used to seal the nanopore chip from both sides

(a-c) Side-view (a), top-view (b), and bottom-view (c) of the chip configuration. Three holes are penetrated in the PDMS blocks. At the center hole, an Ag/AgCl rod was inserted to measure the ionic current. The other two holes were used as inlets and outlets of particle-containing PBS solution. (d) Close-up view of the polyimide-coated region. Polyimide was coated on the SiN_x front surface. The polymeric sheet had a rectangular shape of 4 mm wide and L_{layer} length. The size of the nanopore is not to scale for the sake of clarity. (e) The dimension of the fluidic channel on the PDMS block. The polyimide layer is also depicted. When flowing PBS solution through the channel, the SiN_x surface touches water except for the polyimide-covered area. Reproduced and adapted with permission under a CC BY-NC-ND 4.0 License from ref.[179]. Copyright 2019 American Chemical Society.

A nanopore configuration employed to evaluate the role of the polymer coating is shown in Figure 7.3. This is constructed with a 300 nm-sized nanopore in a 50 nm-thick SiN_x membrane partially covered with a 5 μm-thick polyimide layer (Figure 7.1a-c). On the membrane, phosphate-buffered saline (PBS) containing 200 nm-sized polystyrene beads at a concentration of 10^9 particles/mL was added through a fluidic channel in a polydimethylsiloxane (PDMS) block (Figure 7.2). Here, the area of water touching the SiNx surface was defined by the length L_{poly} of the polymeric sheet (Figure 7.3b). From equivalent circuit model points of view (Figure 7.3d), the cross-plane net capacitance C_{net} would be determined using the polyimide-coated SiN_x structure as it is orders of magnitude smaller than that of the other serial components such as the doped Si substrate and the electric double layer C_{EDL}.[176] C_{net} can then be approximated as $C_{net} = C_{poly} + C_{SiNx}$. Here, C_{poly} is described as $\varepsilon_{poly}\,\varepsilon_v\,w_{thin}\,L_{poly}/t_{poly}$ when $L_{poly} \le 12$ mm where $\varepsilon_v = 8.9 \times 10^{-12}$ F/m and $\varepsilon_{poly} = 3.4$ are the vacuum permittivity and the relative permittivity of the polyimide, respectively, $w_{thin} = 0.5$ mm is the PDMS channel width, and $t_{poly} = 5$ μm is the thickness of the polyimide sheet. Meanwhile, it becomes $(0.012\,\varepsilon_{poly}\,\varepsilon_v\,w_{thin} / t_{poly} + (L_{poly} - 0.012)\,\varepsilon_{poly}\,\varepsilon_v\,w_{sq} / t_{poly})$ in case when $L_{poly} = 16$ mm because of the contribution at the square regions of the width $w_{sq} = 2$ mm. Similarly, C_{SiNx} at the non-coated 50 nm-thick SiN_x domain is calculated as $\varepsilon_{SiNx}\,\varepsilon_v\,w_{thin}\,(0.012 - L_{poly}) / t_{SiNx}$ and $\varepsilon_{SiNx}\,\varepsilon_v\,w_{thin}\,(L_{poly} - 0.012) / t_{SiNx}$ when $L_{poly} \le 12$ mm and $L_{poly} > 12$ mm, respectively, with $\varepsilon_{SiNx} = 7.5$ of the SiN_x relative permittivity and $t_{SiNx} = 50$ nm of the thickness of the silicon nitride layer. Because $t_{poly} \gg t_{SiNx}$, C_{net} decreases steadily with L_{poly}. In this way, the net cross-membrane capacitance is expected to be controlled by the polyimide length. As for the pore resistance R_{pore}, on the other hand, the polyimide layer was designed to have a 50 μm-sized micropore around the nanopore so as to make its influence on R_{pore} to be negligible small.

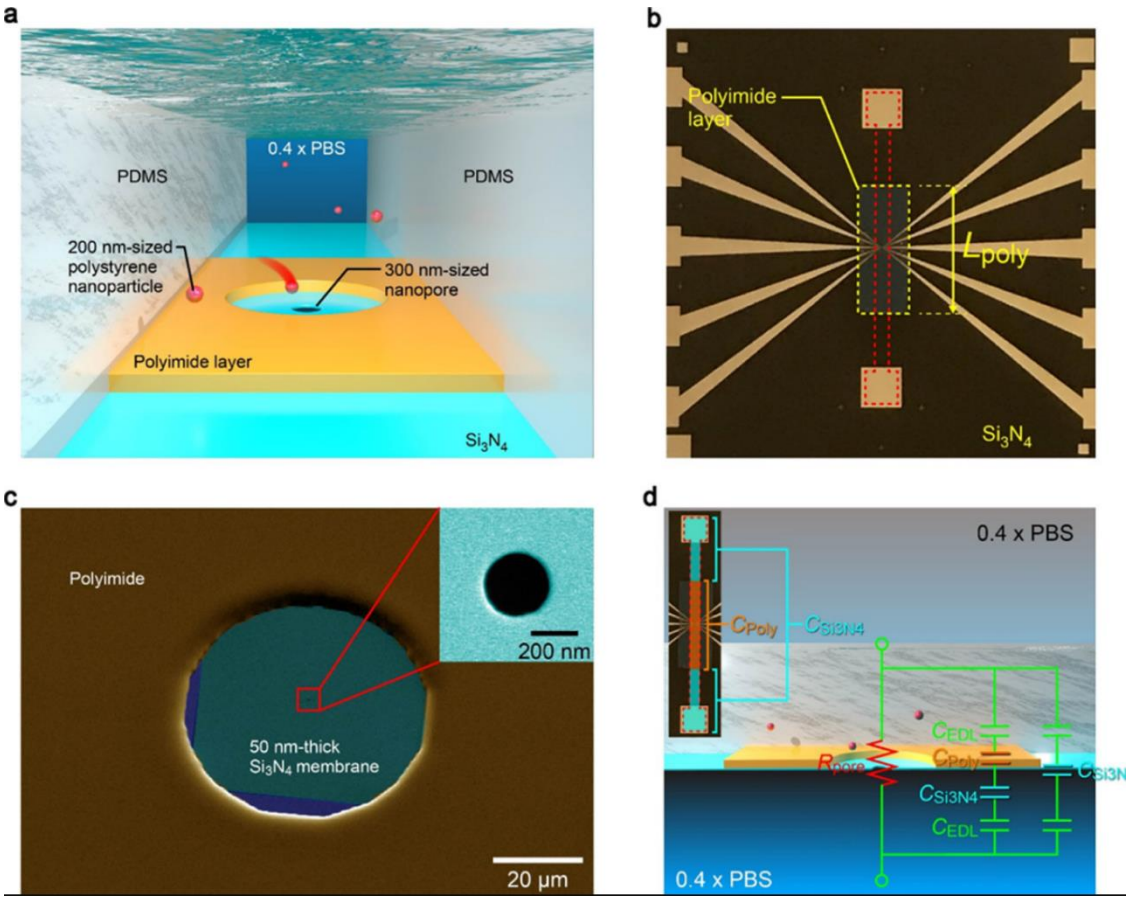

Figure 7.3 Structure of polymer-coated SiN_x nanopores

(a) Schematic illustration depicting single-particle detections of polystyrene nanobeads in an electrolyte buffer using a polymer-coated nanopore. The membrane-side of the nanopore chip was partially coated with a photolithography-defined 5 μm-thick polyimide layer. (b) Optical image of a polyimide-coated nanopore chip. The red dashed line indicates the region where the chip surface was exposed to the buffer solution. L_{poly} denotes the length of the polyimide layer. (c) Scanning electron micrograph showing a nanopore with a diameter of 300 nm sculpted in a 50 nm-thick SiN_x membrane. The polyimide layer was patterned to have a 50 μm-sized pore around the SiN_x nanopore. The inset displays a magnified view of the 300 nm-sized nanopore. (d) Equivalent circuit of the polyimide-coated nanopore structure. C_{EDL}, C_{poly}, and C_{SiNx} are the capacitance components of the electric double layer, the

polyimide sheet, and the SiN_x film, respectively. R_{pore} is the resistance at the nanopore in 0.4× PBS. The inset image represents the PBS-exposed (sky blue) and -non-exposed (orange) SiN_x surface area. Reproduced and adapted with permission under a CC BY-NC-ND 4.0 License from ref.[179]. Copyright 2019 American Chemical Society.

7.3. Results of the coating area of the insulated layer

Polyimide-coated nanopore chips were prepared of various L_{pore} from 0 mm (non-coated) up to 16 mm and performed resistive pulse detections of 200 nm-sized carboxylated polystyrene nanobeads in 0.4× PBS at 0.1 V. Irrespective of L_{pore}, the open pore ionic current I_{ion} was around 14 nA (Figure 7.4), which agrees with an analytical expression[4,55,118] of the ionic resistance $R_{pore} \approx \rho/d_{pore}$ with the solution resistivity ρ = 1.4 Ω m for the diluted buffer and d_{pore} = 200 nm. This is not surprising, as the polymer sheets were designed to cause no notable influence on I_{ion} by virtue of the micropore configuration at the SiN_x nanopore. When the buffer contains the polymeric nanobeads, stochastic temporal drops of the ionic current were observed suggestive of successive nanoparticle translocation through the nanopore (Figure 7.5a,b). These resistive pulses show relatively wide variation in the line shapes at the onset that reflects the random nature of the particle capture approaching toward the orifice at variable angles, which is a characteristic feature in the nanopore having a relatively low thickness-to-diameter aspect ratio structure (Figure 7.5c and 7.6).[59,180] In contrast, the tails are less scattered indicating the regular motions of the escaping particles by virtue of the physical confinement in the nanochannel.[146]

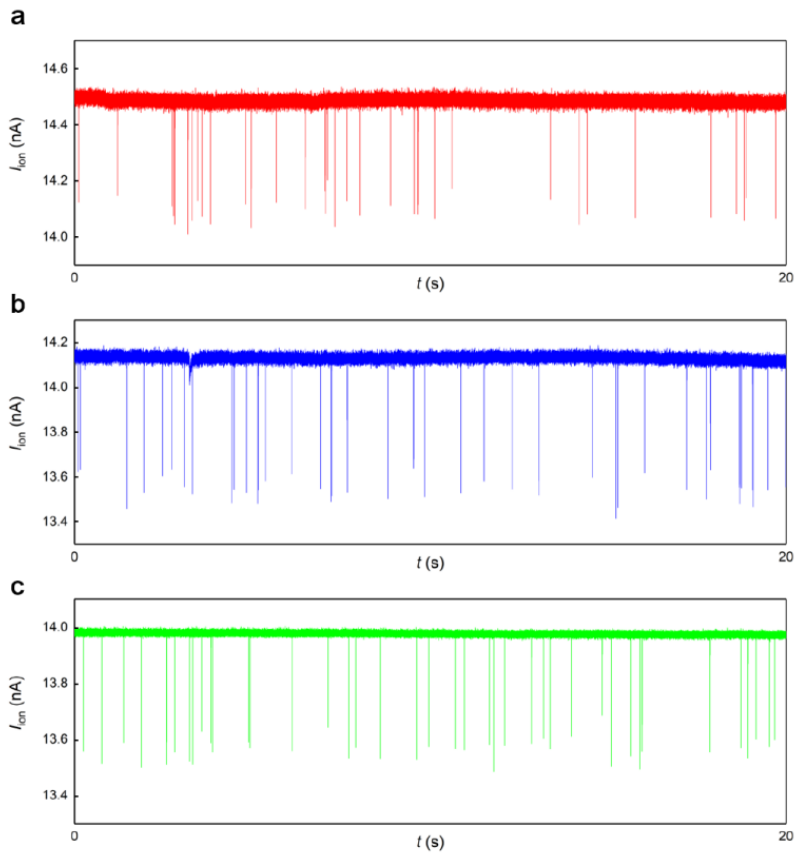

Figure 7.4 Raw ionic current curves obtained with the partially-polyimide-coated 300 nm-sized nanopores

(a-c) The length of the polyimide covers L_{poly} is 2 mm (a), 3 mm (b), and 12 mm (c) with 200 nm-sized polystyrene nanoparticles contained in 0.4 x PBS under 0.1 V. Reproduced and adapted with permission under a CC BY-NC-ND 4.0 License from ref.[179]. Copyright 2019 American Chemical Society.

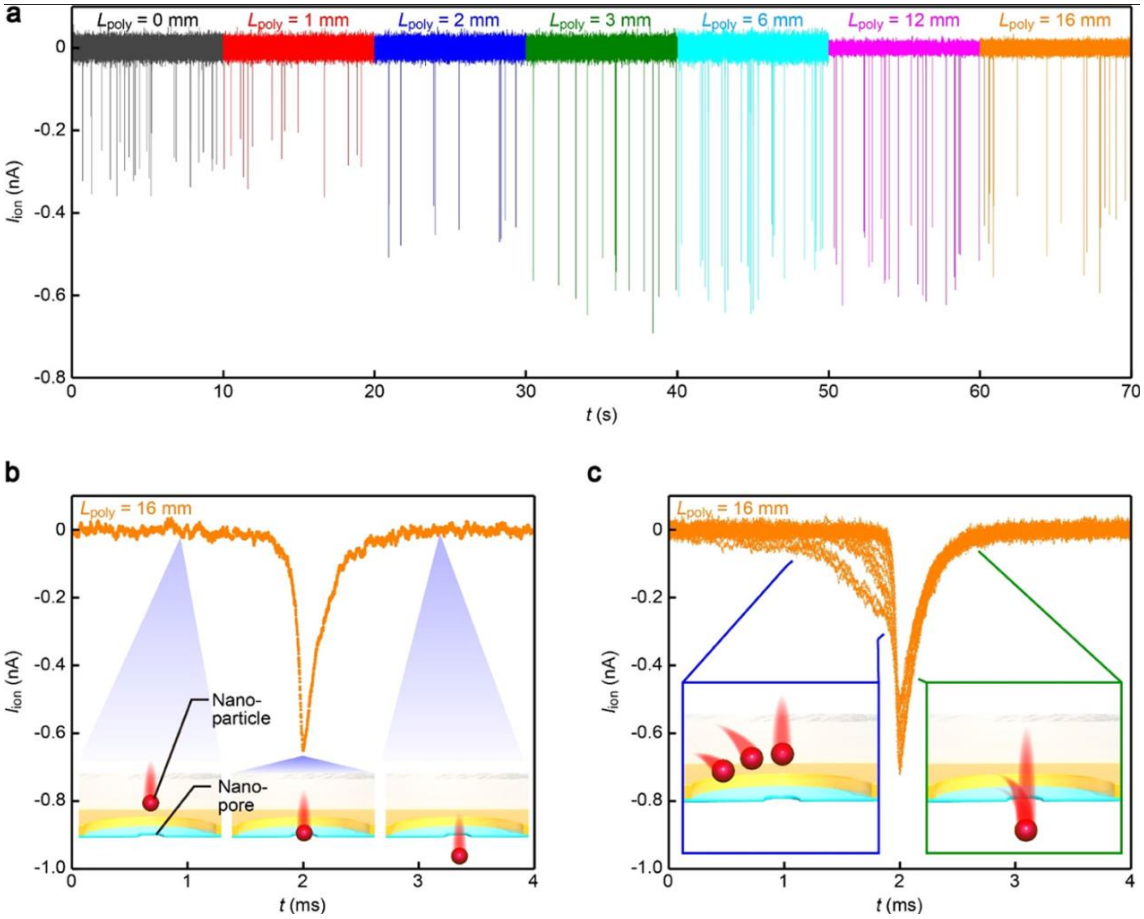

Figure 7.5 Ionic current traces and resistive pulses

(a) The cross-pore ionic current Iion through a polyimide-coated 300 nm-sized SiNx nanopore recorded at 0.1 V in 0.4× PBS containing 200 nm-sized carboxylated polystyrene nanoparticles. The polymer layer had lengths L_{poly} of 0 mm (gray), 1 mm (red), 2 mm (blue), 3 mm (green), 6 mm (sky-blue), 12 mm (purple), and 16 mm (orange). (b) Close view of a resistive pulse signifying translocation of a single nanoparticle through the nanopore. (c) Trajectory-dependent ionic current traces. 30 pulses were overplotted. The onset line-shapes vary widely due to the variable incident angle of the particles approaching the nanopore. In contrast, the tails demonstrate little variation reflecting the regulated motions of the particles in the post-translocation stage. Reproduced and adapted with permission under a CC BY-NC-ND 4.0 License from ref.[179]. Copyright 2019 American Chemical Society.

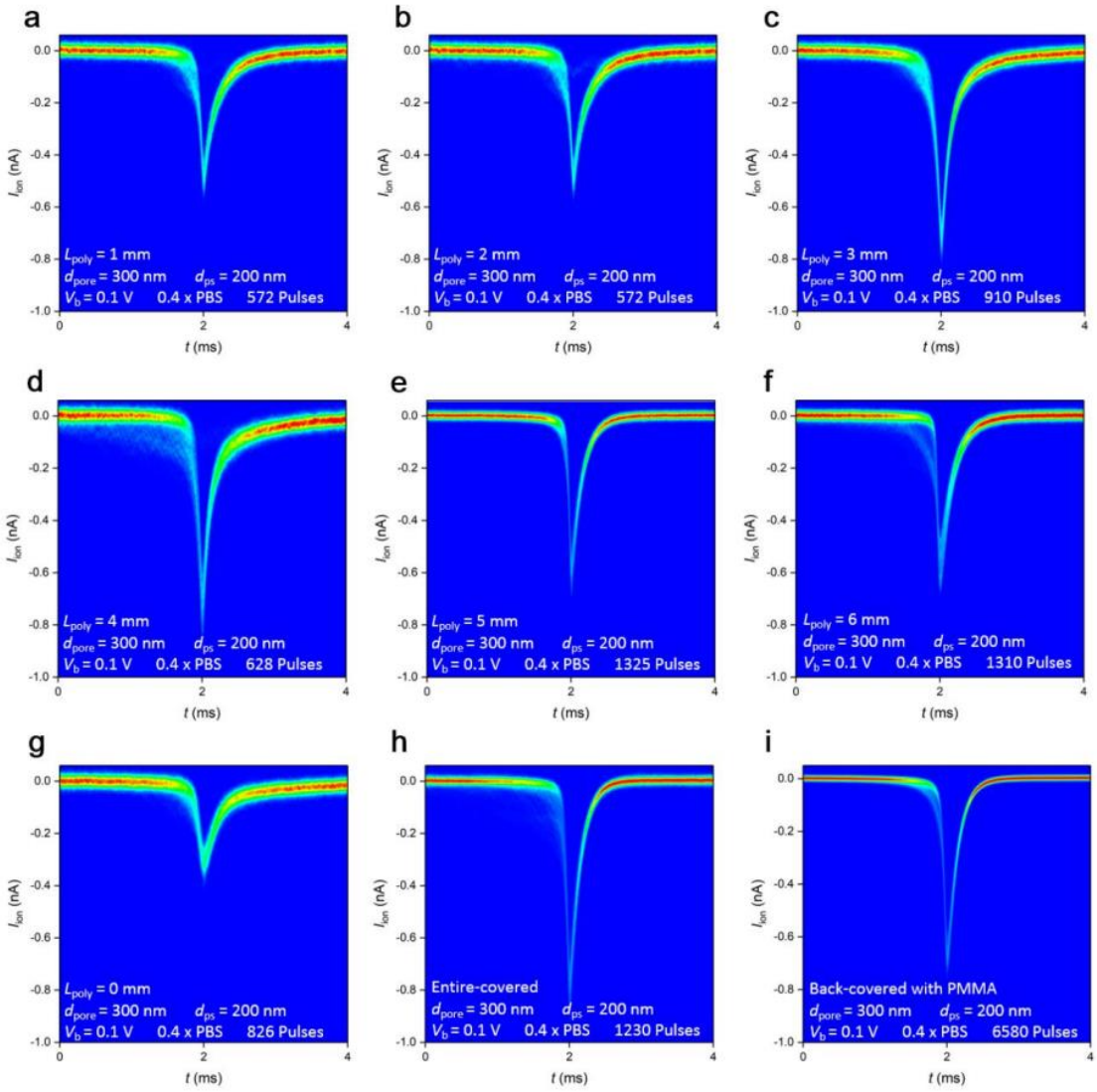

Figure 7.6 Variations in the resistive pulse waveforms

(a-i) Two-dimensional histograms of resistive pulses. The open pore current was offset to zero. Nanopore chip configurations and the number of pulses used are as indicated in each plot. Reproduced and adapted with permission under a CC BY-NC-ND 4.0 License from ref.[179]. Copyright 2019 American Chemical Society.

Here, as shown in Figure 7.5a, it is noticeable that there is a marked difference in the height of the resistive pulses as a whole depending on the dimension of the polyimide layers: longer L_{poly} tends to provide larger signals. As it was already confirmed above that the polyimide layer contributes little to the cross-pore ion conductance, the distinct L_{poly} dependence of the pulse height is naturally ascribed to capacitance effects. When this is the case, it anticipates the charging-derived slow response of the ionic current compared to the temporal blockage of the ion transport by fast electrophoresis of the polymeric nanoparticles through the nanopore.[146,181] As a result, the Iion spike-like signals would be blunted to small pulses yet with an equivalent area.[175] Indeed, despite the large difference in the height (Figure 7.7), the pulse area was found to be the same in the entire L_{poly}-range tested, thereby signifying the prominent role of the polyimide to change the net capacitance of the nanopore chip.

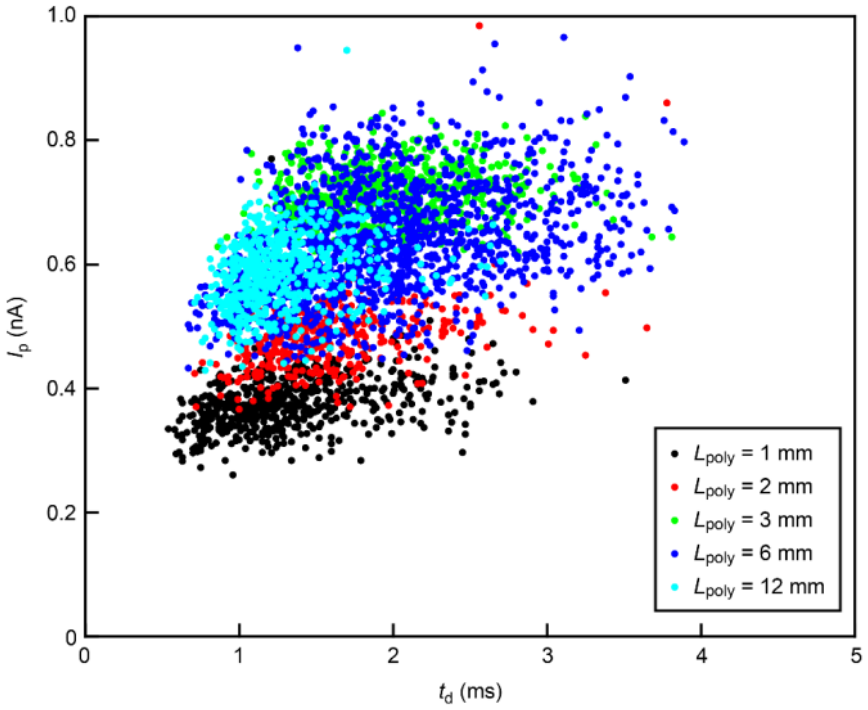

Figure 7.7 Scatter plots of the resistive pulse

Scatter plots of the resistive pulse height Ip versus the width td for 200 nm-sized carboxylated polystyrene nanobeads in 0.4 x PBS measured with partially-polyimide-coated 300 nm-sized nanopores under 0.1 V. Color code denotes the length L_{poly} of the polyimide sheet used. Reproduced and adapted with permission under a CC BY-NC-ND 4.0 License from ref.[179]. Copyright 2019 American Chemical Society.

The equivalent circuit (Figure 7.3d) predicts that the capacitance contribution tends to retard the current response as $I_{ion} = I_0\exp(-t/\tau_{delay})$ where the charging time of capacitor elements enters through $\tau_{delay} = C_{net}R_{pore}$ with the net cross-membrane capacitance C_{net}. To investigate the capacitive contributions in the polymer-coated nanopores, τ_{delay} was reduced by exponential fitting to the tails of the average resistive pulses (Figure 7.8). The result revealed an overall tendency of a steady decrease in τ_{delay} with increasing the size of the polymer sheet (Figure 7.8b, see also Figure 7.9 for the capacitance of each component). This is in qualitative accordance with the aforementioned reduction in C_{net} with $\underline{L}_{poly}$ (Figure 7.9), though quantitatively the theoretical $C_{net}R_{pore}$ is much longer than τ_{delay}.

It should also be noted that the current noise is strongly suppressed with $L_{poly} \geq 12$ mm (Figure 7.5a, see also Figure 7.10 for the RMS noise data). This can be interpreted as another outcome of the lowered capacitance by the polymer coating.[182,183] Specifically, it was reported that the ionic current noise tends to be dominated by that stemming from a coupling between the amplifier voltage noise and the nanopore chip capacitance at high frequencies.[184,185] Similarly, it is likely that the decrease in the noise level by the polymer coating is due to diminished capacitance-derived current fluctuations. As for why the noise does not simply become weaker with L_{poly} from 0 to 6 mm is attributable to the counteracting effects of the lowered capacitance providing not only suppression of the high-frequency noise but also a faster response of I_{ion} which in turn means less damping of the fast current fluctuations.

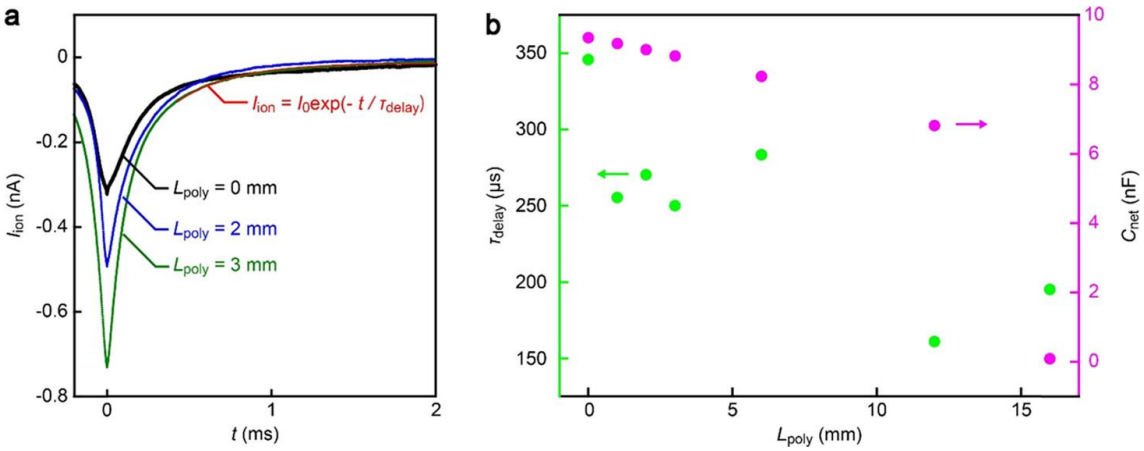

Figure 7.8 Polymer layer effects on the temporal response of the ionic current through a nanopore

(a) Close views of resistive pulse tails obtained for 200 nm-sized polystyrene nanobeads with 300 nm diameter Si3N4 nanopores coated with polyimide layers of different lengths L_{poly}. The red line denotes an exponential fitting to the polymer-coated nanopore with L_{poly} = 3 mm. (b) L_{poly}-dependent temporal resolution of the nanopore sensor. Reproduced and adapted with permission under a CC BY-NC-ND 4.0 License from ref.[179]. Copyright 2019 American Chemical Society.

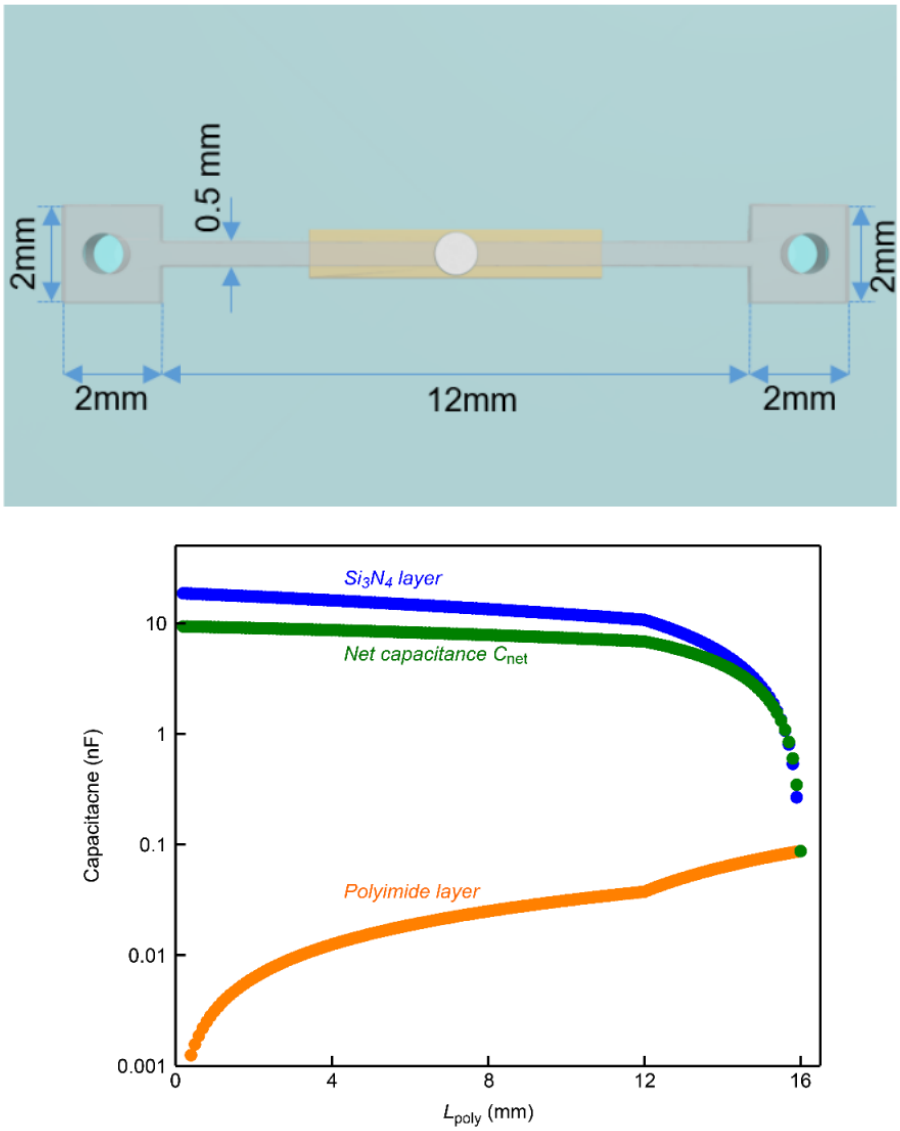

Figure 7.9 Capacitance estimations of the device

The cross-membrane net-capacitance was assessed from the calculated water-touching SiN_x (C_{SiNx}; blue region) and polyimide (C_{poly}; yellow region) capacitance. C_{poly} is given as $C_{poly} = \varepsilon_{vac}\varepsilon_{poly}wL_{poly}t_{poly}$ where $\varepsilon_{vac} = 8.85 \times 10^{-12}$ F/m is the vacuum permittivity, $\varepsilon_{poly} = 3.4$ is the relative permittivity of polyimide, $w = 0.5$ mm is the width of the PDMS channel, and L_{poly} and $t_{poly} = 5$ μm are respectively the lengths and the thickness of the polyimide sheet. Analogously, C_{SiNx} can be described as $C_{SiNx} = \varepsilon_{vac}\,\varepsilon_{SiNx}\,t_{SiNx}\,\{\,w\,(\,0.012 - L_{poly}\,) + 2w_{sq}\,L_{sq}\}$ with the width $w_{sq} = 2$ mm and length $L_{sq} = 2$ mm at the square channel regions and the

thickness of the SiNx film t_{SiNx} = 50 nm when Lpoly ≤ 12 mm and C_{SiNx} = 0 for the case of L_{poly} = 16 mm. In addition to this frontside capacitance, there is another water-touching 50 nm-thick SiNx layer at the back side amounting to 18.7 nF. The rest of the components such as the electric double layer capacitance C_{EDL} and the capacitance at the 0.3 mm-thick doped Si substrate C_{dSi} are expected to contribute little to C_{net} as $C_{SiNx} << C_{EDL}$, C_{dSi}. Orange and blue plots are the capacitance of the polyimide sheet and the un-covered SiNx layer, respectively while green plots denote the net capacitance. The kink at L_{poly} = 16 mm is due to the contribution of the 2 mm square regions of the PDMS channel as depicted in (a). Reproduced and adapted with permission under a CC BY-NC-ND 4.0 License from ref.[179]. Copyright 2019 American Chemical Society.

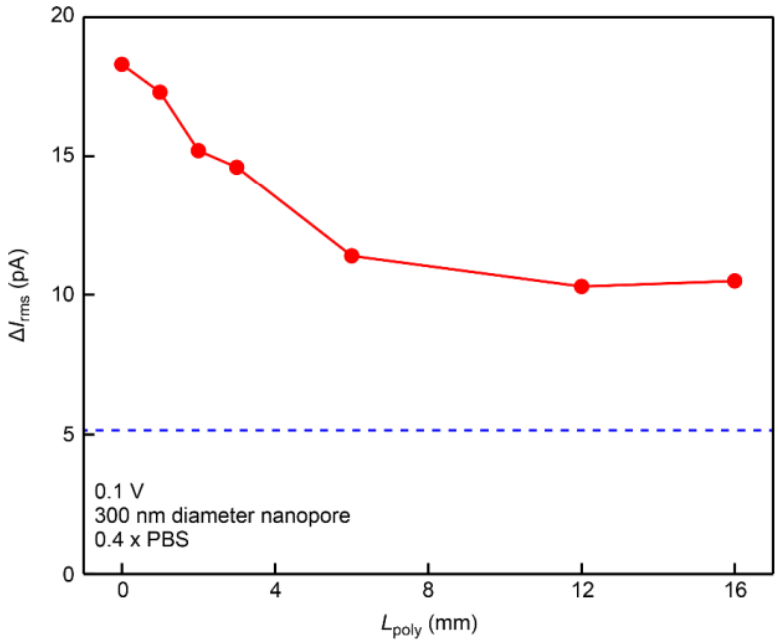

Figure 7.10 Ionic current noise in RMS units

ΔI_{rms} plotted as a function of the length L_{poly} of the polyimide layer on the membrane surface. The blue dashed line is the noise observed in a PMMA back-covered nanopore. Reproduced and adapted with permission under a CC BY-NC-ND 4.0 License from ref.[179]. Copyright 2019 American Chemical Society.

7.4. Back-side polymer-coated solid-state nanopore sensors

The above findings imply that the capacitance relevant to the response speed of Iion can be tailored by only one-side substrate coating. Thus, a polymer layer may not necessarily cover a membrane surface to improve the sensor temporal resolution but it would be equivalently functional when covering the opposite side of the nanopore chip. Furthermore, the choice of material should be rather unimportant as long as the thickness can be made thick. To verify this assertion, a nanopore substrate (d_{pore} = 200 nm) was prepared with the back-side surface being coated with a 5 μm-thick polymethyl-methacrylate (PMMA) layer (Figure 7.11a). PMMA was employed to verify whether the coating effect is material-dependent. In this back-coating design, the capacitance CPMMA at the PMMA layer is anticipated to determine C_{net} as C_{PMMA} (44 pF) $\ll$ C_{SiNx} (13 nF) $\ll$ C_{dSi} where C_{dSi} is a huge capacitance at the doped-Si substrate (Figure 7.11b). As a comparison, a polyimide-coated nanopore with the polymer layer covering the entire area of the membrane-side surface was also tested. Interestingly, these two designs led to further suppression of the noise from that in the partially coated nanopore chips suggesting even lower capacitance achieved by the insertion of the large polymer sheet (Figure 7.11c). More importantly, they offered an equally well-diminished Iion noise platform thereby inferring the expected role of the back cover in decreasing the capacitance.

How about the resistive pulse waveforms? It was addressed by assessing the delay time for the two sensor configurations through an exponential fit to the tails of the average Iion pulses that yielded τ_{delay} of 145 and 149 μs for the PMMA back-covered and the polyimide front-covered chips (Figure 7.11; and Figure 7.12 for statistical distributions of τ_{delay}). The slightly faster current decays than that of L_{poly} = 16 mm are consistent with the lowered capacitance

suggested by the decreased noise level. More directly, the two pulses completely overlap with each other at the tails demonstrating that the capacitance charging time was adequately short compared to the actual speed of the dynamic change in Iion upon the fast electrophoretic translocation of the polystyrene nanoparticles (Figure 7.11b). It can thus be concluded that polymer coating at the back-side surface is equally effective for the front-covering for lowering the capacitance to achieve better sensor temporal resolutions as well as a noise platform. More quantitatively, when the assumption that a τ_{delay} of 145 μs is reflecting the actual translocation motions of the nanoparticles, the capacitive effect on the effective delay time $\tau = \tau_{delay} - 145$ μs can be described as $\tau = \alpha R_{pore} C_{net}$ with a coefficient α amounting to 0.002. This finding may be useful in building integrated nanopore structures as they usually involve constructions of additional structures such as nanofluidic channels, nanopillars, and nanoelectrodes on the membrane-side of the chip surface,[186–189] that makes the front-side coating technically difficult.

In summary, a series of experiments have been established to inspect the influence of capacitance on the temporal resolution of a solid-state nanopore sensor by adjusting the contact area of the electrolyte solution and the thin dielectric layer on the substrate by a polymer coating. The results demonstrated that sufficient coverage of a thick polyimide layer on the membrane-side of the surface could fasten the speed of the response of the cross-membrane ionic current because of the lowered capacitance by the organic layer. Learning from this finding, covering the PMMA layer at the back-side surface was designed and verified, which provided an equivalent effect to that observed for the polyimide coating. The back cover structure facilitates the integration of nanofluidic structures on the membrane side without compromising the sensor temporal resolution of resistive pulse measurements.

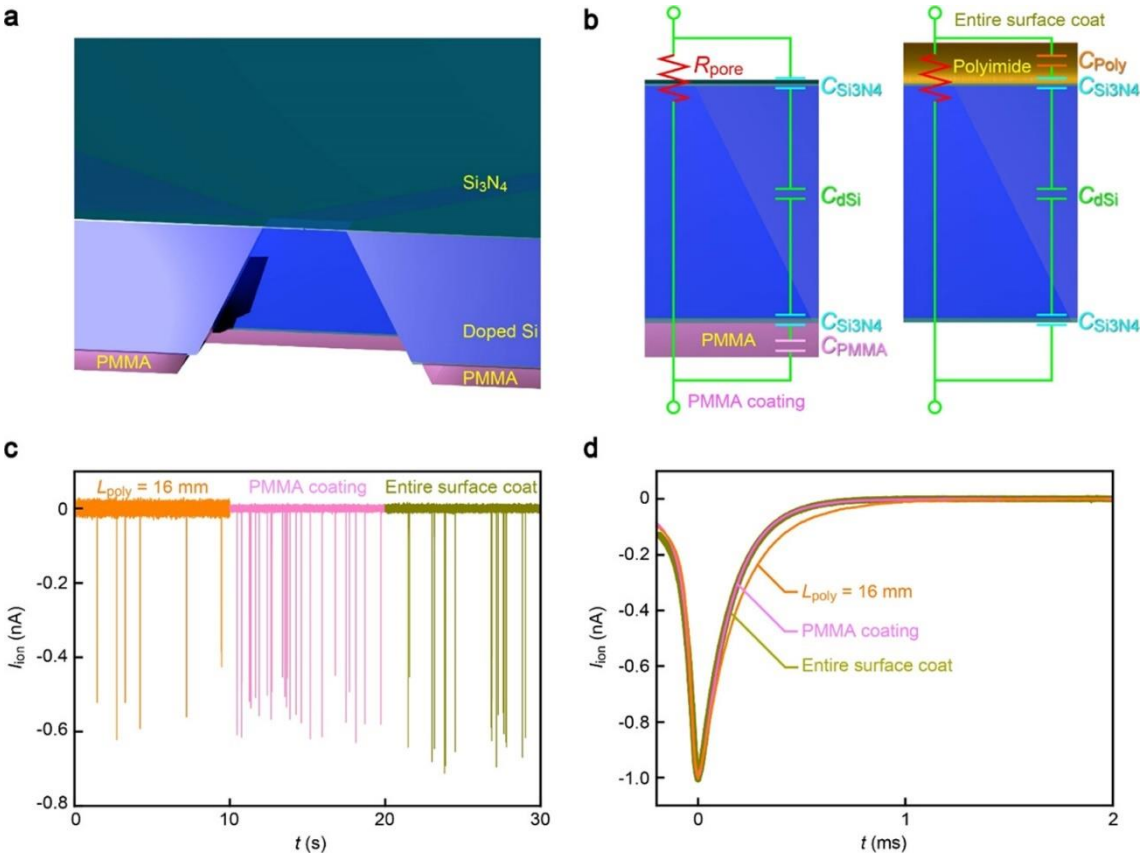

Figure 7.11 Effects of back-side polymer coating on the sensor temporal resolution

(a) Schematic model of a nanopore chip with a PMMA layer coated on the back-side of the substrate surface. (b) Equivalent circuits of the back- (left) and front-side coated nanopore chip (right). (c) Ionic current curves were obtained with front-side polyimide coated (L_{poly} = 16 mm, orange) and back-side PMMA coated (pink) SiN_x nanopores. The result of a nanopore with a polyimide layer covering the entire front surface (except the 50 μm region around the nanopore) was also shown (dark yellow). (d) Magnified views of resistive pulse tails. Color coding is the same as that in (b). Reproduced and adapted with permission under a CC BY-NC-ND 4.0 License from ref.[179]. Copyright 2019 American Chemical Society.

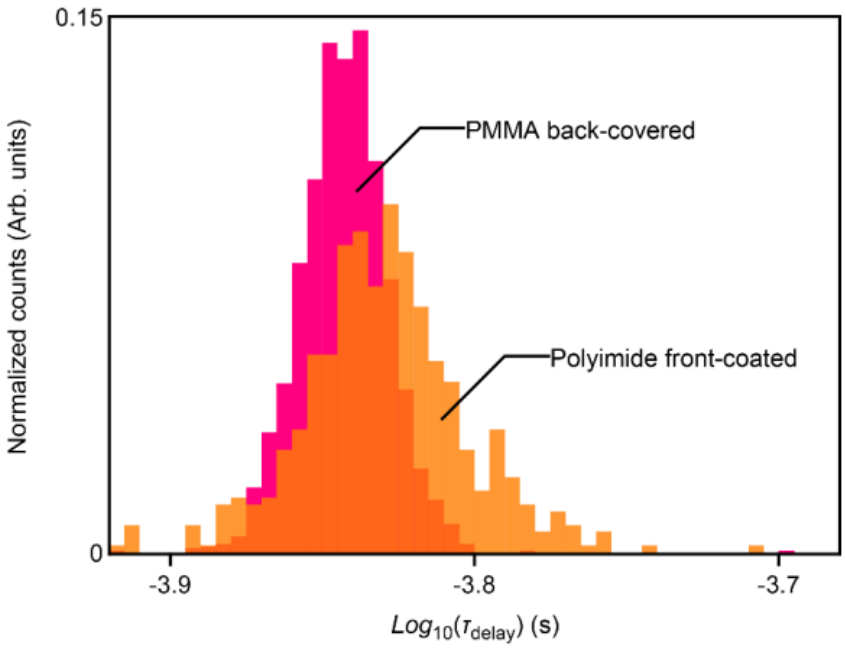

Figure 7.12 Statistical distributions of the ionic current decay constant

Statistical distributions of the ionic current decay constant at the resistive pulse tails for 200 nm-sized carboxylated polystyrenes in 0.4 x PBS in the PMMA back-covered (pink) and the polyimide front-coated (orange) nanopores under 0.1 V. The slightly longer time constant of the front-coated nanopore is consistent with that deduced from the average ionic curve presented in the main text. Reproduced and adapted with permission under a CC BY-NC-ND 4.0 License from ref.[179]. Copyright 2019 American Chemical Society.

Chapter 8 Single particles sensing with solid-state nanopores under salt gradient condition

8.1. Introduction

A solid-state nanopore is a resistive pulse detector of small objects in electrolyte solutions. Tremendous efforts have been devoted to exploiting this nanosensor for studying the translocation dynamics of DNA and reading its genome sequence at a high speed in a label-free fashion.[65] Meanwhile, recent progress in the field also led to growing interest in leveraging the capability for things beyond sequencing. One of the emerging applications is proteomics which foresees identifications of amino acids by ionic blockade currents as denatured proteins pass through the nanoscale conduit.[190,191] At a larger scale, lithographically defined nanopores were also reported to allow single-virion discriminations to digital infection diagnosis.[192–198] Despite the expectations, however, excessively rapid electrophoretic motions of analytes have remained as a technical bottleneck for detecting minute changes in the ionic current upon their instantaneous transits through the nanoscopic sensing zone. It is thus of fundamental importance to find an effective way for slowing down the translocation dynamics in a nanopore.

Several approaches have been verified to face this challenge.[199] Among the various strategies examined, such as active controls by means of adding external forces through light irradiation[200] and gate voltages[11] as well as passive methods via changing viscosity[29,201] and temperature[202] of liquid, a salt gradient approach was reported to be useful for manipulating the translocation dynamics through the induced self-built electric field that serves not only

to slow down the motions of objects such as DNA[31,122,203–206] and nanoparticles[32,207–211] but also to raise the capture rates in the conduit.[5,18,212–217] Meanwhile, the mechanism is predicted to become ineffective in pores of size much larger than the Debye length since it relies on ion-selective transport across the membrane to induce ion concentration polarization via the profound influence of surface charges on the nanopore wall.[218–220] Even though such a condition is common in nanopore sensing of relatively large particles and molecules such as viruses and amyloids, along with the fact that various intriguing phenomena have been found in resistive pulse sensing using submicrometer channels[57] such as pore shape-dependent ion blockage characteristics,[211,221,222] deformations of soft particles,[223–225] and concentration-polarization-induced ionic current enhancements,[210,226] little experimental efforts have been devoted so far to assess the feasibility of the salt gradient approach for controlling the translocation dynamics of non-DNA objects in the non-ion-selective channels.

Herein, in this chapter, the impact of salt gradients on electrophoretically driven translocation motions of nanoparticles in submicrometer-sized solid-state nanopores was investigated. It was found the significant roles that asymmetric electric potential profiles across the membrane[5] and salinity-gradient-mediated electroosmotic flow[22,30,48] are not only enabled to slow down the translocation motions of particles, but also served to facilitate or completely inhibit their electrophoretic capture via a salt concentration control. The present findings suggest the usefulness of the salinity gradient approach for resistive pulse sensing even in a non-ion-selective pore of size much larger than Debye length.

8.2. Single particle translocation under an asymmetric salt condition

A lithographically defined 300 nm diameter nanopore was formed in a 50 nm thick SiN_x membrane (Figure 8.1) that separated the cis and trans chambers filled with phosphate-buffered saline (PBS) of different ion concentrations from 0.1 to 1 c_0, where c0 represents a NaCl concentration of 137 mM in a non-diluted buffer (Figure 8.1). Resistive pulse measurements of 200 nm-sized carboxylated polystyrene beads (added to cis at 10^9 particles/mL) were performed by applying DC voltage V_b across the membrane and recording the ionic current at a 1 MHz sampling rate. When the particles diffuse to approach in the vicinity of the orifice, they tend to be drawn electrophoretically into the pore via the focused electric field (the ζ potential of the polymeric nanobeads was negative ranging from −30 to −38 mV in the electrolyte buffer of different ionic strengths (Figure 8.2)). As a consequence, resistive pulses were observed each time the particles transited the conduit (Figure 8.1b, c).

It is known that surface charges on analytes may affect the cross-membrane ionic current upon their translocation. This is due to the fact that in general, more counterions are attracted on a surface of an object with larger ζ potential. Since these counterions serve to enlarge the ion density inside the channel upon the translocation, it counteracts the volume exclusion effect and even gives rise to ionic current enhancement instead of resistive pulses.[159,160] However, this mechanism is effective only under a condition where the electric double layers at the object and the pore wall surfaces overlap with each other,[160] which is not the case for the present system where the nanopore size is orders of magnitude larger than the Debye length (less than 1 nm) in the salt solution. Meanwhile, Qiu et al.[226] observed a significant influence of surface charge densities of submicrometer-sized particles on the resistive pulse heights.[226] The results were attributed to the electric-field-induced ion

concentration polarization at the particles when they move through a polymeric microchannel. While this may have affected the current blockage characteristics in the 300 nm-sized nanopores, its contribution is predicted to be small,[226] as the surface charge densities vary by only less than 30% under the ion concentration conditions tested (Figure 8.2).

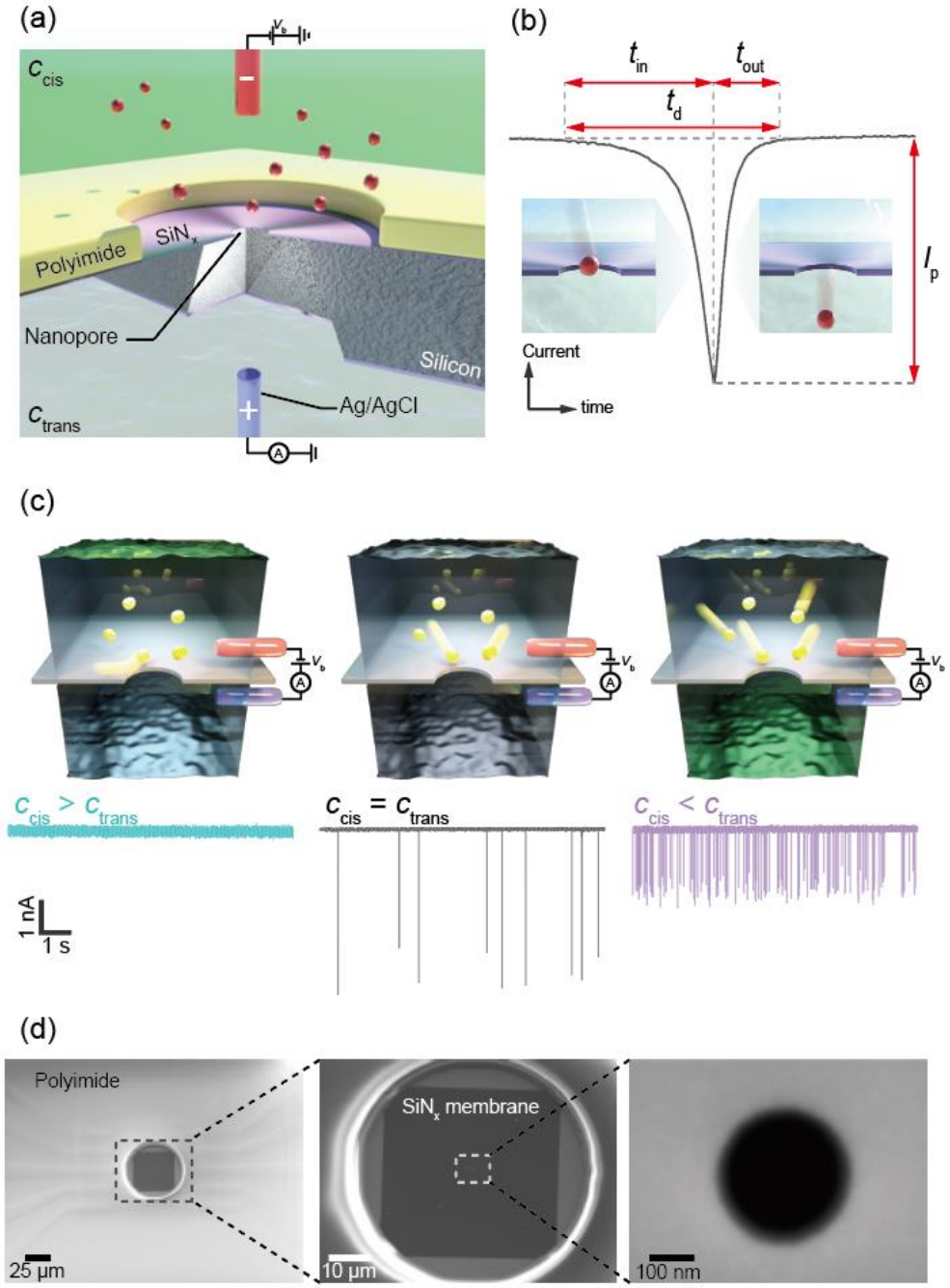

Figure 8.1 Schematic diagram of nanoparticle measurement with nanopores

(a) Setup of a polyimide-coated solid-state nanopore sensor. (b) Ionic current blockade by a nanoparticle passing through the nanopore. The pulse height I_p and the width td in general denote the size and the translocation time of the nanoparticles. t_d is further decomposed into the width at the onset (t_{in}) and the tail (t_{out}), which represent the particle speed when entering

and escaping the nanopore. (c) Three configurations of the electrolyte concentration difference at the two chambers. Nanoparticles were always added to the cis chamber. Positive and negative salt gradients were created by changing the ion concentration at the cis or trans to lower than 1 c_0 while keeping the other side at 1 c_0. (d) Scanning electron micrographs showing a 50 μm-sized polyimide pore around a 300 nm-sized nanopore sculpted in a 50 nm-thick SiNx membrane. Reproduced and adapted with permission from ref.[227]. Copyright 2021 American Chemical Society.

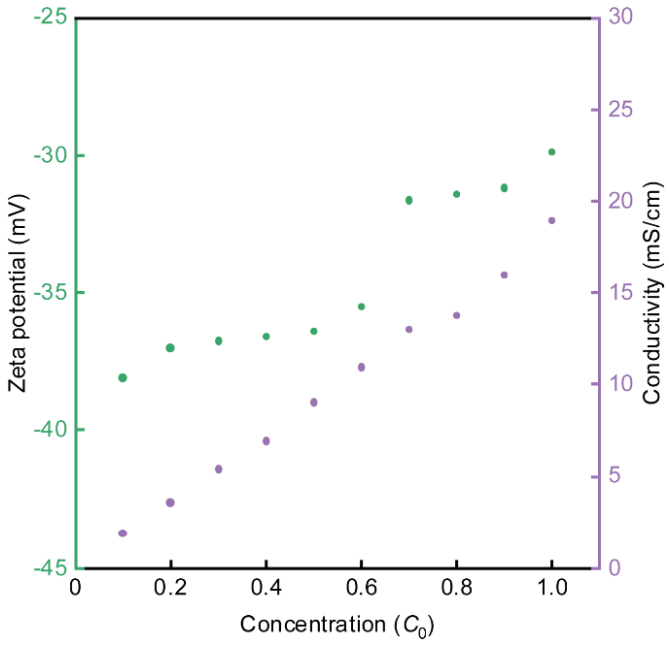

Figure 8.2 Zeta potential of 200 nm diameter carboxylated polystyrene beads in PBS of different ion concentrations

Reproduced and adapted with permission from ref.[227]. Copyright 2021 American Chemical Society.

The roles of the salt gradient on the single-nanoparticle electrokinetics were explored by analyzing the signal widths and also the pulse-to-pulse intervals representing, respectively, the time they took to pass through the membrane and the electrophoretic capture rate (Figure 8.1b).[29] When the ion concentration c_{cis} of the particle-containing solution was made lower than that in trans c_{trans}. First, the results explained that under positive salt gradient conditions, i.e., when the ion concentration of the particle-containing solution at cis (c_{cis}) was made lower than that in trans (c_{trans}). Specifically, the electrolyte buffer in cis was changed in a range from 1 to 0.2 c_0, while that in the trans was kept at 1 c_0. The decrease in c_{cis} tends to lower the open pore current (Figure 8.3a) as well as the resistive pulse heights (Figure 8.3b) due to the less number of current-carrying ions around the nanopore. This trend can be found clearly in the scatter plots of the pulse height I_p as a function of width td (Figure 8.3c). On the other hand, it is also noticeable that td tends to be wider with decreasing c_{cis}, indicating slower translocation speed under the larger salinity difference. This is somewhat counterintuitive since the particle ζ potential is larger under lower salt concentrations[228] predicts shorter t_d with c_{cis}.

Before getting into detailed analyses of the translocation motions, it was added to note that the salt concentration difference causes dissimilar electrode potentials at cis and trans whose amount is approximately given by $\Delta V = -GkT/q \log(c_{cis}/c_{trans})$,[215] where G is the nanopore conductance, kT is the thermal energy, and q is the elementary charge. In fact, it found that the measured base current was well matched with the series resistance model (consisting of the resistance inside ($R_{pore} = 4\rho L/\pi d_{pore}^2$) and outside ($R_{acc} = d_{pore}/2\rho$),[4,229] where ρ is the resistivity of the electrolyte solution, dpore is the diameter of the pore, and L is the thickness of the membrane[54,55] by taking the potential shifts into account (Table 8-1). In the following,

therefore, the effective cross-membrane electrical potential difference V_{eff} ($=V_b + \Delta V$) was used for deducing the electrokinetic particle transport through the salinity gradient-biased nanopore.

To clarify the mechanism responsible for the salt gradient-dependent translocation dynamics, the electrophoretic motions of the nanoparticles was investigated in more detail by analyzing the first (t_{in}) and second (t_{out}) halves of the resistive pulse widths denoting the particle velocity before and after the translocation, respectively (Figure 8.1b).[138] With no salt gradient, the resistive pulse waveforms were asymmetric with tin being longer than tout (Figure 8.3d,e). This can be understood as a result of more confined particle trajectories after escaping the pore as reported in the previous literature. [138] Unexpectedly, on the other hand, tin tended to become larger, while tout became smaller with decreasing salt concentration, leading to $t_{in} < t_{out}$ when $c_{cis} \leq 0.6\ c_0$ (Figure 8.3d, 8.3e). The c_{cis}-dependent td found in Figure 8.3c is thus attributed to the pronounced effects of the salt gradients to retard the electrophoretic motions of the particles after exiting the nanopore.

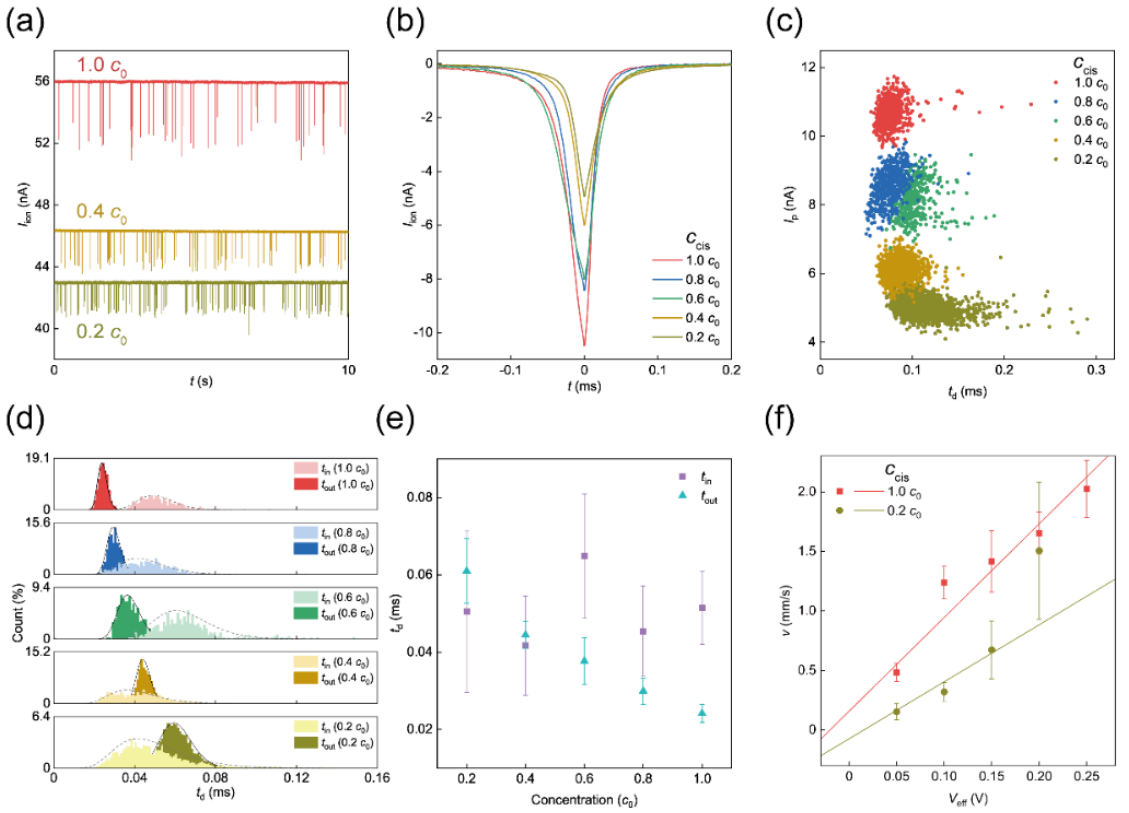

Figure 8.3 Single-nanoparticle detections by nanopore sensors under salt gradients

(a) Partial ionic current traces recorded in the nanoparticle-containing PBS of ion concentrations 1 (red), 0.4 (orange), and 0.2 c_0 (dark yellow) at the cis chamber and 1 c_0 at the *trans* under an applied cross-membrane voltage V_b of 0.2 V. c_0 represents 1× PBS (137 mM NaCl). (b) Averaged resistive pulses were calculated from the signal data obtained under various salt gradient conditions denoted by the ion concentration at the *cis* chamber. The numbers of pulses used for the estimations were 644 (1 c_0), 513 (0.8 c_0), 426 (0.6 c_0), 1083 (0.4 c_0), and 2345 (0.2 c_0). (c) Scatter plots of the resistive pulse height I_p with respect to the width td. (d) Histograms of the signal width at the pulse onset (t_{in}) and the tails (t_{out}). Solid curves are Gaussian fitting to the distributions. (e) The average tin and tout deduced from (d). (f) Nanoparticle translocation speed under different cross-membrane electric potential differences V_{eff}. Translocation velocity at zero voltage (V_{eff} = 0) is approximately −208 μm/s

under a 5-fold difference in the salt concentration. Reproduced and adapted with permission from ref.[227]. Copyright 2021 American Chemical Society.

Table 8-1 Concentration gradient-dependent open pore conductance

*1 Measured ionic current under the applied cross-membrane voltage V_b of 0.2 V.

*2 Theoretical conductance values calculated with a series resistance model, i.e. $R_{total} = R_{pore} + R_{acc} = 4\rho L/\pi d_{pore}^2 + \rho/d_{pore}$ where ρ, L, and d_{pore} are the resistivity of the electrolyte solutions, the membrane thickness, and the diameter of nanopores, respectively.

*3 Electrode potential difference ΔV under different concentrations at the cis and trans chambers obtained from $\Delta V = -GkT/q \log(c_{cis}/c_{trans})$.

*4 Open pore ionic current under $V_b + \Delta V$.

Concentration of c_{cis} (c_0)	Measured Ionic Current (nA)	Theoretical Current (nA)	Potential Difference with c_{trans} = 1 c_0 (mV)	Corrected Current (nA)
1	55.84	54.94	0	54.94
0.8	50.33	49.81	5.71	51.23
0.6	47.04	43.09	13.08	45.91
0.4	46.21	33.94	23.46	37.92
0.2	42.97	20.73	41.20	25.00

It is interesting to see if reverse effects can be found when applying the salt gradient in an opposite direction. The result was verified by extending the resistive pulse measurements under conditions $c_{cis} > c_{trans}$. Precisely, the cis chamber was filled with PBS of 1 c_o while changing c_{trans} in the range from 1 to 0.2 c_o. By adding the nanoparticles in *cis*, long-t_{in} pulse signals were observed (Figure 8.4a, 8.4b). On the other hand, while c_{trans} lowered to below 0.6 c_o, it was observed that resistive pulses became significantly weaker and eventually disappeared in the ionic current traces. The absence of the signals cannot be attributed to the decreased open pore conductance under the lower ion concentrations, as can be detected in the signals even when c_{cis} was 0.2 c_o. Instead, it is more likely to consider that the polymeric beads started to be rejected from the nanopore. This is certainly a possible case for the electroosmosis at the SiNx wall surface with negative native surface charges inducing water flow in a direction opposite to that of the electrophoresis of the negatively charged carboxylated polystyrenes, thereby causing the hydrodynamic drag force to be stronger than the electrostatic counterparts under the extremely weak electric field at the trans side of the orifice so that the nanoparticles were rejected without being captured into the pore.

In fact, the result also demonstrated that it was able to hold a nanoparticle at the nanopore under the salt gradient control. This can be found in the ionic current trace under c_{trans} = 0.6 c_o where significant ionic current fluctuations were ascribed to oscillatory motions of a nanoparticle under a balance of the hydrodynamic drag and electrophoretic forces (Figure 8.4c).[11,148] The change in the pre- and posttranslocation speeds of nanoparticles can be explained qualitatively by the salinity-gradient-derived asymmetric electric potential profile across the membrane. Due to the stronger dependence of R_{pore} on d_{pore}, the ionic conductance is dominated by R_{acc} in the present nanopores having a low thickness-to-diameter aspect

ratio structure.[54,55] When there is no ion concentration difference between the *cis* and *trans* chambers, the R_{acc} is the same at both sides of the conduit, giving rise to an equal amount of electric potential drop across the membrane (while the polyimide layer adds additional resistance at the *cis*, its contribution is negligibly small due to an order of magnitude larger size compared to d_{pore}). Meanwhile, this is not the case when there is a difference in salt concentration. For example, $c_{cis} < c_{trans}$ leads to higher ρ, and equivalently larger R_{acc}, at the *cis* side of the nanopore. As a result, the voltage drops more largely at the *cis* side of the orifice which anticipates stronger electrophoretic forces on the particles at the inlet with decreasing c_{cis}. At the same time, the electric field becomes weaker at the *trans* region, thereby causing a steady decrease in the particle velocities after escaping the pore under larger salt gradients. In fact, finite element analyses[230] revealed a focused electric field at the cis region when $c_{cis} < c_{trans}$ (Figure 8.5). These findings indicate the effectiveness of the salt gradient to tailor the single-nanoparticle translocation dynamics. The slower motions at the nanopore exit would be particularly useful for resistive pulse analyses of small molecules like proteins since one can also benefit from the suppressed variation in the motion trajectories.[148]

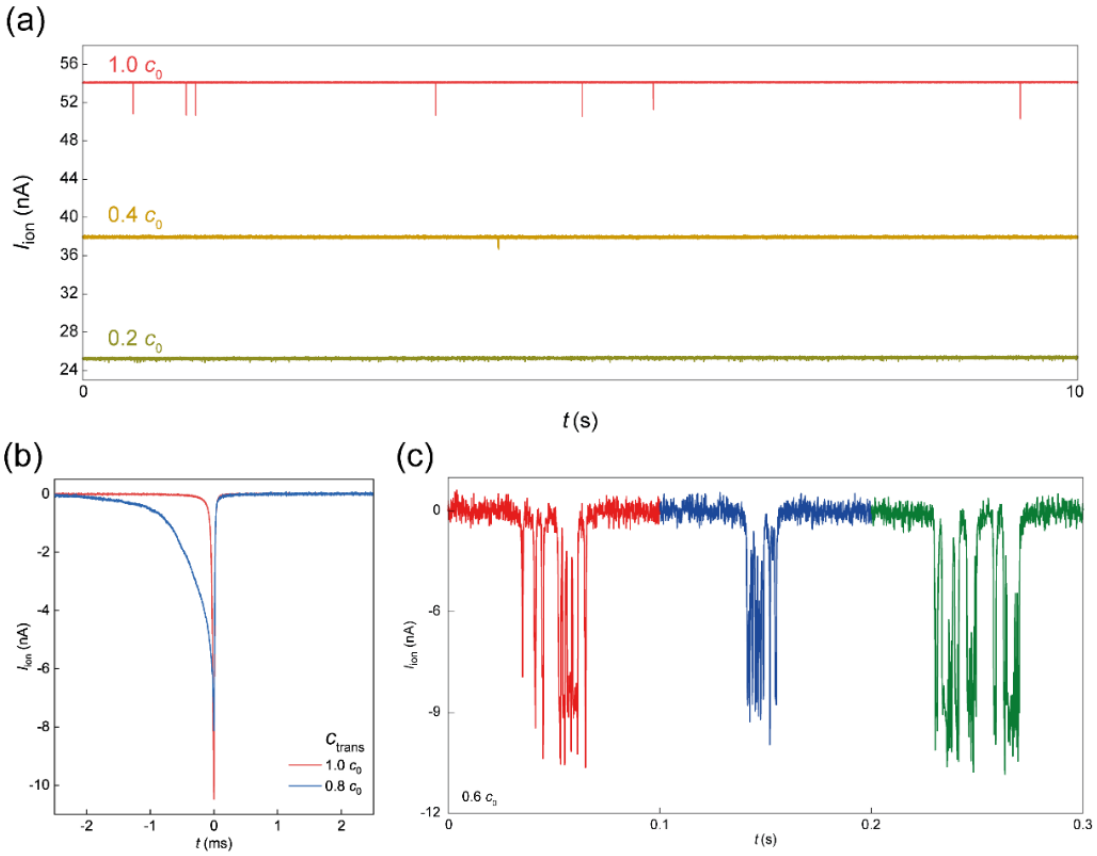

Figure 8.4 Nanoparticle translocation event with a negative salt gradient

(a) Ionic current curves recorded in dispersion PBS solution of the 200 nm-sized polystyrene beads using a nanopore of 300 nm-diameter in a 50 nm-thick SiNx membrane under V_b = -0.2 V with the applied negative salt gradient. 1, 0.4, and 0.2 c_0 denote the ion concentration of the buffer added to the cis. In this experiment, the trans chamber was always filled with PBS of 1 c_0.(b) Typical resistive pulses were observed under a negative salt gradient imposed by adding diluted PBS of 0.8 c_0 to the trans while keeping cis at 1 c_0 (blue). The signal under no salt difference was also displayed for comparison (red). (c) Examples of the fluctuated ionic current signals signifying trapping of a nanoparticle via the balanced electrophoretic and hydrodynamic drag forces when c_{cis} = 0.6 c_0 and c_{trans} = 1.0 c_0. Reproduced and adapted with permission from ref.[227]. Copyright 2021 American Chemical Society.

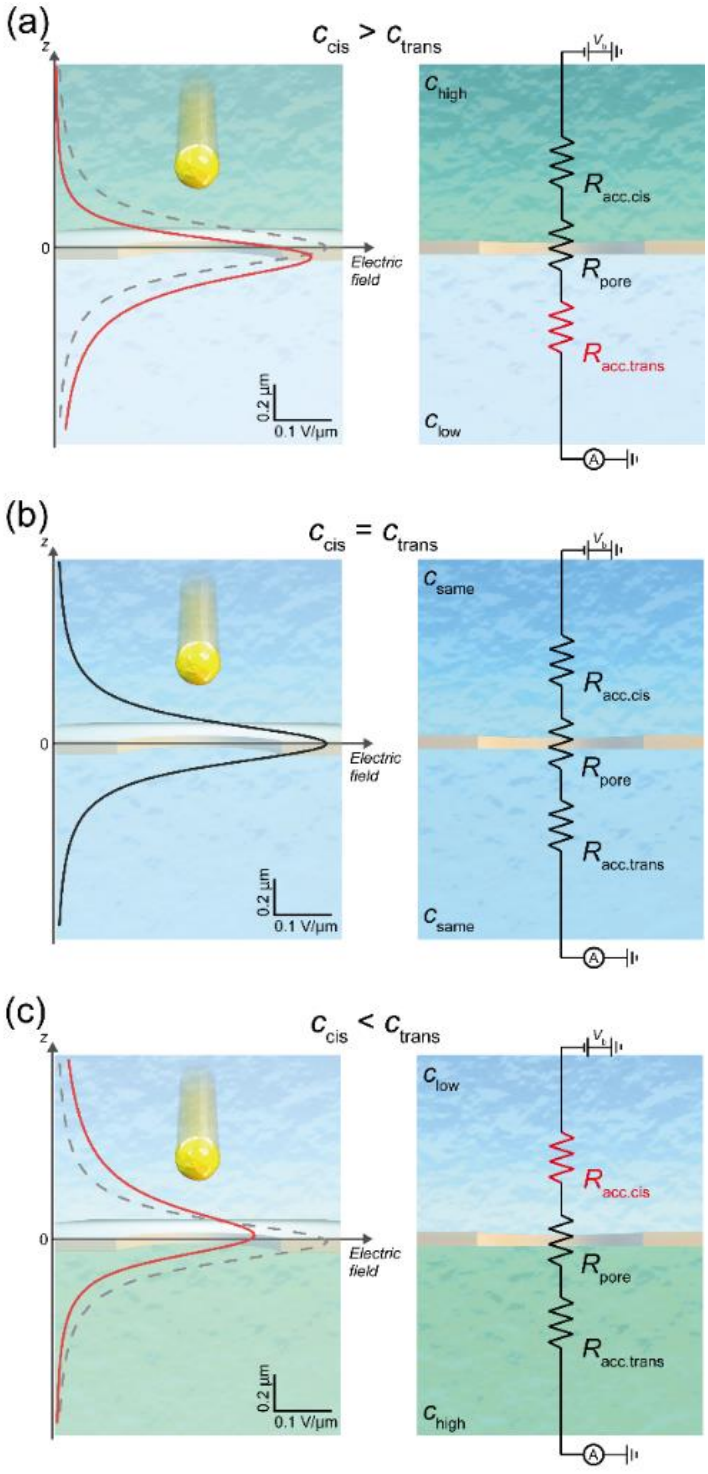

Figure 8.5 Salt-gradient-dependent electric potential profiles across the nanopore

Numerical simulations of the cross-membrane electric field distributions with a 200 nm diameter nanoparticle translocating from z = 800 to −800 nm through the 300 nm sized

nanopore under (a) a positive salt gradient (c_{cis} = 10 c_{trans}), (b) no salt gradient (c_{cis} = c_{trans}), and (c) a negative salt gradient (10 c_{cis} = c_{trans}). Dashed curves in (a) and (c) are the electric field in (b) shown for comparison. The right panels describe the equivalent circuits where the largest resistance components at the low c regions are depicted in red. Reproduced and adapted with permission from ref.[227]. Copyright 2021 American Chemical Society.

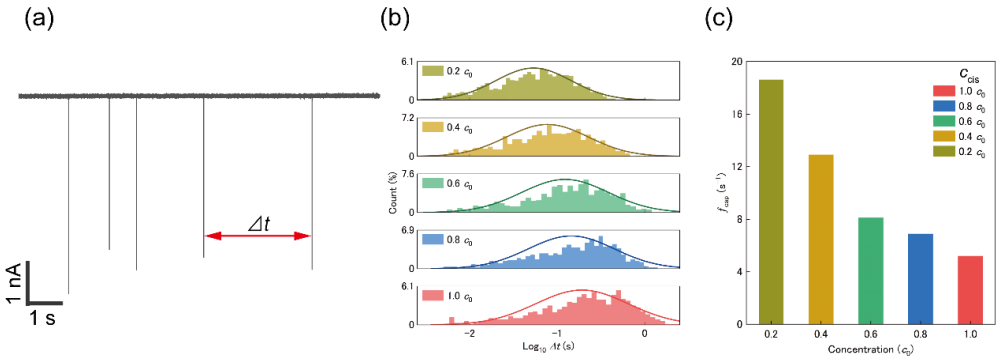

Figure 8.6 The result of capture rate with asymmetric concentration condition

(a) Time interval Δt between the consecutive two signals. (b) Histograms of log Δt. Solid curves are Gaussian fits the distributions. (c) The average particle capture rates f_{cap} were obtained from (b). Reproduced and adapted with permission from ref.[227]. Copyright 2021 American Chemical Society.

So far, the salt gradient is proven capable to lower the electrophoretic speed of objects at the pore exit. Further investigation suggested another outcome of the ion concentration difference to enhance the particle capture efficiencies. The evaluation was carried out by calculating the time interval Δt between the two consecutive signals (Figure 8.6a).[231] The average particle capture rates f_{cap} were then estimated by $f_{cap} = 1 / \Delta t_{ave}$, where Δt_{ave} is the time interval deduced by Gaussian fitting to the histograms (Figure 8.6b). f_{cap} demonstrated a steady increase (decrease) under larger (smaller) salinity gradients enabling up to a factor of 3.6 enhancement by a 5-fold ion concentration difference (Figure 8.6c). The tendency is consistent with the stronger (weaker) electric field at the nanopore opening filled with lower (higher) ion concentration buffer that serves to draw the polystyrene beads in the inlet more effectively into the nanopore (Figure 8.5).

Besides the electrophoretic and electroosmotic contributions, the salinity gradient alone gives osmotic pressure to a local electric field at the nanopore. To assess this effect of diffusiophoresis and diffusioosmosis, resistive pulse measurements of the nanoparticles in a 300 nm sized nanopore with and without a salinity gradient under various cross-membrane voltage were performed.[5] When there was no salt concentration difference, the average translocation speed of the nanoparticles deduced from the widths of the resistive pulses demonstrated a linear increase with the cross-membrane voltage (red plots in Figure 8.3f). Extrapolating the dependence to zero voltage, it was found that there was almost zero velocity of the particles as expected since no driving force exists to move them through the pore. On the other hand, the translocation speed became much slower and showed weaker dependence on V_{eff} under a 5-fold difference in the salt concentrations (blue plots in Figure 8.3f), which was attributed to the smaller forces exerted on the nanobeads as shown by the finite element

simulations of the electrostatic and electrophoretic drag forces (Figure 8.5). Linear fitting revealed a negative translocation velocity of approximately −208 μm/s at V_{eff} = 0 V, suggesting particle motions in the direction of decreasing salinity gradient via diffusion osmosis/phoresis. Although this may affect the electrophoretically driven translocation dynamics of the nanoparticles, its influence is anticipated to be only minor considering the order of magnitude lower velocity under zero V_{eff} compared to that at above 0.2 V.

8.3. Numerical simulation results of particle passing process

While the salt-gradient-mediated capture-to-translocation dynamics can be qualitatively explained by the asymmetric cross-membrane electric potential profiles, it is worth discussing in a more quantitative manner by taking into account the influence of the electroosmotic flow. For this, finite element simulations of hydrodynamics were exhibited in the 300 nm sized SiN_x nanopore assumed to have a surface charge density of −45 mC/m^2 (see Figure 8.7 for the estimation of the charge density at the nanopore wall surface) at the wall surface[232,233] by solving coupled Poisson–Nernst–Planck and Navier–Stokes equations using COMSOL 5.6 Multiphysics.[230] The deduced fluid flow occurred mostly in the direction opposite to the electrophoresis of the negatively charged nanoparticles at the cis due to the field-driven motions of dense countercations at the negatively charged pore wall surface irrespective of the ion concentration conditions (Figure 8.8). On the other hand, eddies were found under the negative salt gradient[48] (Figure 8.9), giving rise to negative fluid velocities at the trans side of the nanopore.

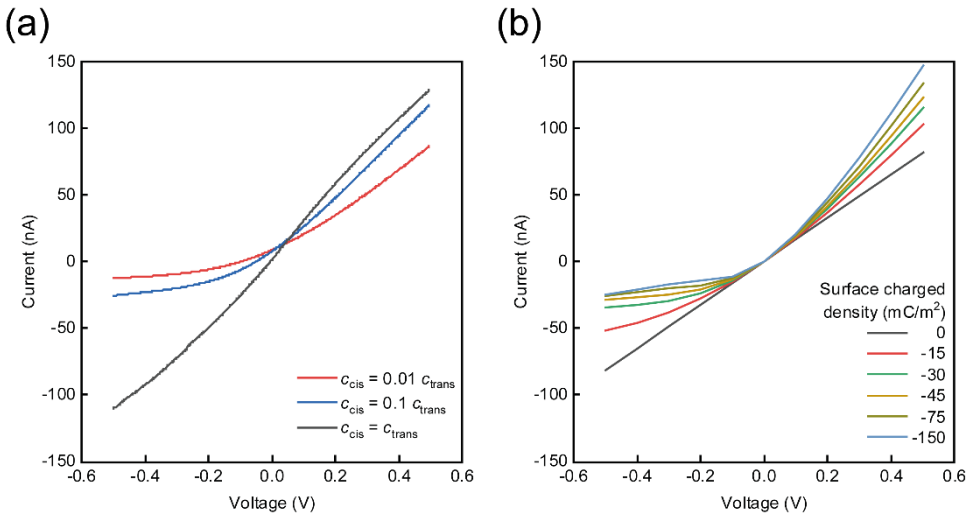

Figure 8.7 Simulated result of *I-V* characteristics with a 300 nm-sized nanopore

(a) Typical current-voltage characteristics of a 300 nm diameter nanopore in a 50 nm thick SiN_x membrane obtained under the conditions of c_{cis} = 0.01 c_{trans} (red curve), c_{cis} = 0.1 c_{trans} (blue curve) and c_{cis} = c_{trans} (black curve). (b) Simulated current-voltage characteristics of a 300 nm-sized and 50 nm-thick nanopore under c_{cis} = 0.1 c_{trans}. The surface charge density at the channel wall was varied in a range from 0 to -150 mC/m^2. Since the simulated curve at -45 mC/m^2 was in close agreement with the experimental counterpart (a), this value was employed in the present work to deduce the electrokinetic transport of particles in the salinity-gradient-biased nanopore. Reproduced and adapted with permission from ref.[227]. Copyright 2021 American Chemical Society.

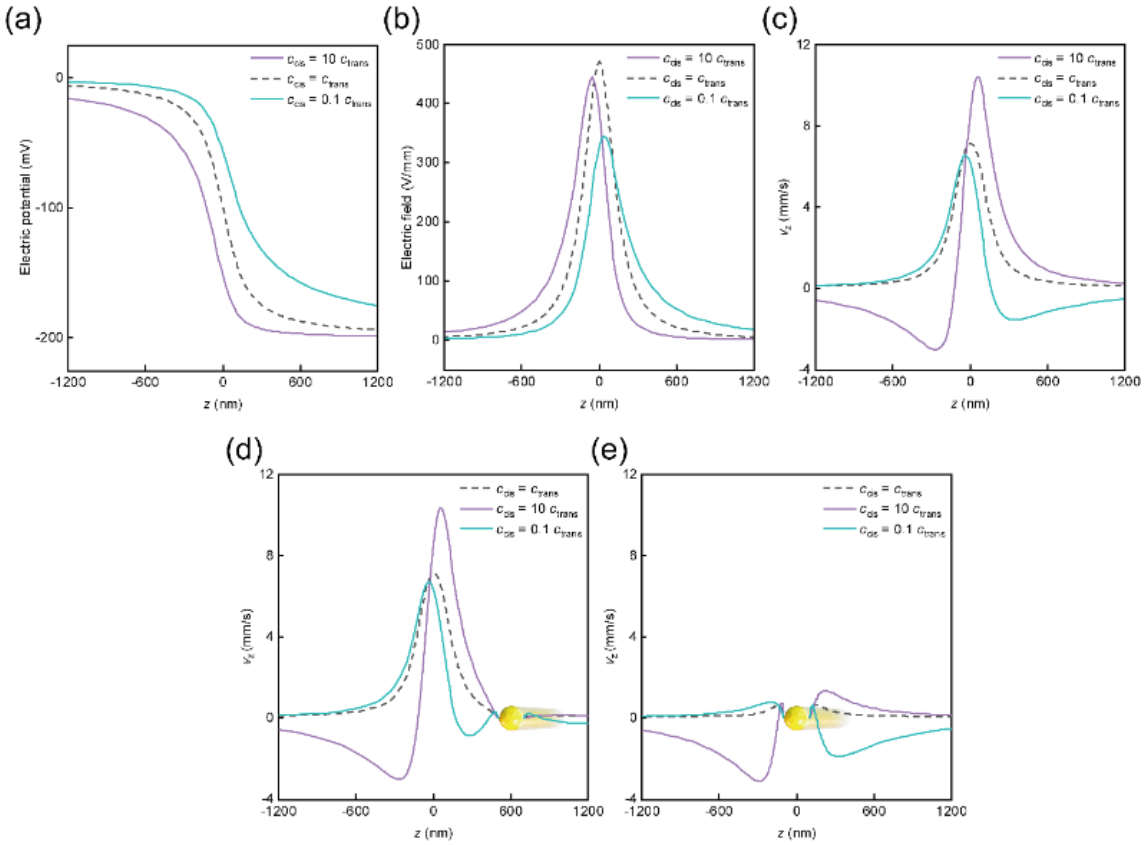

Figure 8.8 Axial result of Simulated EOF and its 2D distribution color mapping

(a-c) Simulated electric potential, electric field, and fluid velocity(v_z) along the pore axis for a 300 nm-diameter and 50 nm-thick nanopore under the different salt gradient conditions. (d, e) v_z distributions when the nanoparticle positioned at z = 600 nm (d) and z = 0 (e). Reproduced and adapted with permission from ref.[227]. Copyright 2021 American Chemical Society.

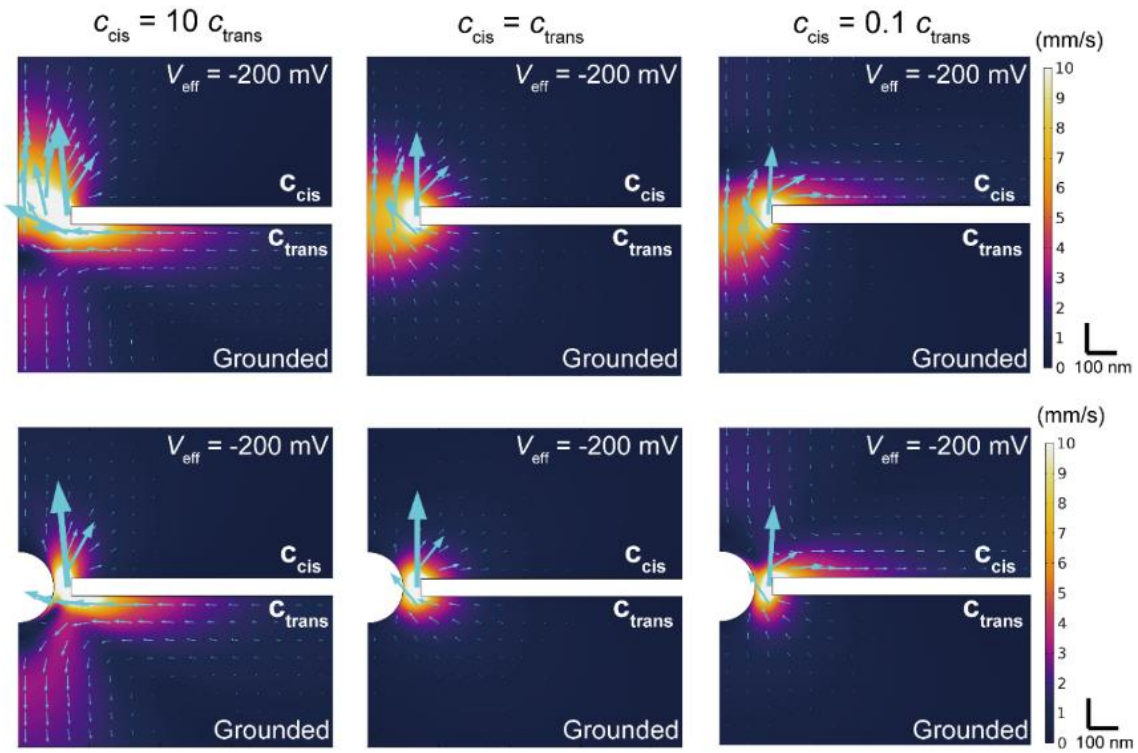

Figure 8.9 Axial result of Simulated EOF and its 2D distribution color mapping

Electroosmotic flow velocity distributions around a 300 nm-sized SiNx nanopore with a 200 nm-sized particle positioned at 5000 nm (out of nanopore, upper part) and 0 (in the middle of the nanopore, lower part). The arrows show the direction of the fluid flow. When there is no salt gradient (c_{cis} = c_{trans}), water flows from trans to cis due to the negative surface charge on the pore wall surface (middle). In contrast, eddies are found in the cis and trans chambers under the positive and negative salt gradients (left and right), respectively. Reproduced and adapted with permission from ref.[227]. Copyright 2021 American Chemical Society.

The finite element analyses provided a physical picture of the capture-to-translocation dynamics in the salt-gradient-biased SiN_x nanopore by revealing the spatial distributions of the electroosmotic flow (Figure 8.10) and the force acting on the nanoparticle (Figure 8.11 and 8.12). Under a uniform salt concentration, both the electrophoretic and electroosmotic flow-derived drag forces (F_{ele} and F_{drag}, respectively) were found to be strongest at the pore center where the electrical field becomes the largest (Figure 8.11a). Once a positive or negative salt gradient was applied, in contrast, the force peak tended to shift toward the *trans* and *cis*, respectively, which is consistent with the change in the solution conductivity associated with the imposed salinity gradients. Here, it can be assumed that the bead was immobilized instead of moving in the electrolyte solution. Although F_{drag} estimated in this way underestimates the actual drag force exerted on the particle in motion, it enables a qualitative assessment of which direction the particles may move under the given cross-membrane electric potential and salinity gradients.

Overall, the calculations predicted an increase in the total force ($=F_{ele} + F_{drag}$) at the nanopore opening under negative salt gradients to draw the negatively charged nanoparticles into the sensing zone consistent with the experimentally observed enhanced capture rates (Figure 8.11b). On the contrary, positive salinity gradients led to a flipping of the force direction at the cis side due to strong electroosmotic flow as expected from the absence of the resistive pulses in the ionic current traces under $c_{cis} > c_{trans}$ (Figure 8.4). These results consistently explain the crucial role of the salinity gradient on the capture-to-translocation dynamics of nanoparticles that allows not only to lower their translocation speed and simultaneously enhance the detection efficiency but also to block their electrophoretic capture via the salinity-gradient-mediated fluid flow (Figure 8.11c).

The salt gradient approach was shown to be effective in slowing down the posttranslocation motions of objects and concurrently increasing the capture rates even in a low-aspect-ratio nanopore of size much larger than the Debye length. This finding may be particularly useful in resistive pulse analyses of small biomolecules and particles such as amyloids[153] and proteins[152] by allowing not only prolonged translocation time for reliable measurements of the ionic current signals but also enabling higher signal intensities; whereas these biomolecules are generally unstable under high ion concentration conditions, which inevitably limits the available ionic conductance to gain a better signal-to-noise ratio, the salt gradient approach can serve to amplify the resistive pulses by allowing applications of an electrolyte buffer of higher ionic strength than the physiological media to impose salt gradients.

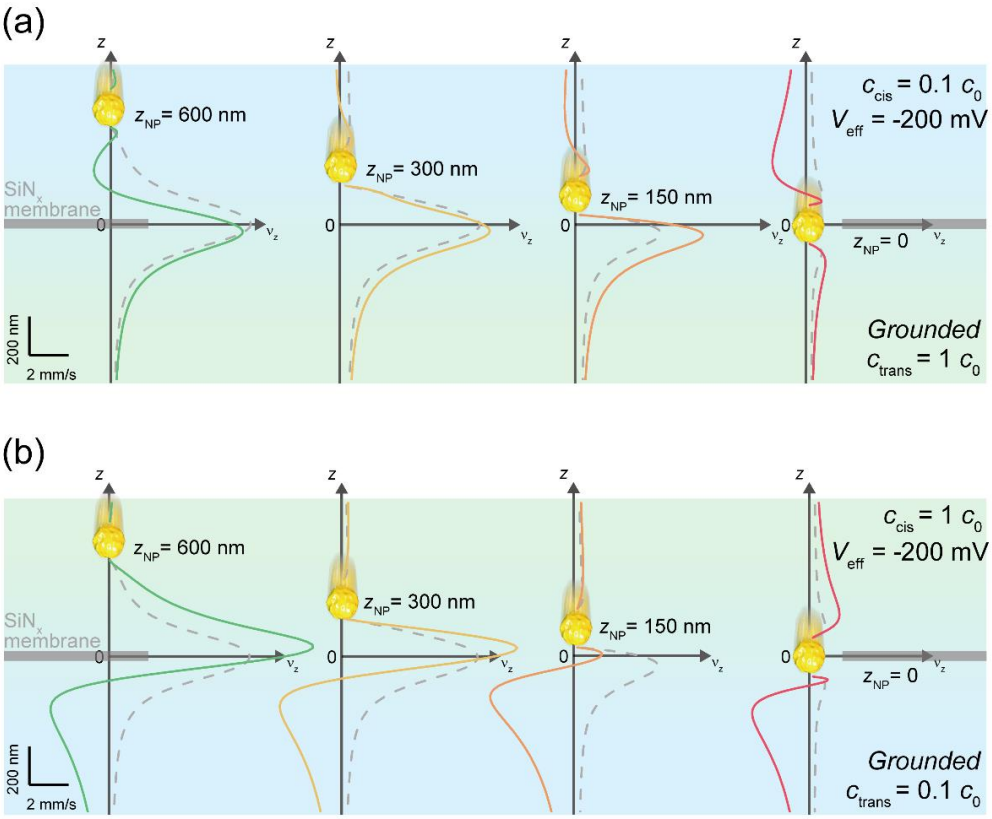

Figure 8.10 Simulated EOF in the particle translocation process

(a, b) Simulated electroosmotic flow velocities (v_z) with a nanoparticle positioned at z_{NP} along the axial direction under the imposed positive (a) and negative (b) salt gradients. Dashed gray lines are v_z without the salt gradient, i.e., c_{cis} = c_{trans} = 1 c_0. Reproduced and adapted with permission from ref.[227]. Copyright 2021 American Chemical Society.

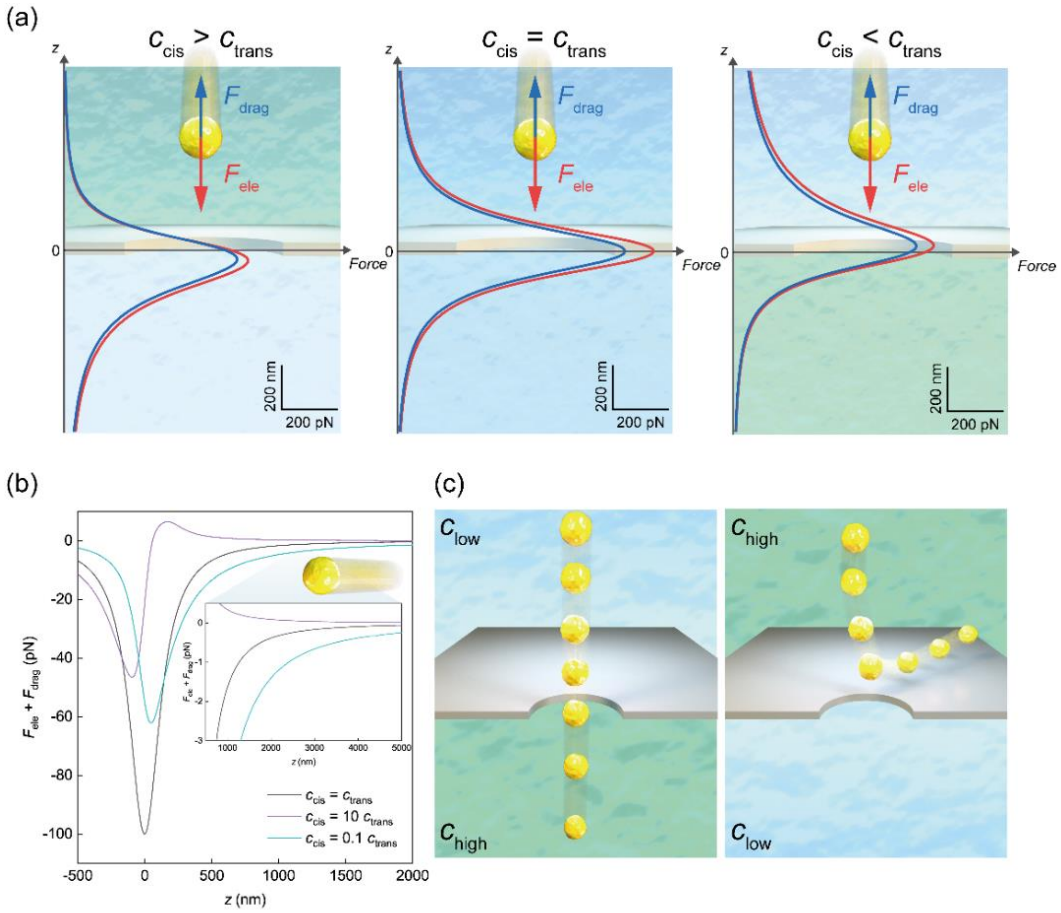

Figure 8.11 Electrokinetic analysis of capture-to-translocation motions of particles

(a) Numerically deduced electrophoretic (F_{ele}; red) and hydrodynamic drag forces (F_{drag}; blue) acting on the 200 nm diameter nanoparticle translocating from z = 800 to −800 nm. While the sign of F_{drag} is opposite to that of F_{ele}, they are shown to be the same for the sake of comparing the strength of the counteracting forces. (b) The total force on the nanoparticle. The inset is a magnified view of the exterior region while the particle tends to enter a nanopore along the z-axis. (c) Schematic illustrations showing a particle translocating through a nanopore under a positive salt gradient (left) or being repelled by the electroosmotic backflow under a negative salt gradient as a result of the balance between the electrophoretic and hydrodynamic drag forces. Reproduced and adapted with permission from ref.[227]. Copyright 2021 American Chemical Society.

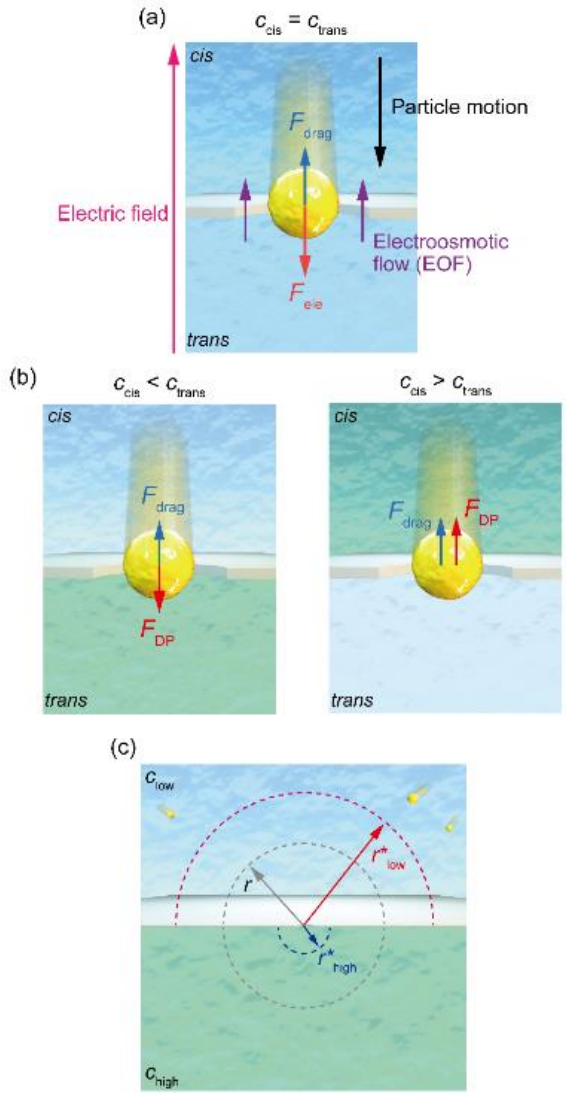

Figure 8.12 Force analysis of particles passing through nanopores

(a) A diagram illustrating the Stokes drag (F_{drag}) and the electrophoretic force (F_{ele}) exerted on a particle with negative surface charge in electrolyte buffer under positive applied voltage at the trans and no salt concentration difference between the cis and trans. (b) When the salt concentration is higher at the cis, the particle feels diffusiophoretic force F_{DP} in addition to the two forces in (a). Furthermore, diffusioosmosis affects the cross-membrane water flow rate that induces F_{drag} different from that in (a). (c) Schematic illustration of capture radius increment and decrement by the applied positive and negative salt gradient. Reproduced and adapted with permission from ref.[227]. Copyright 2021 American Chemical Society.

Chapter 9 Conclusion and perspectives

9.1. Conclusion

In summary, this thesis discusses the ion transport phenomenon under concentration gradients and its application to single nanoparticle detection. In the presence of an ion concentration gradient, the ionic current-voltage characteristic through the nanopores exhibits a diode-like behaviour, and this result is attributed to the combined effects of electrophoresis, electroosmosis, and diffusioosmosis. The mechanism by which ionic current rectification occurs has been studied thoroughly. In addition to the measurements, numerical simulations provide the ion flux, fluidic flow, and electric field distribution near the nanopore. The key achievements of this thesis are listed as follows:

(i) Extended-size nanopores with no notable ion-selectivity demonstrated ICR under applied salt gradients. The combined effects of electro-diffusio-osmosis induce conductance switching, causing the access resistance and pore resistance to change significantly under repeated voltage ramps.

(ii) Deposition of a layer of 10 nm-thick dielectric metal oxides on nanopore membranes altered the ICR properties, demonstrating that modulating the surface potentials can change electro-diffusio-osmosis-driven transport.

(iii) The asymmetric concentration condition was applied to study the complex dynamics of nanoparticle capture and translocation through nanopores. A detailed discussion was provided for both the pre- and post-entry processes of the nanoparticles.

9.2. Outlook

Although nanopore technologies have been developed and studied for decades,[234–236] more and more extended applications are reported recently. Accordingly, design, fabrication methods, and materials must meet different requirements based on the applied scenario. Combining various advanced techniques (*e.g.*, optical[237], FET[238], and electrochemistry[239]) is also a clear vision for the future. In the following discussion, the application including sensors, artificial ion channels, and osmotic energy generators using solid-state nanopores will be discussed.

Bio-nanopore-based technology has achieved remarkable success in DNA sequencing. Scientists are now attempting to apply this to proteomics.[240,241] However, the current problem is how to pass a weakly charged or charge-free substance through the nanopore and collect information from the ionic current signal. As compared to electrophoresis, electroosmosis is more likely to allow a substance to pass through nanopores without charge. As described in the present research, electroosmotic flow is dependent on surface properties. Studying the material engineering of membrane surfaces may prove useful for controlling electroosmosis and for customizing the translocation dynamics of uncharged analytes.

Solid-state nanopores are also used in the research of artificial ion channels. Nanofluidic channels could be used for controllable ion transport in diodes, transistors, and memristors. For example, ionic circuits can create more complex and versatile nanofluidic systems for realizing device functions such as long-term memory and synapse dynamics in nanofluidics.[242] The result of NDR and resistive switching properties was observed in Chapter 4. Nanopores are shown to be feasible as memristor-like nanofluidic devices under asymmetric

solution conditions. The usage of room temperature ionic liquids has been reported.[23,62] It is foreseeable that there will be more possible combinations of membrane materials and electrolyte choices in the future, which will lead to new insights on advanced nanofluidic memristors.

In this paper, concentration gradients are used to provide the diffusioosmosis environment in the nanopore experiments. Osmotic energy harvesting with nanoporous materials is a very promising way to solve the energy issue.[73] A nanopore-based osmotic power generator is primarily based on ion selectivity.[66] However, increasing the pore size to obtain higher ion flux results in a weakening of ion selectivity. The efficiency of output power is expected to decrease. A possible role of electroosmosis on transmembrane salt concentration distributions under diffusion potential differences has been predicted in this study. The role of nanopores in energy harvesters will need to be addressed in the future to enable better designs. The influence of EOF on the osmotic power generation also deserves exploration.

Bibliography

(1) Kasianowicz, J. J.; Brandin, E.; Branton, D.; Deamer, D. W. Characterization of Individual Polynucleotide Molecules Using a Membrane Channel. *Proc. Natl. Acad. Sci.* **1996**, *93* (24), 13770–13773. https://doi.org/10.1073/pnas.93.24.13770.

(2) Meller, A.; Nivon, L.; Branton, D. Voltage-Driven DNA Translocations through a Nanopore. *Phys. Rev. Lett.* **2001**, *86* (15), 3435–3438. https://doi.org/10.1103/PhysRevLett.86.3435.

(3) Coulter, W. H. Means for Counting Particles Suspended in a Fluid. US Patent, 2656508. US2656508A, 1953.

(4) Hall, J. E. Access Resistance of a Small Circular Pore. *J. Gen. Physiol.* **1975**, *66* (4), 531–532. https://doi.org/10.1085/jgp.66.4.531.

(5) Wanunu, M.; Morrison, W.; Rabin, Y.; Grosberg, A. Y.; Meller, A. Electrostatic Focusing of Unlabelled DNA into Nanoscale Pores Using a Salt Gradient. *Nat. Nanotechnol.* **2010**, *5* (2), 160–165. https://doi.org/10.1038/nnano.2009.379.

(6) Li, J.; Stein, D.; McMullan, C.; Branton, D.; Aziz, M. J.; Golovchenko, J. A. Ion-Beam Sculpting at Nanometre Length Scales. *Nature* **2001**, *412* (6843), 166–169. https://doi.org/10.1038/35084037.

(7) Storm, A. J.; Chen, J. H.; Ling, X. S.; Zandbergen, H. W.; Dekker, C. Fabrication of Solid-State Nanopores with Single-Nanometre Precision. *Nat. Mater.* **2003**, *2* (8), 537–540. https://doi.org/10.1038/nmat941.

(8) Vlassiouk, I.; Apel, P. Y.; Dmitriev, S. N.; Healy, K.; Siwy, Z. S. Versatile Ultrathin Nanoporous Silicon Nitride Membranes. *Proc. Natl. Acad. Sci. U. S. A.* **2009**, *106* (50), 21039–21044. https://doi.org/10.1073/pnas.0911450106.

(9) Kwok, H.; Briggs, K.; Tabard-Cossa, V. Nanopore Fabrication by Controlled Dielectric Breakdown. *PLoS One* **2014**, *9* (3). https://doi.org/10.1371/journal.pone.0092880.

(10) Taniguchi, M.; Tsutsui, M.; Yokota, K.; Kawai, T. Fabrication of the Gating Nanopore Device. *Appl. Phys. Lett.* **2009**, *95* (12). https://doi.org/10.1063/1.3236769.

(11) Tsutsui, M.; Ryuzaki, S.; Yokota, K.; He, Y.; Washio, T.; Tamada, K.; Kawai, T. Field Effect Control of Translocation Dynamics in Surround-Gate Nanopores. *Commun. Mater.* **2021**, *2* (1). https://doi.org/10.1038/s43246-021-00132-3.

(12) Kalman, E. B.; Vlassiouk, I.; Siwy, Z. S. Nanofluidic Bipolar Transistors. *Adv. Mater.* **2008**, *20* (2), 293–297. https://doi.org/10.1002/adma.200701867.

(13) Guan, W.; Fan, R.; Reed, M. A. Field-Effect Reconfigurable Nanofluidic Ionic Diodes. *Nat. Commun.* **2011**, *2* (1), 2–9. https://doi.org/10.1038/ncomms1514.

(14) Zhang, S.; Yin, X.; Li, M.; Zhang, X.; Zhang, X.; Qin, X.; Zhu, Z.; Yang, S.; Shao, Y. Ionic Current Behaviors of Dual Nano- and Micropipettes. *Anal. Chem.* **2018**, *90* (14), 8592–8599. https://doi.org/10.1021/acs.analchem.8b01765.

(15) Zhu, Z.; Wang, D.; Tian, Y.; Jiang, L. Ion/Molecule Transportation in Nanopores and Nanochannels: From Critical Principles to Diverse Functions. *J. Am. Chem. Soc.* **2019**, *141* (22), 8658–8669. https://doi.org/10.1021/jacs.9b00086.

(16) Gao, J.; Guo, W.; Feng, D.; Wang, H.; Zhao, D.; Jiang, L. High-Performance Ionic Diode Membrane for Salinity Gradient Power Generation. *J. Am. Chem. Soc.* **2014**, *136* (35), 12265–12272. https://doi.org/10.1021/ja503692z.

(17) Feng, J.; Graf, M.; Liu, K.; Ovchinnikov, D.; Dumcenco, D.; Heiranian, M.; Nandigana, V.; Aluru, N.

R.; Kis, A.; Radenovic, A. Single-Layer MoS2 Nanopores as Nanopower Generators. *Nature* **2016**, *536* (7615), 197–200. https://doi.org/10.1038/nature18593.

(18) He, Y.; Huang, Z.; Chen, B.; Tsutsui, M.; Shui Miao, X.; Taniguchi, M. Electrokinetic Analysis of Energy Harvest from Natural Salt Gradients in Nanochannels. *Sci. Rep.* **2017**, *7* (1), 1–15. https://doi.org/10.1038/s41598-017-13336-w.

(19) Hsu, J. P.; Su, T. C.; Peng, P. H.; Hsu, S. C.; Zheng, M. J.; Yeh, L. H. Unraveling the Anomalous Surface-Charge-Dependent Osmotic Power Using a Single Funnel-Shaped Nanochannel. *ACS Nano* **2019**, *13* (11), 13374–13381. https://doi.org/10.1021/acsnano.9b06774.

(20) Cantley, L.; Swett, J. L.; Lloyd, D.; Cullen, D. A.; Zhou, K.; Bedworth, P. V.; Heise, S.; Rondinone, A. J.; Xu, Z.; Sinton, S.; Bunch, J. S. Voltage Gated Inter-Cation Selective Ion Channels from Graphene Nanopores. *Nanoscale* **2019**, *11* (20), 9856–9861. https://doi.org/10.1039/c8nr10360g.

(21) Siwy, Z. S. Ion-Current Rectification in Nanopores and Nanotubes with Broken Symmetry. *Adv. Funct. Mater.* **2006**, *16* (6), 735–746. https://doi.org/10.1002/adfm.200500471.

(22) Lin, C. Y.; Wong, P. H.; Wang, P. H.; Siwy, Z. S.; Yeh, L. H. Electrodiffusioosmosis-Induced Negative Differential Resistance in PH-Regulated Mesopores Containing Purely Monovalent Solutions. *ACS Appl. Mater. Interfaces* **2020**, *12* (2), 3198–3204. https://doi.org/10.1021/acsami.9b18524.

(23) Zhang, P.; Xia, M.; Zhuge, F.; Zhou, Y.; Wang, Z.; Dong, B.; Fu, Y.; Yang, K.; Li, Y.; He, Y.; Scheicher, R. H.; Miao, X. S. Nanochannel-Based Transport in an Interfacial Memristor Can Emulate the Analog Weight Modulation of Synapses. *Nano Lett.* **2019**, *19* (7), 4279–4286. https://doi.org/10.1021/acs.nanolett.9b00525.

(24) Siwy, Z.; Kosińska, I. D.; Fuliński, A.; Martin, C. R.; Kosinska, I. D.; Fulinski, A.; Martin, C. R. Asymmetric Diffusion through Synthetic Nanopores. *Phys. Rev. Lett.* **2005**, *94* (4), 1–4. https://doi.org/10.1103/PhysRevLett.94.048102.

(25) Feng, J.; Liu, K.; Graf, M.; Dumcenco, D.; Kis, A.; Di Ventra, M.; Radenovic, A. Observation of Ionic Coulomb Blockade in Nanopores. *Nat. Mater.* **2016**, *15* (8), 850–855. https://doi.org/10.1038/nmat4607.

(26) Ai, Y.; Zhang, M.; Joo, S. W.; Cheney, M. A.; Qian, S. Effects of Electroosmotic Flow on Ionic Current Rectification in Conical Nanopores. *J. Phys. Chem. C* **2010**, *114* (9), 3883–3890. https://doi.org/10.1021/jp911773m.

(27) Firnkes, M.; Pedone, D.; Knezevic, J.; Döblinger, M.; Rant, U. Electrically Facilitated Translocations of Proteins through Silicon Nitride Nanopores: Conjoint and Competitive Action of Diffusion, Electrophoresis, and Electroosmosis. *Nano Lett.* **2010**, *10* (6), 2162–2167. https://doi.org/10.1021/nl100861c.

(28) Hsu, J. P.; Yang, S. T.; Lin, C. Y.; Tseng, S. Ionic Current Rectification in a Conical Nanopore: Influences of Electroosmotic Flow and Type of Salt. *J. Phys. Chem. C* **2017**, *121* (8), 4576–4582. https://doi.org/10.1021/acs.jpcc.6b09907.

(29) Qiu, Y.; Siwy, Z. S.; Wanunu, M. Abnormal Ionic-Current Rectification Caused by Reversed Electroosmotic Flow under Viscosity Gradients across Thin Nanopores. *Anal. Chem.* **2019**, *91* (1), 996–1004. https://doi.org/10.1021/acs.analchem.8b04225.

(30) Leong, I. W.; Tsutsui, M.; Murayama, S.; He, Y.; Taniguchi, M. Electroosmosis-Driven Nanofluidic Diodes. *J. Phys. Chem. B* **2020**, *124* (32), 7086–7092. https://doi.org/10.1021/acs.jpcb.0c04677.

(31) He, Y.; Tsutsui, M.; Scheicher, R. H.; Fan, C.; Taniguchi, M.; Kawai, T. Mechanism of How Salt-Gradient-Induced Charges Affect the Translocation of

DNA Molecules through a Nanopore. *Biophys. J.* **2013**, *105* (3), 776–782. https://doi.org/10.1016/j.bpj.2013.05.065.

(32) Hsu, W. L.; Hwang, J.; Daiguji, H. Theory of Transport-Induced-Charge Electroosmotic Pumping toward Alternating Current Resistive Pulse Sensing. *ACS Sensors* **2018**, *3* (11), 2320–2326. https://doi.org/10.1021/acssensors.8b00635.

(33) Yeh, L. H.; Chen, F.; Chiou, Y. T.; Su, Y. S. Anomalous PH-Dependent Nanofluidic Salinity Gradient Power. *Small* **2017**, *13* (48), 6–11. https://doi.org/10.1002/smll.201702691.

(34) Cao, L.; Wen, Q.; Feng, Y.; Ji, D.; Li, H.; Li, N.; Jiang, L.; Guo, W. On the Origin of Ion Selectivity in Ultrathin Nanopores: Insights for Membrane-Scale Osmotic Energy Conversion. *Adv. Funct. Mater.* **2018**, *28* (39), 1–8. https://doi.org/10.1002/adfm.201804189.

(35) Macha, M.; Marion, S.; Nandigana, V. V. R.; Radenovic, A. 2D Materials as an Emerging Platform for Nanopore-Based Power Generation. *Nat. Rev. Mater.* **2019**, *4* (9), 588–605. https://doi.org/10.1038/s41578-019-0126-z.

(36) Xiao, K.; Jiang, L.; Antonietti, M. Ion Transport in Nanofluidic Devices for Energy Harvesting. *Joule* **2019**, *3* (10), 2364–2380. https://doi.org/10.1016/j.joule.2019.09.005.

(37) Siwy, Z. S.; Howorka, S. Engineered Voltage-Responsive Nanopores. *Chem. Soc. Rev.* **2010**, *39* (3), 1115–1132. https://doi.org/10.1039/b909105j.

(38) Pérez-Mitta, G.; Albesa, A. G.; Trautmann, C.; Toimil-Molares, M. E.; Azzaroni, O. Bioinspired Integrated Nanosystems Based on Solid-State Nanopores: "Iontronic" Transduction of Biological, Chemical and Physical Stimuli. *Chem. Sci.* **2017**, *8* (2), 890–913. https://doi.org/10.1039/c6sc04255d.

(39) Wang, Y.; Chen, H.; Jiang, J.; Zhai, J.; You, T. Ion Transport Behaviors of Nanofluidic Diode Bichannel Systems in the Independent and Synergistic Cascade Mode. *ACS Appl. Mater. Interfaces* **2019**, *11* (29), 26467–26473. https://doi.org/10.1021/acsami.9b07598.

(40) Ali, M.; Ramirez, P.; Nasir, S.; Cervera, J.; Mafe, S.; Ensinger, W. Ionic Circuitry with Nanofluidic Diodes. *Soft Matter* **2019**, *15* (47), 9682–9689. https://doi.org/10.1039/c9sm01654f.

(41) Kim, M. J.; Wanunu, M.; Bell, D. C.; Meller, A. Rapid Fabrication of Uniformly Sized Nanopores and Nanopore Arrays for Parallel DNA Analysis. *Adv. Mater.* **2006**, *18* (23), 3149–3153. https://doi.org/10.1002/adma.200601191.

(42) Dekker, C. Solid-State Nanopores. *Nat. Nanotechnol.* **2007**, *2* (4), 209–215. https://doi.org/10.1038/nnano.2007.27.

(43) Lan, W. J.; Edwards, M. A.; Luo, L.; Perera, R. T.; Wu, X.; Martin, C. R.; White, H. S. Voltage-Rectified Current and Fluid Flow in Conical Nanopores. *Acc. Chem. Res.* **2016**, *49* (11), 2605–2613. https://doi.org/10.1021/acs.accounts.6b00395.

(44) Yan, R.; Liang, W.; Fan, R.; Yang, P. Nanofluidic Diodes Based on Nanotube Heterojunctions. *Nano Lett.* **2009**, *9* (11), 3820–3825. https://doi.org/10.1021/nl9020123.

(45) Zhang, Z.; Wen, L.; Jiang, L. Bioinspired Smart Asymmetric Nanochannel Membranes. *Chem. Soc. Rev.* **2018**, *47* (2), 322–356. https://doi.org/10.1039/c7cs00688h.

(46) Pérez-Mitta, G.; Marmisolle, W. A.; Burr, L.; Toimil-Molares, M. E.; Trautmann, C.; Azzaroni, O. Proton-Gated Rectification Regimes in Nanofluidic Diodes Switched by Chemical Effectors. *Small* **2018**, *14* (18), 1–8. https://doi.org/10.1002/smll.201703144.

(47) Laucirica, G.; Marmisollé, W. A.; Toimil-Molares, M. E.; Trautmann, C.; Azzaroni, O. Redox-

Driven Reversible Gating of Solid-State Nanochannels. *ACS Appl. Mater. Interfaces* **2019**, *11* (33), 30001–30009. https://doi.org/10.1021/acsami.9b05961.

(48) Rabinowitz, J.; Edwards, M. A.; Whittier, E.; Jayant, K.; Shepard, K. L. Nanoscale Fluid Vortices and Nonlinear Electroosmotic Flow Drive Ion Current Rectification in the Presence of Concentration Gradients. *J. Phys. Chem. A* **2019**, *123* (38), 8285–8293. https://doi.org/10.1021/acs.jpca.9b04075.

(49) Lan, W. J.; Holden, D. A.; White, H. S. Pressure-Dependent Ion Current Rectification in Conical-Shaped Glass Nanopores. *J. Am. Chem. Soc.* **2011**, *133* (34), 13300–13303. https://doi.org/10.1021/ja205773a.

(50) Kowalczyk, S. W.; Wells, D. B.; Aksimentiev, A.; Dekker, C. Slowing down DNA Translocation through a Nanopore in Lithium Chloride. *Nano Lett.* **2012**, *12* (2), 1038–1044. https://doi.org/10.1021/nl204273h.

(51) Luo, L.; Holden, D. A.; Lan, W. J.; White, H. S. Tunable Negative Differential Electrolyte Resistance in a Conical Nanopore in Glass. *ACS Nano* **2012**, *6* (7), 6507–6514. https://doi.org/10.1021/nn3023409.

(52) Lu, B.; Hoogerheide, D. P.; Zhao, Q.; Zhang, H.; Tang, Z.; Yu, D.; Golovchenko, J. A. Pressure-Controlled Motion of Single Polymers through Solid-State Nanopores. *Nano Lett.* **2013**, *13* (7), 3048–3052. https://doi.org/10.1021/nl402052v.

(53) Zeng, Z.; Yeh, L. H.; Zhang, M.; Qian, S. Ion Transport and Selectivity in Biomimetic Nanopores with PH-Tunable Zwitterionic Polyelectrolyte Brushes. *Nanoscale* **2015**, *7* (40), 17020–17029. https://doi.org/10.1039/c5nr05828g.

(54) Garaj, S.; Hubbard, W.; Reina, A.; Kong, J.; Branton, D.; Golovchenko, J. A. Graphene as a Subnanometre Trans-Electrode Membrane. *Nature* **2010**, *467* (7312), 190–193. https://doi.org/10.1038/nature09379.

(55) Kowalczyk, S. W.; Grosberg, A. Y.; Rabin, Y.; Dekker, C. Modeling the Conductance and DNA Blockade of Solid-State Nanopores. *Nanotechnology* **2011**, *22* (31), 315101. https://doi.org/10.1088/0957-4484/22/31/315101.

(56) Bu, Y.; Ahmed, Z.; Yobas, L. A Nanofluidic Memristor Based on Ion Concentration Polarization. *Analyst* **2019**, *144* (24), 7168–7172. https://doi.org/10.1039/c9an01561b.

(57) Faucher, S.; Aluru, N.; Bazant, M. Z.; Blankschtein, D.; Brozena, A. H.; Cumings, J.; Pedro De Souza, J.; Elimelech, M.; Epsztein, R.; Fourkas, J. T.; Rajan, A. G.; Kulik, H. J.; Levy, A.; Majumdar, A.; Martin, C.; McEldrew, M.; Misra, R. P.; Noy, A.; Pham, T. A.; Reed, M.; Schwegler, E.; Siwy, Z.; Wang, Y.; Strano, M. Critical Knowledge Gaps in Mass Transport through Single-Digit Nanopores: A Review and Perspective. *J. Phys. Chem. C* **2019**, *123* (35), 21309–21326. https://doi.org/10.1021/acs.jpcc.9b02178.

(58) Leong, I. W.; Tsutsui, M.; Murayama, S.; Hayashida, T.; He, Y.; Taniguchi, M. Quasi-Stable Salt Gradient and Resistive Switching in Solid-State Nanopores. *ACS Appl. Mater. Interfaces* **2020**, *12* (46), 52175–52181. https://doi.org/10.1021/acsami.0c15538.

(59) Tsutsui, M.; He, Y.; Yokota, K.; Arima, A.; Hongo, S.; Taniguchi, M.; Washio, T.; Kawai, T. Particle Trajectory-Dependent Ionic Current Blockade in Low-Aspect-Ratio Pores. *ACS Nano* **2016**, *10* (1), 803–809. https://doi.org/10.1021/acsnano.5b05906.

(60) Tsutsui, M.; Yokota, K.; Nakada, T.; Arima, A.; Tonomura, W.; Taniguchi, M.; Washio, T.; Kawai, T. Particle Capture in Solid-State Multipores. *ACS Sensors* **2018**, *3* (12), 2693–2701. https://doi.org/10.1021/acssensors.8b01214.

(61) Sun, G.; Slouka, Z.; Chang, H. C. Fluidic-Based Ion Memristors and Ionic Latches. *Small* **2015**, *11* (39), 5206–5213. https://doi.org/10.1002/smll.201501229.

(62) Sheng, Q.; Xie, Y.; Li, J.; Wang, X.; Xue, J.

Transporting an Ionic-Liquid/Water Mixture in a Conical Nanochannel: A Nanofluidic Memristor. *Chem. Commun.* **2017**, *53* (45), 6125–6127. https://doi.org/10.1039/c7cc01047h.

(63) Sangwan, V. K.; Hersam, M. C. Neuromorphic Nanoelectronic Materials. *Nat. Nanotechnol.* **2020**, *15* (7), 517–528. https://doi.org/10.1038/s41565-020-0647-z.

(64) He, Y.; Tsutsui, M.; Zhou, Y.; Miao, X. S. Solid-State Nanopore Systems: From Materials to Applications. *NPG Asia Mater.* **2021**, *13* (1), 1–26. https://doi.org/10.1038/s41427-021-00313-z.

(65) Xue, L.; Yamazaki, H.; Ren, R.; Wanunu, M.; Ivanov, A. P.; Edel, J. B. Solid-State Nanopore Sensors. *Nat. Rev. Mater.* **2020**, *5* (12), 931–951. https://doi.org/10.1038/s41578-020-0229-6.

(66) Zhang, Z.; Wen, L.; Jiang, L. Nanofluidics for Osmotic Energy Conversion. *Nat. Rev. Mater.* **2021**, *6* (7), 622–639. https://doi.org/10.1038/s41578-021-00300-4.

(67) Werber, J. R.; Osuji, C. O.; Elimelech, M. Materials for Next-Generation Desalination and Water Purification Membranes. *Nat. Rev. Mater.* **2016**, *1* (5), 16018. https://doi.org/10.1038/natrevmats.2016.18.

(68) Liu, Y.; Zhang, Z.; Wang, S. Carbon Nanopore-Tailored Reverse Osmotic Water Desalination. *ACS ES&T Water* **2021**, *1* (1), 34–47. https://doi.org/10.1021/acsestwater.0c00015.

(69) Esfandiar, A.; Radha, B.; Wang, F. C.; Yang, Q.; Hu, S.; Garaj, S.; Nair, R. R.; Geim, A. K.; Gopinadhan, K. Size Effect in Ion Transport through Angstrom-Scale Slits. *Science (80-.).* **2017**, *358* (6362), 511–513. https://doi.org/10.1126/science.aan5275.

(70) Mouterde, T.; Keerthi, A.; Poggioli, A. R.; Dar, S. A.; Siria, A.; Geim, A. K.; Bocquet, L.; Radha, B. Molecular Streaming and Its Voltage Control in Ångström-Scale Channels. *Nature* **2019**, *567* (7746), 87–90. https://doi.org/10.1038/s41586-019-0961-5.

(71) Zhang, Z.; Yang, S.; Zhang, P.; Zhang, J.; Chen, G.; Feng, X. Mechanically Strong MXene/Kevlar Nanofiber Composite Membranes as High-Performance Nanofluidic Osmotic Power Generators. *Nat. Commun.* **2019**, *10* (1), 1–9. https://doi.org/10.1038/s41467-019-10885-8.

(72) Ding, L.; Li, L.; Liu, Y.; Wu, Y.; Lu, Z.; Deng, J.; Wei, Y.; Caro, J.; Wang, H. Effective Ion Sieving with Ti3C2Tx MXene Membranes for Production of Drinking Water from Seawater. *Nat. Sustain.* **2020**, *3* (4), 296–302. https://doi.org/10.1038/s41893-020-0474-0.

(73) Liu, Y. C.; Yeh, L. H.; Zheng, M. J.; Wu, K. C. W. Highly Selective and High-Performance Osmotic Power Generators in Subnanochannel Membranes Enabled by Metal-Organic Frameworks. *Sci. Adv.* **2021**, *7* (10), eabe9924. https://doi.org/10.1126/sciadv.abe9924.

(74) Cao, Z.; Liu, V.; Farimani, A. B. Water Desalination with Two-Dimensional Metal-Organic Framework Membranes. *Nano Lett.* **2019**, *19* (12), 8638–8643. https://doi.org/10.1021/acs.nanolett.9b03225.

(75) Lucas, R. A.; Lin, C. Y.; Baker, L. A.; Siwy, Z. S. Ionic Amplifying Circuits Inspired by Electronics and Biology. *Nat. Commun.* **2020**, *11* (1), 1568. https://doi.org/10.1038/s41467-020-15398-3.

(76) Queralt-Martín, M.; Perini, D. A.; Alcaraz, A. Specific Adsorption of Trivalent Cations in Biological Nanopores Determines Conductance Dynamics and Reverses Ionic Selectivity. *Phys. Chem. Chem. Phys.* **2021**, *23* (2), 1352–1362. https://doi.org/10.1039/d0cp04486e.

(77) Vlassiouk, I.; Smirnov, S.; Siwyt, Z. Ionic Selectivity of Single Nanochannels. *Nano Lett.* **2008**, *8* (7), 1978–1985. https://doi.org/10.1021/nl800949k.

(78) Vlassiouk, I.; Siwy, Z. S. Nanofluidic Diode. *Nano Lett.* **2007**, *7* (3), 552–556. https://doi.org/10.1021/nl062924b.

(79) Huang, X.; Kong, X.-Y.; Wen, L.; Jiang, L. Bioinspired Ionic Diodes: From Unipolar to Bipolar. *Adv. Funct. Mater.* **2018**, *28* (49), 1801079. https://doi.org/10.1002/adfm.201801079.

(80) Novotný, T.; Gaš, B. Mathematical Model of Electromigration Allowing the Deviation from Electroneutrality. *Electrophoresis* **2021**, *42* (7–8), 881–889. https://doi.org/10.1002/elps.202000207.

(81) Lin, K.; Lin, C. Y.; Polster, J. W.; Chen, Y.; Siwy, Z. S. Charge Inversion and Calcium Gating in Mixtures of Ions in Nanopores. *J. Am. Chem. Soc.* **2020**, *142* (6), 2925–2934. https://doi.org/10.1021/jacs.9b11537.

(82) Fuest, M.; Rangharajan, K. K.; Boone, C.; Conlisk, A. T.; Prakash, S. Cation Dependent Surface Charge Regulation in Gated Nanofluidic Devices. *Anal. Chem.* **2017**, *89* (3), 1593–1601. https://doi.org/10.1021/acs.analchem.6b03653.

(83) Tshwenya, L.; Marken, F.; Mathwig, K.; Arotiba, O. A. Switching Anionic and Cationic Semipermeability in Partially Hydrolyzed Polyacrylonitrile: A PH-Tunable Ionic Rectifier. *ACS Appl. Mater. Interfaces* **2020**, *12* (2), 3214–3224. https://doi.org/10.1021/acsami.9b18583.

(84) Wu, Y.; Yao, Y.; Cheong, S.; Tilley, R. D.; Gooding, J. J. Selectively Detecting Attomolar Concentrations of Proteins Using Gold Lined Nanopores in a Nanopore Blockade Sensor. *Chem. Sci.* **2020**, *11* (46), 12570–12579. https://doi.org/10.1039/d0sc04552g.

(85) Zhang, D.; Wang, Q.; Fan, X.; Zhang, M.; Zhai, J.; Jiang, L. An Effective Dark–Vis–UV Ternary Biomimetic Switching Based on N3/Spiropyran-Modified Nanochannels. *Adv. Mater.* **2018**, *30* (46), 1–8. https://doi.org/10.1002/adma.201804862.

(86) Zhang, Q.; Cao, P. S.; Cheng, Y.; Yang, S. S.; Yin, Y. D.; Lv, T. Y.; Gu, Z. Y. Nonlinear Ion Transport through Ultrathin Metal–Organic Framework Nanosheet. *Adv. Funct. Mater.* **2020**, *30* (42), 1–8. https://doi.org/10.1002/adfm.202004854.

(87) Pérez-Mitta, G.; Marmisollé, W. A.; Trautmann, C.; Toimil-Molares, M. E.; Azzaroni, O. An All-Plastic Field-Effect Nanofluidic Diode Gated by a Conducting Polymer Layer. *Adv. Mater.* **2017**, *29* (28), 1–6. https://doi.org/10.1002/adma.201700972.

(88) Li, X.; Zhang, H.; Yu, H.; Xia, J.; Zhu, Y. B.; Wu, H. A.; Hou, J.; Lu, J.; Ou, R.; Easton, C. D.; Selomulya, C.; Hill, M. R.; Jiang, L.; Wang, H. Unidirectional and Selective Proton Transport in Artificial Heterostructured Nanochannels with Nano-to-Subnano Confined Water Clusters. *Adv. Mater.* **2020**, *32* (24), 1–7. https://doi.org/10.1002/adma.202001777.

(89) Sui, X.; Zhang, Z.; Li, C.; Gao, L.; Zhao, Y.; Yang, L.; Wen, L.; Jiang, L. Engineered Nanochannel Membranes with Diode-like Behavior for Energy Conversion over a Wide PH Range. *ACS Appl. Mater. Interfaces* **2019**, *11* (27), 23815–23821. https://doi.org/10.1021/acsami.8b02578.

(90) Youn, Y.; Han, S. Investigation of Field Effects in a Solid-State Nanopore Transistor. *Phys. Chem. Chem. Phys.* **2015**, *17* (41), 27806–27811. https://doi.org/10.1039/c5cp03125g.

(91) Daiguji, H.; Oka, Y.; Shirono, K. Nanofluidic Diode and Bipolar Transistor. *Nano Lett.* **2005**, *5* (11), 2274–2280. https://doi.org/10.1021/nl051646y.

(92) Vlassiouk, I.; Smimov, S.; Siwy, Z. Nanofluidic Ionic Diodes. Comparison of Analytical and Numerical Solutions. *ACS Nano* **2008**, *2* (8), 1589–1602. https://doi.org/10.1021/nn800306u.

(93) Abu-Rjal, R.; Green, Y. Bipolar Nanochannels: A Systematic Approach to Asymmetric Problems. *ACS Appl. Mater. Interfaces* **2021**, *13* (23), 27622–27634. https://doi.org/10.1021/acsami.1c05643.

(94) Hou, X.; Liu, Y.; Dong, H.; Yang, F.; Li, N.;

Jiang, L. A PH-Cating Ionic Transport Nanodevice: Asymmetric Chemical Modification of Single Nanochannels. *Adv. Mater.* **2010**, *22* (22), 2440–2443. https://doi.org/10.1002/adma.200904268.

(95) Zhang, Q.; Liu, Q.; Kang, J.; Huang, Q.; Liu, Z.; Diao, X.; Zhai, J. Robust Sandwich-Structured Nanofluidic Diodes Modulating Ionic Transport for an Enhanced Electrochromic Performance. *Adv. Sci.* **2018**, *5* (9), 1800163. https://doi.org/10.1002/advs.201800163.

(96) Tybrandt, K.; Larsson, K. C.; Richter-Dahlfors, A.; Berggren, M. Ion Bipolar Junction Transistors. *Proc. Natl. Acad. Sci. U. S. A.* **2010**, *107* (22), 9929–9932. https://doi.org/10.1073/pnas.0913911107.

(97) Ma, Y.; Guo, J.; Jia, L.; Xie, Y. Entrance Effects Induced Rectified Ionic Transport in a Nanopore/Channel. *ACS Sensors* **2018**, *3* (1), 167–173. https://doi.org/10.1021/acssensors.7b00793.

(98) Tagliazucchi, M.; Rabin, Y.; Szleifer, I. Transport Rectification in Nanopores with Outer Membranes Modified with Surface Charges and Polyelectrolytes. *ACS Nano* **2013**, *7* (10), 9085–9097. https://doi.org/10.1021/nn403686s.

(99) Lin, C. Y.; Hsu, J. P.; Yeh, L. H. Rectification of Ionic Current in Nanopores Functionalized with Bipolar Polyelectrolyte Brushes. *Sensors Actuators, B Chem.* **2018**, *258*, 1223–1229. https://doi.org/10.1016/j.snb.2017.11.172.

(100) Khatibi, M.; Sadeghi, A.; Ashrafizadeh, S. N. Tripling the Reverse Electrodialysis Power Generation in Conical Nanochannels Utilizing Soft Surfaces. *Phys. Chem. Chem. Phys.* **2021**, *23* (3), 2211–2221. https://doi.org/10.1039/d0cp05974a.

(101) Ma, L.; Li, Z.; Yuan, Z.; Wang, H.; Huang, C.; Qiu, Y. High-Performance Nanofluidic Osmotic Power Generation Enabled by Exterior Surface Charges under the Natural Salt Gradient. *J. Power Sources* **2021**, *492*, 229637. https://doi.org/10.1016/j.jpowsour.2021.229637.

(102) Ma, L.; Li, Z.; Yuan, Z.; Huang, C.; Siwy, Z. S.; Qiu, Y. Modulation of Ionic Current Rectification in Ultrashort Conical Nanopores. *Anal. Chem.* **2020**, *92* (24), 16188–16196. https://doi.org/10.1021/acs.analchem.0c03989.

(103) Gao, P.; Ma, Q.; Ding, D.; Wang, D.; Lou, X.; Zhai, T.; Xia, F. Distinct Functional Elements for Outer-Surface Anti-Interference and Inner-Wall Ion Gating of Nanochannels. *Nat. Commun.* **2018**, *9* (1), 1–11. https://doi.org/10.1038/s41467-018-06873-z.

(104) Ma, Q.; Li, Y.; Wang, R.; Xu, H.; Du, Q.; Gao, P.; Xia, F. Towards Explicit Regulating-Ion-Transport: Nanochannels with Only Function-Elements at Outer-Surface. *Nat. Commun.* **2021**, *12* (1), 1573. https://doi.org/10.1038/s41467-021-21507-7.

(105) Cabello-Aguilar, S.; Chaaya, A. A.; Bechelany, M.; Pochat-Bohatier, C.; Balanzat, E.; Janot, J.-M.; Miele, P.; Balme, S. Dynamics of Polymer Nanoparticles through a Single Artificial Nanopore with a High-Aspect-Ratio. *Soft Matter* **2014**, *10* (42), 8413–8419. https://doi.org/10.1039/C4SM00392F.

(106) Ma, L.; An, X.; Song, F.; Qiu, Y. Effective Charged Exterior Surfaces for Enhanced Ionic Diffusion through Nanopores under Salt Gradients. *J. Phys. Chem. Lett.* **2022**, *13* (24), 5669–5676. https://doi.org/10.1021/acs.jpclett.2c01351.

(107) Dai, Y.; Zhang, Y.; Ma, Q.; Lin, M.; Zhang, X.; Xia, F. Inner Wall and Outer Surface Distinguished Solid-State Nanopores for Sensing. *Anal. Chem.* **2022**, *94* (50), 17343–17348. https://doi.org/10.1021/acs.analchem.2c04216.

(108) Wu, S.; Wildhaber, F.; Vazquez-Mena, O.; Bertsch, A.; Brugger, J.; Renaud, P. Facile Fabrication of Nanofluidic Diode Membranes Using Anodic Aluminium Oxide. *Nanoscale* **2012**, *4* (18), 5718–5723.

https://doi.org/10.1039/c2nr31243c.

(109) Cheng, L. J.; Guo, L. J. Ionic Current Rectification, Breakdown, and Switching in Heterogeneous Oxide Nanofluidic Devices. *ACS Nano* **2009**, *3* (3), 575–584. https://doi.org/10.1021/nn8007542.

(110) Larkin, J.; Henley, R.; Bell, D. C.; Cohen-Karni, T.; Rosenstein, J. K.; Wanunu, M. Slow DNA Transport through Nanopores in Hafnium Oxide Membranes. *ACS Nano* **2013**, *7* (11), 10121–10128. https://doi.org/10.1021/nn404326f.

(111) Shim, J.; Rivera, J. A.; Bashir, R. Electron Beam Induced Local Crystallization of HfO2 Nanopores for Biosensing Applications. *Nanoscale* **2013**, *5* (22), 10887–10893. https://doi.org/10.1039/c3nr02608f.

(112) Park, K. B.; Kim, H. J.; Kang, Y. H.; Yu, J. S.; Chae, H.; Lee, K.; Kim, H. M.; Kim, K. B. Highly Reliable and Low-Noise Solid-State Nanopores with an Atomic Layer Deposited ZnO Membrane on a Quartz Substrate. *Nanoscale* **2017**, *9* (47), 18772–18780. https://doi.org/10.1039/c7nr05755e.

(113) Zhu, X.; Li, X.; Gu, C.; Ye, Z.; Cao, Z.; Zhang, X.; Jin, C.; Liu, Y. Monolithic Integration of Vertical Thin-Film Transistors in Nanopores for Charge Sensing of Single Biomolecules. *ACS Nano* **2021**, *15* (6), 9882–9889. https://doi.org/10.1021/acsnano.1c01042.

(114) Ulrich, N.; Spende, A.; Burr, L.; Sobel, N.; Schubert, I.; Hess, C.; Trautmann, C.; Toimil-Molares, M. E. Conical Nanotubes Synthesized by Atomic Layer Deposition of Al2O3, TiO2, and SiO2 in Etched Ion-Track Nanochannels. *Nanomaterials* **2021**, *11* (8), 1874. https://doi.org/10.3390/nano11081874.

(115) Wang, R.; Gilboa, T.; Song, J.; Huttner, D.; Grinstaff, M. W.; Meller, A. Single-Molecule Discrimination of Labeled DNAs and Polypeptides Using Photoluminescent-Free TiO2 Nanopores. *ACS Nano* **2018**, *12* (11), 11648–11656. https://doi.org/10.1021/acsnano.8b07055.

(116) Zeng, Z.; Song, R.; Zhang, S.; Han, X.; Zhu, Z.; Chen, X.; Wang, L. Biomimetic N-Doped Graphene Membrane for Proton Exchange Membranes. *Nano Lett.* **2021**, *21* (10), 4314–4319. https://doi.org/10.1021/acs.nanolett.1c00813.

(117) Hayashida, T.; Yokota, K.; Murayama, S.; Arima, A.; Tsutsui, M.; Taniguchi, M. Tailoring Dielectric Surface Charge via Atomic Layer Thickness. *ACS Appl. Mater. Interfaces* **2020**, *12* (4), 5025–5030. https://doi.org/10.1021/acsami.9b18444.

(118) Tsutsui, M.; Hongo, S.; He, Y.; Taniguchi, M.; Gemma, N.; Kawai, T. Single-Nanoparticle Detection Using a Low-Aspect-Ratio Pore. *ACS Nano* **2012**, *6* (4), 3499–3505. https://doi.org/10.1021/nn300530b.

(119) Xia, Z.; Rozyyev, V.; Mane, A. U.; Elam, J. W.; Darling, S. B. Surface Zeta Potential of ALD-Grown Metal-Oxide Films. *Langmuir* **2021**, *37* (39), 11618–11624. https://doi.org/10.1021/acs.langmuir.1c02028.

(120) Leong, I. W.; Tsutsui, M.; Yokota, K.; Murayama, S.; Taniguchi, M. Regulating Nonlinear Ion Transport through a Solid-State Pore by Partial Surface Coatings. *ACS Appl. Mater. Interfaces* **2023**, *0* (0). https://doi.org/10.1021/acsami.2c19485.

(121) Hayashida, T.; Tsutsui, M.; Murayama, S.; Nakada, T.; Taniguchi, M. Dielectric Coatings for Resistive Pulse Sensing Using Solid-State Pores. *ACS Appl. Mater. Interfaces* **2021**, *13* (8), 10632–10638. https://doi.org/10.1021/acsami.0c22548.

(122) Sha, J.; Shi, H.; Zhang, Y.; Chen, C.; Liu, L.; Chen, Y. Salt Gradient Improving Signal-to-Noise Ratio in Solid-State Nanopore. *ACS Sensors* **2017**, *2* (4), 506–512. https://doi.org/10.1021/acssensors.6b00718.

(123) Lastra, L. S.; Bandara, Y. M. N. D. Y.; Nguyen, M.; Farajpour, N.; Freedman, K. J. On the Origins of Conductive Pulse Sensing inside a Nanopore. *Nat.*

Commun. **2022**, *13* (1), 2186. https://doi.org/10.1038/s41467-022-29758-8.

(124) Fried, J. P.; Swett, J. L.; Nadappuram, B. P.; Mol, J. A.; Edel, J. B.; Ivanov, A. P.; Yates, J. R. In Situ Solid-State Nanopore Fabrication. *Chem. Soc. Rev.* **2021**, *50* (8), 4974–4992. https://doi.org/10.1039/d0cs00924e.

(125) Hu, Z.; Huo, M.; Ying, Y.; Long, Y. Biological Nanopore Approach for Single-Molecule Protein Sequencing. *Angew. Chemie* **2021**, *133* (27), 14862–14873. https://doi.org/10.1002/ange.202013462.

(126) Henriquez, R. R.; Ito, T.; Sun, L.; Crooks, R. M. The Resurgence of Coulter Counting for Analyzing Nanoscale Objects. *Analyst* **2004**, *129* (6), 478–482. https://doi.org/10.1039/b404251b.

(127) Sun, T.; Morgan, H. Single-Cell Microfluidic Impedance Cytometry: A Review. *Microfluid. Nanofluidics* **2010**, *8* (4), 423–443. https://doi.org/10.1007/s10404-010-0580-9.

(128) Gao, R.; Lin, Y.; Ying, Y. L.; Hu, Y. X.; Xu, S. W.; Ruan, L. Q.; Yu, R. J.; Li, Y. J.; Li, H. W.; Cui, L. F.; Long, Y. T. Wireless Nanopore Electrodes for Analysis of Single Entities. *Nat. Protoc.* **2019**, *14* (7), 2015–2035. https://doi.org/10.1038/s41596-019-0171-5.

(129) Zhang, Y.; Zhang, B.; White, H. S. Electrochemistry of Nanopore Electrodes in Low Ionic Strength Solutions. *J. Phys. Chem. B* **2006**, *110* (4), 1768–1774. https://doi.org/10.1021/jp054704c.

(130) Messerschmitt, F.; Kubicek, M.; Schweiger, S.; Rupp, J. L. M. Memristor Kinetics and Diffusion Characteristics for Mixed Anionic-Electronic SrTiO3-δ Bits: The Memristor-Based Cottrell Analysis Connecting Material to Device Performance. *Adv. Funct. Mater.* **2014**, *24* (47), 7448–7460. https://doi.org/10.1002/adfm.201402286.

(131) Lee, G. Y.; Park, J. H.; Chang, Y. W.; Cho, S.; Kang, M. J.; Pyun, J. C. Chronoamperometry-Based Redox Cycling for Application to Immunoassays. *ACS Sensors* **2018**, *3* (1), 106–112. https://doi.org/10.1021/acssensors.7b00681.

(132) Plesa, C.; Ruitenberg, J. W.; Witteveen, M. J.; Dekker, C. Detection of Individual Proteins Bound along DNA Using Solid-State Nanopores. *Nano Lett.* **2015**, *15* (5), 3153–3158. https://doi.org/10.1021/acs.nanolett.5b00249.

(133) Plesa, C.; Kowalczyk, S. W.; Zinsmeester, R.; Grosberg, A. Y.; Rabin, Y.; Dekker, C. Fast Translocation of Proteins through Solid State Nanopores. *Nano Lett.* **2013**, *13* (2), 658–663. https://doi.org/10.1021/nl3042678.

(134) Leong, I. W.; Kishimoto, S.; Tsutsui, M.; Taniguchi, M. Interference of Electrochemical Ion Diffusion in Nanopore Sensing. *iScience* **2022**, *25* (10), 105073. https://doi.org/10.1016/j.isci.2022.105073.

(135) Mojtabavi, M.; Tsai, W. Y.; VahidMohammadi, A.; Zhang, T.; Gogotsi, Y.; Balke, N.; Wanunu, M. Ionically Active MXene Nanopore Actuators. *Small* **2022**, *18* (11), 2105857. https://doi.org/10.1002/smll.202105857.

(136) Wang, D.; Wang, Y.; Li, H.; Han, Y.; Hu, P.; Ma, K.; Sheves, M.; Jin, Y. Photoactivated Bacteriorhodopsin/SiNx Nanopore-Based Biological Nanofluidic Generator with Single-Protein Sensitivity. *ACS Nano* **2022**, *16* (1), 1589–1599. https://doi.org/10.1021/acsnano.1c10255.

(137) Liao, C.; Antaw, F.; Wuethrich, A.; Anderson, W.; Trau, M. Configurable Miniaturized 3D Pores for Robust Single-Nanoparticle Analysis. *Small Struct.* **2020**, *1* (2), 2000011. https://doi.org/10.1002/sstr.202000011.

(138) Tsutsui, M.; Yokota, K.; Arima, A.; He, Y.; Kawai, T. Solid-State Nanopore Time-of-Flight Mass Spectrometer. *ACS Sensors* **2019**, *4* (11), 2974–2979. https://doi.org/10.1021/acssensors.9b01470.

(139) Van Dorp, S.; Keyser, U. F.; Dekker, N. H.; Dekker, C.; Lemay, S. G. Origin of the Electrophoretic

Force on DNA in Solid-State Nanopores. *Nat. Phys.* **2009**, *5* (5), 347–351. https://doi.org/10.1038/Nphys1230.

(140) Van Der Niet, M. J. T. C.; Garcia-Araez, N.; Hernández, J.; Feliu, J. M.; Koper, M. T. M. Water Dissociation on Well-Defined Platinum Surfaces: The Electrochemical Perspective. *Catal. Today* **2013**, *202* (1), 105–113. https://doi.org/10.1016/j.cattod.2012.04.059.

(141) Jaksic, M. M.; Johansen, B.; Tunold, R. Electrochemical Behaviour of Platinum in Alkaline and Acidic Solutions of Heavy and Regular Water. *Int. J. Hydrogen Energy* **1993**, *18* (10), 817–837. https://doi.org/10.1016/0360-3199(93)90136-X.

(142) Lee, S. H.; Rasaiah, J. C. Proton Transfer and the Mobilities of the H+ and OH- Ions from Studies of a Dissociating Model for Water. *J. Chem. Phys.* **2011**, *135* (12), 124505. https://doi.org/10.1063/1.3632990.

(143) Holz, M.; Heil, S. R.; Sacco, A. Temperature-Dependent Self-Diffusion Coefficients of Water and Six Selected Molecular Liquids for Calibration in Accurate 1H NMR PFG Measurements. *Phys. Chem. Chem. Phys.* **2000**, *2* (20), 4740–4742. https://doi.org/10.1039/b005319h.

(144) Baehre, D.; Ernst, A.; Weißhaar, K.; Natter, H.; Stolpe, M.; Busch, R. Electrochemical Dissolution Behavior of Titanium and Titanium-Based Alloys in Different Electrolytes. *Procedia CIRP* **2016**, *42* (Isem Xviii), 137–142. https://doi.org/10.1016/j.procir.2016.02.208.

(145) Luo, J.; Sam, A.; Hu, B.; DeBruler, C.; Wei, X.; Wang, W.; Liu, T. L. Unraveling PH Dependent Cycling Stability of Ferricyanide/Ferrocyanide in Redox Flow Batteries. *Nano Energy* **2017**, *42* (October), 215–221. https://doi.org/10.1016/j.nanoen.2017.10.057.

(146) Tsutsui, M.; Yokota, K.; Arima, A.; Tonomura, W.; Taniguchi, M.; Washio, T.; Kawai, T. Temporal Response of Ionic Current Blockade in Solid-State Nanopores. *ACS Appl. Mater. Interfaces* **2018**, *10* (40), 34751–34757. https://doi.org/10.1021/acsami.8b11819.

(147) Kishimoto, S.; Murayama, S.; Tsutsui, M.; Taniguchi, M. Crucial Role of Out-of-Pore Resistance on Temporal Response of Ionic Current in Nanopore Sensors. *ACS Sensors* **2020**, *5* (6), 1597–1603. https://doi.org/10.1021/acssensors.0c00014.

(148) Xu, C.; Liu, Y.; Xiong, T.; Wu, F.; Yu, P.; Wang, J.; Mao, L. Dynamic Behavior of Charged Particles at the Nanopipette Orifice. *ACS Sensors* **2021**, *6* (6), 2330–2338. https://doi.org/10.1021/acssensors.1c00418.

(149) Stein, D.; Deurvorst, Z.; Van Der Heyden, F. H. J.; Koopmans, W. J. A.; Gabel, A.; Dekker, C. Electrokinetic Concentration of DNA Polymers in Nanofluidic Channels. *Nano Lett.* **2010**, *10* (3), 765–772. https://doi.org/10.1021/nl902228p.

(150) Bacri, L.; Oukhaled, A. G.; Schiedt, B.; Patriarche, G.; Bourhis, E.; Gierak, J.; Pelta, J.; Auvray, L. Dynamics of Colloids in Single Solid-State Nanopores. *J. Phys. Chem. B* **2011**, *115* (12), 2890–2898. https://doi.org/10.1021/jp200326w.

(151) Arima, A.; Tsutsui, M.; Yoshida, T.; Tatematsu, K.; Yamazaki, T.; Yokota, K.; Kuroda, S.; Washio, T.; Baba, Y.; Kawai, T. Digital Pathology Platform for Respiratory Tract Infection Diagnosis via Multiplex Single-Particle Detections. *ACS Sensors* **2020**, *5* (11), 3398–3403. https://doi.org/10.1021/acssensors.0c01564.

(152) Houghtaling, J.; List, J.; Mayer, M. Nanopore-Based, Rapid Characterization of Individual Amyloid Particles in Solution: Concepts, Challenges, and Prospects. *Small* **2018**, *14* (46), 1802412. https://doi.org/10.1002/smll.201802412.

(153) Houghtaling, J.; Ying, C.; Eggenberger, O. M.; Fennouri, A.; Nandivada, S.; Acharjee, M.; Li, J.; Hall, A. R.; Mayer, M. Estimation of Shape, Volume, and Dipole Moment of Individual Proteins Freely Transiting a

Synthetic Nanopore. *ACS Nano* **2019**, *13* (5), 5231–5242. https://doi.org/10.1021/acsnano.8b09555.

(154) Chia, C.; Jeffrey, S. S.; Howe, R. T. Anomalous Hysteresis and Current Fluctuations in Cyclic Voltammograms at Microelectrodes Due to Ag Leaching from Ag/AgCl Reference Electrodes. *Electrochem. commun.* **2019**, *105* (July), 106499. https://doi.org/10.1016/j.elecom.2019.106499.

(155) Reiner, J. E.; Balijepalli, A.; Robertson, J. W. F.; Campbell, J.; Suehle, J.; Kasianowicz, J. J. Disease Detection and Management via Single Nanopore-Based Sensors. *Chem. Rev.* **2012**, *112* (12), 6431–6451. https://doi.org/10.1021/cr300381m.

(156) Luo, L.; German, S. R.; Lan, W. J.; Holden, D. A.; Mega, T. L.; White, H. S. Resistive-Pulse Analysis of Nanoparticles. *Annu. Rev. Anal. Chem.* **2014**, *7*, 513–535. https://doi.org/10.1146/annurev-anchem-071213-020107.

(157) Howorka, S.; Siwy, Z. Nanopore Analytics: Sensing of Single Molecules. *Chem. Soc. Rev.* **2009**, *38* (8), 2360–2384. https://doi.org/10.1039/b813796j.

(158) Weatherall, E.; Willmott, G. R. Applications of Tunable Resistive Pulse Sensing. *Analyst* **2015**, *140* (10), 3318–3334. https://doi.org/10.1039/c4an02270j.

(159) Smeets, R. M. M.; Keyser, U. F.; Krapf, D.; Wu, M. Y.; Dekker, N. H.; Dekker, C. Salt Dependence of Ion Transport and DMA Translocation through Solid-State Nanopores. *Nano Lett.* **2006**, *6* (1), 89–95. https://doi.org/10.1021/nl052107w.

(160) He, Y.; Tsutsui, M.; Fan, C.; Taniguchi, M.; Kawai, T. Controlling DNA Translocation through Gate Modulation of Nanopore Wall Surface Charges. *ACS Nano* **2011**, *5* (7), 5509–5518. https://doi.org/10.1021/nn201883b.

(161) Haywood, D. G.; Saha-Shah, A.; Baker, L. A.; Jacobson, S. C. Fundamental Studies of Nanofluidics: Nanopores, Nanochannels, and Nanopipets. *Anal. Chem.* **2015**, *87* (1), 172–187. https://doi.org/10.1021/ac504180h.

(162) Keyser, U. F. Controlling Molecular Transport through Nanopores. *J. R. Soc. Interface* **2011**, *8* (63), 1369–1378. https://doi.org/10.1098/rsif.2011.0222.

(163) Valencia, P. M.; Farokhzad, O. C.; Karnik, R.; Langer, R. Microfluidic Technologies for Accelerating the Clinical Translation of Nanoparticles. *Nat. Nanotechnol.* **2012**, *7* (10), 623–629. https://doi.org/10.1038/nnano.2012.168.

(164) Yasaki, H.; Yasui, T.; Yanagida, T.; Kaji, N.; Kanai, M.; Nagashima, K.; Kawai, T.; Baba, Y. Substantial Expansion of Detectable Size Range in Ionic Current Sensing through Pores by Using a Microfluidic Bridge Circuit. *J. Am. Chem. Soc.* **2017**, *139* (40), 14137–14142. https://doi.org/10.1021/jacs.7b06440.

(165) Kong, C. Y.; Muthukumar, M. Polymer Translocation through a Nanopore. II. Excluded Volume Effect. *J. Chem. Phys.* **2004**, *120* (7), 3460–3466. https://doi.org/10.1063/1.1642588.

(166) Tsutsui, M.; Yoshida, T.; Yokota, K.; Yasaki, H.; Yasui, T.; Arima, A.; Tonomura, W.; Nagashima, K.; Yanagida, T.; Kaji, N.; Taniguchi, M.; Washio, T.; Baba, Y.; Kawai, T. Discriminating Single-Bacterial Shape Using Low-Aspect-Ratio Pores. *Sci. Rep.* **2017**, *7* (1), 17371. https://doi.org/10.1038/s41598-017-17443-6.

(167) Yusko, E. C.; Bruhn, B. R.; Eggenberger, O. M.; Houghtaling, J.; Rollings, R. C.; Walsh, N. C.; Nandivada, S.; Pindrus, M.; Hall, A. R.; Sept, D.; Li, J.; Kalonia, D. S.; Mayer, M. Real-Time Shape Approximation and Fingerprinting of Single Proteins Using a Nanopore. *Nat. Nanotechnol.* **2017**, *12* (4), 360–367. https://doi.org/10.1038/nnano.2016.267.

(168) Arjmandi, N.; Van Roy, W.; Lagae, L.; Borghs, G. Measuring the Electric Charge and Zeta Potential of Nanometer-Sized Objects Using Pyramidal-Shaped Nanopores. *Anal. Chem.* **2012**, *84* (20), 8490–8496.

https://doi.org/10.1021/ac300705z.

(169) Arima, A.; Tsutsui, M.; Harlisa, I. H.; Yoshida, T.; Tanaka, M.; Yokota, K.; Tonomura, W.; Taniguchi, M.; Okochi, M.; Washio, T.; Kawai, T. Selective Detections of Single-Viruses Using Solid-State Nanopores. *Sci. Rep.* **2018**, *8* (1), 1–7. https://doi.org/10.1038/s41598-018-34665-4.

(170) Chen, S.; Tang, Y.; Zhan, K.; Sun, D.; Hou, X. Chemiresistive Nanosensors with Convex/Concave Structures. *Nano Today* **2018**, *20*, 84–100. https://doi.org/10.1016/j.nantod.2018.04.006.

(171) Zhu, Y.; Zhan, K.; Hou, X. Interface Design of Nanochannels for Energy Utilization. *ACS Nano* **2018**, *12* (2), 908–911. https://doi.org/10.1021/acsnano.7b07923.

(172) Arima, A.; Harlisa, I. H.; Yoshida, T.; Tsutsui, M.; Tanaka, M.; Yokota, K.; Tonomura, W.; Yasuda, J.; Taniguchi, M.; Washio, T.; Okochi, M.; Kawai, T. Identifying Single Viruses Using Biorecognition Solid-State Nanopores. *J. Am. Chem. Soc.* **2018**, *140* (48), 16834–16841. https://doi.org/10.1021/jacs.8b10854.

(173) Hou, X. Smart Gating Multi-Scale Pore/Channel-Based Membranes. *Adv. Mater.* **2016**, *28* (33), 7049–7064. https://doi.org/10.1002/adma.201600797.

(174) Hou, X.; Yang, F.; Li, L.; Song, Y.; Jiang, L.; Zhu, D. A Biomimetic Asymmetric Responsive Single Nanochannel. *J. Am. Chem. Soc.* **2010**, *132* (33), 11736–11742. https://doi.org/10.1021/ja1045082.

(175) Hou, X.; Guo, W.; Jiang, L. Biomimetic Smart Nanopores and Nanochannels. *Chem. Soc. Rev.* **2011**, *40* (5), 2385–2401. https://doi.org/10.1039/c0cs00053a.

(176) Tsutsui, M.; Yokota, K.; Nakada, T.; Arima, A.; Tonomura, W.; Taniguchi, M.; Washio, T.; Kawai, T. Silicon Substrate Effects on Ionic Current Blockade in Solid-State Nanopores. *Nanoscale* **2019**, *11* (10), 4190–4197. https://doi.org/10.1039/c8nr09042d.

(177) Lee, M. H.; Kumar, A.; Park, K. B.; Cho, S. Y.; Kim, H. M.; Lim, M. C.; Kim, Y. R.; Kim, K. B. A Low-Noise Solid-State Nanopore Platform Based on a Highly Insulating Substrate. *Sci. Rep.* **2014**, *4*, 1–7. https://doi.org/10.1038/srep07448.

(178) Jain, T.; Guerrero, R. J. S.; Aguilar, C. A.; Karnik, R. Integration of Solid-State Nanopores in Microfluidic Networks via Transfer Printing of Suspended Membranes. *Anal. Chem.* **2013**, *85* (8), 3871–3878. https://doi.org/10.1021/ac302972c.

(179) Leong, I. W.; Tsutsui, M.; Nakada, T.; Taniguchi, M.; Washio, T.; Kawai, T. Back-Side Polymer-Coated Solid-State Nanopore Sensors. *ACS Omega* **2019**, *4* (7), 12561–12566. https://doi.org/10.1021/acsomega.9b00946.

(180) Weatherall, E.; Hauer, P.; Vogel, R.; Willmott, G. R. Pulse Size Distributions in Tunable Resistive Pulse Sensing. *Anal. Chem.* **2016**, *88* (17), 8648–8656. https://doi.org/10.1021/acs.analchem.6b01818.

(181) Plesa, C.; Kowalczyk, S. W.; Zinsmeester, R.; Grosberg, A. Y.; Rabin, Y.; Dekker, C. Erratum: Fast Translocation of Proteins through Solid State Nanopores (Nano Letters (2013) 13:2 (658-663) DOI:10.1021/Nl3042678). *Nano Lett.* **2013**, *13* (7), 3445. https://doi.org/10.1021/nl4019269.

(182) Goto, Y.; Yanagi, I.; Matsui, K.; Yokoi, T.; Takeda, K. Integrated Solid-State Nanopore Platform for Nanopore Fabrication via Dielectric Breakdown, DNA-Speed Deceleration and Noise Reduction. *Sci. Rep.* **2016**, *6* (1), 31324. https://doi.org/10.1038/srep31324.

(183) Tabard-Cossa, V.; Trivedi, D.; Wiggin, M.; Jetha, N. N.; Marziali, A. Noise Analysis and Reduction in Solid-State Nanopores. *Nanotechnology* **2007**, *18* (30), 305505. https://doi.org/10.1088/0957-4484/18/30/305505.

(184) Rosenstein, J. K.; Wanunu, M.; Merchant, C. A.; Drndic, M.; Shepard, K. L. Integrated Nanopore

Sensing Platform with Sub-Microsecond Temporal Resolution. *Nat. Methods* **2012**, *9* (5), 487–492. https://doi.org/10.1038/nmeth.1932.

(185) Shekar, S.; Niedzwiecki, D. J.; Chien, C. C.; Ong, P.; Fleischer, D. A.; Lin, J.; Rosenstein, J. K.; Drndić, M.; Shepard, K. L. Measurement of DNA Translocation Dynamics in a Solid-State Nanopore at 100 Ns Temporal Resolution. *Nano Lett.* **2016**, *16* (7), 4483–4489. https://doi.org/10.1021/acs.nanolett.6b01661.

(186) Ivanov, A. P.; Instuli, E.; McGilvery, C. M.; Baldwin, G.; McComb, D. W.; Albrecht, T.; Edel, J. B. DNA Tunneling Detector Embedded in a Nanopore. *Nano Lett.* **2011**, *11* (1), 279–285. https://doi.org/10.1021/nl103873a.

(187) Fanget, A.; Traversi, F.; Khlybov, S.; Granjon, P.; Magrez, A.; Forró, L.; Radenovic, A. Nanopore Integrated Nanogaps for DNA Detection. *Nano Lett.* **2014**, *14* (1), 244–249. https://doi.org/10.1021/nl403849g.

(188) Tsutsui, M.; Yokota, K.; Yoshida, T.; Hotehama, C.; Kowada, H.; Esaki, Y.; Taniguchi, M.; Washio, T.; Kawai, T. Identifying Single Particles in Air Using a 3D-Integrated Solid-State Pore. *ACS Sensors* **2019**, *4* (3), 748–755. https://doi.org/10.1021/acssensors.9b00113.

(189) Zhang, Y.; Reisner, W. Fabrication and Characterization of Nanopore-Interfaced Nanochannel Devices. *Nanotechnology* **2015**, *26* (45), 455301. https://doi.org/10.1088/0957-4484/26/45/455301.

(190) Zeng, S.; Wen, C.; Solomon, P.; Zhang, S. L.; Zhang, Z. Rectification of Protein Translocation in Truncated Pyramidal Nanopores. *Nat. Nanotechnol.* **2019**, *14* (11), 1056–1062. https://doi.org/10.1038/s41565-019-0549-0.

(191) Brinkerhoff, H.; Kang, A. S. W.; Liu, J.; Aksimentiev, A.; Dekker, C. Multiple Rereads of Single Proteins at Single-Amino Acid Resolution Using Nanopores. *Science (80-.).* **2021**, *374* (6574), 1509–1513. https://doi.org/10.1126/science.abl4381.

(192) McMullen, A.; De Haan, H. W.; Tang, J. X.; Stein, D. Buckling Causes Nonlinear Dynamics of Filamentous Viruses Driven through Nanopores. *Phys. Rev. Lett.* **2018**, *120* (7), 078101. https://doi.org/10.1103/PhysRevLett.120.078101.

(193) McMullen, A. J.; Tang, J. X.; Stein, D. Nanopore Measurements of Filamentous Viruses Reveal a Sub-Nanometer-Scale Stagnant Fluid Layer. *ACS Nano* **2017**, *11* (11), 11669–11677. https://doi.org/10.1021/acsnano.7b06767.

(194) McMullen, A.; De Haan, H. W.; Tang, J. X.; Stein, D. Stiff Filamentous Virus Translocations through Solid-State Nanopores. *Nat. Commun.* **2014**, *5* (1), 1–10. https://doi.org/10.1038/ncomms5171.

(195) Arima, A.; Tsutsui, M.; Washio, T.; Baba, Y.; Kawai, T. Solid-State Nanopore Platform Integrated with Machine Learning for Digital Diagnosis of Virus Infection. *Anal. Chem.* **2021**, *93* (1), 215–227. https://doi.org/10.1021/acs.analchem.0c04353.

(196) Misiunas, K.; Ermann, N.; Keyser, U. F. QuipuNet: Convolutional Neural Network for Single-Molecule Nanopore Sensing. *Nano Lett.* **2018**, *18* (6), 4040–4045. https://doi.org/10.1021/acs.nanolett.8b01709.

(197) Zhou, J.; Kondylis, P.; Haywood, D. G.; Harms, Z. D.; Lee, L. S.; Zlotnick, A.; Jacobson, S. C. Characterization of Virus Capsids and Their Assembly Intermediates by Multicycle Resistive-Pulse Sensing with Four Pores in Series. *Anal. Chem.* **2018**, *90* (12), 7267–7274. https://doi.org/10.1021/acs.analchem.8b00452.

(198) Maugi, R.; Hauer, P.; Bowen, J.; Ashman, E.; Hunsicker, E.; Platt, M. A Methodology for Characterising Nanoparticle Size and Shape Using Nanopores. *Nanoscale* **2020**, *12* (1), 262–270. https://doi.org/10.1039/c9nr09100a.

(199) Fragasso, A.; Schmid, S.; Dekker, C. Comparing Current Noise in Biological and Solid-State Nanopores. *ACS Nano* **2020**, *14* (2), 1338–1349. https://doi.org/10.1021/acsnano.9b09353.

(200) Di Fiori, N.; Squires, A.; Bar, D.; Gilboa, T.; Moustakas, T. D.; Meller, A. Optoelectronic Control of Surface Charge and Translocation Dynamics in Solid-State Nanopores. *Nat. Nanotechnol.* **2013**, *8* (12), 946–951. https://doi.org/10.1038/nnano.2013.221.

(201) Feng, J.; Liu, K.; Bulushev, R. D.; Khlybov, S.; Dumcenco, D.; Kis, A.; Radenovic, A. Identification of Single Nucleotides in MoS 2 Nanopores. *Nat. Nanotechnol.* **2015**, *10* (12), 1070–1076. https://doi.org/10.1038/nnano.2015.219.

(202) Peng, P. H.; Ou Yang, H. C.; Tsai, P. C.; Yeh, L. H. Thermal Dependence of the Mesoscale Ionic Diode: Modeling and Experimental Verification. *ACS Appl. Mater. Interfaces* **2020**, *12* (14), 17139–17146. https://doi.org/10.1021/acsami.0c02214.

(203) Hatlo, M. M.; Panja, D.; Van Roij, R. Translocation of DNA Molecules through Nanopores with Salt Gradients: The Role of Osmotic Flow. *Phys. Rev. Lett.* **2011**, *107* (6), 1–5. https://doi.org/10.1103/PhysRevLett.107.068101.

(204) Chou, T. Enhancement of Charged Macromolecule Capture by Nanopores in a Salt Gradient. *J. Chem. Phys.* **2009**, *131* (3). https://doi.org/10.1063/1.3170952.

(205) Zhang, Y.; Wu, G.; Si, W.; Ma, J.; Yuan, Z.; Xie, X.; Liu, L.; Sha, J.; Li, D.; Chen, Y. Ionic Current Modulation from DNA Translocation through Nanopores under High Ionic Strength and Concentration Gradients. *Nanoscale* **2017**, *9* (2), 930–939. https://doi.org/10.1039/c6nr08123a.

(206) Charron, M.; Philipp, L.; He, L.; Tabard-Cossa, V. Elucidating the Dynamics of Polymer Transport through Nanopores Using Asymmetric Salt Concentrations. *Nano Res.* **2022**, *15* (11), 9943–9953. https://doi.org/10.1007/s12274-022-4886-3.

(207) Lin, C.-Y.; Chen, F.; Yeh, L.-H.; Hsu, J.-P. Salt Gradient Driven Ion Transport in Solid-State Nanopores: The Crucial Role of Reservoir Geometry and Size. *Phys. Chem. Chem. Phys.* **2016**, *18* (43), 30160–30165. https://doi.org/10.1039/c6cp06459k.

(208) Lin, C. Y.; Yeh, L. H.; Hsu, J. P.; Tseng, S. Regulating Current Rectification and Nanoparticle Transport Through a Salt Gradient in Bipolar Nanopores. *Small* **2015**, *11* (35), 4594–4602. https://doi.org/10.1002/smll.201501210.

(209) Joo, S. W.; Qian, S. Electrophoretic Motion of a Nanorod along the Axis of a Nanopore under a Salt Gradient. *J. Colloid Interface Sci.* **2011**, *356* (1), 331–340. https://doi.org/10.1016/j.jcis.2010.12.062.

(210) Menestrina, J.; Yang, C.; Schiel, M.; Vlassiouk, I.; Siwy, Z. S. Charged Particles Modulate Local Ionic Concentrations and Cause Formation of Positive Peaks in Resistive-Pulse-Based Detection. *J. Phys. Chem. C* **2014**, *118* (5), 2391–2398. https://doi.org/10.1021/jp412135v.

(211) Davenport, M.; Healy, K.; Pevarnik, M.; Teslich, N.; Cabrini, S.; Morrison, A. P.; Siwy, Z. S.; Létant, S. E. The Role of Pore Geometry in Single Nanoparticle Detection. *ACS Nano* **2012**, *6* (9), 8366–8380. https://doi.org/10.1021/nn303126n.

(212) Ivica, J.; Williamson, P. T. F.; De Planque, M. R. R. Salt Gradient Modulation of MicroRNA Translocation through a Biological Nanopore. *Anal. Chem.* **2017**, *89* (17), 8822–8829. https://doi.org/10.1021/acs.analchem.7b01246.

(213) Yan, H.; Zhou, D.; Shi, B.; Zhang, Z.; Tian, H.; Yu, L.; Wang, Y.; Guan, X.; Wang, Z.; Wang, D. Slowing down DNA Translocation Velocity Using a LiCl Salt

Gradient and Nanofiber Mesh. *Eur. Biophys. J.* **2019**, *48* (3), 261–266. https://doi.org/10.1007/s00249-019-01350-x.

(214) Bello, J.; Mowla, M.; Troise, N.; Soyring, J.; Borgesi, J.; Shim, J. Increased Dwell Time and Occurrence of DsDNA Translocation Events through Solid State Nanopores by LiCl Concentration Gradients. *Electrophoresis* **2019**, *40* (7), 1082–1090. https://doi.org/10.1002/elps.201800426.

(215) McMullen, A.; Araujo, G.; Winter, M.; Stein, D. Osmotically Driven and Detected DNA Translocations. *Sci. Rep.* **2019**, *9* (1), 1–10. https://doi.org/10.1038/s41598-019-51049-4.

(216) Zhang, Y.; Zhao, J.; Si, W.; Kan, Y.; Xu, Z.; Sha, J.; Chen, Y. Electroosmotic Facilitated Protein Capture and Transport through Solid-State Nanopores with Diameter Larger than Length. *Small Methods* **2020**, *4* (11), 1–8. https://doi.org/10.1002/smtd.201900893.

(217) Sohi, A. N.; Beamish, E.; Tabard-Cossa, V.; Godin, M. DNA Capture by Nanopore Sensors under Flow. *Anal. Chem.* **2020**, *92* (12), 8108–8116. https://doi.org/10.1021/acs.analchem.9b05778.

(218) He, Y.; Tsutsui, M.; Scheicher, R. H.; Miao, X. S.; Taniguchi, M. Salt-Gradient Approach for Regulating Capture-to-Translocation Dynamics of DNA with Nanochannel Sensors. *ACS Sensors* **2016**, *1* (6), 807–816. https://doi.org/10.1021/acssensors.6b00176.

(219) Rollings, R. C.; Kuan, A. T.; Golovchenko, J. A. Ion Selectivity of Graphene Nanopores. *Nat. Commun.* **2016**, *7* (1), 11408. https://doi.org/10.1038/ncomms11408.

(220) Velegol, D.; Garg, A.; Guha, R.; Kar, A.; Kumar, M. Origins of Concentration Gradients for Diffusiophoresis. *Soft Matter* **2016**, *12* (21), 4686–4703. https://doi.org/10.1039/c6sm00052e.

(221) Pevarnik, M.; Healy, K.; Toimil-Molares, M. E.; Morrison, A.; Letant, S. E.; Siwy, Z. S.; Létant, S. E.; Siwy, Z. S.; Letant, S. E.; Siwy, Z. S.; Létant, S. E.; Siwy, Z. S. Polystyrene Particles Reveal Pore Substructure As They Translocate. *ACS Nano* **2012**, *6* (8), 7295–7302. https://doi.org/10.1021/nn302413u.

(222) Qiu, Y.; Vlassiouk, I.; Hinkle, P.; Toimil-Molares, M. E.; Levine, A. J.; Siwy, Z. S. Role of Particle Focusing in Resistive-Pulse Technique: Direction-Dependent Velocity in Micropores. *ACS Nano* **2016**, *10* (3), 3509–3517. https://doi.org/10.1021/acsnano.5b07709.

(223) Pevarnik, M.; Schiel, M.; Yoshimatsu, K.; Vlassiouk, I. V.; Kwon, J. S.; Shea, K. J.; Siwy, Z. S. Particle Deformation and Concentration Polarization in Electroosmotic Transport of Hydrogels through Pores. *ACS Nano* **2013**, *7* (4), 3720–3728. https://doi.org/10.1021/nn400774e.

(224) Darvish, A.; Goyal, G.; Aneja, R.; Sundaram, R. V. K.; Lee, K.; Ahn, C. W.; Kim, K. B.; Vlahovska, P. M.; Kim, M. J. Nanoparticle Mechanics: Deformation Detection: Via Nanopore Resistive Pulse Sensing. *Nanoscale* **2016**, *8* (30), 14420–14431. https://doi.org/10.1039/c6nr03371g.

(225) Darvish, A.; Lee, J. S.; Peng, B.; Saharia, J.; VenkatKalyana Sundaram, R.; Goyal, G.; Bandara, N.; Ahn, C. W.; Kim, J.; Dutta, P.; Chaiken, I.; Kim, M. J. Mechanical Characterization of HIV-1 with a Solid-State Nanopore Sensor. *Electrophoresis* **2019**, *40* (5), 776–783. https://doi.org/10.1002/elps.201800311.

(226) Qiu, Y.; Lin, C. Y.; Hinkle, P.; Plett, T. S.; Yang, C.; Chacko, J. V.; Digman, M. A.; Yeh, L. H.; Hsu, J. P.; Siwy, Z. S. Highly Charged Particles Cause a Larger Current Blockage in Micropores Compared to Neutral Particles. *ACS Nano* **2016**, *10* (9), 8413–8422. https://doi.org/10.1021/acsnano.6b03280.

(227) Leong, I. W.; Tsutsui, M.; Yokota, K.; Taniguchi, M. Salt Gradient Control of Translocation Dynamics in a Solid-State Nanopore. *Anal. Chem.* **2021**,

93 (49), 16700–16708. https://doi.org/10.1021/acs.analchem.1c04342.

(228) Salgin, S.; Salgin, U.; Bahadir, S. Zeta Potentials and Isoelectric Points of Biomolecules: The Effects of Ion Types and Ionic Strengths. *Int. J. Electrochem. Sci.* **2012**, *7* (12), 12404–12414.

(229) Sahu, S.; Zwolak, M. Maxwell-Hall Access Resistance in Graphene Nanopores. *Phys. Chem. Chem. Phys.* **2018**, *20* (7), 4646–4651. https://doi.org/10.1039/c7cp07924a.

(230) Melnikov, D. V.; Hulings, Z. K.; Gracheva, M. E. Electro-Osmotic Flow through Nanopores in Thin and Ultrathin Membranes. *Phys. Rev. E* **2017**, *95* (6), 1–8. https://doi.org/10.1103/PhysRevE.95.063105.

(231) Charron, M.; Briggs, K.; King, S.; Waugh, M.; Tabard-Cossa, V. Precise DNA Concentration Measurements with Nanopores by Controlled Counting. *Anal. Chem.* **2019**, *91* (19), 12228–12237. https://doi.org/10.1021/acs.analchem.9b01900.

(232) Van Dorp, S.; Keyser, U. F.; Dekker, N. H.; Dekker, C.; Lemay, S. G. Origin of the Electrophoretic Force on DNA in Solid-State Nanopores. *Nat. Phys.* **2009**, *5* (5), 347–351. https://doi.org/10.1038/nphys1230.

(233) Kirby, B. J.; Hasselbrink, E. F. Zeta Potential of Microfluidic Substrates: 1. Theory, Experimental Techniques, and Effects on Separations. *Electrophoresis* **2004**, *25* (2), 187–202. https://doi.org/10.1002/elps.200305754.

(234) Deamer, D.; Akeson, M.; Branton, D. Three Decades of Nanopore Sequencing. *Nat. Biotechnol.* **2016**, *34* (5), 518–524. https://doi.org/10.1038/nbt.3423.

(235) Drndić, M. 20 Years of Solid-State Nanopores. *Nat. Rev. Phys.* **2021**, *3* (9), 606. https://doi.org/10.1038/s42254-021-00363-w.

(236) Ying, Y.-L.; Hu, Z.-L.; Zhang, S.; Qing, Y.; Fragasso, A.; Maglia, G.; Meller, A.; Bayley, H.; Dekker, C.; Long, Y.-T. Nanopore-Based Technologies beyond DNA Sequencing. *Nat. Nanotechnol.* **2022**, *17* (11), 1136–1146. https://doi.org/10.1038/s41565-022-01193-2.

(237) Spitzberg, J. D.; Zrehen, A.; van Kooten, X. F.; Meller, A. Plasmonic-Nanopore Biosensors for Superior Single-Molecule Detection. *Adv. Mater.* **2019**, *31* (23), 1–18. https://doi.org/10.1002/adma.201900422.

(238) Parkin, W. M.; Drndić, M. Signal and Noise in FET-Nanopore Devices. *ACS Sensors* **2018**, *3* (2), 313–319. https://doi.org/10.1021/acssensors.7b00708.

(239) Fu, K.; Bohn, P. W. Nanopore Electrochemistry: A Nexus for Molecular Control of Electron Transfer Reactions. *ACS Cent. Sci.* **2018**, *4* (1), 20–29. https://doi.org/10.1021/acscentsci.7b00576.

(240) Schmid, S.; Stömmer, P.; Dietz, H.; Dekker, C. Nanopore Electro-Osmotic Trap for the Label-Free Study of Single Proteins and Their Conformations. *Nat. Nanotechnol.* **2021**, *16* (11), 1244–1250. https://doi.org/10.1038/s41565-021-00958-5.

(241) Yu, L.; Kang, X.; Li, F.; Mehrafrooz, B.; Makhamreh, A.; Fallahi, A.; Foster, J. C.; Aksimentiev, A.; Chen, M.; Wanunu, M. Unidirectional Single-File Transport of Full-Length Proteins through a Nanopore. *Nat. Biotechnol.* **2023**, 2021.09.28.462155. https://doi.org/10.1038/s41587-022-01598-3.

(242) Robin, P.; Emmerich, T.; Ismail, A.; Niguès, A.; You, Y.; Nam, G.-H.; Keerthi, A.; Siria, A.; Geim, A. K.; Radha, B.; Bocquet, L. Long-Term Memory and Synapse-like Dynamics in Two-Dimensional Nanofluidic Channels. *Science (80-.).* **2023**, *379* (6628), 161–167. https://doi.org/10.1126/science.adc9931.

Biography

Iat Wai Leong received a Bachelor of Science degree in Chemistry in 2015 from National Cheng Kung University. In 2015-2017, he worked as a research assistant at the University of Macau. After that, he moved to Osaka University and received his Master of Science degree in Chemistry in 2020. He is currently pursuing a Ph.D. degree in Chemistry at Osaka University working on the development of solid-state nanopores. The research topics are mainly focused on single-molecule, single-particle analysis technology and nanofluidic devices.

List of publications and conference presentations

Publications

1. **Iat Wai Leong**; Makusu Tsutsui; Kazumichi Yokota; Sanae Murayama; Masateru Taniguchi, Regulating Nonlinear Ion Transport through a Solid-State Pore by Partial Surface Coatings, *ACS Applied Materials & Interfaces*, 2023, in press.
2. Makusu Tsutsui; Kazumichi Yokota; **Iat Wai Leong**; Yuhui He; Tomoji Kawai, Sparse multi-nanopore osmotic power generators. *Cell Reports Physical Science*, 2022, 3, 101065
3. **Iat Wai Leong**; Shohei Kishimoto; Makusu Tsutsui; Masateru Taniguchi, Interference of electrode ion diffusion in nanopore sensing. *iScience*, 2022, 25, 105073
4. Shohei Kishimoto; **Iat Wai Leong**; Sanae Murayama; Tomoko Nakada; Yuki Komoto; Makusu Tsutsui; Masateru Taniguchi, 3D designing of resist membrane pores via direct electron beam lithography, *Sensors and Actuators B: Chemical*, 2022, 357, 131380
5. **Iat Wai Leong**; Makusu Tsutsui; Kazumichi Yokota; Masateru Taniguchi, Salt gradient control of translocation dynamics in a solid-state nanopore, *Analytical Chemistry*, 2021, 93, 16700-16708
6. **Iat Wai Leong**; Makusu Tsutsui; Sanae Murayama; Tomoki Hayashida; Yuhui He; Masateru Taniguchi, Quasi-Stable Salt Gradient and Resistive Switching in Solid-State Nanopores. *ACS Applied Materials & Interfaces*, 2020, 12, 52175−52181
7. Shota Hattori; Rintaro Sekido; **Iat Wai Leong**; Makusu Tsutsui; Akihide Arima; Masayoshi Tanaka; Kazumichi Yokota; Takashi Washio; Tomoji Kawai; Mina Okochi, Machine learning-driven electronic identifications of single pathogenic bacteria. *Scientific Reports*, 2020, 10, 15525
8. **Iat Wai Leong**; Makusu Tsutsui; Sanae Murayama; Yuhui He; Masateru Taniguchi, Electroosmosis-Driven Nanofluidic Diodes. *The Journal of Physical Chemistry B*, 2020, 124, 7086−7092 (Featured on back cover)
9. **Iat Wai Leong**; Makusu Tsutsui; Tomoko Nakada; Masateru Taniguchi; Takashi Washio; Tomoji Kawai, Back-Side Polymer-Coated Solid-State Nanopore Sensors. *ACS Omega*, 2019, 4, 12561−12566

Conference presentations

1. **梁逸偉**、筒井真楠、谷口正輝、“固体ナノポアを介したイオン輸送におけるカチオン依存性”、第 16 回分子科学討論会 2022、横浜、2022 年 9 月、ポスター講演
2. **梁逸偉**、筒井真楠、谷口正輝、“クラウンエーテル錯体における固体ナノポアのイオン輸送特性”、第 82 回応用物理学会秋季学術講演会、仙台、2022 年 9 月、ポスター講演
3. **Iat Wai Leong**, Makusu Tsutsui, Masateru Taniguchi, “Asymmetric Ion and Fluid Transport in Solid-State Pores for Nanofluidic Circuits”, IUMRS-ICYRAM 2022, Fukuoka, Japan (hybrid meeting), August 2022, Oral presentation
4. **Iat Wai Leong**, Salt Gradient Control of Translocation Dynamics in a Solid-State Nanopore, Nanopore weekly meeting (Webinar), February 2022, Oral presentation (invited presentation)
5. **Iat Wai Leong**, Makusu Tsutsui, Masateru Taniguchi, “Rectification of ionic current in asymmetric dielectric coating solid-state nanopore under salt gradient”, The 102nd The Chemical Society of Japan Annual Meeting (2022), Online, March 2021, Poster presentation
6. **梁逸偉**、筒井真楠、谷口正輝、“固体ナノポアにおけるイオン濃度勾配を伴う 1 粒子ダイナミクス”、第 82 回応用物理学会秋季学術講演会、オンライン、2021 年 9 月、口頭講演
7. **Iat Wai Leong**, Makusu Tsutsui, Masateru Taniguchi, “Negative Differential Resistance in a Nanopore under Salt Gradient: Models of Surface Charge Effect”, The 101st The Chemical Society of Japan Annual Meeting (2021), Online, March 2021, Oral presentation（日本化学会第 101 春季年会 学生講演賞）
8. **梁逸偉**、筒井真楠、谷口正輝、“固体ナノポアにおける非対称イオン輸送”、第 81 回応用物理学会秋季学術講演会、オンライン、2020 年 9 月、口頭講演
9. **Iat Wai Leong**, Makusu Tsutsui, Masateru Taniguchi, “Asymmetric ionic transport through low-aspect-ratio nanopore under electrolyte concentration gradient”, The 100th The Chemical Society of Japan Annual Meeting (2020), Tokyo, March 2020, Oral presentation
10. **Iat Wai Leong**, Makusu Tsutsui, Masateru Taniguchi, “Asymmetric ionic-voltage relation in low-aspect-ratio nanopore under salt gradients”, International Symposium for Nano Science (ISNS) 2019, Interactive Materials Science Cadet (IMSC) Program, Osaka, Japan, November 2019, Poster presentation

11. **梁逸偉**、筒井真楠、谷口正輝、“ナノポアによる単一ナノ粒子の形状解析の開発”、大阪大学インタラクティブ物質科学・カデットプログラム第 7 回インタラクティブ交流会、2019 年 8 月、滋賀、ポスター発表（最優秀ポスター賞）
12. **Iat Wai Leong**, Makusu Tsutsui, Masateru Taniguchi, “Characterization of single nanoparticle shape using solid state nanopore”, The 66th The Japan Society of Applied Physic Spring Meeting (2019), Tokyo, March 2019, Oral presentation
13. **梁逸偉**、筒井真楠、谷口正輝、“ナノポアによる非球面ナノ粒子の計測”、日本化学会新領域ナノスケール分子デバイス第 8 回若手セミナー、2019 年 3 月、埼玉、口頭発表（学生講演賞）
14. **Iat Wai Leong**, Makusu Tsutsui, Masateru Taniguchi, “Non-spherical gold nanoparticle translocation through a solid-state nanopores”, The 99th The Chemical Society of Japan Annual Meeting (2019), Kobe, March 2019, Oral presentation

Acknowledgment

This work was carried out at SANKEN, Osaka University from 2018 to 2023. I would like to sincerely thank my advisor Professor Masateru Taniguchi for his excellent guidance and for providing me with the precious opportunity to study in his laboratory. It's my great honor to work here and I am really enjoying the time. I would like to thank Professor Makusu Tsutsui, who has given me professional supervision on my research and given much advice for my academic career.

I would like to express my gratitude to Professor Nakazawa and Professor Matsumoto, for their crucial and fruitful comments on this thesis.

I am very grateful to Dr. Kazumichi Yokota, Professor Yuki Komoto and Professor Akihide Arima. Thanks very much for their helpful suggestions and during my Ph.D. period. Also, I would like to thank all administrative and technical support from Ms. Noriko Fujibayashi and Mrs. Sanae Murayama. I would like to thank all my dear alumni and labmates.

Thanks for the financial support from the IMSC program, JSPS and ACT-X project.

I would like to thank my parents, who gave the freedom, financial support, and warm encouragement to me for exploring the world and doing what I want to do. This thesis would not exist without them.

Iat Wai LEONG

Osaka, January 2023

“His true monument lies not on the shelves of libraries, but in the thoughts of men, and in the history of more than one science.” - Josiah Willard Gibbs.

2023 SANKEN, Osaka University

Mihogaoka 8-1, Ibaraki, Osaka 567-0047. JAPAN